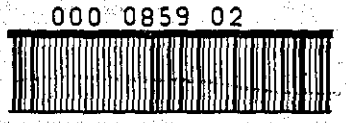

This book was bound by

Badminton Press
18 Half Croft, Syston, Leicester, LE7 8LD
Telephone: Leicester (0533) 602918.

A STUDY OF GRAPHITE MORPHOLOGY CONTROL IN CAST IRON

by

STEVEN ERNEST FRANKLIN, BSc

A Doctoral Thesis

Submitted in partial fulfilment of the requirements for the award of Doctor of Philosophy of the Loughborough University of Technology.

May 1986

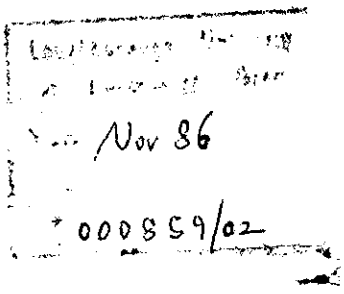
Nov 86
000859/02

DEDICATION

This work is dedicated to Marina, for her great patience and understanding, and to my Mother, who has always shown faith in my academic ability.

ABSTRACT

The objectives of the research project were to gain a deeper understanding of the factors influencing the graphite morphology in cast iron, particularly the role of different solute elements in relation to the industrial manufacture of compacted graphite iron.

A number of melt treatment processes were assessed for their abilities to produce low nodularity compacted graphite microstructures over a range of casting section thicknesses. In this respect, the magnesium-titanium method was found to be superior to treatment using cerium mischmetall and calcium additives, and very promising results were obtained with methods using zirconium as a major constituent of the treatment alloy.

Scanning electron microscopy, secondary ion mass spectrometry and X-ray microanalysis were used to study the structural characteristics of different cast iron microstructures and the elemental distributions of important solutes between the phases. This information was used to clarify the role of the main solute elements in graphite morphology control and to assess current graphite growth theories.

CONTENTS

CHAPTER 1

INTRODUCTION

1. INTRODUCTION

In the industrial production of cast iron, the most important of the range of graphite forms that can occur are flake, spheroidal and compacted. Each of these morphologies has a distinctive appearance, both in a plane polished section and in three dimensions, and gives rise to a particular range of cast iron properties. In a grey iron, for example, the graphite flakes have an interconnected structure which provides paths for efficient thermal conduction. However, the relatively sharp edges of the flakes act as stress-concentrators which substantially reduce the strength, ductility and toughness of cast iron. In contrast, the isolated graphite spheroids which occur in a nodular iron do not encourage thermal conductivity but act as crack-arrestors and improve the ductility and strength.

The graphite in compacted graphite (CG) iron is also interconnected, having structural characteristics which are between those of the flake and spheroidal forms. For a given matrix type, this material has improved thermal, casting, and machining properties compared to nodular cast iron, and superior ductility and strength compared to grey iron. This unique range of cast iron properties is attractive for particular engineering applications, and the main uses of CG iron are for the production of ingot moulds, internal combustion engine components and certain other vehicle and machinery parts. More extensive commercial exploitation of this material has been hindered by production problems such as a high sensitivity to variations in the melt composition and cooling rate. In the development of compacted graphite cast iron, attention has therefore focused on the difficulties associated with graphite morphology control in general.

During the solidification of cast iron melts, graphite is nucleated by potent substrates such as sulphide or oxide particles. The subsequent growth of the graphite determines its morphology and is influenced by several factors. The most important of these is the bulk melt chemistry, but the local conditions adjacent to the graphite/iron interface and the cooling rate are clearly also significant. Although a great deal of previous research has centred on the investigation of these factors, the mechanisms involved in the graphite growth process are still not well understood. This applies particularly to the role of solute elements, for which several different theories have been proposed in the literature.

The aim of this research was to provide information about the growth characteristics of different graphite forms and the influence of solute elements on the growth process. This would then serve as a basis for the development of improved melt treatments for cast iron production.

1.1 Scope of the Research

In order to investigate the effect of different elements on the graphite growth process, a programme of experiments was devised in which the individual and combined influences of various additives on the graphite morphology could be assessed. This was achieved by examining the microstructures present in castings which were produced using different treatment compositions. All other variables in the casting process were maintained as constant as possible within the limitations of the resources available. In addition, the casting pattern used was designed in such a way that the effect of section size on the microstructure could also be assessed for each treatment composition.

These experiments subsequently allowed a comparison to be made between several common methods of CG iron production, and also provided a range of samples containing different graphite morphologies including the flake, compacted and spheroidal forms. Selected examples of these were examined using optical and scanning electron microscopy together with specialised etching techniques to facilitate a close study of their individual structures.

The roles of solute elements in graphite morphology control were studied with the aid of Secondary Ion Mass Spectrometry (SIMS) and energy-dispersive X-ray microanalysis. These techniques were used to carry out a detailed investigation of the elemental distributions of important solutes between the phases in cast iron samples produced using different treatment compositions.

This information was used to clarify the role of the main solute elements in the graphite growth process and to assess current graphite growth theories.

CHAPTER 2

GRAPHITE GROWTH CHARACTERISTICS

2. GRAPHITE GROWTH CHARACTERISTICS

In order to understand the factors influencing the graphite growth process in cast iron, it is necessary to be aware of the substructure of different graphite forms and the solidification processes involved. Figure 1 illustrates the hexagonal crystal structure of graphite and defines the 'a' and 'c' axis directions in the lattice.

2.1 Flake Graphite

Flake graphite grows predominantly in the 'a' axis direction by the successive addition of atoms onto the prism planes (1-5). Growth is influenced by the diffusion of surface-active impurities to the graphite/iron interface where they lower the interfacial energy (5). The importance of sulphur and oxygen in this respect is well documented (5-8) although the precise mechanisms involved and the relative importance of these solutes are uncertain.

The growth rate of flake graphite is high in comparison with the spheroidal form and this causes the graphite to form a coupled eutectic with the austenite phase. The ends of the flakes are in contact with the melt during growth (3, 9-11) and undergo frequent branching so that a continuous network of interconnected graphite flakes is produced throughout each eutectic cell.

2.2 Spheroidal Graphite

The production of SG iron can be achieved either by melt treatment with strong sulphide and oxide forming elements such as magnesium, cerium, and calcium, or by using a vacuum casting process with high purity Fe-C-Si alloys. This indicates that spheroidal graphite growth is influenced by either the neutralisation of sulphur and

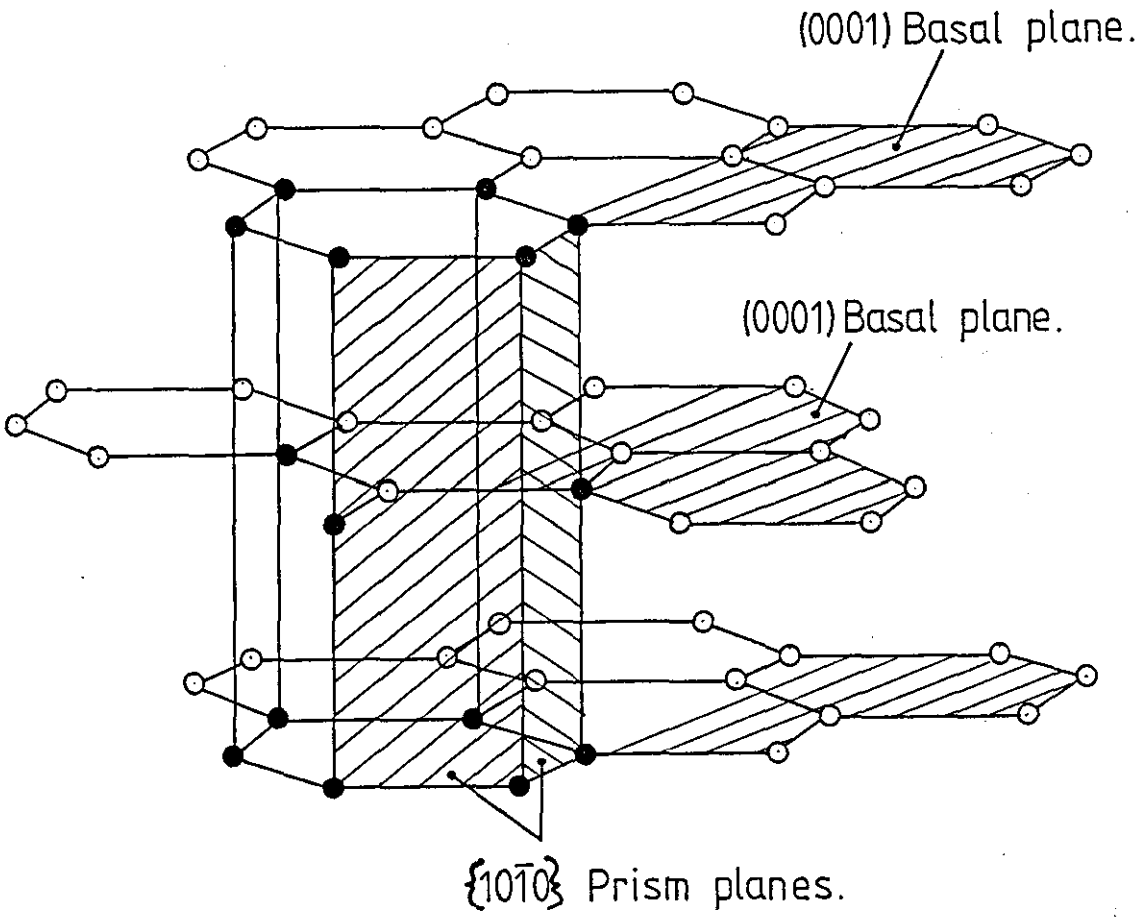

Direction normal to basal planes = 'c'- axis.
Direction normal to prism planes = 'a'- axis.

Figure 1. The crystal structure of graphite.

oxygen or the removal of these solutes from the melt. It has also been suggested that some of the elements used in SG iron production may affect the growth process in a more direct fashion (12, 13, 14).

Experimental techniques such as electron and X-ray diffraction have provided a limited amount of information on the crystal structure of nodular graphite. These studies have shown that in regions at and close to the surface of a graphite spheroid, the basal planes show a preferred orientation perpendicular to the radii (15, 16, 17). In addition, optical microscopy using polarised light indicates the presence of numerous crystallites radiating from a common centre (2, 3, 11, 18, 19). Based on these observations, one model of a graphite spherulite which is often cited in the literature (4, 12, 20-25) involves a radial arrangement of graphite crystallites with their basal planes aligned as shown in Figure 2.

With the aid of polarised light microscopy, Morrogh (26) has demonstrated that neighbouring crystallites in graphite nodules are often oriented at angles other than would be expected on the basis of the simple model illustrated in Figure 2. Morrogh suggests an alternative, more complex configuration in which the crystallites are twisted about their growth axes and curved in space so that their basal planes are no longer necessarily perpendicular to the radius of the spherulite. A schematic representation of this arrangement is shown in Figure 3 (26). As with the previous model (Figure 2), growth of the crystallites is assumed to occur by a defect-assisted mechanism involving the addition of atoms onto the steps of screw dislocations whose axes are perpendicular to the basal planes (5, 12, 27, 28, 29). The edge of each screw dislocation winds around the dislocation axis, resulting in a

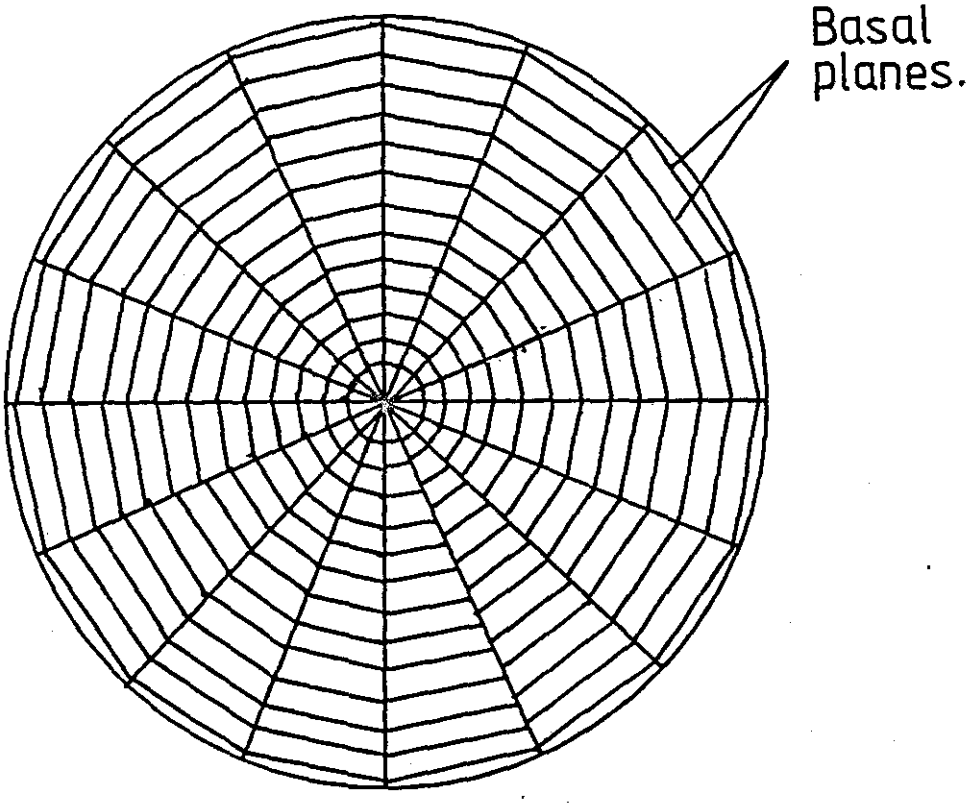

Figure 2. Simplified model of a graphite nodule.

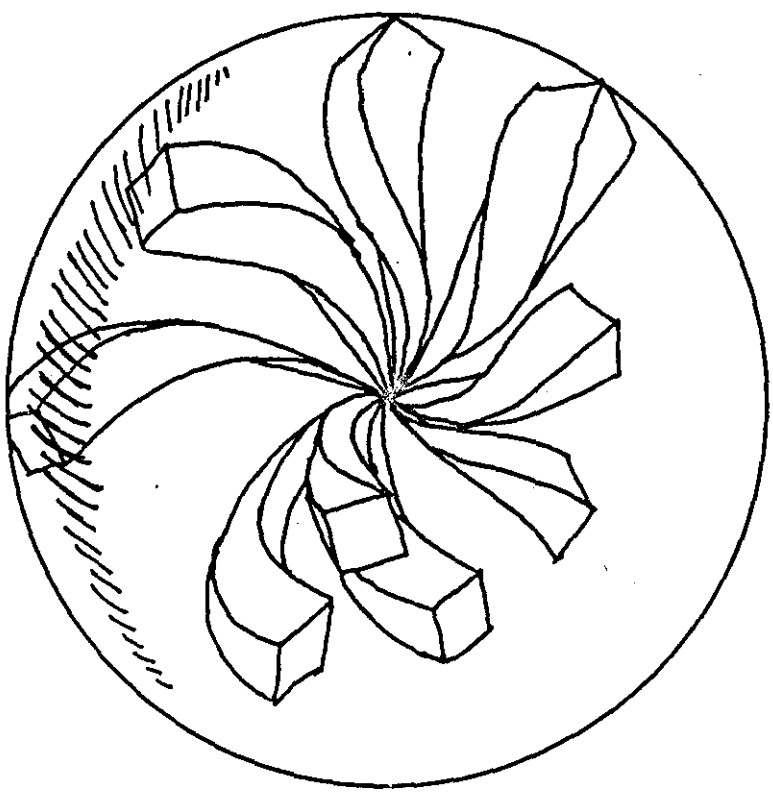

Figure 3. Morrogh's model of a graphite spherulite (26).

predominant growth direction normal to the basal planes. Oldfield et al (27) have suggested that the curved and twisted aspect of the crystallites in Figure 3 is due to the presence of a small edge component on each screw dislocation.

Other methods which have been employed to study the crystal structure of graphite have involved the use of scanning electron microscopy following preparation of the graphite surface using ion (2, 4, 11, 30, 31, 32), thermal (1), or plasma (33) etching. These techniques produce relief patterns on the graphite surface which indicate the orientation of the basal planes (1). Graphite nodules etched in this way usually exhibit one of the pattern types illustrated in Figure 4, which for the sake of clarity will be referred to as the concentric ring (Figure 4a) and the chevron (Figure 4b) patterns. In one report, Hunter and Chadwick (1) examined several graphite nodules to gain information on how the basal plane structure of spheroidal graphite was arranged in three dimensions. This was assessed by alternately polishing and thermally re-etching an SG iron sample, and photographically recording the etched surfaces of selected nodules prior to each successive polish. The results showed that the chevron patterns and radial intercrystallite boundary markings appeared more frequently in sections at and close to the nodule diameter, whereas the concentric ring patterns occured more often in non-diametral sections. It was also observed that the chevron angle increased from 50-100^{o} near the centre of the spheroid to 100-180^{o} near the periphery.

The observations recorded by Hunter and Chadwick do not lend themselves readily to explanation using the models illustrated in

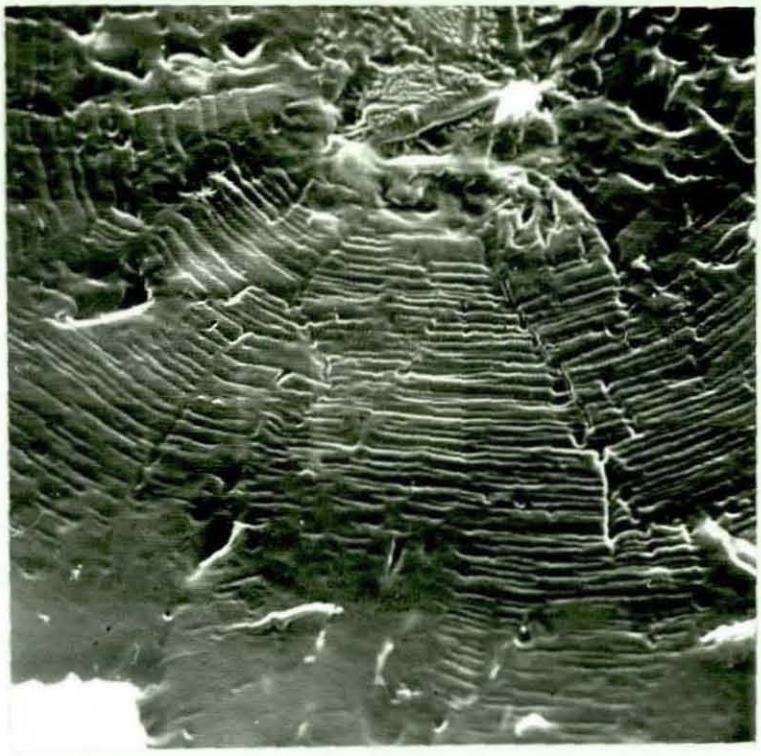

5000X

(a) Concentric Ring Pattern

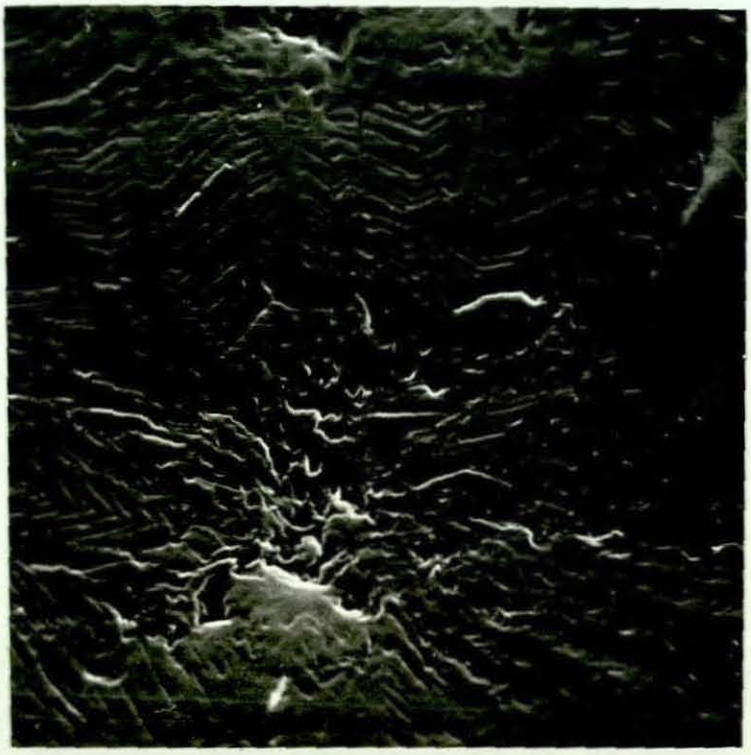

5000X

(b) Chevron Pattern

Figure 4 Surface Relief Patterns Produced by Ion Etching Graphite Nodules

Figures 2 and 3. For example, although Figure 2 clearly demonstrates how a concentric ring pattern could be produced by a radial arrangement of crystallites, this model would offer no explanation for the chevron effect observed in diametral sections. Conversely, it is apparent from Figure 5 that the basal planes of a number of crystallites growing randomly in the twisted manner suggested by Morrogh (Figure 3) could form a type of chevron pattern. This effect, however, would only occur in certain regions of the etched nodule surface where adjacent crystallites are suitably oriented, and the model has difficulty accounting for the regularity of the pattern variations occurring within the spheroid structure. This applies to both the change in chevron angle with position along the nodule radius, and the transition from chevron pattern in sections close to the spheroid diameter to concentric ring pattern in non-diametral sections.

Double and Hellawell (3, 34) have suggested a refinement of Morrogh's model for spherulitic growth which provides a more substantial explanation of the observed phenomena. In the refined model, the concept of a radial dispersion of graphite crystallites is conserved, but each of the crystallites is assumed to grow in a conical-helix fashion by the successive addition of carbon atoms onto the prism planes. This is illustrated schematically in Figure 6. It was proposed that this type of structure is formed by the helical growth of a basal graphite sheet about a central axis due to the advancement of a screw dislocation.

Figures 7a and 7b demonstrate that different sections through the cone-helix configuration can produce patterns similar to those observed experimentally in etched graphite nodules. It is prudent

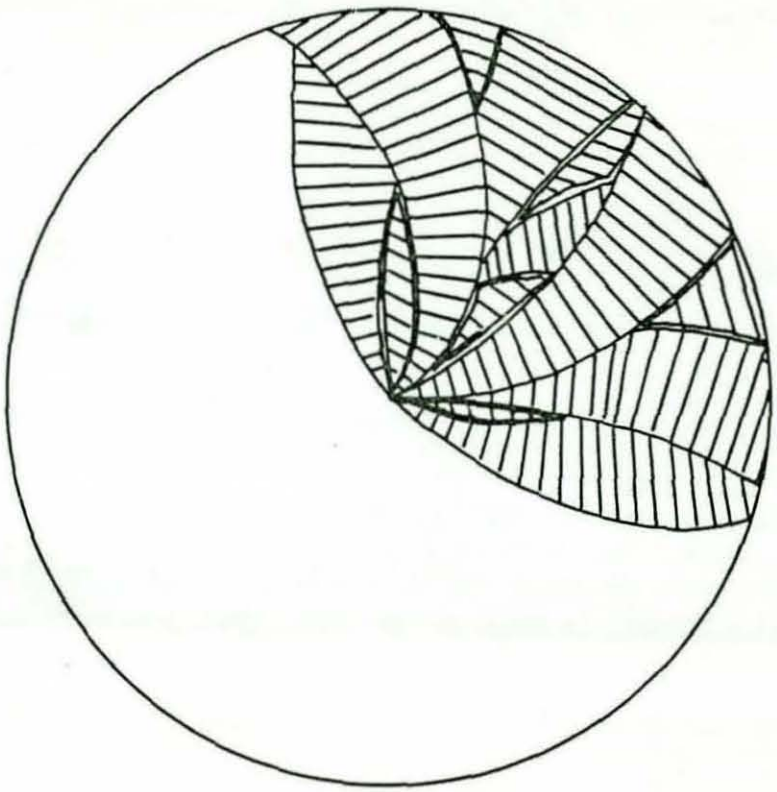

Figure 5. Possible patterns produced by the basal planes of a number of intersecting crystallites.

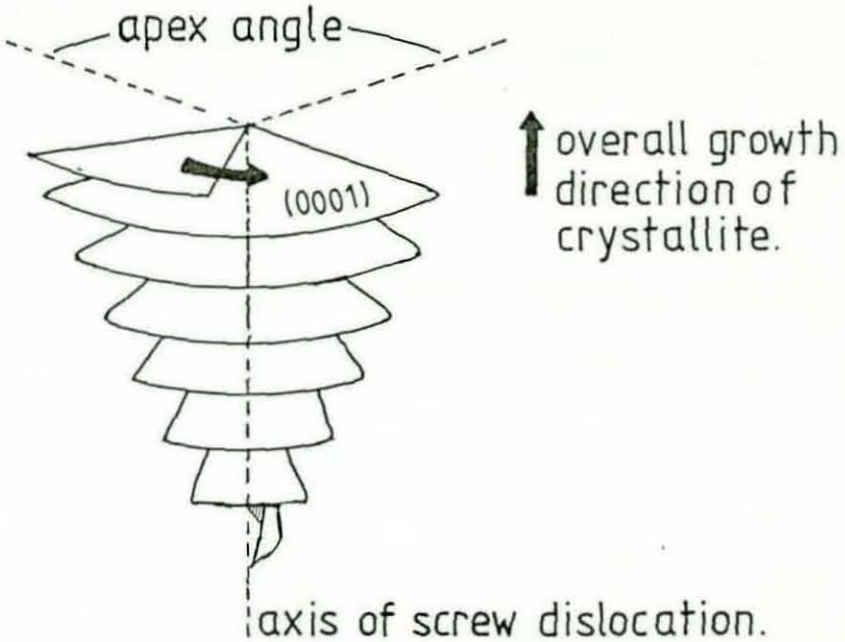

Figure 6 Cone-helix structure.

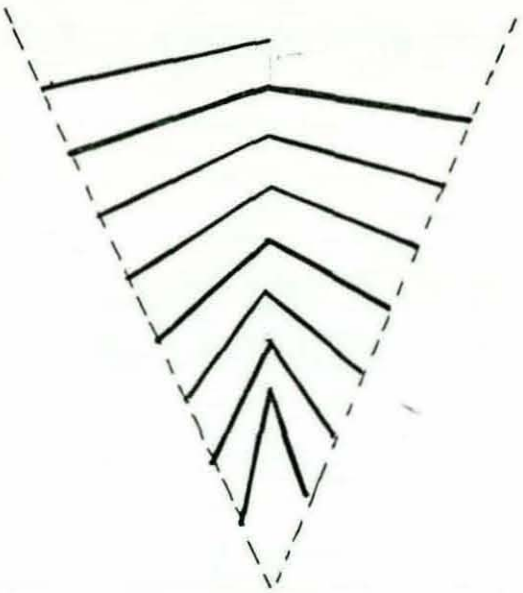

a) Section close to the growth axis.

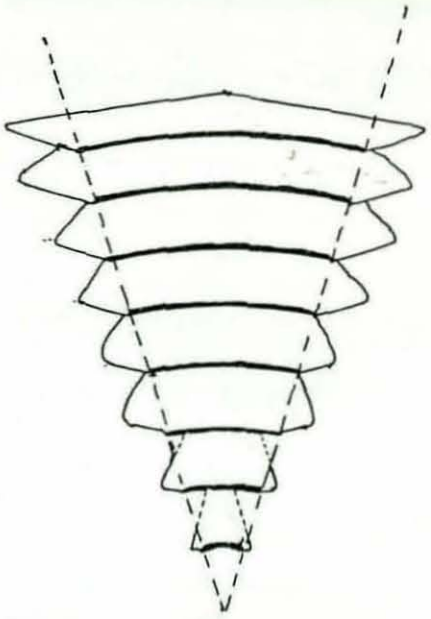

b) Section positioned away from the growth axis.

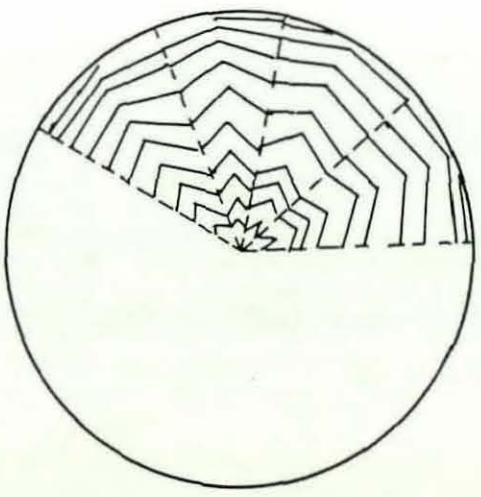

Diametral spheroid section.

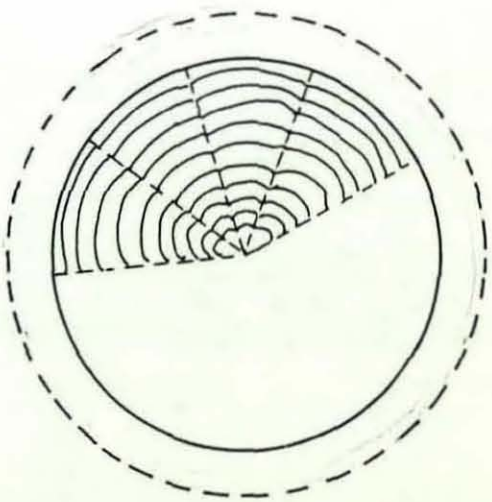

Non-diametral spheroid section.

Figure 7. Cone-helix model for crystallites in a graphite spheroid.

to note that these figures are necessarily simplified to clearly illustrate the above points. It would be expected that in a real situation, the crystallites would be more irregular, and curved to account for the observations of curved crystallites noted by Morrogh (26) using polarised light microscopy. Since the crystallites are arranged radially in the spheroid, a section across the diameter of a nodule would be expected to cut a large proportion of the cone-helix structures longitudinally in a position close to their growth axes. Figure 7a shows that in this case, adjacent sectioned crystallites would tend to produce a chevron-like pattern of basal planes. The radial variation in the chevron angle also observed experimentally by Hunter and Chadwick (1) is accounted for by a gradual increase in the apex angle of the cone helix as growth of the crystallite proceeds. In a non-diametral section through the spheroid structure, a greater proportion of the sectioned crystallites would be expected to exhibit a curved pattern of basal planes similar to that shown in Figure 7b. A concentric ring effect would be produced by a radial arrangement of the latter patterns.

One feature common to the models suggested by Morrogh (26) and Double and Hellawell (3, 34) is that nodular graphite growth is aided by the presence of crystal defects including dislocations. Subramanian et al (28) have estimated the growth kinetic curve for defect-assisted spheroidal growth in comparison with the diffusion-controlled growth curves for austenite, cementite and flake graphite. Cementite is one of the most kinetically favourable of all the competing phases, although its formation can be suppressed in cast irons by appropriate ternary additions such as silicon, to the binary Fe-C alloy. The effect of silicon is to simultaneously

raise the austenite-graphite eutectic temperature and lower the austenite-carbide eutectic temperature (35). This is caused by an alteration of the free energies of the austenite, graphite and carbide phases and through the interaction effect of silicon on the carbon in solution. With regard to spheroidal graphite formation, Subramanian et al (28) estimated that a defect-assisted growth mechanism requires a higher driving force than a diffusion-controlled mechanism to achieve the same growth velocity. Thus, a relatively high undercooling is recorded in the solidification of nodular cast iron when compared to flake graphite iron (see Figure 8). Due to the large difference in growth rates between spheroidal graphite and austenite, coupled eutectic growth is not possible and the graphite and austenite phases must solidify as a divorced eutectic. The spheroids are in contact with the liquid at least in the initial growth stages (11, 28, 36-42).

2.3 Compacted Graphite

Interrupted solidification has been used by a number of investigators (11, 42-46) to gain information about the solidification process of compacted graphite cast iron. These experiments have been shown beyond doubt that compacted graphite grows as a weakly cooperative eutectic with austenite, and that one end of the graphite is in contact with the melt during growth as with the flake form. Some researchers (42, 43, 46) have also attempted to identify the morphology of graphite particles at very early stages in the solidification of CG irons. In agreement with proposals made in other publications (47, 48, 49), these results suggest that compacted graphite may develop following the degeneration of spheroidal-shaped graphite particles nucleated prior

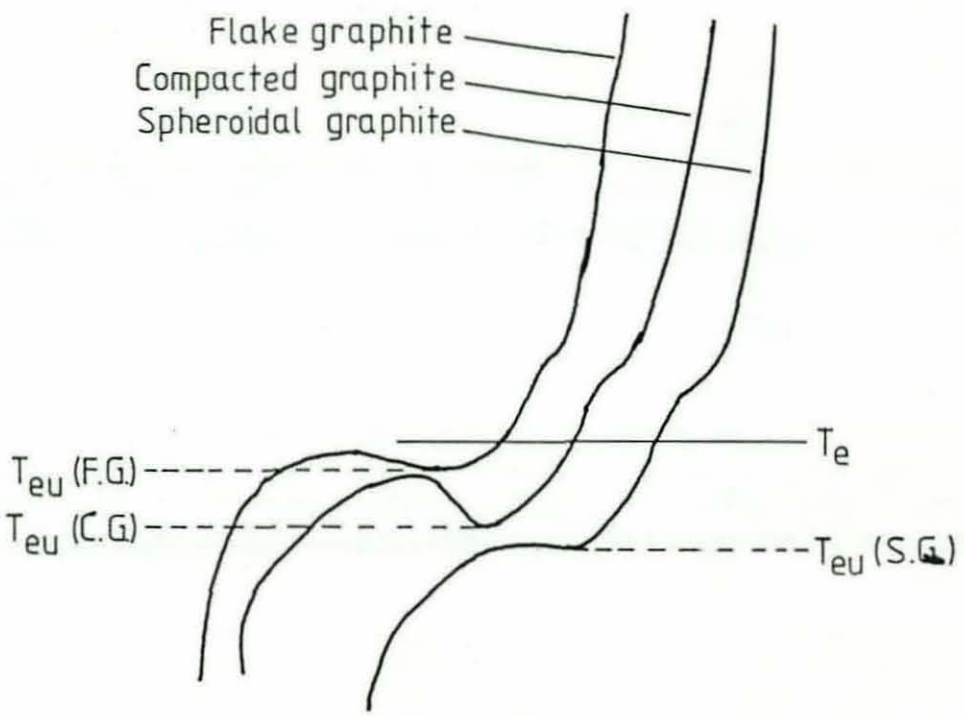

T_e = Eutectic Temperature.

T_{eu} = Eutectic Undercooling Temperature.

Figure 8. Typical cooling curves for different cast irons (50).

to the eutectic temperature. However, this hypothesis is not proven since the possibility of significant graphite growth occurring during the quenching period cannot be ruled out in these experiments.

The cooling curve for CG iron typically exhibits a low eutectic undercooling temperature (Teu) followed by a high recalescence. The latter is caused by the release of latent heat associated with the cooperative growth of the graphite and the austenite phases (43). The general forms of the cooling curve for flake, spheroidal and compacted graphite cast irons are shown in Figure 8 (50).

Although the cooperative eutectic growth of compacted graphite together with its interconnected structure suggests a similarity with flake graphite, other features indicate that it also has some of the characteristics of spheroidal graphite growth. For example, it has been noted in a number of publications (20, 21, 29, 51, 52, 53) that overlapping basal laths can be observed at the ends of compacted graphite particles, and that a similar structure can be seen on the surface of graphite spheroids.

In studies which have used ion etching to reveal the orientation of the basal planes, compacted graphite has been reported to exhibit near-concentric ring patterns (11) and markings oriented at right angles to the overall growth direction (43, 51, 54). In two cases (11, 54), however, the graphite did not appear to be fully compacted and resembled an imperfect form of spheroidal graphite. Furthermore, an examination of the micrographs presented in the reports of Pan et al (43) and Liu et al (51) reveals that the markings which were taken to represent basal plane traces are unlike

those shown in a greater number of other ion etching studies (2, 4, 11, 30, 31). Whether the results recorded by Pan et al and Liu et al truly indicate the basal plane structure of compacted graphite, or whether the markings observed were due to a misleading experimental effect cannot be resolved on the basis of the current experimental evidence.

Electron diffraction studies using transmission electron microscopy (55) have shown that the external surfaces of compacted graphite particles are composed of (0001) basal planes layered predominantly parallel to the surface. This lends support to other reported suggestions (45, 56, 57) that compacted graphite growth occurs predominantly along the 'a' axis for the bulk of the growth, but that the basal planes become oriented perpendicular to the overall growth direction at the end of the growth period. Although these proposals have not been confirmed by studies of the internal structure of compacted graphite, it is reasonable to expect different growth mechanisms to predominate at different parts of the compacted graphite structure depending on the local conditions adjacent to the graphite/iron interface. This is because during the graphite growth period, the remaining liquid is enriched with certain solutes including sulphur, oxygen and nodularising elements.

CHAPTER 3

THE ROLE OF SOLUTE ELEMENTS IN GRAPHITE MORPHOLOGY CONTROL

3. THE ROLE OF SOLUTE ELEMENTS IN GRAPHITE MORPHOLOGY CONTROL

The graphite morphology that will form in a cast iron is strongly dependant on the melt chemistry. For example, the significance of the melt sulphur and oxygen contents in the graphite growth process has long been recognised (5-8). These elements encourage the formation of the flake graphite form and there is some evidence to suggest that oxygen may be more important than sulphur in this respect (6, 8, 58). Melt treatment with elements such as magnesium, calcium and the rare earths encourages nodularisation of the graphite phase and these additives act primarily through the control of the sulphur and oxygen contents of the melt. A further group of elements which include titanium and aluminium are also known to interfere directly or indirectly with the spheroidisation process and are thus often termed denodularising elements. The published literature regarding the respective effects of these groups of elements on the graphite morphology in cast iron is reviewed below.

3.1 Sulphur and Oxygen

It has been demonstrated by a number of investigators that sulphur and oxygen are surface-active in cast iron. For example, Johnson and Smartt (58, 59) used Auger electron spectroscopy to show that in a flake graphite iron containing 0.04 wt % sulphur, the graphite/iron interfaces are enriched in sulphur and oxygen. The reported levels of these elements in the interfacial region were 5 and 20 atomic percent respectively, and using a similar technique, Hrusovsky (57) also detected a small but unspecified level of sulphur at compacted graphite/iron interfaces. Studies carried out by Kevarian and Taylor (6) and McSwain and Bates (7) using the sessile drop method, have additionally shown that both oxygen and

sulphur lower the surface energy of liquid iron and also the interfacial energy between the iron and the graphite. The results of Kevarian and Taylor further indicated that oxygen has a comparatively greater effect than sulphur on the graphite/melt interfacial energy.

In the experiments carried out by McSwain and Bates (7), molten iron droplets of different compositions were placed onto single-crystal graphite substrates of known orientation. The results revealed that for a given increase in the melt sulphur content (not balanced by an increase in the level of nodularising element), the graphite/melt interfacial energy was reduced by the greatest extent when the prism planes were oriented parallel to the substrate surface. A smaller reduction was noted when the procedure was repeated with the basal planes oriented in the above way. The influence of oxygen in this respect was not determined, however, these results suggest that adsorption of surface-active impurities in general takes place preferentially on the prism planes of the graphite crystal lattice. A consideration of the bonding energies between the atoms in the prism and basal planes supports this suggestion. This is because in a pure graphite crystal, the Van der Waals forces that form the bond between adjacent basal planes (4-8 kJ mol^{-1} (5)) are much weaker than the bonding between carbon atoms in the 'a' axis direction, ie between adjacent prism planes (420-500 kJ mol^{-1} (5)). Consequently, in the absence of surface active impurities, the prism planes possess a higher surface energy than the basal planes and will therefore present more attractive adsorption sites (5, 22, 60).

Subramanian et al (5) suggest that sulphur and oxygen form bonds with the carbon atoms on the prism planes and convert the faceted

prism face of the pure graphite crystal to one that is atomically rough, or non-faceted. Support for this proposal stems from experiments using transmission electron microscopy to examine the morphology of the growing prism face of the graphite in irons of differing sulphur content. The studies revealed a much rougher (less faceted) prism face on the graphite in an iron containing a high sulphur concentration (0.05 wt %) compared to that in a lower sulphur content iron (0.005 wt % S). Since non-faceted interfaces are known to exhibit high mobility and grow under only small driving forces (61), it follows that the adsorption of sulphur and oxygen allows the prism face to grow rapidly at low undercooling. This results in flake graphite formation and the establishment of coupled eutectic growth with the austenite phase, which also has a non-faceted interface.

Sadocha and Gruzleski (62) have suggested that a further role for sulphur and oxygen in graphite morphology control may be to hinder dislocation movement in the graphite crystal lattice, which could otherwise assist in the growth of graphite spheroids. As mentioned in the previous chapter, crystal defects are considered to play an essential part in the nodular graphite growth process. The impurities would be expected to have their effect by adsorbing on the defects which, like the prism planes, represent regions of relatively high energy in the lattice. This would reduce the energy and mobility of the defects and increase their stability. A similar effect has also been suggested by Purdy and Audier (17).

The results reported by Johnson and Smartt (58) and Kevarian and Taylor (6) also indicate that compared to sulphur, oxygen may have a

greater influence on the graphite growth process. Furthermore, by chemically analysing flake graphite extracted from a cast iron, Francis (8) determined that approximately 0.25 atomic percent oxygen was present in the graphite but comparatively little sulphur, which also suggests that oxygen is the more important growth modifier. This is further supported by a comparison of the carbon-oxygen (1077 kJ mol^{-1}) and carbon-sulphur (699 kJ mol^{-1}) bond strengths (63) indicating that oxygen will adhere more strongly than sulphur to the graphite crystal surface.

3.2 Nodularising Elements

The most common nodularising elements used for graphite morphology control in industrial melt treatment processes are magnesium, calcium, and the rare earth elements. There is considerable evidence to support the proposal that the major function of these additives is to form stable sulphides and oxides, and thus prevent sulphur and oxygen from adsorbing at the graphite/melt interface. For example, using Auger electron spectroscopy, Johnson and Smartt (58) demonstrated that sulphur and oxygen enrichment occurred at the graphite/iron interface in a flake graphite iron, but not with a spheroidal graphite iron produced using a magnesium melt treatment. From experiments which involved chemically analysing graphite extracted from the iron matrix of cast irons, Francis (8) additionally concluded that excepting the graphite nuclei, very little sulphur and oxygen were present in graphite nodules compared to the levels of these elements that occurred in the flake form. In the latter experiments, the spheroidal graphite iron was produced using magnesium and rare earth additions, and had a similar residual bulk sulphur content to the flake graphite iron.

There is also strong evidence to suggest that the products formed in the desulphurisation and deoxidation reactions act as heterogenous substrates for the nucleation of graphite spheroids. For example, several publications have reported observations of non-metallic particles containing one or more of the elements magnesium, cerium and calcium in addition to sulphur and/or oxygen, in the centre of graphite nodules (8, 33, 49, 64-67). Although it is expected that these nuclei will be crystallographically compatible with the graphite lattice, it is unlikely that the substrate can exert a lasting influence on the graphite growth process because similar species have been observed in both flake and nodular graphite (8, 44, 65). In addition, commercial inoculants containing calcium, aluminium, barium or strontium have been shown to be effective in increasing the eutectic cell or nodule count of both grey and spheroidal graphite iron (7).

Other investigators have proposed models that describe a more direct role for the nodularising elements in graphite morphology control. Although the models differ in detail, the most important general assumption is that the nodularising elements themselves adsorb on the graphite crystal and affect growth in a specified crystallographic direction. Hillert and Lindblom (12), for example, suggest that magnesium and the rare earth elements form non-metallic bonds with carbon atoms on the graphite surface and are incorporated into the lattice during growth. This is considered to provide disturbances leading to the development of new screw dislocations which aid in the growth of spheroidal graphite. In contrast, Basdogan et al (13) suggest that the nodularising elements are adsorbed on the prism planes of the graphite crystal, and that this

hinders the attachment of carbon atoms to the prism face and retards the rapid 'a' axis growth required for the formation of flake graphite. Minkoff and Nixon (14) propose an alternative model based on observations made using a scanning electron microscope. In this hypothesis the nodulariser atoms adsorb on to the high-energy steps of existing screw dislocations occurring on the basal plane surface, and hinder the thickening of the graphite in the 'c' axis direction by impeding screw dislocation movement. The sequential adsorption of nodulariser atoms leads to increased branching and curving of the graphite crystal and eventually to spherulitic growth.

Although it is difficult to provide substantive evidence for any one of the above theories, the detection of some species of nodularising elements in certain parts of graphite spheroids has been reported in several publications. For example, X-ray microanalysis techniques have been used to examine graphite spheroids in hyper-eutectic cast irons and nickel-carbon alloys treated with rare earth metals (32, 68). In these experiments, several nodules were identified as having a duplex structure consisting of an inner region and an outer shell. The results indicated that cerium was distributed uniformly in the inner volume, and comparatively little cerium was detected elsewhere in the graphite phase. Whether the cerium occurred as a compound or in its elemental form was not determined in these experiments. The duplex structure has been attributed to a two-stage growth process where primary growth takes place in contact with the liquid to form the inner region, and secondary growth occurs after the spheroid is enveloped by austenite (18, 36, 37, 69). On this basis, the local concentration of cerium in the inner area must occur during the period of time that the graphite is surrounded by liquid iron.

Lanthanum segregation in the graphite phase in lanthanum treated nickel-carbon alloys has also been reported by Minkoff and Nixon (14). However, the paper chromatographic technique employed for quantitative analysis in these experiments is not spatially sensitive and could not be used to detect local variations in composition within the graphite.

The results of studies carried out by Fidos (70, 71) using secondary ion mass spectrometry also indicate that the graphite nodules which occurred in cast irons produced using magnesium additions contained significantly higher levels of magnesium and calcium compared to the surrounding iron matrix. Examination of the published data from these experiments reveals that the approximate atomic concentrations of magnesium and calcium in the graphite phase were recorded as 0.2% and 0.17% respectively. Other reported incidences of magnesium and calcium segregation in graphite nodules have been based on experiments using autoradiography (12, 69, 72, 73, 74) which is subject to large experimental errors associated with the high penetrating power of radioactive emission, leading to poor spatial resolution (75). These autoradiography results are therefore inconclusive.

Although the above observations indicate that enrichment of graphite spheroids can occur with at least some species of nodularisers, this does not necessarily imply that these elements have a direct role in the graphite growth process. Other evidence which has been used to support the direct influence of nodularising elements in graphite morphology control can also be interpreted in a number of ways. For example, it has been reported in several publications (22, 76, 77, 78) that an excess of magnesium, above that required for complete

desulphurisation, must be present in the melt for all the graphite to be precipitated out in the form of nodules. Initially, this appears to suggest that magnesium has an additional role to play in the graphite growth process, other than through its effect on the free sulphur content. It is also possible however, that the excess magnesium required is necessary to react with the dissolved oxygen level which was not taken into account in these experiments. The fact that nodular graphite can be produced by casting very high purity Fe-C-Si alloys or by using a vacuum purification process (58, 62, 79, 80, 81) further suggests that the main condition for spheroidal graphite growth is not the presence of nodularising elements, but the absence of dissolved impurities including sulphur and oxygen.

3.3 Denodularising Elements

In a foundry involved in the manufacture of SG iron, denodularising elements often originate from the unwanted impurities contained in the pig iron and scrap melted during the production process. However, titanium and aluminium can be used in conjunction with magnesium or other nodularising elements to promote the formation of compacted graphite (82, 83, 84). It is interesting, therefore, to review the published literature regarding the role of these elements in graphite growth processes.

The distribution of titanium and aluminium in compacted graphite cast irons produced using Mg-Ti-Al melt treatments have been investigated by Hrusovsky (57) and Su et al (45) using energy-dispersive X-ray microanalysis. The results of these experiments indicated that with normal compacted graphite, aluminium was enriched at the graphite/iron interface. However, when an area of a

compacted graphite particle that exhibited a more nodular appearance was analysed, this element appeared at a much lower level in the interfacial region (45). This result appears to indicate that aluminium has a direct influence on the graphite growth process, although it is also interesting to note that in experiments carried out by Young (85) using an electron microprobe to examine aluminium-bearing flake and nodular cast irons, aluminium was not detected in the graphite phase. With regard to titanium, the results of Hrusovsky (57) and Su et al (45) also indicate that this element does not segregate to graphite/iron interfaces, but occurs in carbo-nitride particles which are situated primarily in the iron matrix. It is well established that at slow cooling rates, the presence of sufficient nitrogen in a grey cast iron melt can result in compacted graphite structures (13, 86, 87, 88, 89). It has therefore been suggested (45, 57) that the denodularising influence of titanium and aluminium, both of which form stable nitrides (90, 91), may be partially attributed to the removal of nitrogen from solution. However, in view of the fact that the concentration of this element normally present in a cast iron melt is not sufficient to modify the flake graphite morphology by any significant extent, the effects of titanium and aluminium on the dissolved nitrogen content are not likely to make an important contribution to the denodularisation process.

Titanium, aluminium and zirconium are also known to promote austenite dendrite formation and refine the dendrite secondary arm spacing by providing suitable nucleation substrates in the form of carbides, nitrides, carbo-nitrides, and increasing the undercooling of the eutectic (23, 91, 92, 93). In a grey iron, this promotes the formation of interdendritic type D flake graphite (23, 92, 93, 94) which is more highly branched than the type A form.

With regard to compacted graphite iron, Hrusovsky (57) suggested that the greater presence of austenite as a result of titanium and/or aluminium additions would increase the segregation of solutes to the liquid regions, and considered the implications of this effect on the individual concentrations of different solute elements in these areas. On the basis of published values for the distribution coefficients and maximum solubilities of a number of elements in pure iron, Hrusovsky proposed that oxygen and sulphur would be partitioned to a greater extent in the interdendritic regions than magnesium and cerium. Thus, more favourable conditions for the formation of flake graphite would be promoted in the liquid areas between the pro-eutectic austenite dendrites.

Although Hrusovsky's proposal would provide a suitable explanation for the denodularising effects of titanium, aluminium and zirconium, the accuracy of the above analysis is questionable. The solubility of oxygen in austenite, for example, is highly sensitive to the presence of other solutes, notably silicon and aluminium (95), whereas Hrusovsky's data is based on the solubilities of the elements in pure iron. In addition, the value of 0.185 which the author lists as the maximum solubility of magnesium in iron in fact corresponds to the solubility of liquid magnesium in liquid iron under a pressure of 25 bar of argon (95). The solubility of magnesium in solid iron is actually reported to be so small that it cannot be measured experimentally (95). On this basis, the proportion of the iron's total magnesium content segregated to the liquid is likely to be much greater than assumed by Hrusovsky. The value of 0.015 referred to by this researcher for the distribution coefficient of sulphur between austenite and liquid iron,

$$\left(\text{distribution coefficient } Ko(x) = \frac{\%X \text{ in solid phase}}{\%X \text{ in liquid adjacent to the solidification front}}\right)$$

is also in some doubt. In a more recent report (96), this coefficient was calculated to be 0.06. Using the latter estimate, the segregation of sulphur would be less than that of cerium, with a distribution coefficient of 0.03 (57).

The formation of compounds between the nodularising and denodularising elements themselves has also been suggested as a likely mechanism for the influence of denodularisers (97, 98, 99). Experimental confirmation of this effect has been reported only for cerium-antimony particles (100, 101) which were detected using electron probe microanalysis when the levels of these elements in the iron were well above those normally encountered in commercial practice. Furthermore, it has been reported (100) that only 0.001% cerium mischmetall is required to neutralise the denodularising influence of 0.05% antimony in magnesium-treated nodular irons. In this case, the stoichiometric combination of the rare earth elements and antimony to form stable intermetallic phases would not be expected to significantly reduce the total antimony content. In addition, although cerium is also known to be effective in controlling the deleterious influence of titanium in spheroidal graphite iron production (100, 102, 103), these elements do not form intermetallic compounds (104). This does not, of course, necessarily exclude the formation of complex compounds other than intermetallics, such as carbides.

The suggestion (99, 105) that the influence of titanium on the graphite morphology in magnesium treated irons is due to its

adsorption on the graphite surface is not shown experimentally (45, 57). However, discrete titanium carbide particles are sometimes associated with degenerate spheroidal graphite particles (100).

3.4 Experimental Difficulties Associated with the Study of Solute Elements in Cast Iron

In spite of the extensive research which has been carried out into the influence of different solute elements on the graphite growth process in cast irons, the exact roles of these solutes remain uncertain. This may largely be attributed to the fact that even very low levels of certain solute elements including sulphur and oxygen are significant in the control of graphite morphology (5, 23, 64, 97, 100, 106). Interaction effects involving residual levels of these elements must also be important, and it is difficult to study their exact function particularly when information is lacking on their distributions in the specimen under consideration. This data is not easily obtained using conventional analytical techniques because the usefulness of methods such as energy and wavelength-dispersive X-ray analysis, Auger electron spectroscopy, and autoradiography are limited, either by a lack of elemental sensitivity or by spatial or elemental resolution problems.

For example, although Johnson and Smartt (58) were able to detect relatively large concentrations of sulphur and oxygen at flake graphite/iron interfaces using Auger electron spectroscopy, the hypothesis that these elements promote flake graphite growth by adsorbing preferentially on the prism planes predicts that sulphur and oxygen concentrations should occur throughout the flake and not only at the graphite/iron interface. It must therefore be assumed that the levels of these elements within the flake graphite were

below the detection limits of the technique used. Additional difficulties arise with Auger electron spectroscopy owing to the overlap that occurs with the characteristic Auger peaks of certain elements. For this reason, it is difficult to detect cerium in cast iron because the main Auger peak for this element occurs at an energy which is very close to that of one of the characteristic iron peaks, and it is therefore over-shadowed by the larger iron signal.

As noted previously, autoradiography is subject to large experimental errors associated with the high penetrating power and non-directional nature of the radioactive emission, which results in poor spatial resolution (75). In the experiments carried out by Bolotov et al (73), for instance, the darkening of the photographic film taken to represent sulphur enrichment within graphite flakes can also be interpreted on the basis of radiation from sulphur concentrations only at the flake/iron interface. Other drawbacks associated with autoradiography are that the distribution of only one element can be studied in any one sample, and that suitable isotopes with the necessary half-life and low-energy radiation must be readily available.

With regard to the X-ray microanalysis techniques, the energy-dispersive method again lacks the sensitivity required for the detection of low concentrations of elements. Also, it is difficult to resolve two elements which have similar characteristic X-ray energies. The latter problem is not as evident with the wavelength-dispersive method (electron microprobe), although neither of the X-ray microanalysis techniques can be used to study small concentrations of elements with a low atomic number. For example, oxygen can only be detected with the wavelength-dispersive method when a special type of crystal is used.

In contrast to the previous techniques, Secondary Ion Mass Spectrometry (SIMS) can detect very small quantities of all the elements of interest in cast iron with good spatial resolution. As a relatively recent development, SIMS has very rarely been used for the study of elemental distributions in cast iron, and only one example of this type of application has previously been reported (70). The latter investigation was restricted to flake and nodular graphite, and emphasis was placed on the segregation of elements to the graphite/iron interface and in the surrounding matrix. Other graphite morphologies were not included in this study and little attention was paid to the segregation of elements within the graphite phase, or to the composition of particles in the iron matrix. The SIMS technique was used extensively in the current research and will be described in greater detail in a subsequent section.

CHAPTER 4

PRODUCTION METHODS FOR COMPACTED GRAPHITE CAST IRON

4. PRODUCTION METHODS FOR COMPACTED GRAPHITE CAST IRON

The effects of some solute elements on the graphite growth process are exploited in the commercial production of different types of cast iron. For example, spheroidal graphite iron is normally produced by the addition of magnesium in the form of either ferro-silicon-magnesium or nickel-magnesium alloy. A small amount of cerium is also often included in the treatment alloy to neutralise the influence of impurities such as titanium, lead, bismuth and antimony, which are deleterious to nodule formation. From the point of view of graphite morphology control, compacted graphite iron is particularly interesting because its production relies upon the achievement of a balance between flake and nodular graphite growth. This is often accomplished commercially by a combined melt treatment with both nodularising and denodularising elements, and other production processes involve the controlled addition of one or more nodularisers in quantities lower than those required to produce a fully spheroidal graphite morphology. The range of industrial methods used for the production of compacted graphite cast iron are reviewed below.

4.1 Methods Based on Magnesium Treatment

The production of compacted graphite iron using conventional ladle treatment with magnesium additions alone (reduced magnesium method) is very difficult owing to the critical control required with the magnesium content of the treated iron (82, 83, 84), where the difference between under- and over-treatment can be as small as 0.005% Mg (82). Whilst the stirring action of the magnesium vapour is clearly beneficial to the treatment process, the rapid fading characteristic of magnesium treatment creates further problems in

achieving a precise melt composition, especially if the cooling rate is variable as in a casting of non-uniform section thickness. In addition, the treatment temperature must normally be kept within a narrow range since higher temperatures lead to under treatment through magnesium loss, and lower temperatures cause an increase in the final magnesium content of the melt and results in excessive nodular graphite formation.

One method of utilising the fading effect of magnesium for compacted graphite iron production is described by Tsutsumi et al (107). In trials carried out by these investigators, a low sulphur (0.006%) melt was initially overtreated with an addition of 0.2% magnesium (in the form of FeSiMg alloy) using the plunging method. Following postinoculation, the melt was held at 1420°C and a gas was blown into the liquid iron at a rate of 10 litre/minute for 60-90 seconds. The morphology of the graphite that occcured in the solidified castings was assessed using an image analysing computer which assigned an average graphite shape factor to the microstructure. Of the gases investigated, argon, nitrogen and air were found to produce acceptable results, although the use of methane or acetylene gases produced a microstructure with slightly better average compaction. This may be partially attributed to reducing conditions, set up in the melt by the presence of methane and acetylene, favouring the magnesium desulphurisation reaction.

The difficulties associated with magnesium treatment can also be reduced by using the Inmold treatment process (108), which employs a reaction chamber containing the required amount of magnesium alloy situated in the first part of the castings' runner system. Since

this chamber is carefully designed to produce a controlled and even solution of magnesium as the molten iron flows over the alloy, the composition of the treated melt can be maintained with the required degree of accuracy (109, 110, 111). In addition, the fading effect of magnesium becomes less significant because of the very short time interval between treatment and casting. The hazards due to the fumes and flaring which accompany magnesium additions are also reduced. However, the additional expense associated with the design of the specialised runner system required for each type of casting produced using the Inmold process means that in many cases, employment of this technique may be limited only to very long production runs.

4.2 Magnesium Used in Conjunction with Other Nodularising Elements

Compacted graphite cast iron can also be produced using magnesium and rare earth additions coupled with the employment of a sealed ladle which contains the treatment reaction and reduces fading (112). An example of the type of vessel that can be used for this process is shown in Figure 9, which illustrates the initial position of the ladle for reception of the melt from the furnace. Following this, the required quantity of magnesium-rare earth alloy is inserted into the shelf illustrated, and the ladle is then securely closed and rotated into the vertical position so that treatment can take place (112).

The use of a calcium-rare earths-magnesium proprietory alloy has been reported (113) to require less stringent control over the base melt composition than the above production process, and can be applied to conventional ladle treatment techniques. This is because

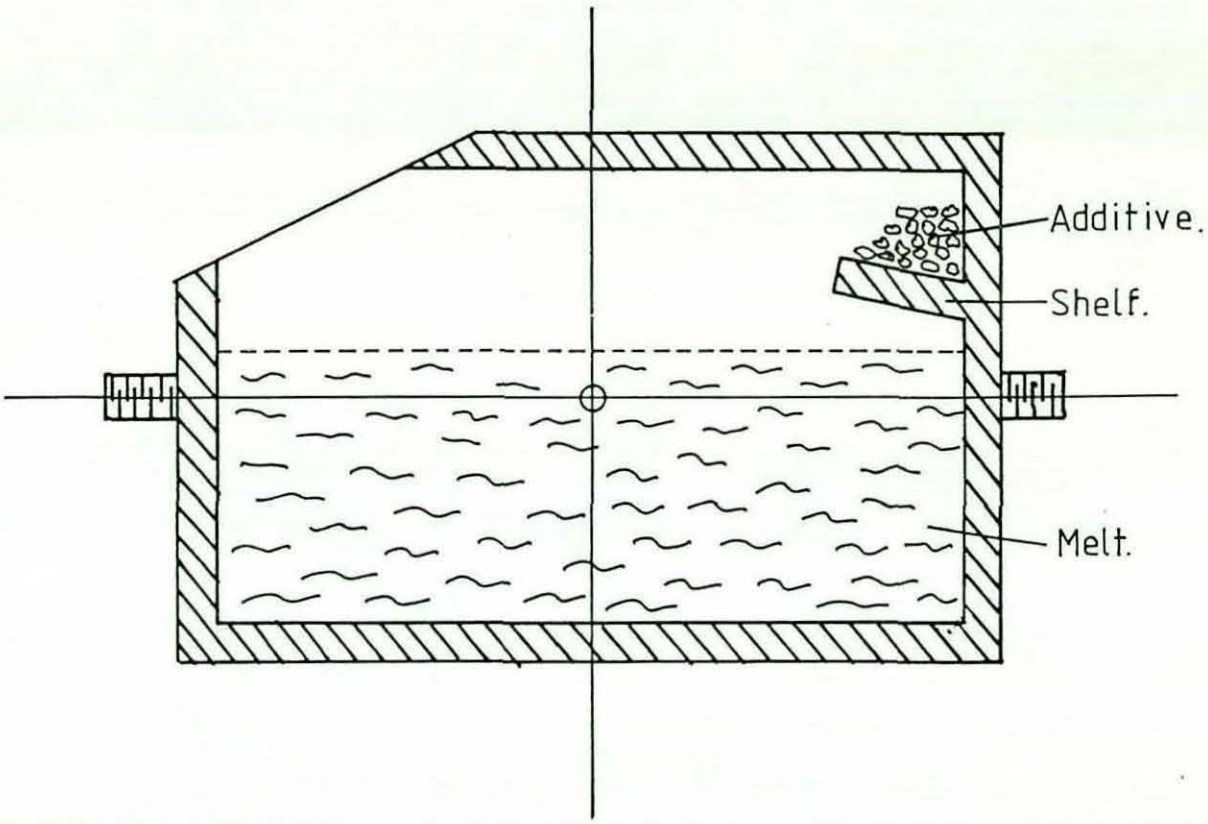

Figure 9. Sealed ladle for containing the melt treatment reaction.

calcium and the rare earth elements have a less powerful effect than magnesium on the graphite morphology (114, 115), although the extent of the advantages gained by employing this method will naturally depend greatly on the exact composition of the treatment alloy used.

4.3 Rare-earth Metal Additions

Rare earth metal additions are widely used for the production of compacted graphite cast iron in Austria and West Germany (84, 116). Conventional ladle treatment techniques can be employed with this method because the high boiling points of the rare earth elements (eg 3467°C in the case of cerium) do not cause vapourisation and fading problems to the same extent as magnesium, with a boiling point of 1107°C. The rare earths are normally introduced into the melt as cerium mischmetall (approximately 50% Ce, balance other rare earths), or rare earth silicides (30-50% total rare earth content), and the quantity added is highly dependant on the melt sulphur content (83, 84, 117). Rapid, accurate sulphur analysis prior to treatment is therefore necessary so that the rare earth addition may be adjusted accordingly. Typical addition levels are between 0.09% and 0.10% cerium mischmetall for a base sulphur content in the range of 0.010%-0.015% (117). An unfavourable aspect of this type of production method is that castings with thin sections are liable to contain some white iron which must be transformed by an annealing treatment (117). This is because the rare earth metals, particularly cerium, have a pronounced chilling effect in cast irons when excess levels of these (uncombined) elements remain dissolved in the melt after desulphurisation and deoxidation has taken place (89, 119, 120). Under these conditions, the high chilling tendency can be attributed to a negative thermodynamic interaction parameter

of, for example, cerium on carbon in liquid iron (e_C^{Ce} = -0.10 (121)), which would tend to stabilise carbon in solution. At low rare earth addition levels, the results of some experiments have suggested that these elements tend to reduce chilling because the formation of rare earth sulphide and oxide particles increases the effective number of nucleation sites in the melt (89, 119, 122, 123).

Recent research (64, 120, 124) has further indicated that the chilling tendency associated with the presence of cerium in the rare earth metals treatment can be reduced by increasing the lanthanum content of the addition. This result may be associated with the lower stability of lanthanum dicarbide compared to cerium dicarbide. The rare earth dicarbides are the most stable of the rare earth-carbon compounds (125) and the free energy changes for the appropriate reactions in liquid iron are given below (125, 126, 127):

$$(\%\ Ce)_{Fe} + 2(\%\ C)_{Fe} = CeC_2(s),\ \Delta G = -321.3\ kJ\ mol^{-1}$$

$$(\%\ La)_{Fe} + 2(\%\ C)_{Fe} = LaC_2(s),\ \Delta G = -281.6\ kJ\ mol^{-1}$$

4.4 Methods Utilising Aluminium as a Major Component of the Treatment

The partial substitution of silicon with aluminium in the base iron has been investigated by Stefanescu and Martinez (128, 129) as a way of reducing the chilling problem present at high cooling rates when using rare earth metal additions for CG iron production. In addition to promoting graphitisation, it was expected that the denodularising property of aluminium would reduce the high degree of

nodularity which often occurs in thin sections of postinoculated compacted graphite iron castings. In the initial trials carried out by Stefanescu and Martinez, ladle treatment was used to introduce rare earth silicides to a base melt containing up to 4.10% Al and up to 0.95% Si. Although the CG irons produced using this method were satisfactory in respect of the average graphite morphology, they exhibited unacceptable levels of chill. The latter effect may be explained by a comparison of the Henrian interaction coefficients in liquid iron of silicon on carbon ($e_C^{Si} = +0.08$) and aluminium on carbon ($e_C^{Al} = +0.043$) (127) which indicates that under conditions of thermodynamic equilibrium in molten iron, aluminium is a less effective graphitiser compared to silicon. In practical cast iron melts, studies carried out to determine the effects of different elements on the eutectic carbide content have shown that the graphitising influence of aluminium and silicon are actually very similar (35). It is therefore unlikely that the partial substitution of silicon with aluminium in the base iron would have a significant effect on the chilling tendencies of cast irons produced using rare earth additions.

Magnesium ferro-silicon additions have also been used to treat irons based on the Fe-C-Al system (83, 129). According to one report (129), a compacted graphite iron produced using this method exhibits a much lower chilling tendency than one produced by rare earth treatment of an iron with similar base melt composition. This can be attributed largely to the absence of the chill-promoting effect of the rare earths, although the result may also indicate that the latter elements are less effective inoculating agents compared to magnesium.

A different method of reducing the chilling propensity of rare earth treated compacted graphite irons has been investigated by Stefanescu et al (130) and involves the use of aluminium as a postinoculant for cast irons based on the conventional Fe-C-Si system. The effectiveness of ferro-silicon postinoculation is well established, but in addition to decreasing chill in thin secions, this method can also cause an unacceptable degree of nodular graphite formation in CG irons if the postinoculation process is not carefully controlled (43, 128, 131-134). The latter effect can be attributed to the improved nucleation conditions in the melt promoting the formation of a greater number of nodules at an early stage in the eutectic transformation. This results in a high nodularity in the final structure (43). Furthermore, the high silicon content of the postinoculation causes local regions of the solidifying melt to be enriched in this element and therefore have a high carbon equivalent value. This also promotes increased nodularity (87, 133, 135). The results obtained by Stefanescu et al (130) suggest that the denodularising effect of aluminium can be usefully employed in postinoculation to restrict excessive nodule formation in compacted graphite irons. The aluminium was also found to be as effective as ferro-silicon in reducing the chilling tendency in thin sections.

Although the previous discussion indicates that aluminium may be beneficial in the control of compacted graphite morphology and chilling propensity, the industrial use of this element in production processes for CG iron is reported to result in poor mechanical properties and casting difficulties associated with the formation of Al_2O_3 (83, 129). The latter problems are significantly reduced by using the Inmold treatment process (129). However, for

the reasons explained earlier, the benefits gained by employing this technique must be weighed against the additional expense involved.

4.5 Cerium-Calcium Treatment

A further method for compacted graphite iron production, employing cerium and calcium additions, has been developed by Simmons and Briggs (114). In foundry trials carried out by these investigators with a 0.01% S base iron, compacted graphite microstructures with less than 15% nodules were produced in a 19 mm section thickness casting using minimum additions of 0.24% calcium and 0.016% cerium in a combined Ca-Ce-Si alloy. This level of cerium addition is much less than that required when only rare earth metals are used (eg 0.10% cerium mischmetall (118)), and it was reported (114) that castings with wall thicknesses as small as 4 mm could be produced in a carbide-free condition. However, the proportion of spheroidal graphite present in this section thickness was excessively high due to the high cooling rate. The general effect of cooling rate on the nodularity of compacted graphite microstructures is well known (20, 43, 57, 136) and can be attributed to variations in the eutectic undercooling temperature, T_{EU}. A high cooling rate promotes a low value for the T_{EU} and a correspondingly high driving force for growth which favours the formation of small graphite nodules (5). The cerium-calcium method has also been reported to be equally effective with both hypo and hyper-eutectic irons, and can be used with a simple open-ladle or sandwich treatment technique (114).

4.6 Methods Based on Treatment with Magnesium and Titanium

One of the most widely-used CG iron production methods is based on melt treatment with magnesium and titanium, which are added either separately, or together in a master alloy that may also contain rare earth elements, calcium, aluminium and other components. A master

alloy is often preferred in industry since the complete treatment can be carried out in the ladle. If the components are separated, the titanium must be charged to the furnace to avoid variable recovery rates (137, 138). The latter effect is due to the relatively high melting point of the titanium (1675°C) which makes it difficult to obtain a uniform solution. A further advantage of using the master alloy is that if the melt is initially overtreated, the effect of the excess magnesium is simultaneously countered by a higher titanium content. The presence of cerium in addition to the major components is beneficial for the neutralisation of deleteroius trace elements such as lead and bismuth (82). The magnesium-titanium-cerium combination was first proposed by Schellęng (139) in a patented treatment specifying residual contents of 0.005-0.060% Mg, 0.001-0.015% Ce, and 0.15-0.50% Ti. Later research showed that it was possible to produce a compacted graphite microstructure by treatment with a master alloy to give residual levels of 0.015-0.035% Mg, 0.06-0.13% Ti, and 0.001-0.015% Ce (82). Some other marketed alloys of this type also contain calcium, which has the reported effect of increasing the tolerance of the process to variations in the base melt sulphur content (138, 140, 141, 142).

Cooper and Loper (104) carried out experiments to compare the merits and limitations of using a Mg-Ti-Ce-Ca-Al-Si alloy, with treatment using rare earth silicides. It was concluded that with the former method, the irons produced were comparatively less sensitive to variations in the casting section size and addition level. One major disadvantage of production methods which utilise titanium, however, is that the CG iron scrap produced must be isolated from that which is used in the charge material for ductile iron production. In many cases, this can increase the overall cost of the process. The isolation is necessary because the high titanium

content of the scrap could, in subsequent use, cause degeneration of the spheroidal graphite shape and result in poor mechanical properties.

4.7 Treatment of a High Sulphur Content Base Iron

The method described by Ruff and Vert (143) utilises the denodularising property of sulphur in essentially the same way as the previous method uses titanium. This process involves treating a normal cupola grey cast iron melt (sulphur content 0.07-0.12%) with a master alloy containing high levels of magnesium and cerium, and smaller quantities of aluminium and calcium. Postinoculation is reported not to be necessary owing to the large number of sulphide particles which serve as substrates for graphite nucleation. Although this method has the obvious benefit that it can be applied in a grey iron foundry without the need for large investment in new capital equipment, the disadvantages associated with the use of high sulphur-content irons for CG iron production include heavy dross formation and a high risk of slag inclusions, particularly in complex-shaped castings (84). Massive sections may also contain regions of flake graphite as a result of resulphurisation in segregation areas (84).

4.8 Section Sensitivity of Compacted Graphite Cast Iron

It is clear from the previous discussion that there are one or more production problems associated with each of the current methods in use for the manufacture of compacted graphite iron. In addition, it is apparent from surveys of the applications of this material (83, 84, 116, 144, 145) that for many of the present and potential uses for CG irons, for example engine cylinder heads and covers, it is desirable that an acceptable microstructure can be produced over a range of section thicknesses. Unfortunately, compacted graphite

iron is known to be sensitive to variations in the solidification cooling rate (20, 43, 57). High cooling rates such as those produced by thin (eg 5 mm) sections of a casting promote high percentages of nodular graphite in the microstructure and cause the compacted graphite to adopt a shorter, thicker appearance when viewed in a plane polished section (127). At the lower temperature of eutectic undercooling, less time is available for diffusion of impurities to the graphite, and the higher driving force encourages a defect-controlled growth mechanism to operate in preference to a growth mechanism controlled by impurity diffusion (5). These factors favour the formation of small graphite nodules. This effect can be reduced in thin sections of a casting by making appropriate adjustments to the quantities of nodularising and/or denodularising additions used, but, depending on the range of section thicknesses present, this may adversely affect the graphite morphology in other parts of the casting.

High cooling rates also promote chilling if the number of suitable nucleation sites in the cast iron is not sufficient to prevent undercooling below the austenite-carbide eutectic temperature. Postinoculation with ferro silicon increases the number of effective nucleation sites, which suppresses carbide formation but, as explained previously, this also causes increased nodularity.

Clearly, there is scope for the further development of melt treatments for compacted graphite cast iron in order to reduce the problems associated with the production of this material. This development process would be aided by an improved understanding of the important factors in graphite morphology control in general, particularly the effects of solute elements, combined with a more certain knowledge of the growth characteristics of different graphite forms.

Chapter 5

EXPERIMENT

5. EXPERIMENT

The experimental programme was divided into three main areas and, where appropriate, these were carried out concurrently. The first part dealt with the production of iron castings using various types and compositions of melt treatment. The aim of this work was to investigate the effects of these factors on the morphology of the graphite phase in different section thicknesses of casting. The castings produced additionally provided the specimens required for the other parts of the experimental programme. These involved an examination of the growth structure of different graphite forms, and detailed studies to investigate the role of various solute elements in graphite morphology control.

5.1 Production of Castings

Two extensive series of melts were carried out to investigate the cerium mischmetall-calcium and magnesium-titanium melt treatments, used in industry for the production of compacted graphite cast iron. Additional experiments were also carried out with cerium-free mischmetall, magnesium-aluminium, calcium-zirconium, and magnesium-zirconium additions.

5.1.1. Basic Casting Procedure

Pig iron ingots of total weight 20.5 Kg (45 lb) were melted and superheated to 1550°C in a 60 lb capacity electric induction furnace. Two castings were produced from each melt by taking successive taps from the furnace. While the first tap was being treated and cast, the remaining melt was maintained at 1550°C in the furnace. The treatment and casting procedures were then repeated for the second tap, using a different composition of treatment addition. The quantities of treatment agents used in each series of

melts were chosen systematically and were based on an assumed melt weight of 10 kg for each casting. It was difficult to accurately control the volume of melt taken in each tap owing to the unavailability of suitable weighing equipment, however, the precise treatment addition levels were calculated later by weighing the casting and the scrap produced from each tap.

Owing to the small melt volume which cooled rapidly in the ladle, postinoculation with 0.6% of FeSi (75% Si) was carried out within a few seconds of treatment. This allowed the castings to be poured at a temperature of 1380-1410^{o}C into greensand moulds. Melt temperatures were gauged with a portable thermocouple stick, using fresh thermocouples for each measurement. The aluminium sheath on each thermocouple was removed prior to use to avoid contamination of the melt with aluminium.

5.1.2 Base Melt Composition

A low sulphur iron was used in order to minimise the effects due to variation in the concentration of this element. The suppliers figures for the composition of this iron are given in Table 1, although it was found in practice that the sulphur and carbon contents of the base melt were usually below the levels shown.

In order to be consistent with industrial practice, extra silicon (in the form of FeSi, 75% Si) and manganese (FeMn, 66% Mn) were added to the melt. The former had a graphitising effect while the latter promoted a small amount of pearlite formation in the solidified castings. The final silicon content of each casting was kept relatively constant by calculating the quantity of silicon to be added in each case according to the silicon content of the treatment additions (eg CaSi, FeSiMg, etc). This normally enabled

	C	Si	S	P	Mn
Specification (%)	3.80 min	0.75-1.25	0.020 max	0.035 max	0.015 max
Typical (%)	4.10	1.05	0.010	0.025	0.009

Table 1 - Composition of the Pig Iron used for the base melt

the final silicon concentration to be maintained within the range 2.5-3.0% (see Appendix I).

The composition of the majority of castings produced was slightly hypereutectic, and this is also in accordance with normal commercial practice for compacted graphite iron production.

5.1.3 Spectrographic Analysis

Samples for spectrographic analysis using X-ray fluorescence were taken firstly from the furnace melt, and secondly from the ladle after treatment and postinoculation had been carried out. The use of copper sample moulds of the form shown in figure 10 ensured maximum retention of the original composition by causing the specimens to solidify as white iron.

5.1.4 Casting Design

In order to gauge the effect of section thickness on the graphite morphology, castings of the form shown in figure 11 were produced. Each casting consisted of a cylinder of constant (40 mm) internal bore, with a stepped wall thickness ranging from 4 mm to 25 mm.

5.1.5 Mould Preparation

Moulds were produced in greensand using a hydraulic moulding machine. The internal bore was produced using a core made from Chelford 60 sand with a cold-setting resin binder. A furane-free resin was used in order to minimise sulphur adsorption from the core which could adversely affect nodular and compacted graphite structures.

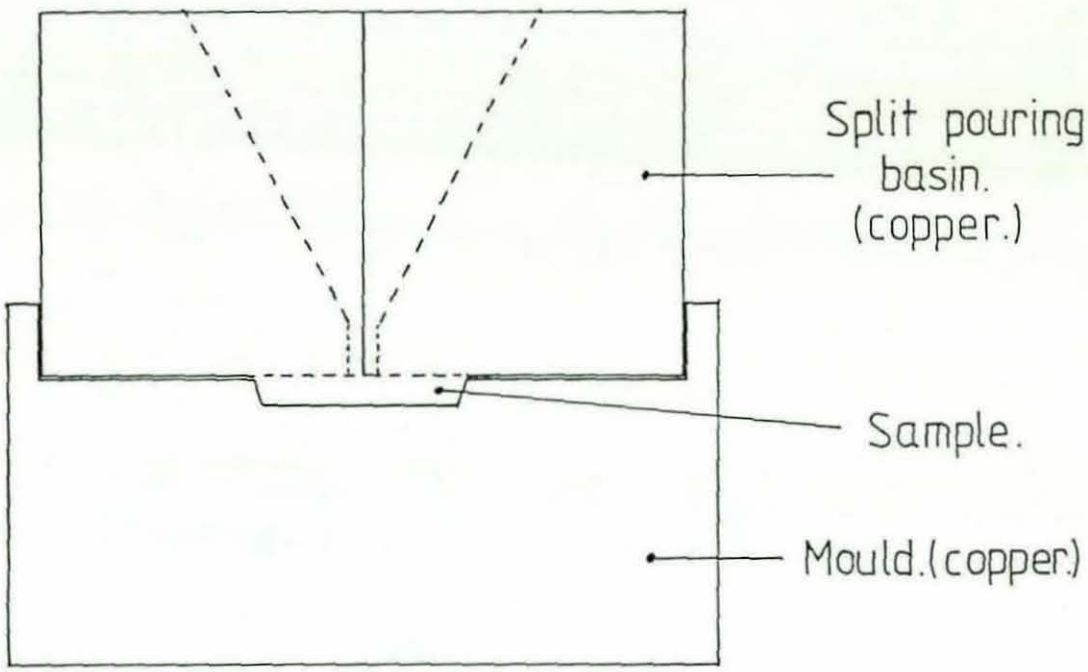

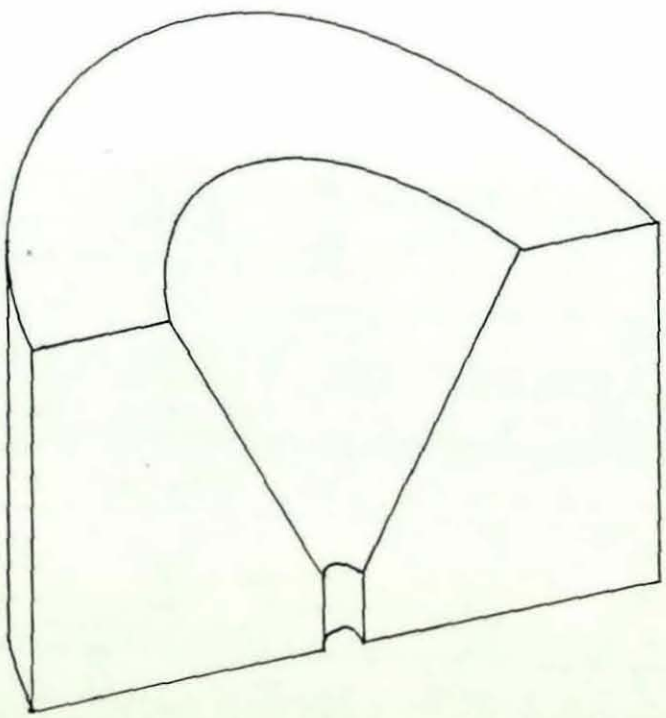

Figure 10. Copper sample - mould.

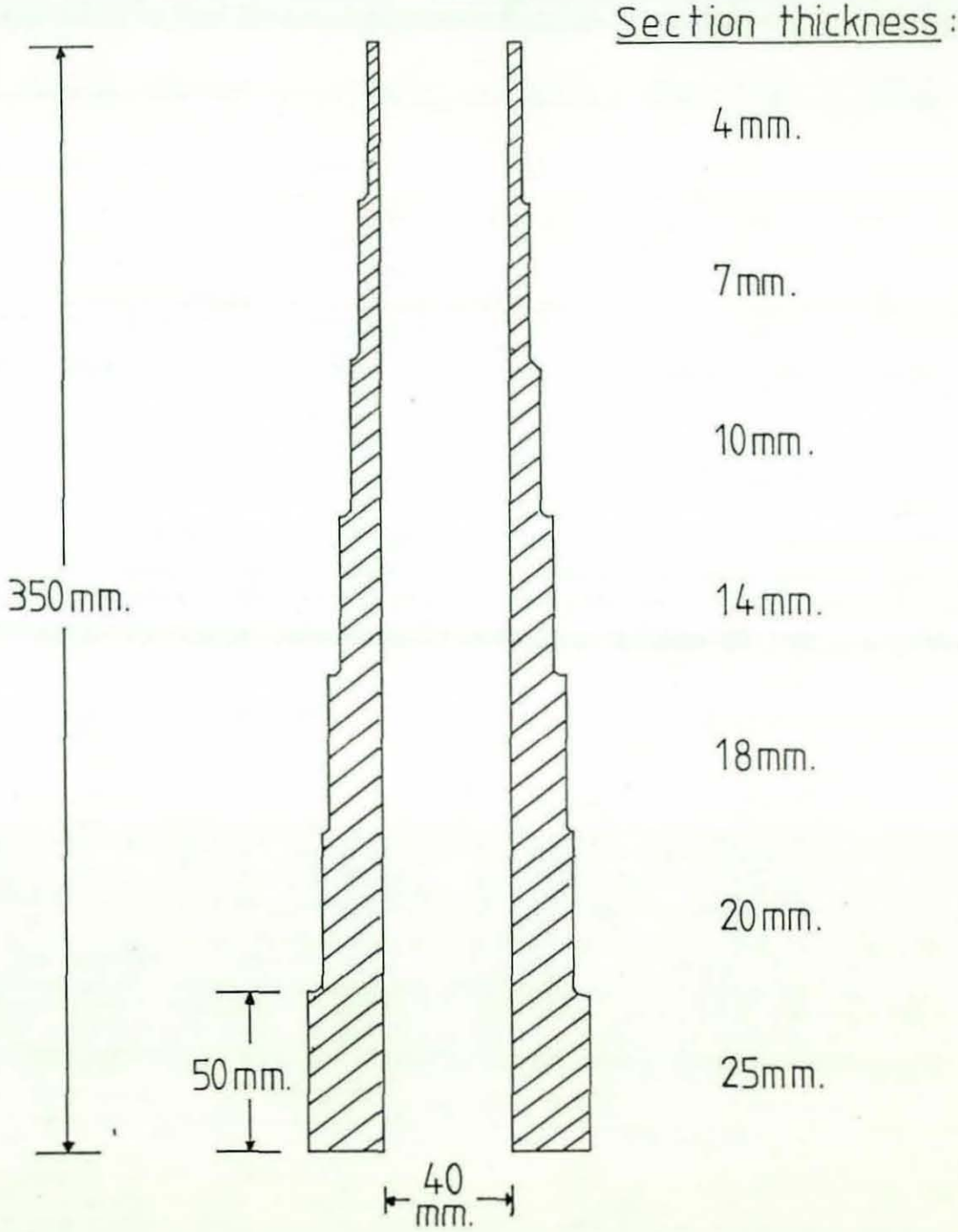

1/2 scale.

Figure 11. Casting design.

The casting pattern and core box were fabricated in the Centre for Industrial Studies (CIS) in the Department of Engineering Production, Loughborough University of Technology.

5.1.6 Melt Treatment

Each treated casting was produced using one or a combination of the alloys listed in table 2. The experimental procedures adopted for each type of melt treatment are described below.

5.1.6.1 Cerium Mischmetall - Calcium Additions (Series 1)

The quantities of cerium mischmetall and calcium used to produce each successive casting were varied for a series of constant calcium/cerium mischmetall addition ratios. Calcium was added in the form of calcium silicide together with a constant 0.14% addition of calcium fluoride which was used for fluxing purposes. A number of melts were also carried out with single additions of either cerium mischmetall, cerium-free mischmetall, or the calcium silicide-calcium fluoride mixture to assess their individual effects on the graphite morphology. Treatment was accomplished by tapping the melt from the furnace on to the required mixture of components in a pre-heated ladle.

5.1.6.2 Magnesium-Titanium Additions (Series 2)

In this series of melts, the titanium was added to the furnace as 70% FeTi a few minutes prior to tapping. After stirring to achieve an homogeneous solution, the titanium-bearing melt was poured over the ferro-silicon-magnesium which was in a pre-heated ladle. The magnesium treatment took place with a violent reaction accompanied by excessive fumes and flaring. The risks of injury were effectively reduced by using a ladle lid fabricated from fibre-reinforced calcium silicate board with an 8 cm hole through which

Principal Element Added	Alloy Used
Calcium	Calcium silicide, CaSi. (33% Ca, bal.Si.) Calcium fluoride, CaF_2. (50% Ca, bal.F.)
Cerium mischmetall	50% Ce, 30% La, bal. other rare earths.
Lanthanum mischmetall	65% La, 25% Nd, bal. other rare earths.
Magnesium	Ferro-silicon magnesium, FeSiMg. (5.5% Mg, 45% Si, 0.5% Ce, bal.Fe.)
Titanium	Ferro-titanium, FeTi. (70% Ti)
Aluminium	Iron-aluminium alloy. (50% Al)
Zirconium	Ferro-silicon-zirconium. (38.2% Zr, 50.3% Si, bal.Fe.)

Table 2 Compositions of Additives Used

the melt from the furnace could be safely poured. This arrangement prevented splashing and contained most of the reaction in the ladle. Each successive melt treatment was chosen in a systematic fashion: the magnesium addition level was varied for each of an increasing series of constant titanium levels. As with the previous series of melts, several castings were produced using single additions of either ferro-silicon-magnesium or ferro-titanium.

5.1.6.3 Magnesium-Aluminium Additions

A few experiments were carried out to provide compacted graphite iron samples which could be used to investigate the role of aluminium in graphite morphology control. A number of ways of introducing the aluminium to the melt were tried, including ladle and furnace additions of pure aluminium, aluminium-silicon alloy, and iron-aluminium alloy. The first two methods resulted in excessive aluminium loss through floatation and the best results were obtained with ladle treatment using the higher melting point iron-aluminium alloy. The ferro-silicon-magnesium was also added in the ladle, as with the magnesium-titanium treatment.

5.1.6.4 Calcium-Zirconium and Magnesium-Zirconium Additions

A small number of melts were carried out to determine whether compacted graphite cast iron could be produced using magnesium-zirconium or calcium-zirconium additions, and to assess the influence of zirconium on the graphite nucleation and growth process.

Owing to the high melting point of metallic zirconium (1852^{o}C), it was extremely difficult to obtain a solution of the metal in liquid iron using either small pieces or fine turnings. Subsequent trials showed that the required solution could be obtained by adding ferro-

silicon-zirconium alloy to the furnace melt. Ladle treatment with ferro silicon magnesium or calcium silicide was then carried out as with the other types of treatment used in the project.

5.2 Optical Microstructual Examination and Assessment

Specimens from each casting were prepared metallographically and the microstructures were examined using an optical microscope.

5.2.1 Specimen Preparation

Each casting was sectioned in several places by cutting at the mid-point of every wall thickness which required assessment, as shown in figure 12a. The sample was taken near to one side of the section, in the position indicated in figure 12b. This position was chosen to minimise any possible irregularities in the sample due to carbon floatation (top of casting), sand inclusions (bottom of casting), and heat-sinking from the runner system. For the 4 mm, 7 mm and 10 mm sections, the specimen width extended across the whole of the section thickness. For the remaining sections, the specimen width was limited to approximately 10 mm in order that the maximum number of samples could be accommodated in one 30 mm diameter mounting.

Specimens were mounted in thermosetting bakelite using a heated hydraulic mounting press. Metallographic preparation was carried out in a similar way to that described by Ahmed and Gawlick (146), and this procedure resulted in good retention of the graphite phase, irrespective of its morphology. The specimens were etched by swabbing with a solution of 2% Nitric acid in methanol.

5.2.2 Nodularity Assessment

In order to guage the effects of section thickness and melt treatment composition on the graphite morphology, the relative

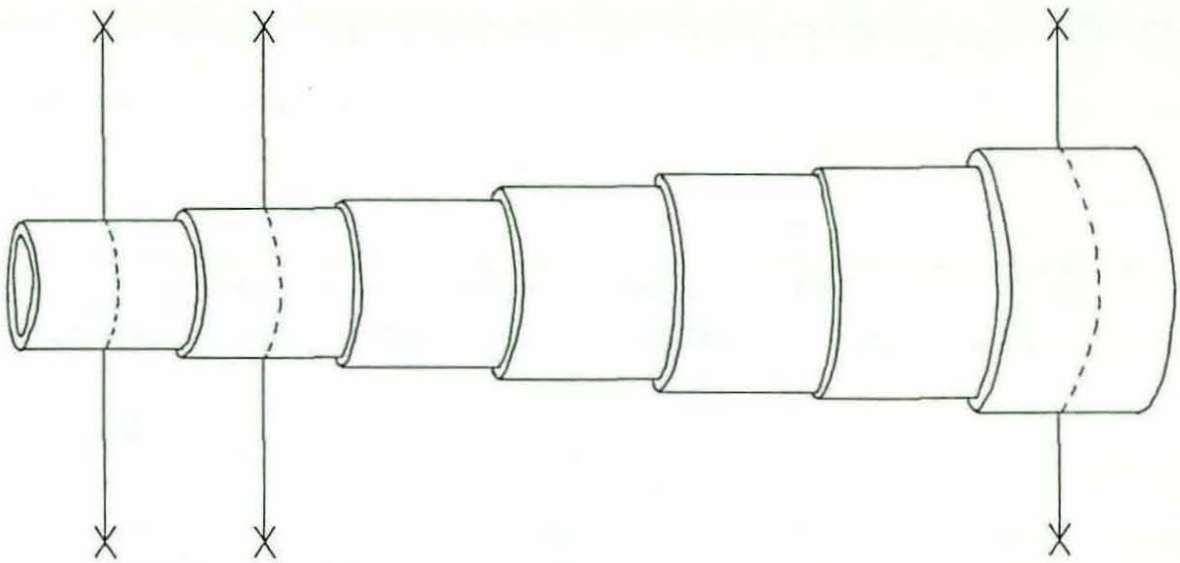

a). Sectioning of castings.

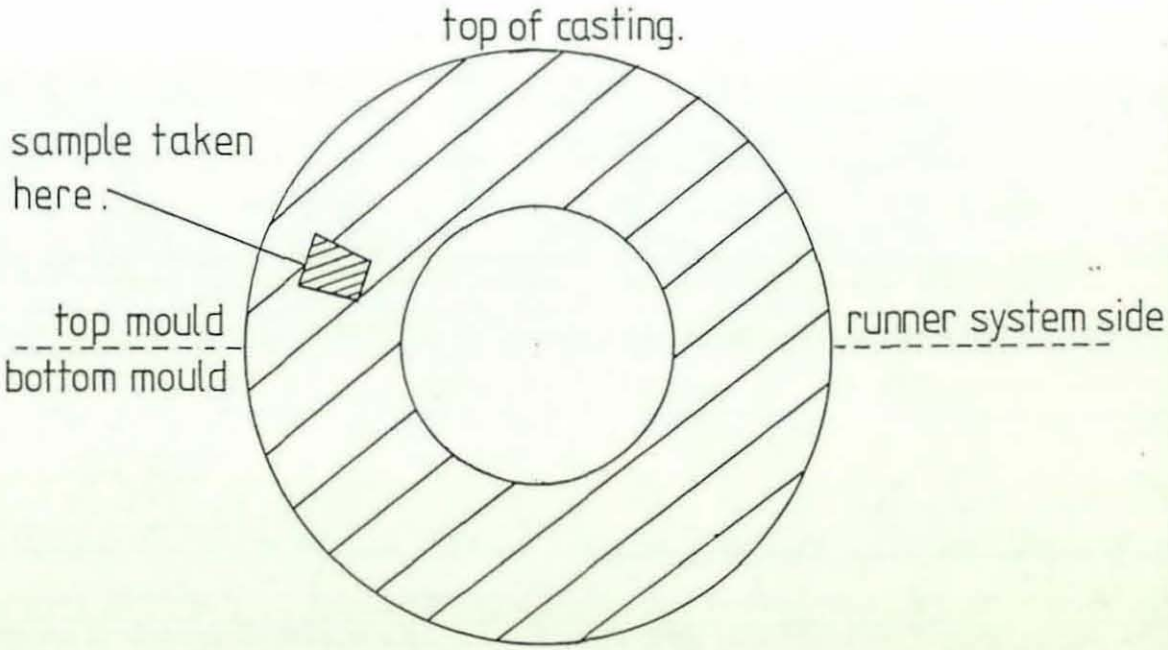

b). Sampling position, 25mm section.

Figure 12. Taking samples from the casting.

percentages of compacted and nodular graphite were assessed for selected section thicknesses of each casting. Several methods of nodularity assessment were considered, and their relative merits are discussed in Appendix II. The procedure that was eventually adopted involved counting the number of compacted and nodular graphite particles visible in an area of the plane polished and mildly etched specimen at a magnification of 400X. The percentage nodularity of the graphite structure as a whole was calculated using the following equation:

$$\% \text{ Nodularity} = 100 \times \left(\frac{\text{Number of nodular and degenerate nodular particles}}{\text{Number of nodular and degenerate nodular particles} + \text{Number of compacted graphite particles}} \right)$$

Examples of nodular, degenerate nodular and compacted graphite forms are shown in figure 13.

The above procedure was repeated for a further eight fields of view which were evenly spaced over the whole specimen. An average value for the percentage nodularity was then calculated using all the results from each sample. For section thicknesses greater than 4 mm, an acceptable compacted graphite microstructure was defined as one that contained less than 20% nodules. In the 4 mm section, nodularity levels less than 50% were considered to be acceptable. These nodularity limits were adopted on the basis that for similar section thicknesses, these values are commonly applied to the quality control of industrial compacted graphite iron castings (116, 147).

118

5.3 Assessment of Chilling Tendency

The chilling tendency of the cast irons was assessed by measuring the average macro-hardness of the 4 mm section specimen from each

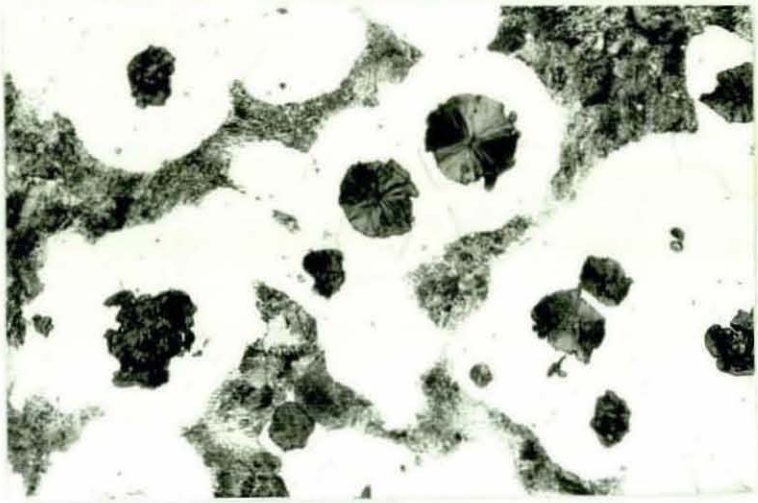

300X

(a) Nodular and Degenerate Nodular Graphite (casting 2/8).

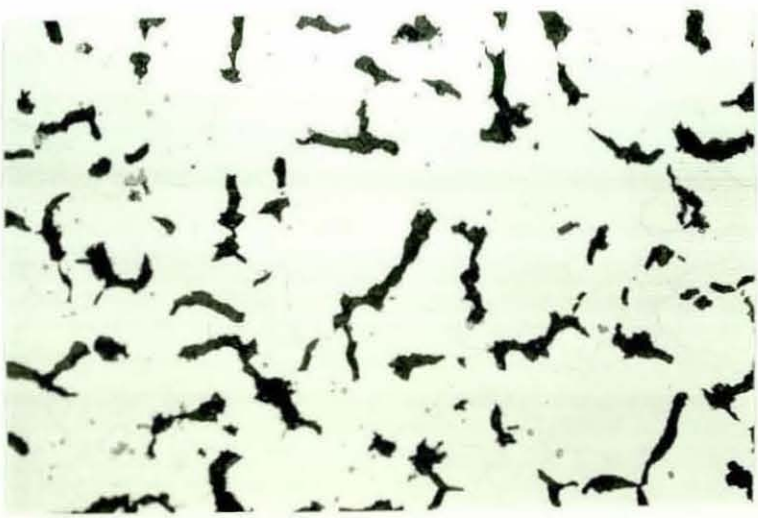

300X

(b) Compacted Graphite (casting 4/1).

Figure 13 Examples of (a) Nodular and Degenerate Nodular Graphite and (b) Compacted Graphite

casting. Eight measurements using a Vickers diamond pyramid hardness testing machine were used to obtain the average value for each specimen. Because the 4 mm sections were often of considerable hardness, and to reduce discrepancies due to small local variations in the microstructural hardness, a heavy load (30 kg) was used with the Vickers test to achieve a large diamond impression.

5.4 Scanning Electron Microscopy

Scanning electron microscopy was used to study deep-etched microstructures and the ion-etched surfaces of individual graphite particles.

5.4.1 Deep Etching

SEM examination of deep-etched microstructures provided information on the three-dimensional appearance of different graphite morphologies. Selected specimens were mounted in electrically-conducting bakelite and prepared metallographically to view the microstructure. The iron matrix surrounding the graphite was then etched away to a depth of approximately 0.5 mm by immersing the mounted specimen in a 15% solution of hydrochloric acid in methanol and leaving it for 18-24 hours in a fume cupboard. The deep-etched specimen was then cleaned by immersion for a few minutes in a 5% solution of hydrofluoric acid in methanol, after which thorough drying was carried out using a hot air dryer. Each specimen was stored in a dessicator prior to SEM examination.

5.4.2 Etching to Reveal Basal Plane Orientations

Scanning electron microscope studies of graphite which had been suitably etched provided information on the orientation of the crystal planes in different graphite forms.

Reported techniques for etching the graphite surface in situ in plane polished cast iron samples involve either oxidation (1), ion beam sputtering (2, 4, 11, 30, 31), or plasma etching (33). These methods delineate the orientation of the basal planes (1, 33).

The thermal etching technique used successfully by Hunter and Chadwick (1) involved heating a polished specimen in air to 475-525^{o}C for approximately one minute. The authors proposed that the etching relief was caused by an oxidation effect. However, several experimental trials carried out using this technique in the present research programme did not yield a readily identifiable pattern of etching relief traces.

Much improved results were obtained by ion etching the specimen with a beam of inert gas ions. Each polished sample was etched using apparatus normally employed for the ion beam thinning of specimens prior to transmission electron microscopy. With this equipment, a beam of argon ions was accelerated to an energy of 5kV and directed onto the surface of the specimen with a beam current of 0.03 mA. Experimental trials showed that the optimum etching time for these conditions was approximately 4 hours.

5.5 Analytical Spectroscopy and Spectrometry

Analytical spectroscopy and spectrometry techniques were employed to study the distributions of elements in flake, compacted and spheroidal graphite cast irons. Initial trials using Auger electron spectroscopy (AES) were of limited value owing to a lack of elemental sensitivity. For instance, it was found that sulphur concentrations below approximately 2% could not be detected using this technique. Additional difficulties arose as a result of the overlap that occurs with the characteristic Auger peaks of certain

elements. For this reason, it was extremely difficult to detect cerium in cast iron since the main cerium peak lies very close to one of the characteristic iron peaks and is therefore overshadowed by the larger iron signal. Subsequent trials were carried out with secondary ion mass spectrometry (SIMS) and X-ray micro-analysis. Owing to higher elemental sensitivities, these techniques were found to be more applicable to a study of elemental distributions in cast irons, and the experimental procedures adopted are described below.

5.5.1 Energy-Dispersive X-ray Microanalysis

X-rays are produced during electron bombardment of a sample and the X-ray energy (or wavelength) spectrum is characteristic of the elements under the electron beam. For energy-dispersive X-ray microanalysis, a LINK energy analysing spectrometer in combination with either a Cambridge scanning electron microscope or a JEOL scanning transmission electron microscope (used in SEM mode) was used to record the intensity of the characteristic X-ray emitted from the surface of the specimen as a function of energy. The information was displayed in one or more of the following ways:

(a) Spot Analysis: In this operation, the electron beam was focused to a spot and positioned on an area of particular interest. After a few minutes, this produced an energy spectrum showing the elements present in the chosen area. With the equipment used, the volume of sample analysed was 1 to 2μm in width and depth.

(b) Linescan: An electronic "window" was set on the spectrometer such that only those X-rays of a selected energy were recorded. The electron beam was then moved slowly across a region of interest so that a plot of the intensity of X-rays

characteristic of a particular element was obtained as a function of position.

(c) Elemental Map: An electronic "window" was set as with the linescan, and the electron beam made to scan over an area of the specimen. The information was displayed on a fluorescent screen producing a map showing the distribution of the chosen element.

Although the energy-dispersive X-ray analysis method was very useful in a number of cases, particularly for locating and analysing small regions of special interest, this technique suffers from a number of drawbacks. For instance, there is a general lack of elemental sensitivity, although the detection limit varies according to the atomic number of the element in question. As a guide, the detection limit for low atomic number species such as magnesium and sulphur was around 2-3%, whereas for the higher atomic number transition metals such as titanium and iron, the limit was approximately 0.2%. Additionally, it was not possible to detect elements with an atomic number less than 11. This precluded the analysis of important elements such as oxygen and carbon. A further limitation was poor energy resolution, such that elements with characteristic X-rays of similar energies overlapped with each other. For instance, the cerium L-alpha and titanium K-alpha X-ray lines lie very close together and a small cerium peak could not easily be resolved on the energy spectrum in the presence of a large titanium peak.

5.5.2 Secondary Ion Mass Spectrometry (SIMS)

Unmounted samples from flake, nodular and compacted graphite cast iron were examined with a Cameca IMS 3F secondary ion mass spectrometer which uses a mass spectrometer of the magnetic sector

type. The samples analysed are listed in Appendix IV with details of the respective melt treatments used. With the exception of specimen G, which was a spheroidal graphite iron obtained from an outside source, all the irons examined were produced during the present research programme.

A simplified block diagram illustrating the main components of a secondary ion mass spectrometer is shown in figure 14. The specimen is bombarded with a beam of ions which penetrate the surface and undergo a series of collisions with the sample atoms, producing recoils and a cascade of secondary collisions between the specimen atoms themselves. As a result, atoms at or near the surface receive sufficient energy to enable them to escape from the specimen. This is known as the sputtering process and a fraction of the sputtered atoms (which are characteristic of those elements situated in the near surface region) are ejected as positive or negative ions. These ions pass through electrostatic optics which extract and transport them in such a way that their spatial relationship is maintained. A mass spectrometer then analyses the ions according to their charge/mass ratio.

As with the X-ray microanalysis technique, several different operations could be used to display the data from the mass spectrometer.

Mass spectra were produced by recording the intensities of all the emitted secondary ions from areas of either 400μm, 150μm or 25μm in diameter. Use of the smallest area provided information analogous to the spot analyses carried out with the previous technique.

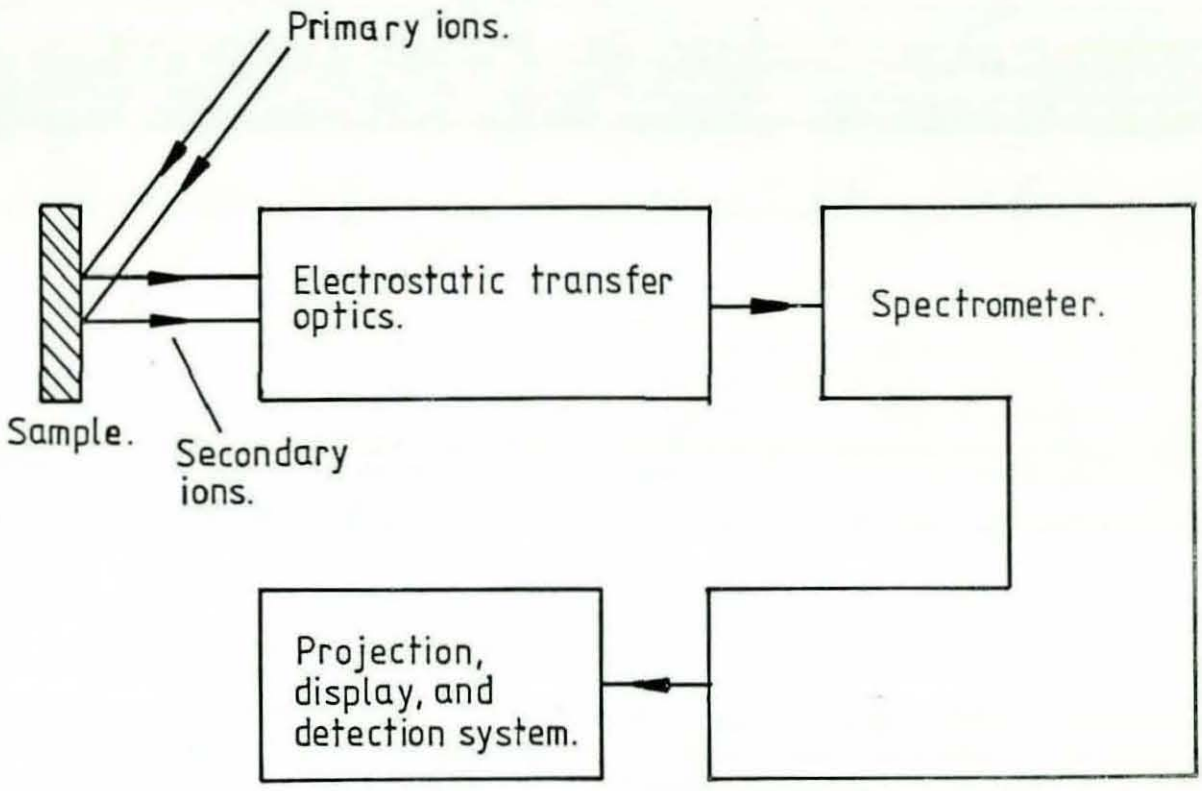

Figure 14. Principal components of a secondary ion mass spectrometer.

By altering the magnetic field in the mass spectrometer, ions of a particular charge/mass ratio could be selected for transmission. In this operation, the resolved ion image of the sample is magnified, converted to an equivalent electron image and displayed on a fluorescent screen, thus showing the distribution of a single element in the specimen under examination. Photographs of the distributions of different elements in a particular region of the sample were obtained for comparison.

By moving the specimen relative to the selectively focused electrostatic optics, the intensities of particular ions could be studied as a function of distance across the specimen surface. The distance along the line was advanced in steps of a predetermined size, depending on the width of the area of interest. The minimum step size possible was 1 μm, and this was used for stepscans across relatively small regions such as the width of a graphite flake. At each step, the cumulative number of secondary ions of each of the selected masses were recorded sequentially. The counting time used for each successive mass of interest was normally one second, but this was increased to five seconds for very low signal levels.

Composition-depth profiles of selected elements were produced by recording the intensities of the appropriate secondary ions from a small area as a function of sputtering time. As sputtering continues, the secondary ions analysed in the mass spectrometer originate from successively deeper layers in the specimen, providing an indication of the distributions of selected elements at right-angles to the specimen surface.

With the instrument employed in this research programme, two types of primary ions, O_2^+ and Cs+, were available for bombarding the

specimen. The use of Cs+ primary ions enhances negative ion yields by reducing the work function of the surface, thus optimising the conditions for electron transfer from the surface to the sputtered atom. O_2^+ primary ion bombardment enhances the yield of sputtered positive ions by forming compounds with electropositive elements, which can then be more easily ionised. Cs+ primary ions were therefore used when an increase in the sensitivity to electronegative elements such as sulphur and oxygen was desired, and O_2^+ primary ions were used to the same end for electropositive elements such as cerium, calcium and magnesium.

The sensitivity of SIMS is dependent on a number of factors including the type of primary ions used to bombard the specimen and the nature of the secondary ions themselves. The type of matrix in which the secondary ions were originally situated also affects the secondary ion yield. For these reasons, the SIMS results are not generally quantitative. However, the concentration of an element occurring in one region of a sample can be compared to the level of the same element in a different area, provided the matrix type, primary ion beam current, and other experimental conditions are the same.

In the present research, SIMS provided information on the distributions in cast irons of several important elements in graphite morphology control, and enabled variations in the levels of individual elements within the graphite phase to be qualitatively assessed.

CHAPTER 6

RESULTS

6. RESULTS

6.1 Castings Production Trials

The results of experiments carried out to study the effects of various melt treatments on the cast iron microstructures associated with different section thicknesses of casting are described below. The treatment levels used and the X-ray fluorescence analyses for each casting are listed in Appendix I. Appendix III lists the average percentage nodularity measured in different section thicknesses and the hardness of the 4 mm section for each casting produced.

The microstructure of the untreated base iron is shown in Figure 15a and contained ASTM type A flake graphite in a predominantly ferritic matrix.

6.1.1 Mischmetall-calcium additions (Series 1)

6.1.1.1 The influence of addition level on the graphite morphology

Systematic increases in the addition levels of cerium mischmetall and calcium caused a regular series of changes in the graphite morphology occurring in the 25 mm section of the casting. This sequence of changes in this section was the same whether the cerium mischmetall and calcium were added individually, or whether they were added together as a combined treatment with constant cerium mischmetall/calcium ratio.

Low addition levels caused a decrease in the size of the ASTM type A graphite flakes, coupled with increases in the degree of curvature and branching tendency of the flakes. Higher addition levels resulted in the formation of compacted graphite and further

increases raised the percentage nodularity of the microstructure. These results can be summarised as follows:

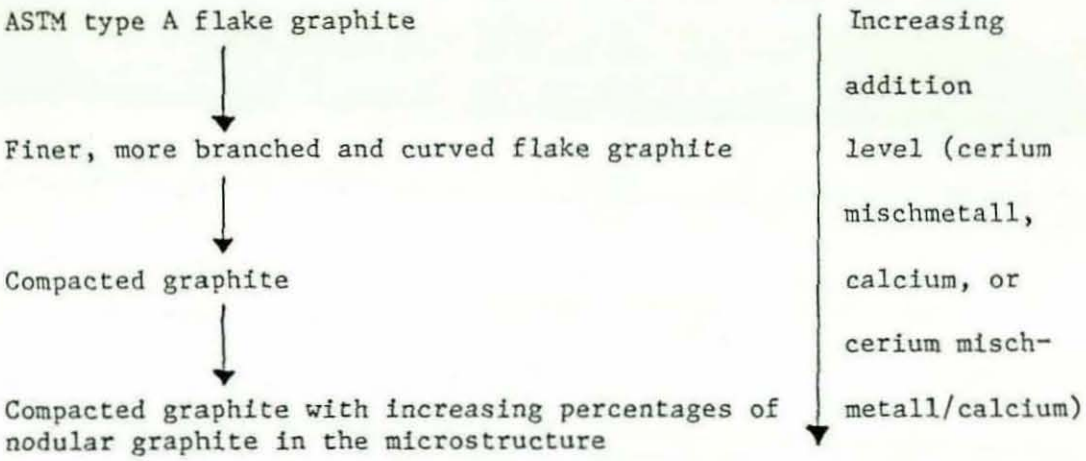

The above effects are illustrated in Figures 15a-e which show the microstructures that occurred in the 25 mm sections of a series of castings produced using increasing cerium mischmetall-calcium addition levels with a mischmetall/calcium addition ratio of approximately 0.12 in each case.

The effect of single and combined additions of cerium mischmetall and calcium on the graphite morphology in the 25 mm section are also represented in Figure 16a. These results show that with the conditions used in the experiments, a typical combination of additives resulting in a compacted graphite microstructure with less than 20% nodules in this section was 0.03% cerium mischmetall, 0.2% calcium. Similar microstructures were also produced using singular additions of either 0.27-0.36% calcium, or 0.055-0.075% cerium mischmetall. The 25 mm sections of two further castings produced using 0.06% and 0.16% lanthanum mischmetall respectively, also contained compacted graphite with less than 20% of the nodular form. These results indicate that the nodularising ability of lanthanum mischmetall is markedly less than that of cerium mischmetall.

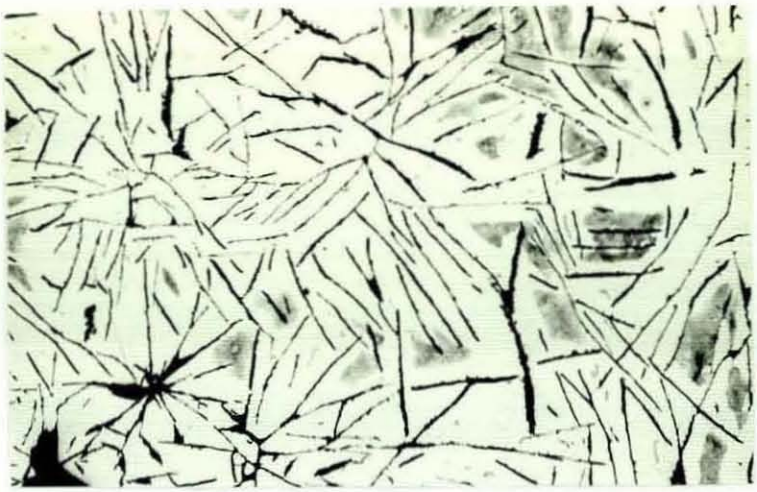

75X

(a) Untreated Base Iron (Casting 2/5)

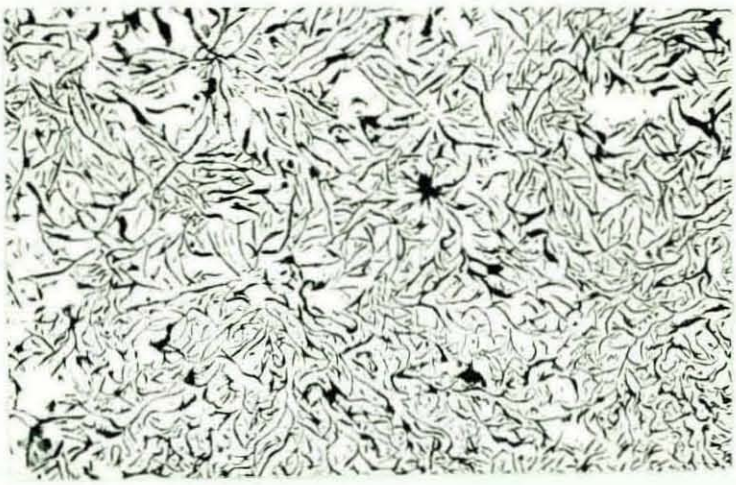

75X

(b) 0.016% Ce MM, 0.16% Ca (Casting 1/6)

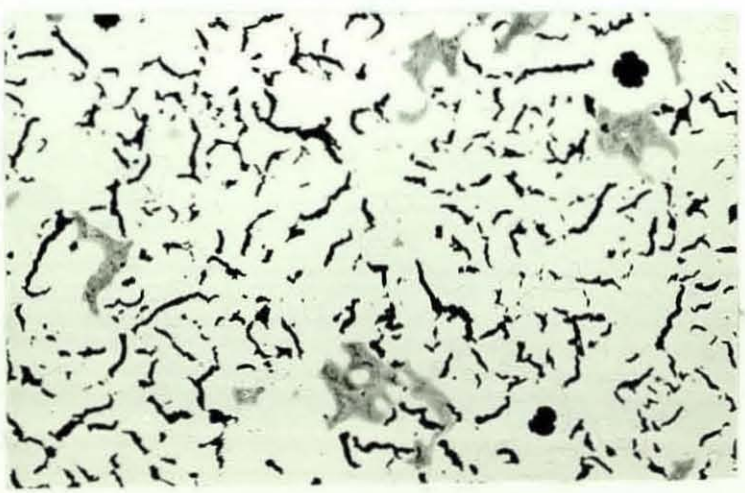

75X

(c) 0.03% Ce MM, 0.26% Ca (Casting 1/2)

Figure 15 Effect of Increasing Cerium Mischmetall-Calcium Additions on the Microstructure Obtained in the 25 mm Section

(Figure continues over page)

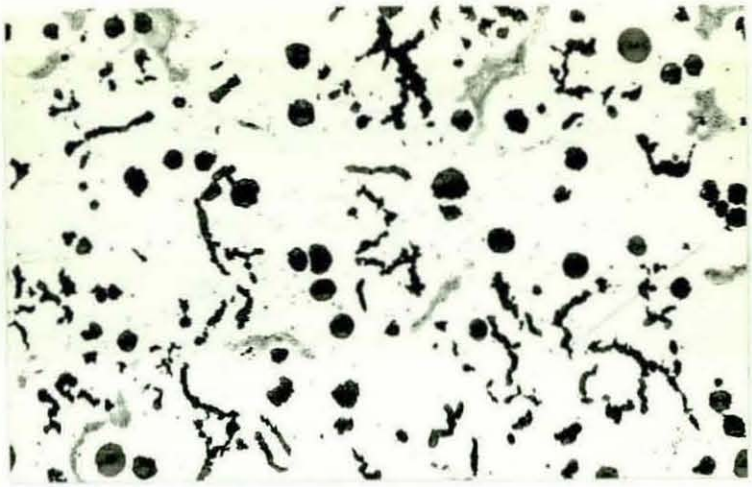

75X

(d) 0.045% Ce MM, 0.33% Ca (Casting 1/3)

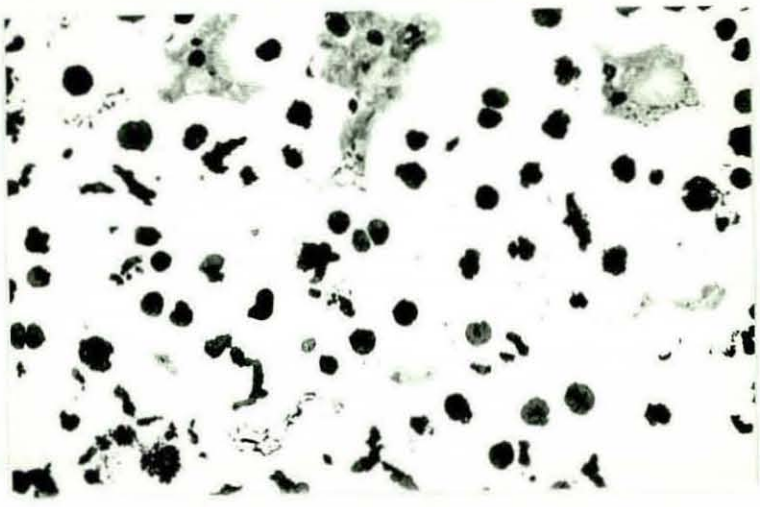

75X

(e) 0.06% Ce MM, 0.48% Ca (Casting 1/1)

Figure 15 Continued

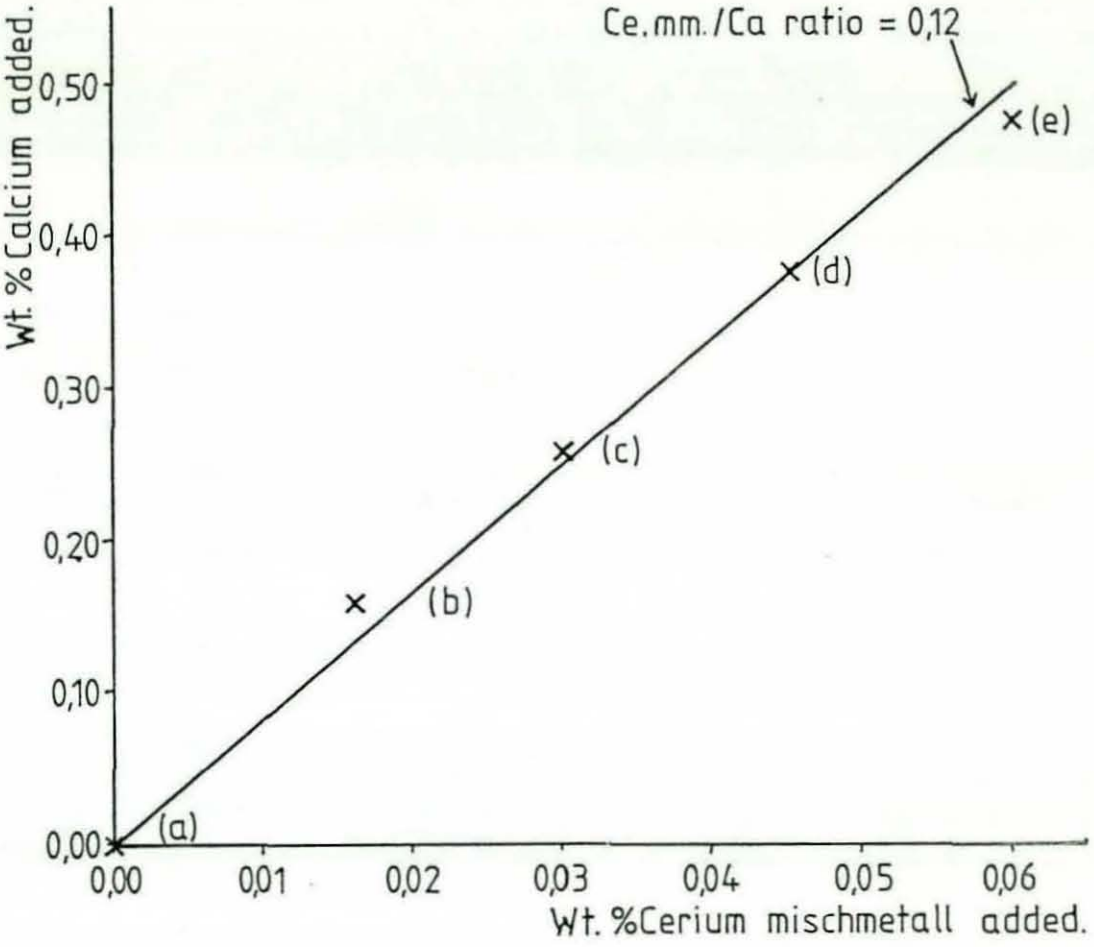

Figure 15 continued – showing addition levels used for microstructures (a) to (e).

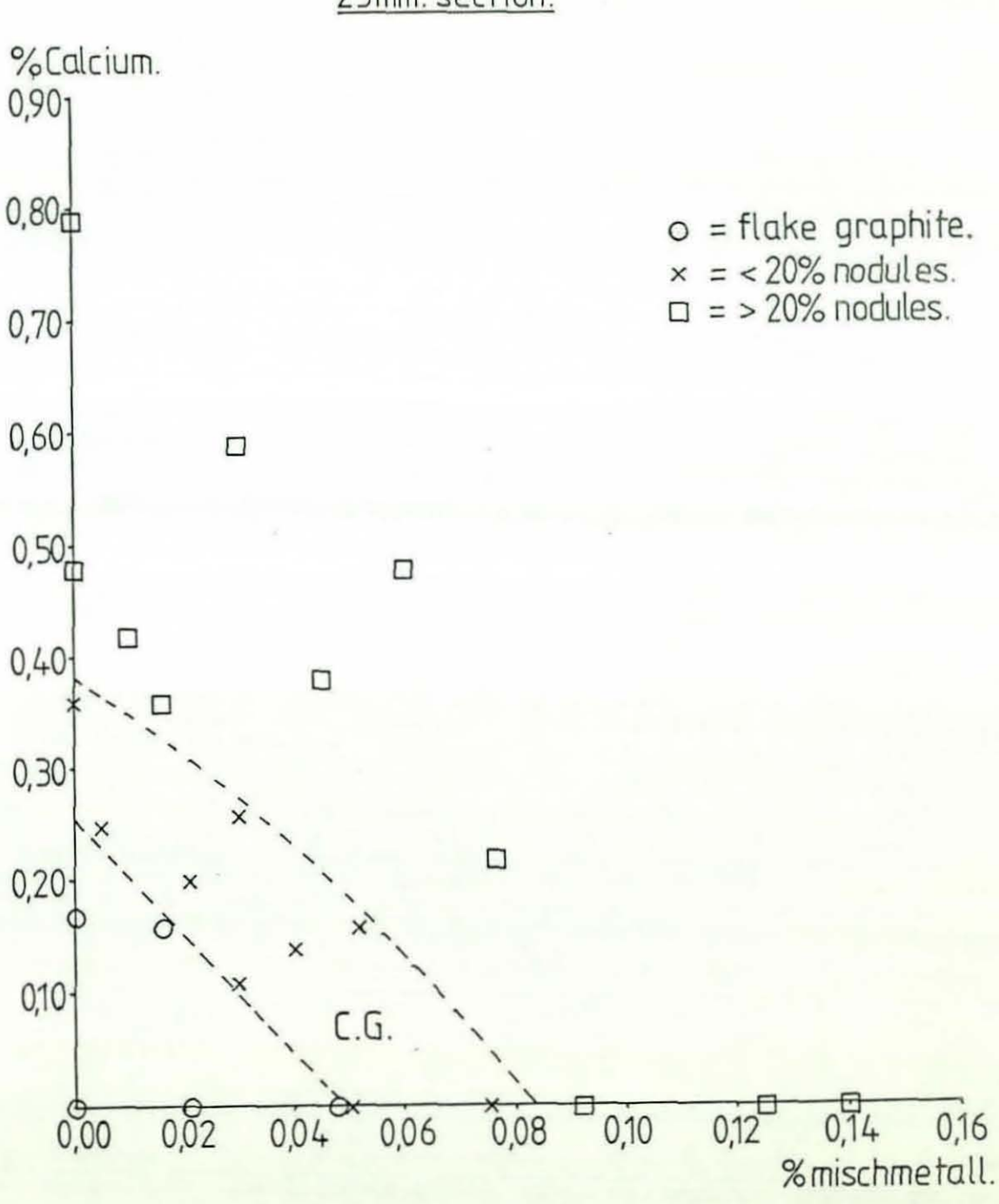

Figure 16. Melt series 1: the effect of addition level and section thickness on the graphite morphology.
16a. 25mm section.

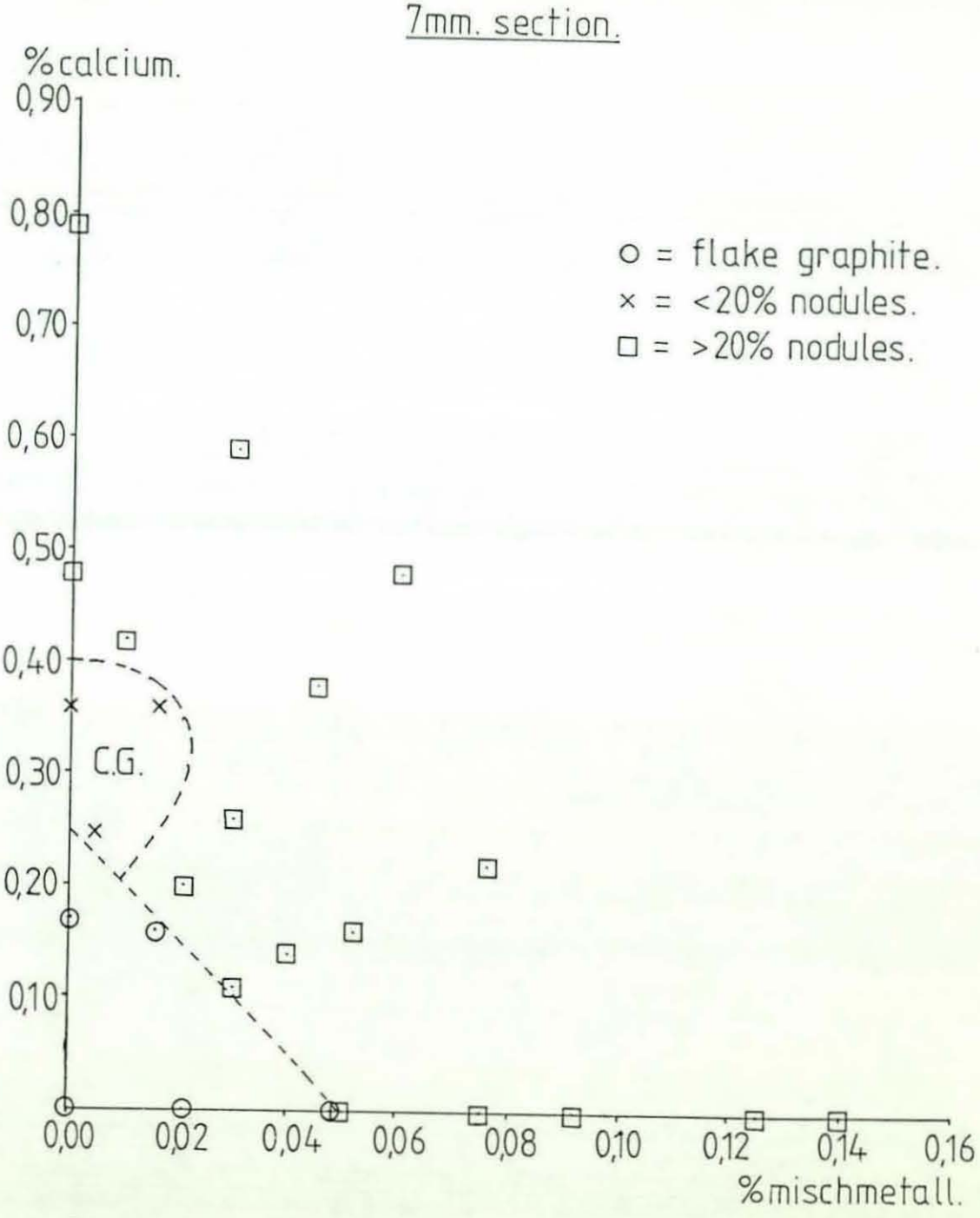

Figure 16 b. 7mm section.

4mm.section.

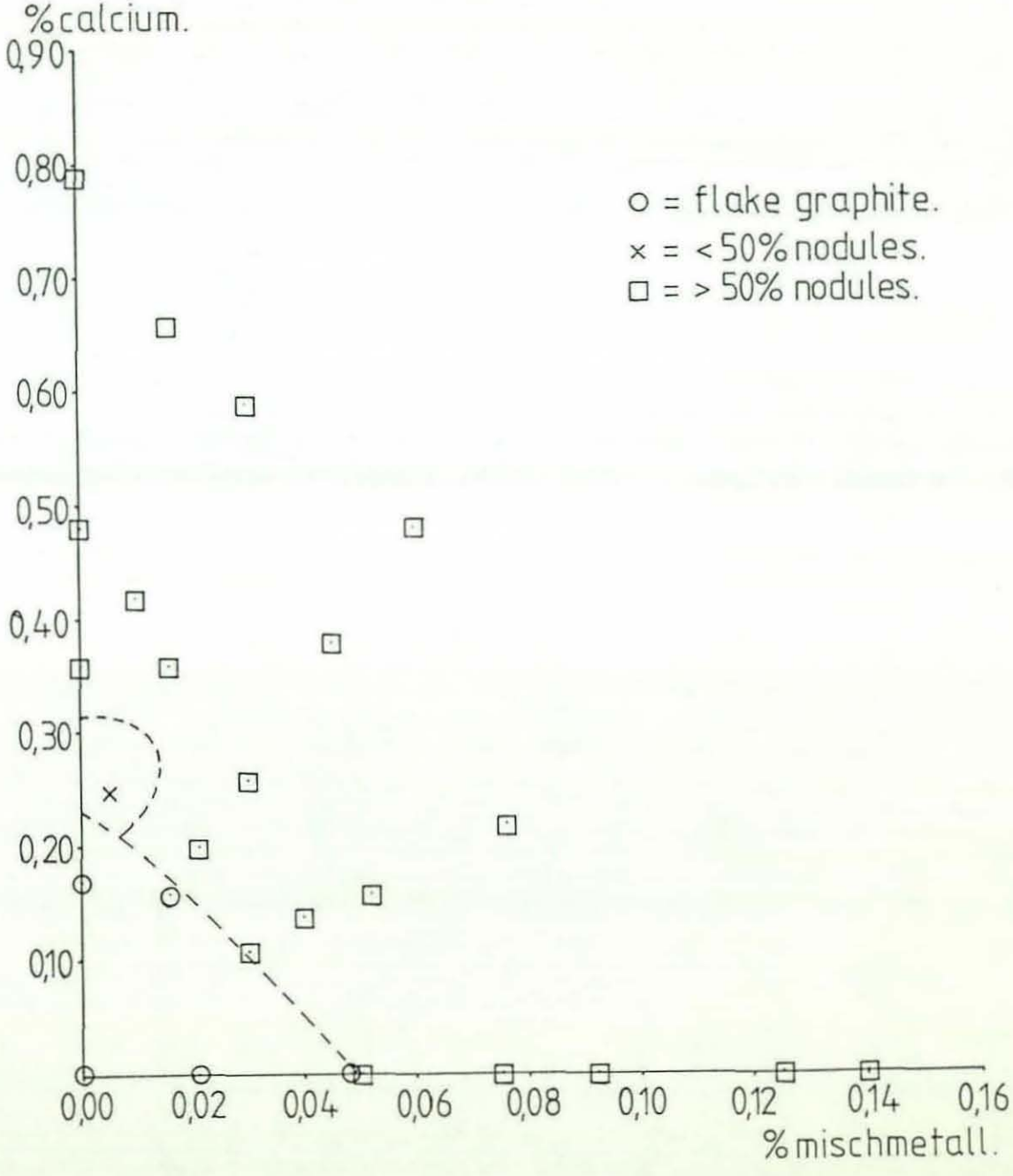

Figure 16 c. 4mm section.

The matrix structure in the 25 mm sections of all the castings produced in the mischmetall-calcium series consisted of ferrite with approximately 5% pearlite. The appearance and hardness of this structure in the 25 mm section were not significantly altered by variations in the mischmetall and calcium addition levels.

6.1.1.2 The Influence of Section Thickness on the Graphite Morphology

The effect of section thickness on the graphite morphology observed in flake graphite iron castings is illustrated by a comparison of the micrographs shown in Figures 17a and 17b, which respectively represent the 25 mm and 4 mm sections of a casting produced using an addition of 0.048% cerium mischmetall. The 25 mm section of this casting had a similar microstructure to that noted previously in a different casting (Figure 15b) and contained ASTM type A flake graphite. In the 4 mm section the comparatively higher solidification cooling rate resulted in the formation of ASTM type D flake graphite. The latter structure is characterised by a pattern of fine, highly branched graphite flakes outlining the original austenite dendrites.

With regard to compacted graphite iron castings, higher cooling rates increased the percentage of perfect and degenerate nodular graphite in the microstructure and decreased the average size of individual graphite particles. This is illustrated in Figure 18, which shows the microstructures that occurred in different sections of a typical cerium mischmetall-calcium treated casting. For the same casting, Figure 19 shows the variation in the percentage nodularity of the microstructure as a function of section thickness. This shows that there was no significant difference between the

75X

(a) 25 mm Casting Section

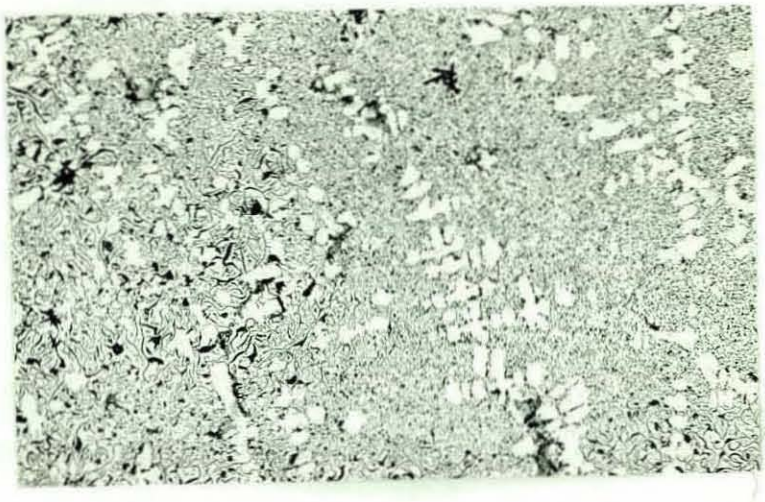

75X

(b) 4 mm Casting Section

Figure 17 The Effect of Cooling Rate on the Morphology of Flake Graphite (Casting 1/18)

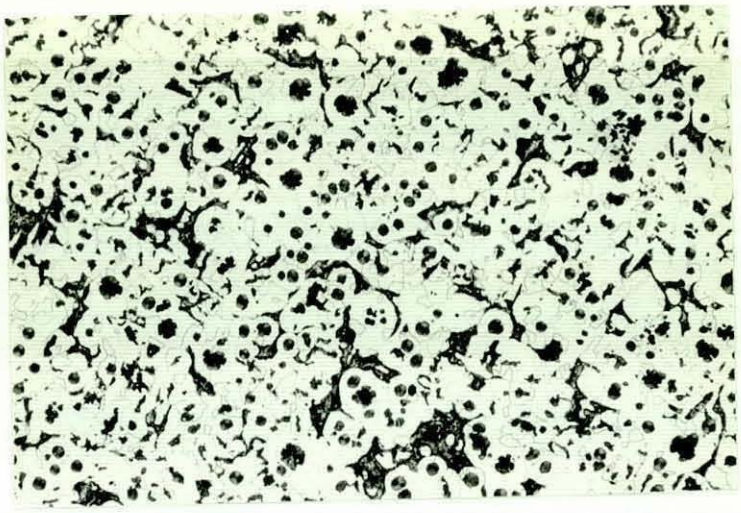

75X

(a) 4 mm Section

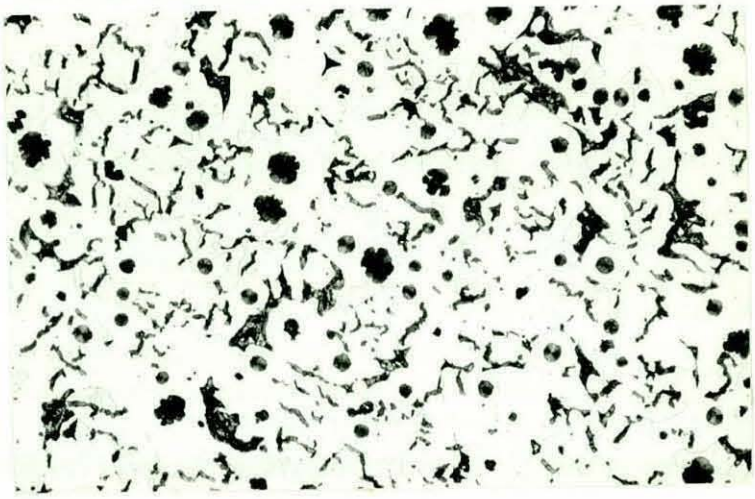

75X

(b) 7 mm Section

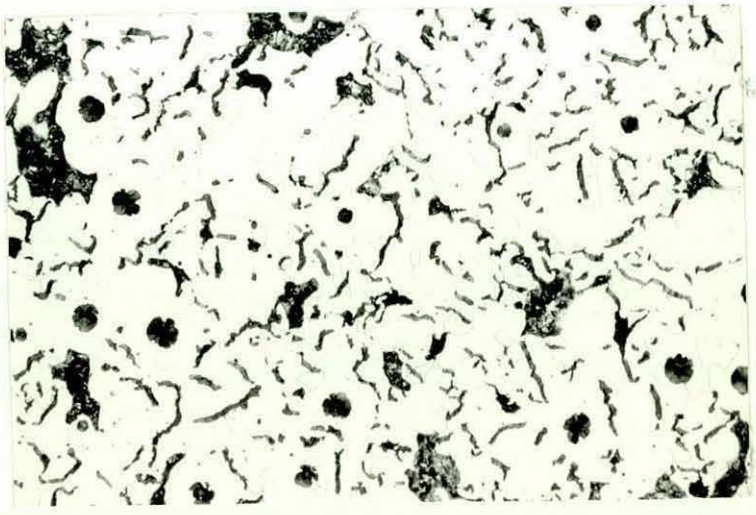

75X

(c) 10 mm Section

Figure 18 The Effect of Cooling Rate on the Morhphology of Compacted Graphite Produced by CeMM-Ca Melt Treatment (Casting 1/2)

(Figure continues over page)

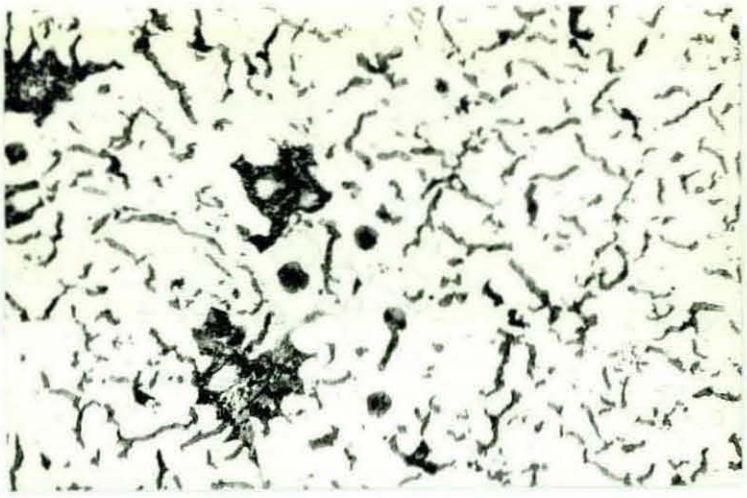

75X

(d) 14 mm Section

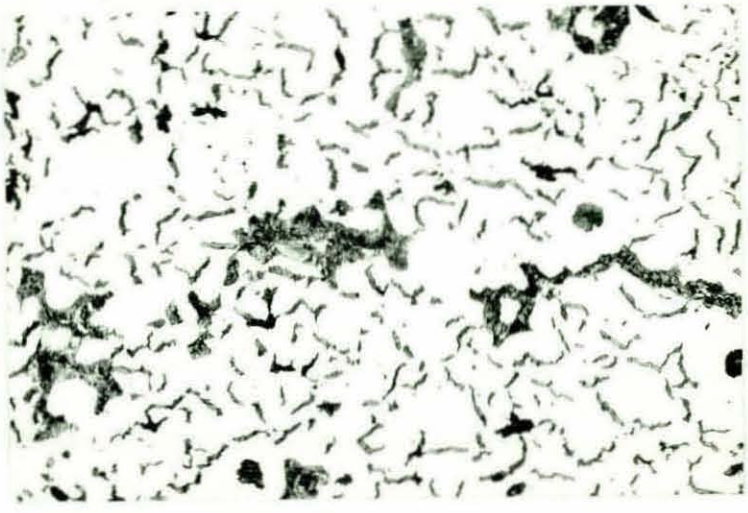

75X

(e) 18 mm Section

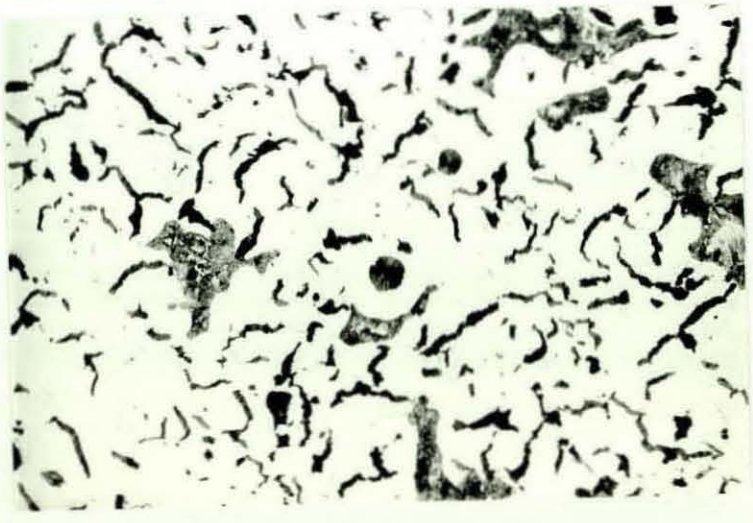

75X

(f) 20 mm Section

Figure 18 Continued

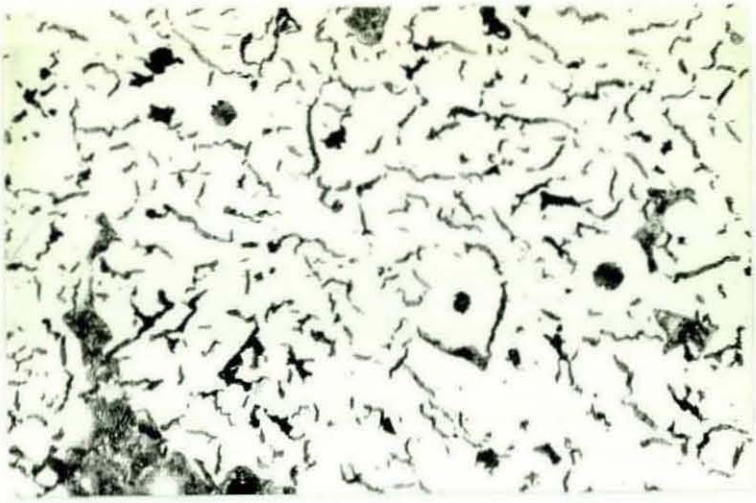

75X

(g) 25 mm Section

Figure 18 Continued

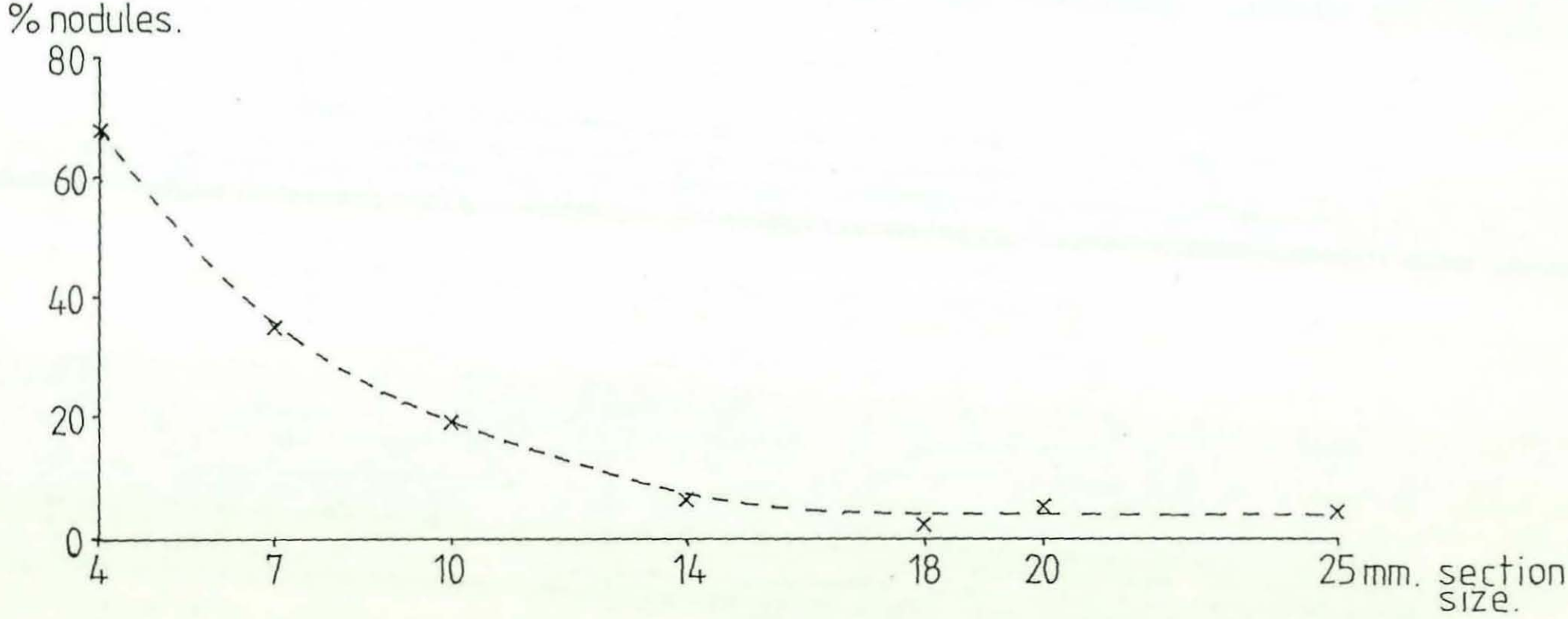

Figure 19. Casting 1/2 : effect of section thickness on nodularity.

graphite morphologies that occurred in sections ranging from 25 mm to 14 mm. At section thicknesses less than this, the percentage nodularity increased progressively with decreasing section size.

The ranges of cerium mischmetall-calcium additions that produced acceptable compacted graphite microstructures are illustrated in Figures 16a, 16b and 16c, for the 25 mm, 7 mm and 4 mm sections respectively. As explained in Chapter 5, acceptable compacted graphite microstructures were defined as having less than or equal to 20% nodules in the 25 mm and 7 mm sections, and less than or equal to 50% nodules in the 4 mm section. This distinction was made in order to conform with normal industrial practice. By comparing Figures 16a, 16b and 16c, it is clear that the compacted graphite morphology zone becomes smaller as the cooling rate increases. Furthermore, a higher percentage of calcium in the combined cerium mischmetall-calcium addition was required to produce acceptable compacted graphite microstructures in the smaller section thicknesses.

6.1.1.3 The Influence of Cerium Mischmetall Additions on the Hardness of the 4 mm Casting Section

The variation in the hardness of the 4 mm section with cerium mischmetall addition level is represented in Figure 20. This shows that for levels up to about 0.12%, the hardness increased gradually with increasing additions. Above 0.12%, the hardness increased at a greater rate, and at addition levels of 0.14% and higher, the microstructure contained a large proportion of free cementite. The difference between the microstructures obtained with 0.125 % and 0.14% cerium mischmetall levels is illustrated by a comparison of the micrographs shown in Figures 21a and 21b respectively.

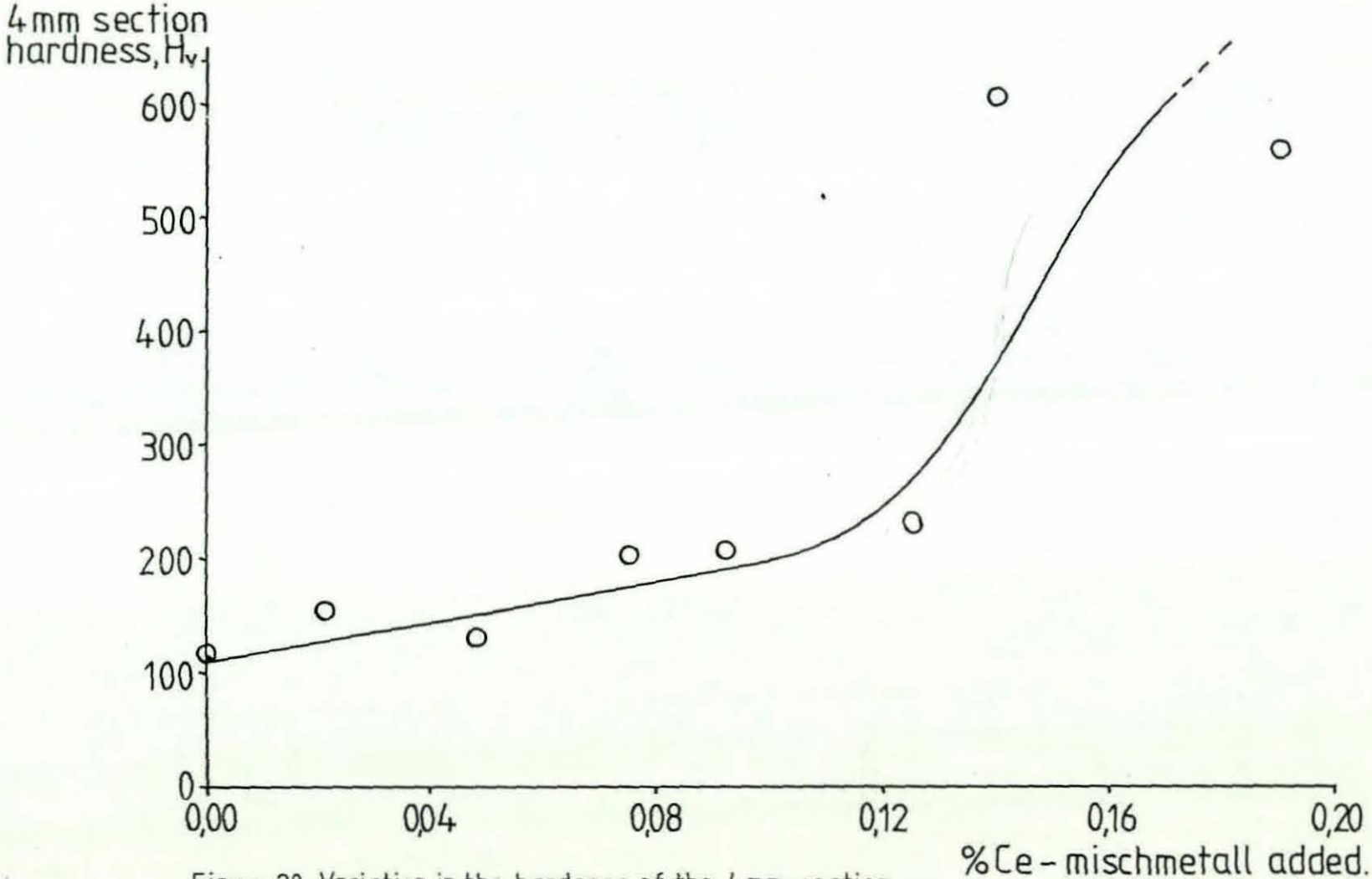

Figure 20. Variation in the hardness of the 4 mm section with percentage mischmetall addition (for castings treated only with cerium mischmetall).

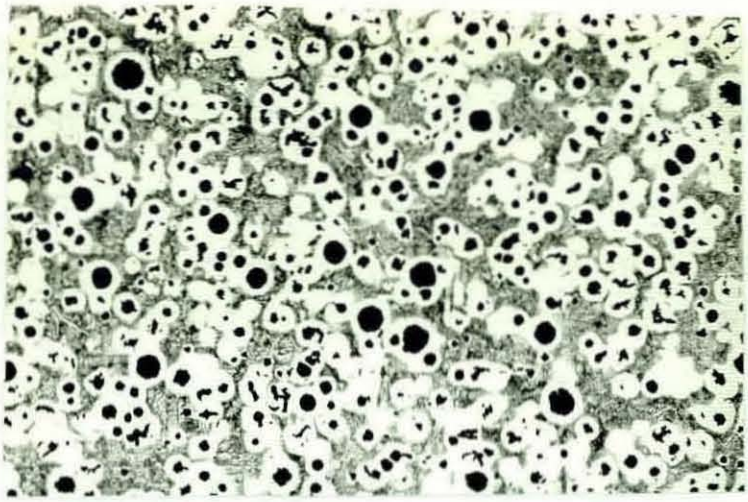

75X

(a) 0.125% Ce-MM (Casting 1/17)

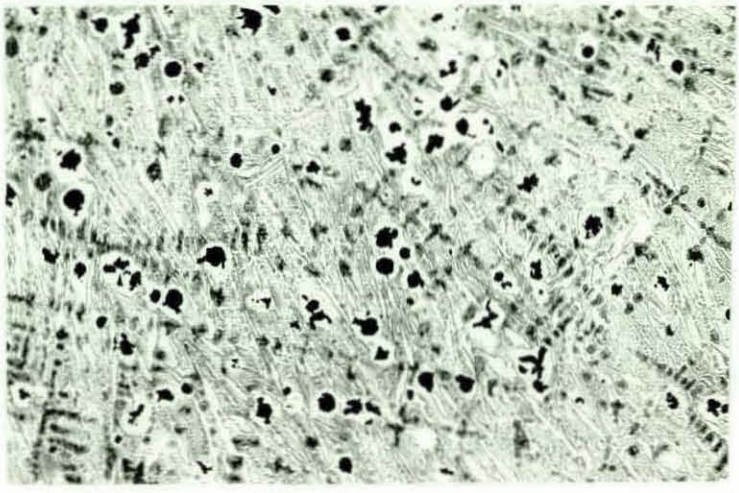

75X

(b) 0.14% Ce-MM (Casting 1/15)

Figure 21 Effect of Cerium Mischmetall Addition Level on the Microstructure Present in the 4 mm Section

With regard to the combined cerium mischmetall-calcium treatment, no significant correlation was detected between the hardness of the 4 mm section of these castings and the levels of calcium and mischmetall used in the addition. Although this was also true of irons 1/22, 1/23 and 1/24, produced using calcium additions alone, it is interesting to note that the 4 mm sections of the latter castings were in all cases harder than the average value for the irons treated with a combined cerium mischmetall-calcium addition.

6.1.2 Magnesium-Titanium Additions (Series 2)

6.1.2.1 The Influence of Addition Level on the Graphite Morphology

The flake, compacted and nodular graphite produced using additions of magnesium and titanium appeared optically to be identical to the corresponding graphite structures produced using mischmetall and calcium additions. For example, Figure 18g and 25g show compacted graphite microstructures produced using cerium mischmetall-calcium and magnesium-titanium additions respectively.

At magnesium addition levels below 0.03%, increasing levels of titanium addition caused a series of changes in the morphology of the flake graphite microstructure occurring in the 25 mm section of the casting. This can be summarised as follows:

ASTM type A flake graphite

↓

Finer, more branched flake graphite

↓

ASTM type D flake graphite

↓ Increasing Ti addition level (Mg addition level < 0.03%)

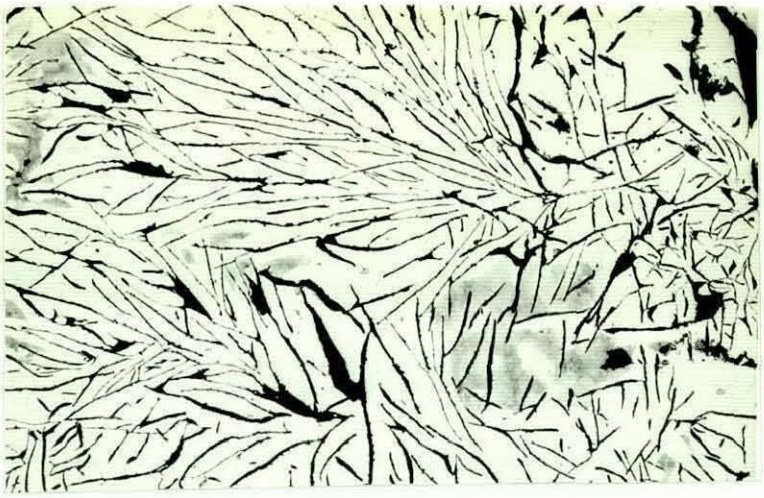

75X

(a) 0.0% Ti, 0.0% Mg (Casting 2/5);
Coarse ASTM Type A Flake Graphite

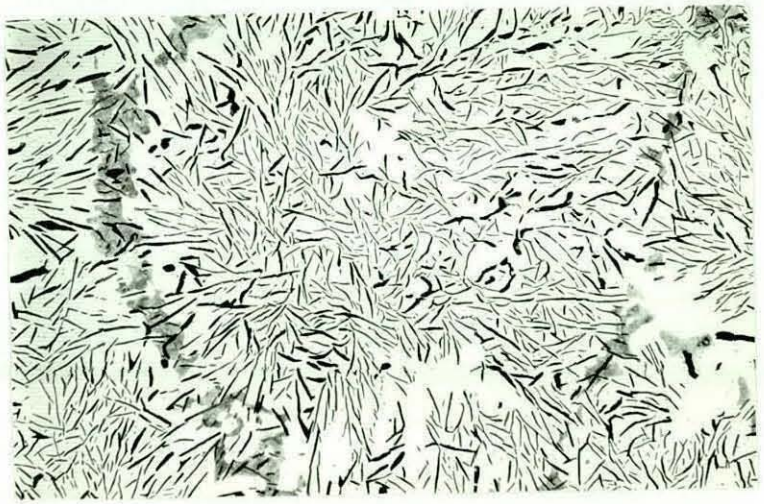

75X

(b) 0.07% Ti, 0.025% Mg Addition (Casting 2/4)

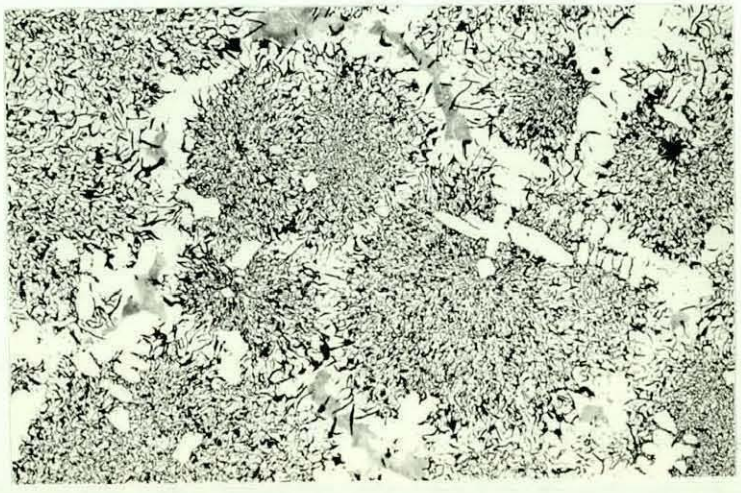

75X

(c) 0.17% Ti, 0.0% Mg Addition (Casting 2/6);
ASTM Type D Flake Graphite

Figure 22 Effect of Titanium on the Flake Graphite Morphology (25 mm Section Thickness)

These effects are illustrated by a comparison of Figures 22a, 22b and 22c, for titanium additions of 0.0%, 0.07% and 0.17% respectively, at magnesium addition levels below 0.03%.

Compacted graphite was produced at magnesium addition levels above 0.03%, and further increases in the level of this element (for a constant titanium addition level) increased the percentage of perfect and degenerated nodular graphite in the microstructure.

The effect of single and combined additions of magnesium and titanium on the graphite morphology in the 25 mm section of castings are represented in Figure 23a. This shows that compacted graphite microstructures with less than 20% nodules were produced using 0.04 to 0.10% magnesium added together with 0.07 to 0.17% titanium. Smaller titanium addition levels resulted in a reduced range of magnesium addition levels over which compacted graphite structures occurred, and only one casting containing less than 20% nodules in the 25 mm section was produced using a magnesium treatment alone. The addition level used in the production of the latter casting was 0.046% magnesium.

Compared to the mischmetall-calcium method, the compacted graphite iron produced using the magnesium-titanium treatment (where the titanium addition was greater than 0.04%) was less sensitive to variations in the treatment composition. For example, at a titanium treatment level of 0.07%, additions of between 0.035% and 0.10% magnesium (a range of 0.065% Mg) produced compacted graphite microstructures with less than 20% nodules in the 25 mm section (Figure 23a). With the mischmetall-calcium treatment, the range of cerium mischmetall additions for which similar microstructures were produced in the 25 mm section was between 0.01% and 0.045% (a range of 0.035%), using a calcium addition of 0.2% (Figure 16a).

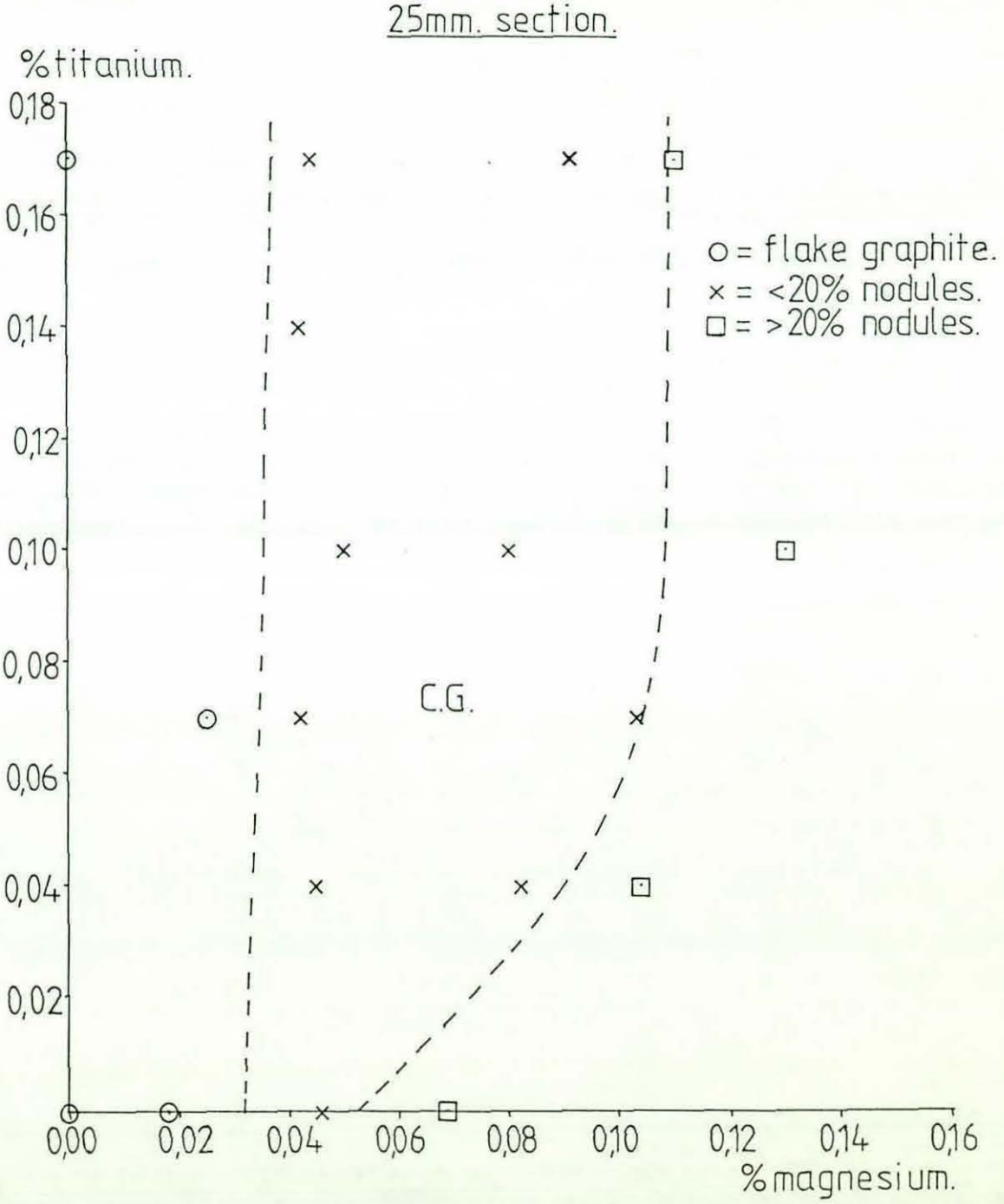

Figure 23. Melt series 2: the effect of addition level and section thickness on the graphite morphology.
23a. 25mm section.

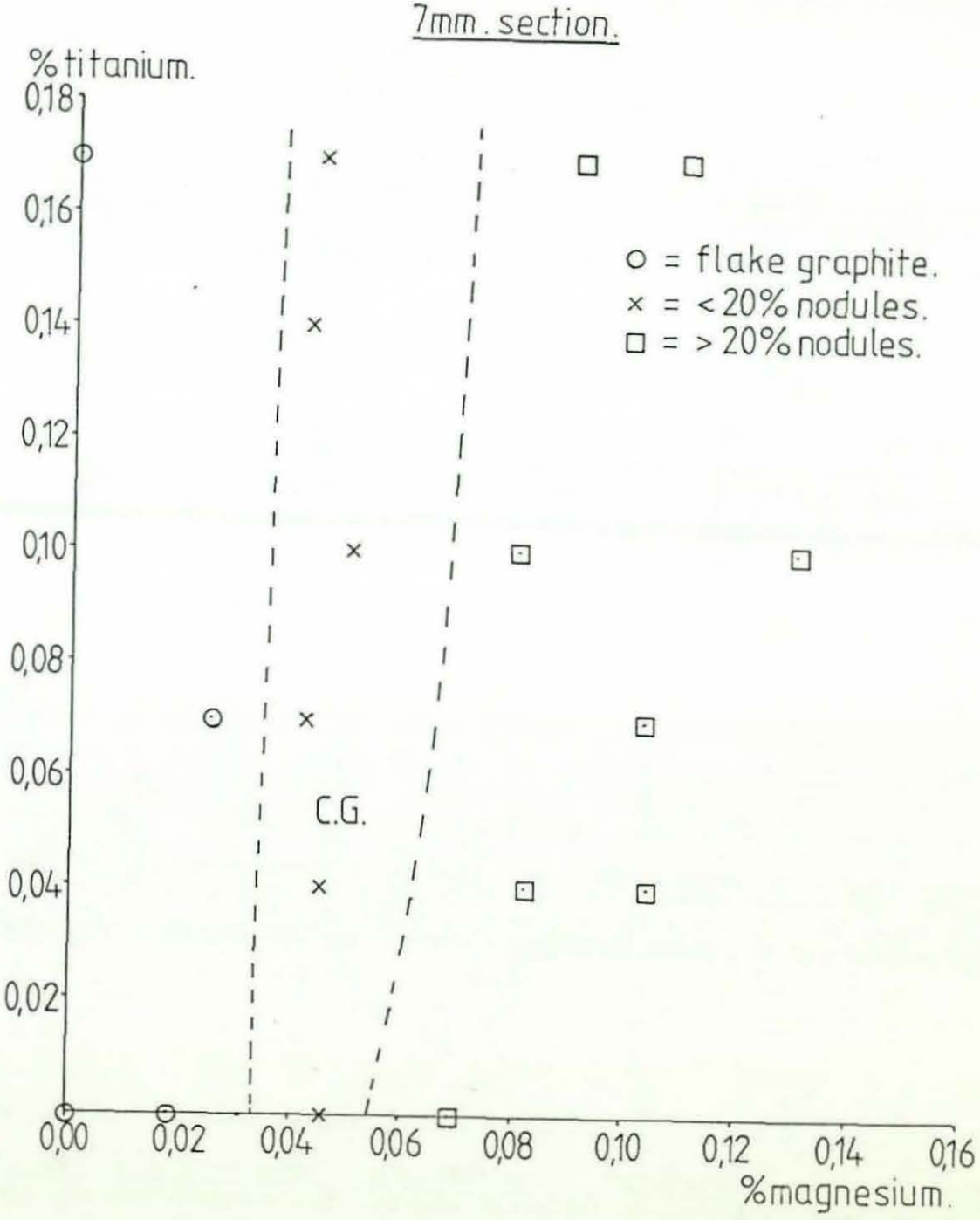

Figure 23 b. 7mm section.

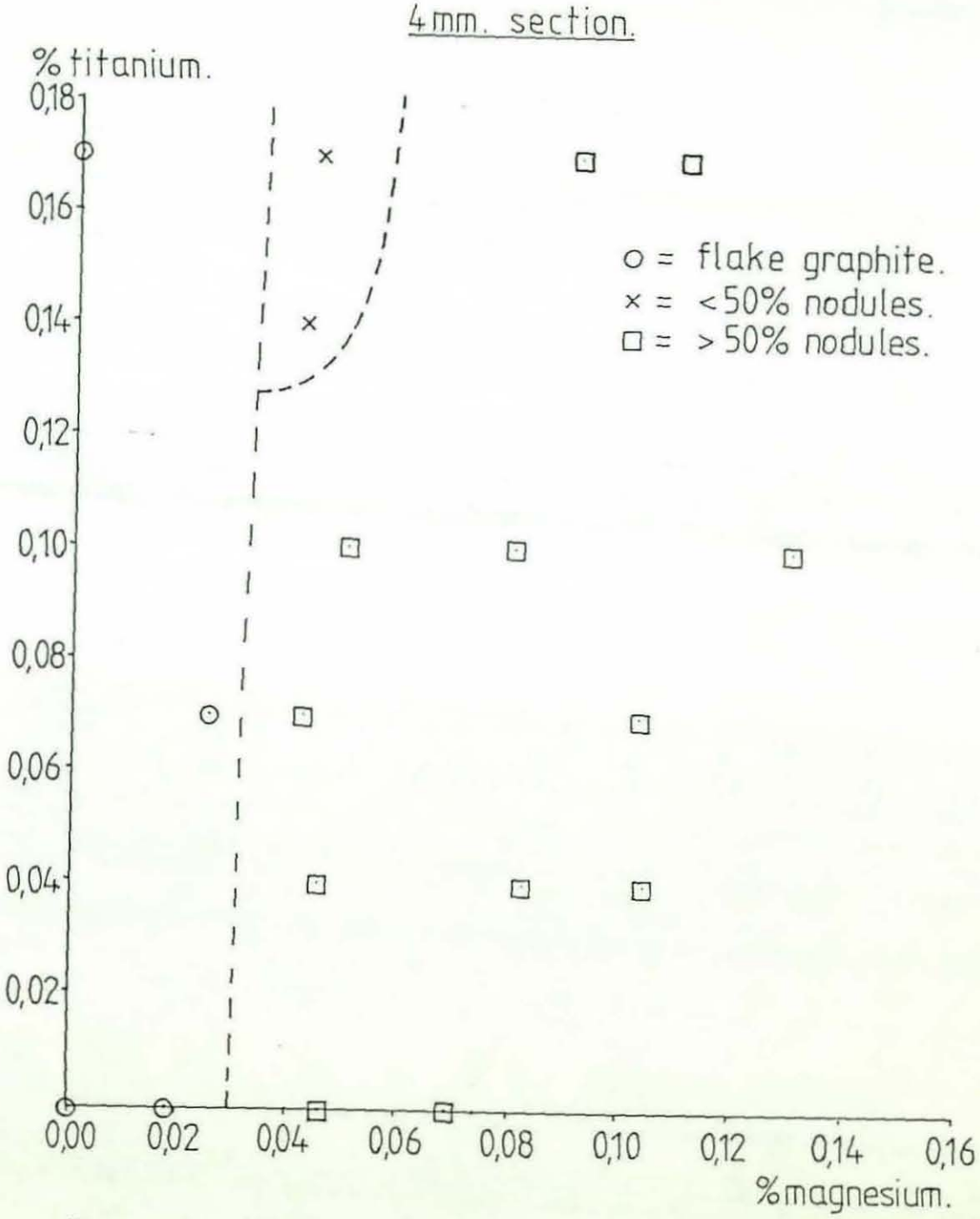

Figure 23c. 4mm section.

Similar matrix structures to those encountered in melt series 1 were produced by using the magnesium-titanium treatment. At all treatment levels, the matrix structure in the 25 mm section was predominantly ferritic with approximately 5% pearlite.

6.1.2.2 The Influence of Section Thickness

With the exception of casting 2/6, the effect of section thickness on the graphite structure in the flake graphite iron castings produced in melt series 2 was identical to that observed with the mischmetall-calcium treatments: ASTM type D flake graphite occurred in the 4 mm section of castings that contained ASTM type A flake graphite in the 25 mm section. In casting 2/6, which contained ASTM type D flake graphite in the 25 mm section (Figure 22c), a more refined form of type D flake graphite occurred in the 4 mm section. The latter structure is illustrated in Figure 24.

The effect of section thickness on the graphite structure in compacted graphite castings in melt series 2 was also similar to that noted with the mischmetall-calcium treatments. For example, Figure 25 shows the microstructures obtained in different section thicknesses of casting 2/2, which was produced using an addition of 0.045% magnesium to a base iron containing 0.04% titanium. Smaller section thicknesses caused an increase in the percentage of perfect and degenerate nodular graphite in the microstructure and a decrease in the average size of individual graphite particles. The variation in the percentage nodularity of the microstructure as a function of section thickness for casting 2/2 is shown in Figure 26. A comparison with the corresponding results shown in Figure 19 for a mischmetall-calcium treated casting indicates that the nodularity of the compacted graphite microstructures produced using magnesium-

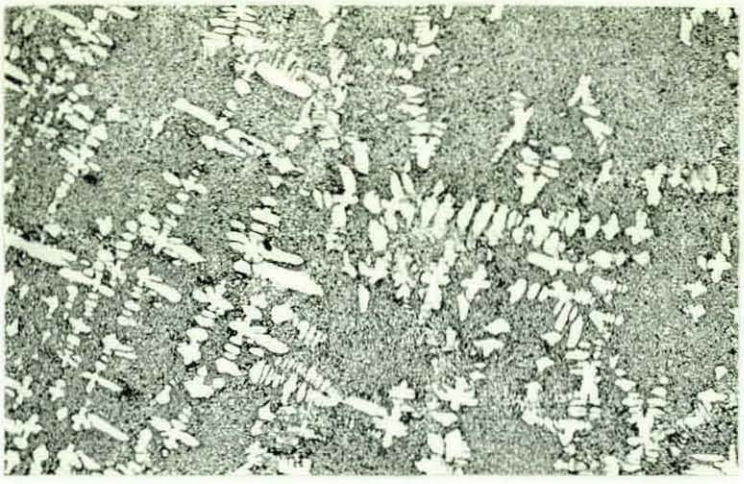

75X

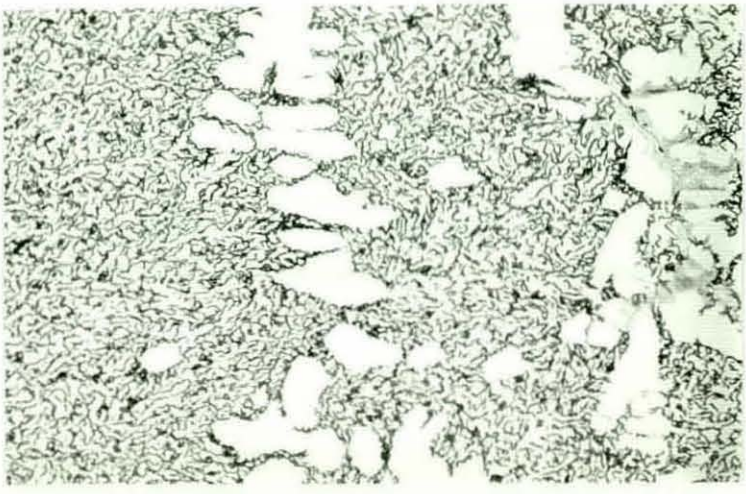

300X

Figure 24 Fine ASTM Type D Flake Graphite Present in the 4 mm Section of Casting 2/6

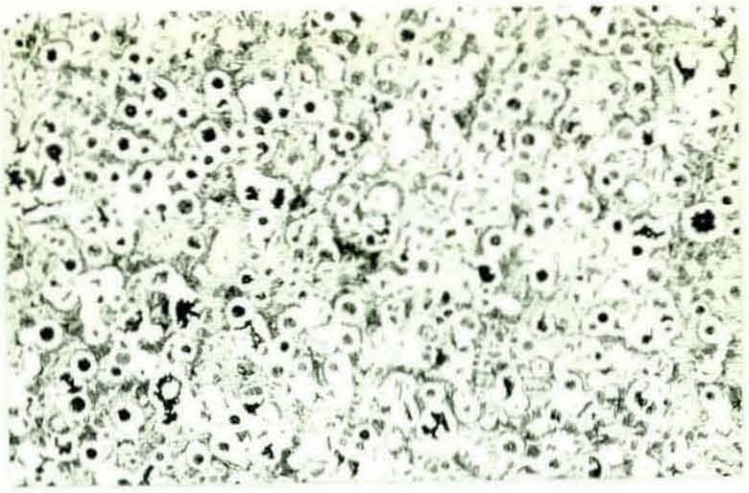

75X

(a) 4 mm Section

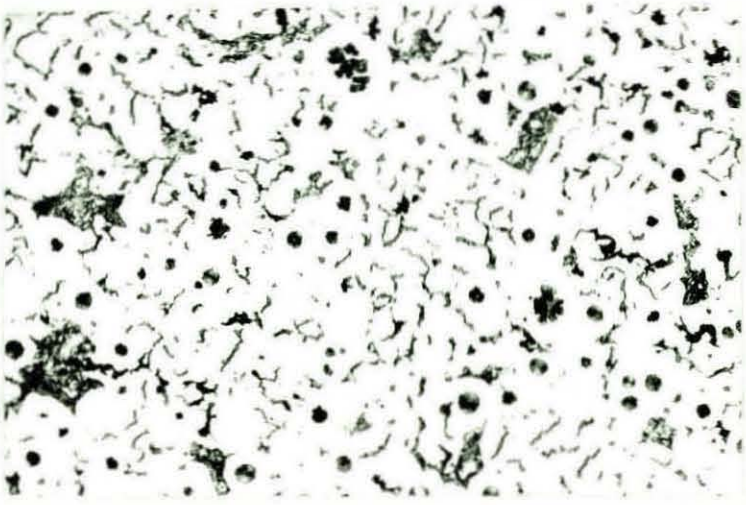

75X

(b) 7 mm Section

75X

(c) 10 mm Section

Figure 25 The Effect of Cooling Rate on the Morphology of Compacted Graphite Produced by Mg-Ti Melt Treatment (Casting 2/2) (Figure Continues over page)

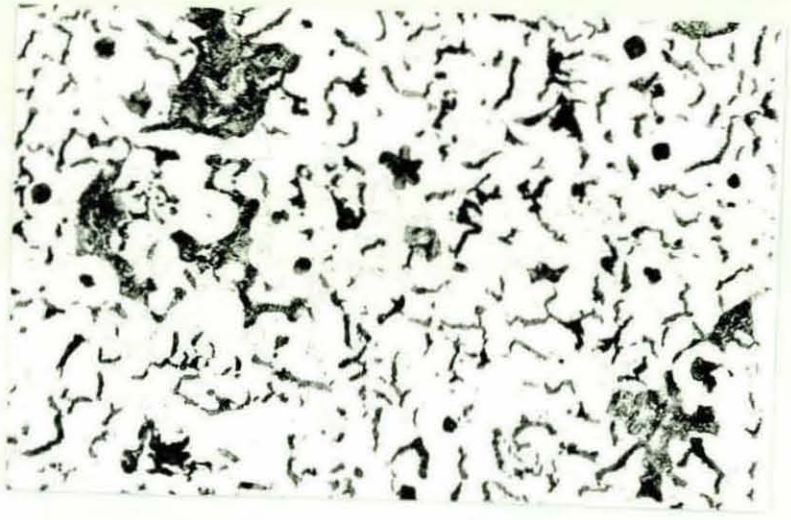

75X

(d) 14 mm Section

75X

(e) 18 mm Section

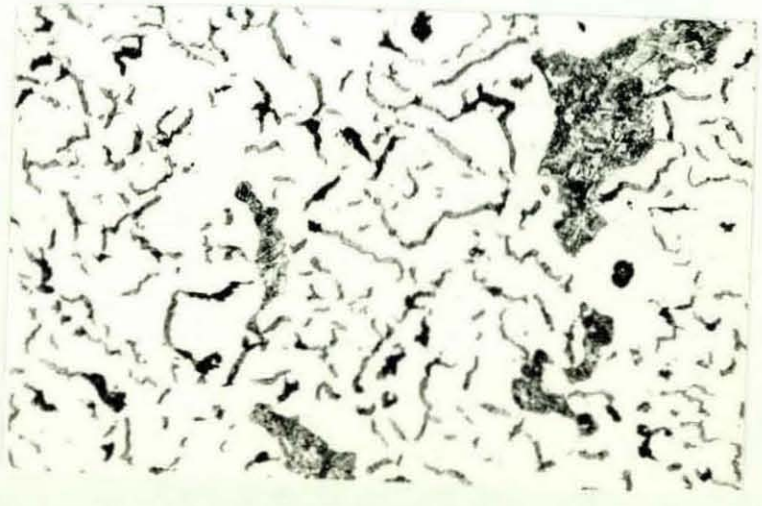

75X

(f) 20 mm Section

Figure 25 Continued

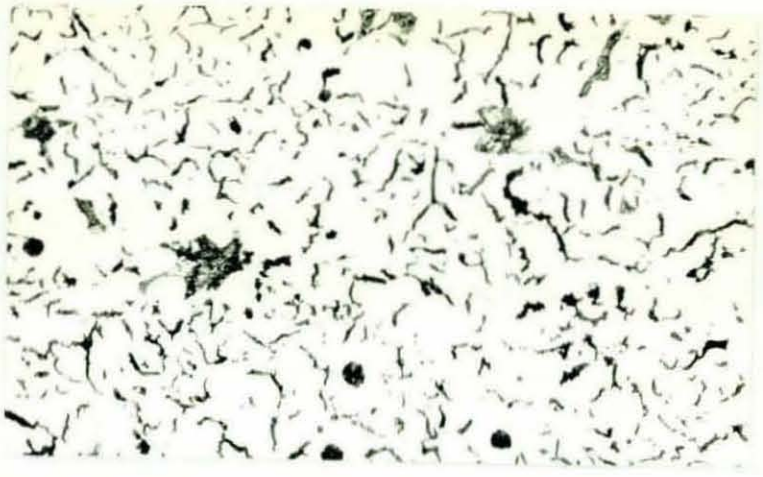

75X

(g) 25 mm Section

Figure 25 Continued

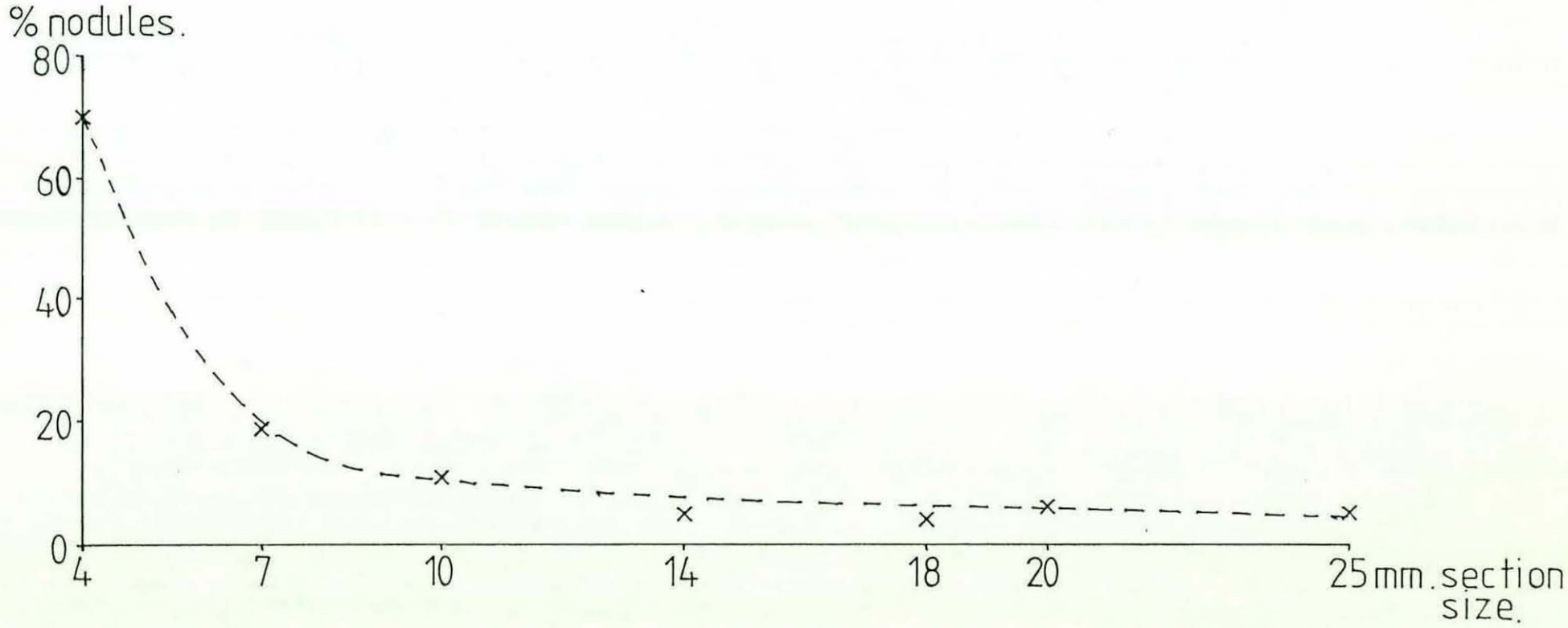

Figure 26. Casting 2/2 : effect of section thickness on % nodularity.

titanium additions is less sensitive to variations in the cooling rate: with the magnesium-titanium treatment, the effect of section thickness on the percentage nodularity appeared to become significant with sections less than 10 mm, as compared to 14 mm for the mischmetall-calcium treatment.

The effect of section thickness on the range of magnesium-titanium addition levels over which acceptable compacted graphite microstructures were produced is illustrated by a comparison of Figures 23a, 23b and 23c, which represent the 25 mm, 7 mm and 4 mm casting sections respectively. The zone representing an acceptable compacted graphite morphology clearly becomes smaller as the section thickness decreases, and additions of at least 0.14% titanium and approximately 0.04% magnesium were required to produce a compacted graphite microstructure with less than 50% nodules in the 4 mm section. A comparison with the corresponding results obtained in melt series 1 (Figure 16) again indicates that the morphology of the graphite present in castings produced using a magnesium-titanium treatment is less sensitive to variations in the cooling rate.

The influence of cooling rate on the matrix structure of the castings produced in melt series 2 was similar to the effect observed with castings produced using mischmetall-calcium additions. The hardness of the 4 mm section varied slightly between the castings depending on the relative amounts of ferrite,pearlite and free cementite present in the microstructure. However, for compacted/nodular graphite castings, no significant correlation could be detected between the hardness value and the levels of magnesium and titanium additions used.

6.1.3 Magnesium-Aluminium Additions

A limited number of melts were carried out using magnesium-aluminium treatment, and the majority of the castings produced by this method contained only ASTM type A flake graphite in all sections. However, a combined addition of 0.08% magnesium and 0.41% aluminium, was found to give a compacted graphite microstructure with less than 20% nodules in the 25 mm section. The morphology of the compacted graphite present in this casting was optically identical to that produced using either of the two previous types of treatment.

6.1.4 Calcium-Zirconium and Magnesium-Zirconium Additions

Zirconium was found to be analogous to titanium in its effect on the graphite morphology. As with titanium, melt treatment with zirconium additions alone produced an ASTM type D flake graphite microstructure, figure 27. Additions of calcium or magnesium to a zirconium-bearing melt resulted in compacted graphite microstructures with various percentages of nodular graphite, depending on the exact addition levels used. The microstructures that occurred in each section of a casting which was produced by melt treatment with 0.5% Zr (resulting in a residual zirconium level of 0.3%), and 0.6% calcium, are shown in Figure 28. It is interesting to note that the graphite structure present in the 7 mm section of this casting showed some evidence of interdendritic segregation. This effect was not as noticeable with irons produced using the previous types of melt treatment. Figure 29 represents the variation in the percentage nodularity of the microstructure as a function of section thickness. These results show that very low nodularity values were obtained in all section thicknesses of this casting, although a high percentage of free cementite occurred in the matrix structure of the 4 mm section. Comparatively higher

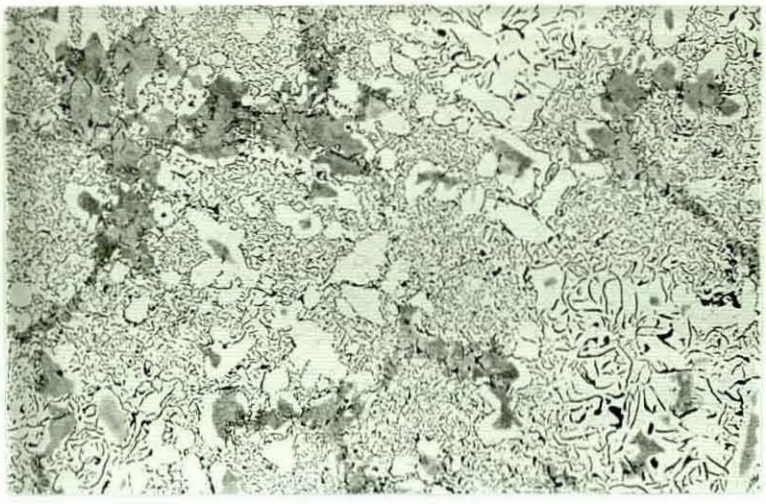

75X

Figure 27 ASTM Type D Flake Graphite Produced by a 1.7% Zr Melt Treatment

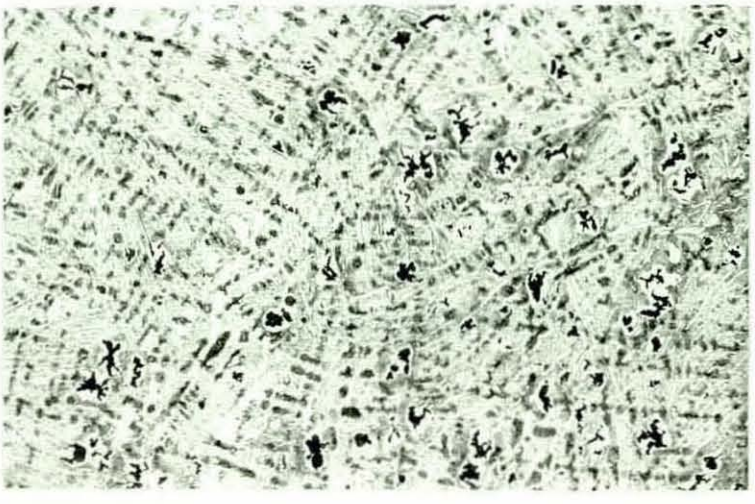

75X

(a) 4 mm Section

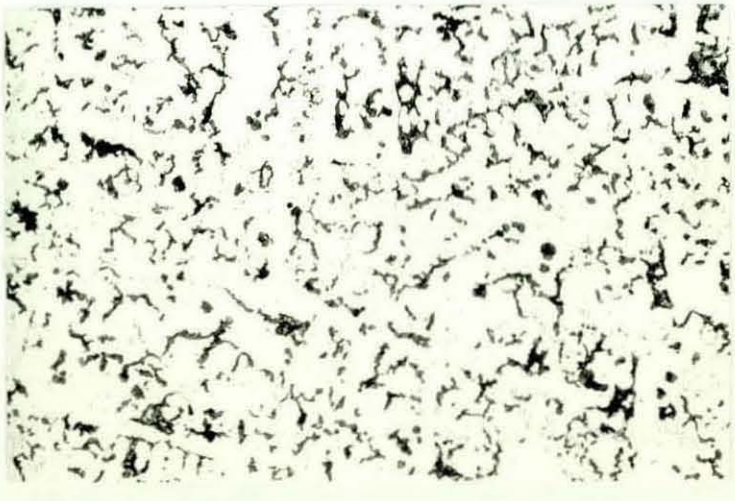

75X

(b) 7 mm Section

Figure 28 The Effect of Cooling Rate on the Morphology of Compacted Graphite Produced by Ca-Zr Treatment
(Figure Continues over page) (casting 4/1)

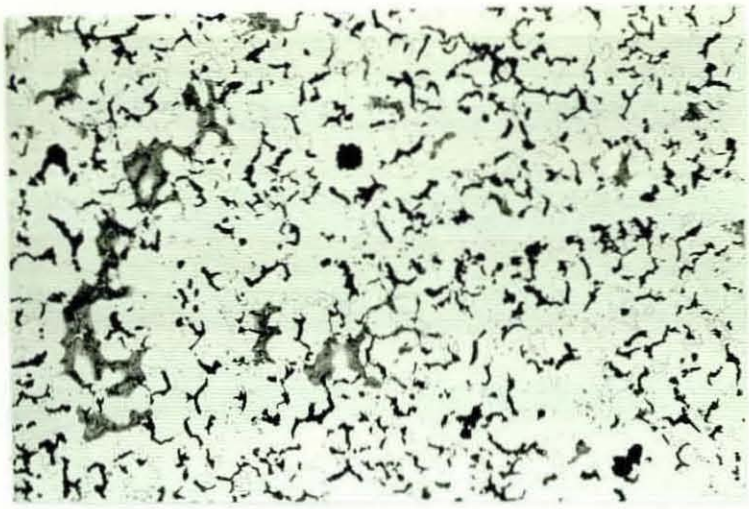

75X

(c) 10 mm Section

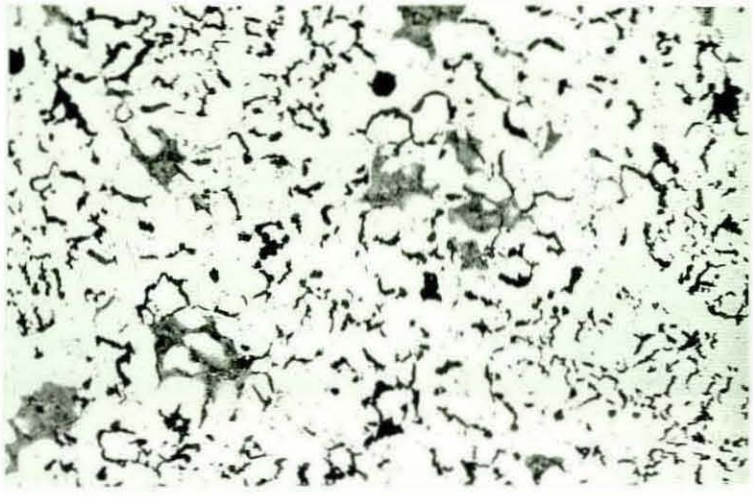

75X

(d) 14 mm Section

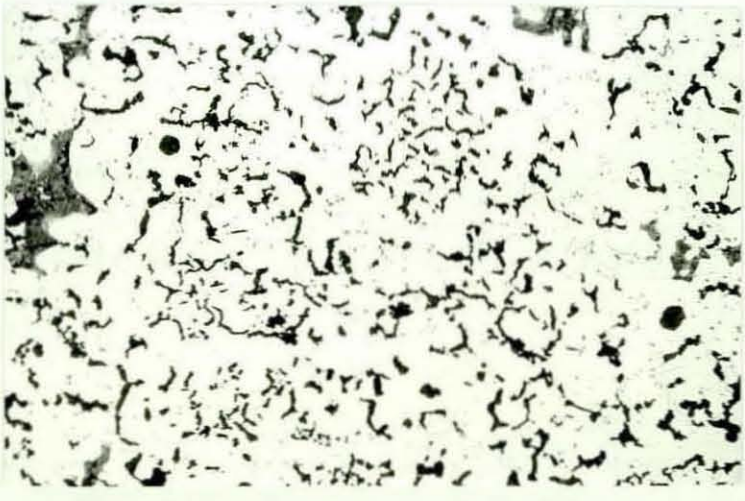

75X

(e) 18 mm Section

Figure 28 Continued

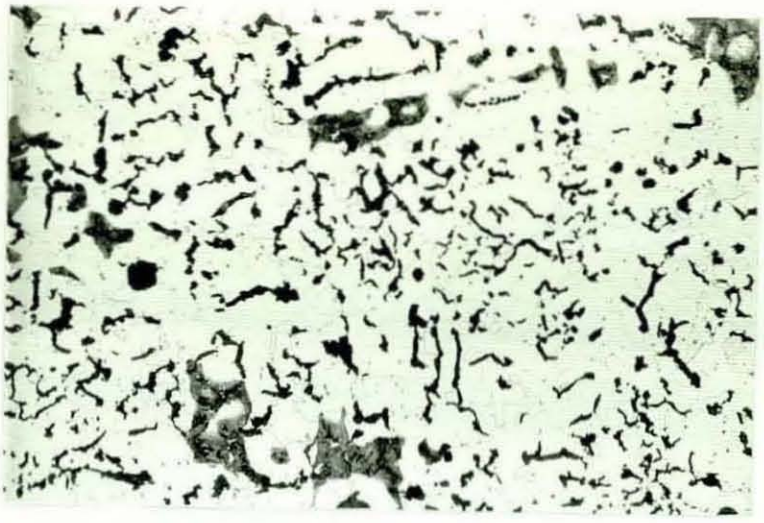

75X

(f) 20 mm Section

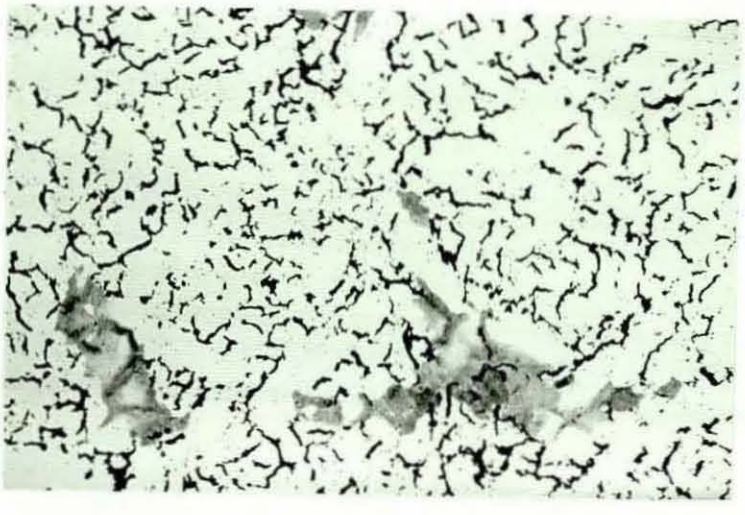

75X

(g) 25 mm Section

Figure 28 Continued

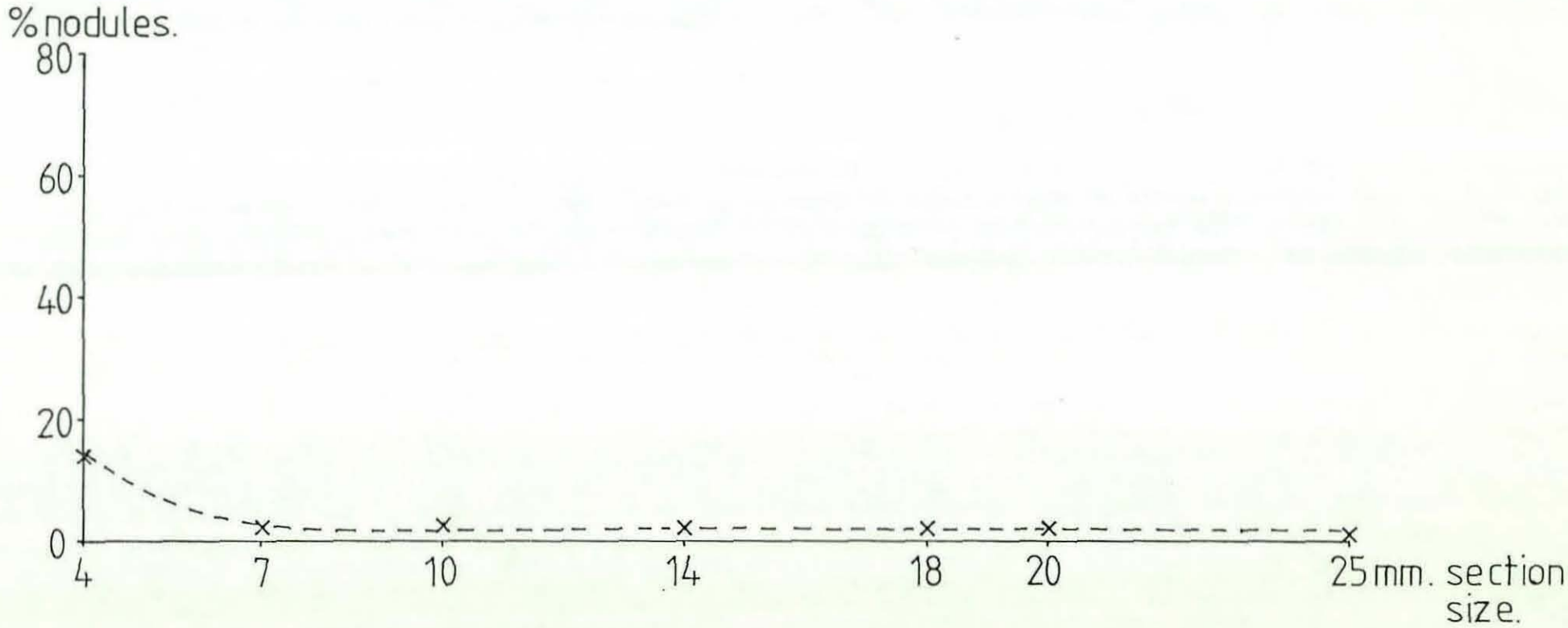

Figure 29. Casting 4/1: effect of section thickness on % nodularity.

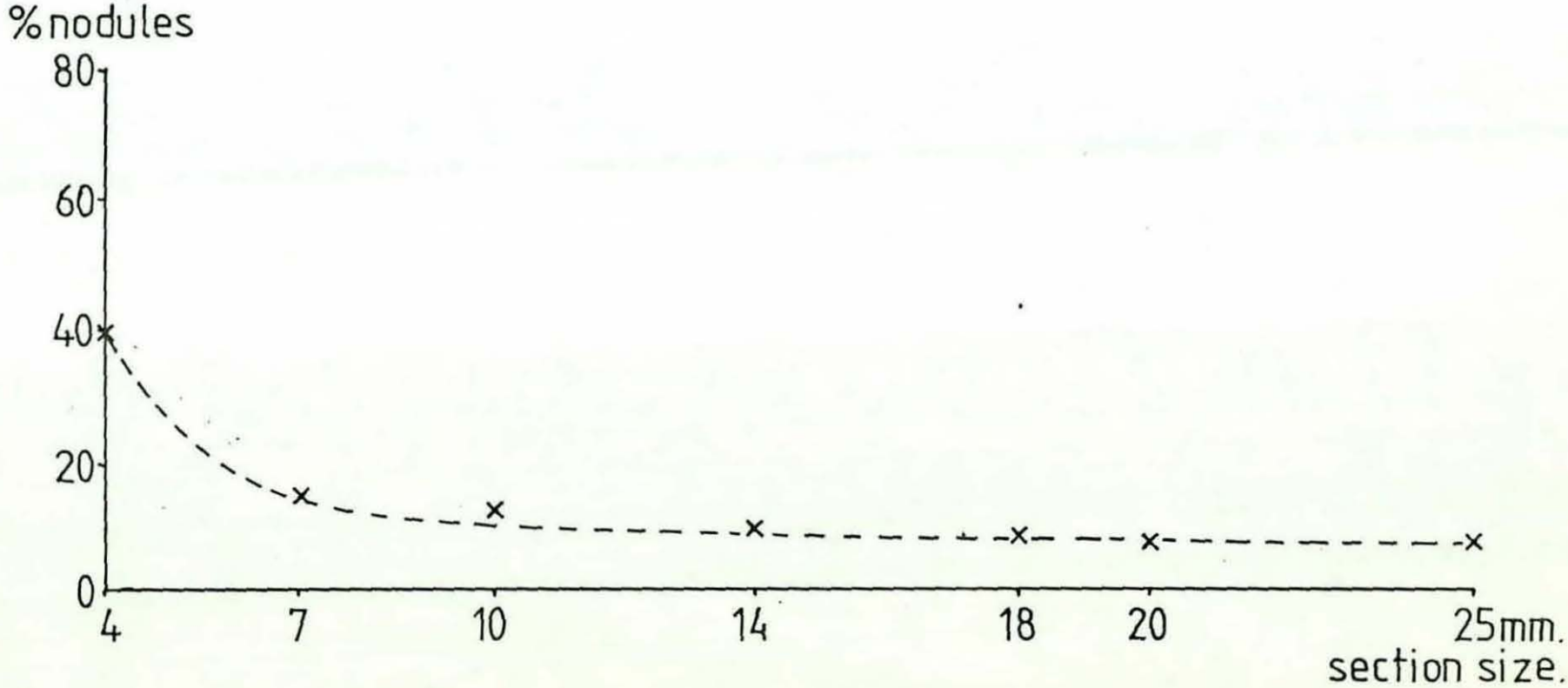

Figure 30. Casting 4/2 : effect of section thickness on %nodularity.

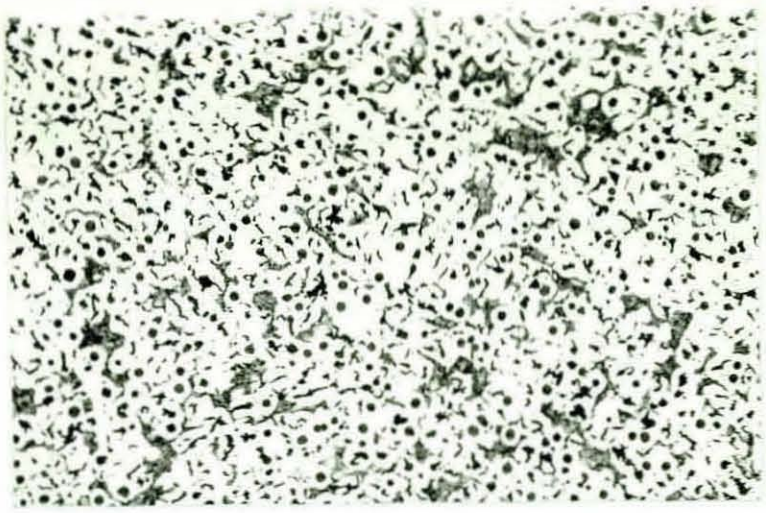

75X

Figure 31 Microstructure Produced in the 4 mm Section by Melt Treatment with 0.055% Mg and 0.5% Zr (Casting 4/2)

nodularity values were obtained in the respective sections of a casting produced using the same level of zirconium treatment, but with the addition of 0.055% magnesium in place of the calcium treatment. This is illustrated in Figure 30, and Figure 31 additionally shows that compared to the previous iron (Figure 28a), the 4 mm section of the magnesium-zirconium treated casting contained a significantly lower percentage of free cementite.

A comparison between the latter results and the corresponding data for mischmetall-calcium (Figures 18 and 19) and magnesium-titanium additions (Figures 25 and 26), indicates that both the calcium-zirconium and the magnesium-zirconium treatments are potentially able to produce compacted graphite microstructures that are significantly less sensitive to variations in the cooling rate than either of the two former types of treatment. Since only a limited number of melts have been carried out with the zirconium treatments, further work would clearly be needed to verify the above results. In addition, the practicalities of using Ca-Zr and Mg-Zr treatments for the industrial production of CG iron castings would require investigation. These aspects are discussed in a subsequent section of this report.

6.2 The Growth Structure of Graphite

In order to gain information on the structural characteristics of flake, spheroidal and compacted graphite, samples from selected castings were studied using optical and scanning electron microscopy.

6.2.1 Flake Graphite

Figure 32 illustrates the eutectic cell structure of ASTM type A flake graphite in an untreated base iron. For the same sample, the

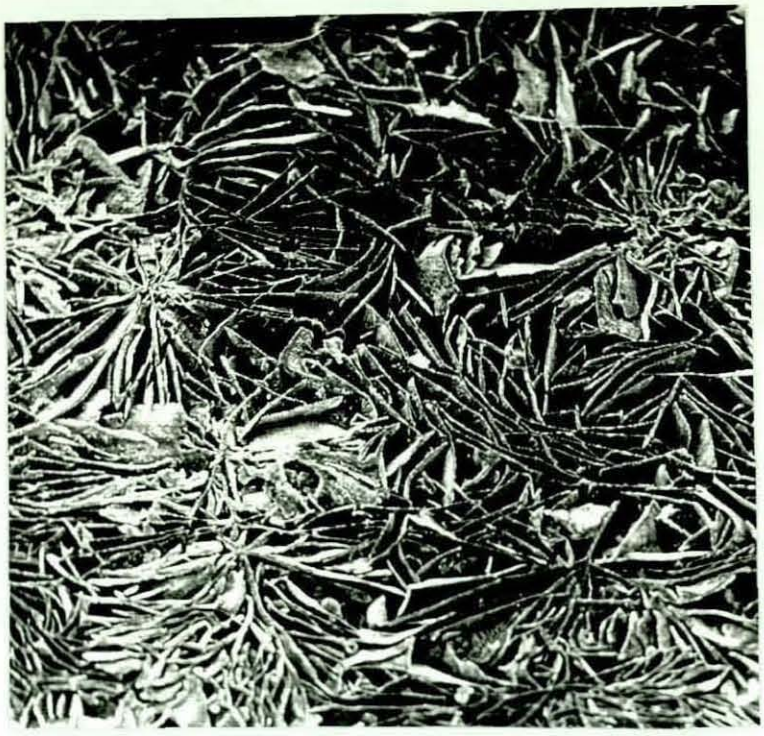

50X

Figure 32 ASTM Type A Flake Graphite, Deep Etched (Casting 2/5)

200X

Figure 33 ASTM Type A Flake Graphite, Deep Etched (Casting 2/5)

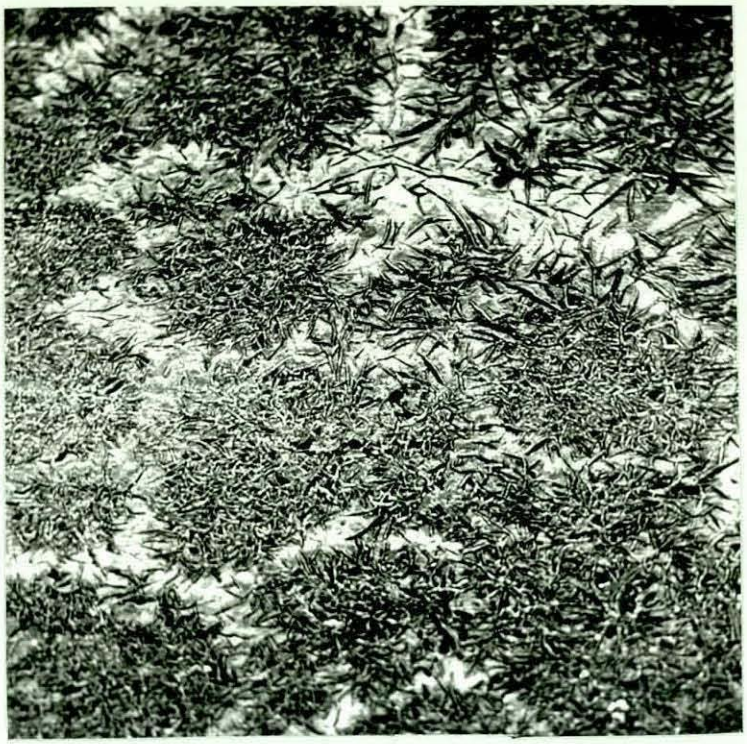

45X

Figure 34 ASTM Type D Flake Graphite Produced by Melt Treatment with 0.17% Ti, Deep Etched (Casting 2/6)

185X

Figure 35 ASTM Type D Flake Graphite, Deep Etched (Casting 2/6)

2100X

Figure 36 Flake Graphite Modified by Melt Treatment with 0.016% Ce MM and 0.16% Ca, Deep Etched (Casting 1/6)

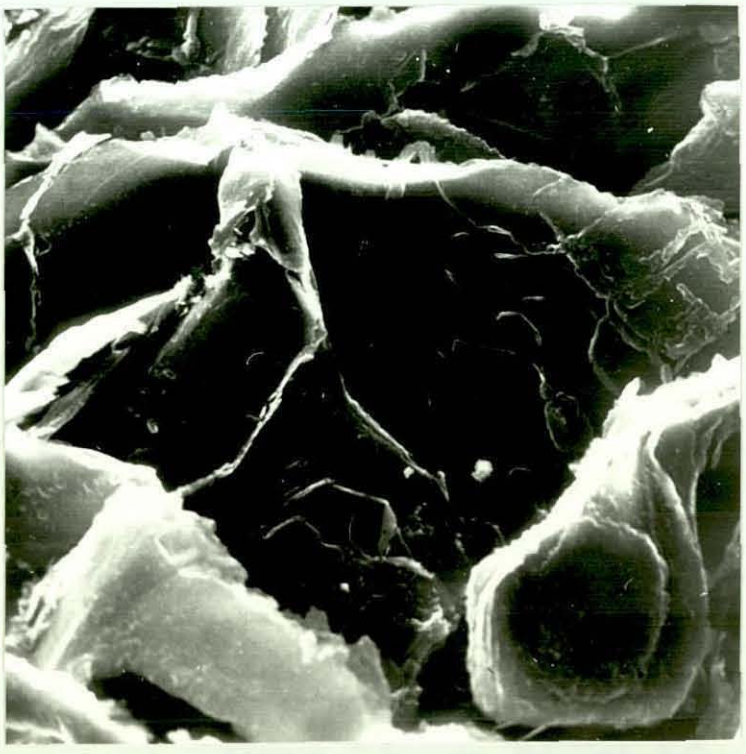

1950X

Figure 37 ASTM Type D Flake Graphite, Deep Etched (Casting 2/6) Note laths of graphite visible on the surface of graphite flakes

interconnection between the graphite flakes in a single eutectic cell is demonstrated in Figure 33. In comparison, Figures 34 and 35 show that the eutectic cell structure of ASTM type D flake graphite produced by melt treatment with 0.17% titanium was much finer.

Compared to the untreated material, Figure 36 shows that the graphite flakes in a casting produced using a cerium mischmetall-calcium melt treatment are more curved and exhibit a greater branching tendency.

At high magnification, individual laths of graphite were often visible on the surfaces of the graphite flakes in both ASTM type A and D microstructures. This effect is illustrated in Figure 37 for the titanium treated sample.

6.2.2 Spheroidal and Compacted Graphite

The spheroidal and compacted graphite morphologies produced by cerium mischmetall-calcium additions were shown to have similar appearances to those resulting from magnesium-titanium melt treatment. Compacted graphite was interconnected within eutectic cells, as illustrated in Figures 38 and 39, whereas graphite nodules were isolated from each other in the iron matrix (Figure 40). An example of a degenerate graphite spheroid which is shown in Figure 41 exhibits a number of protuberances that may represent the ends of individual crystallites in the structure.

Graphite laths similar to those observed on flake graphite were also visible on the surfaces of the compacted and spheroidal forms (Figures 42 and 43).

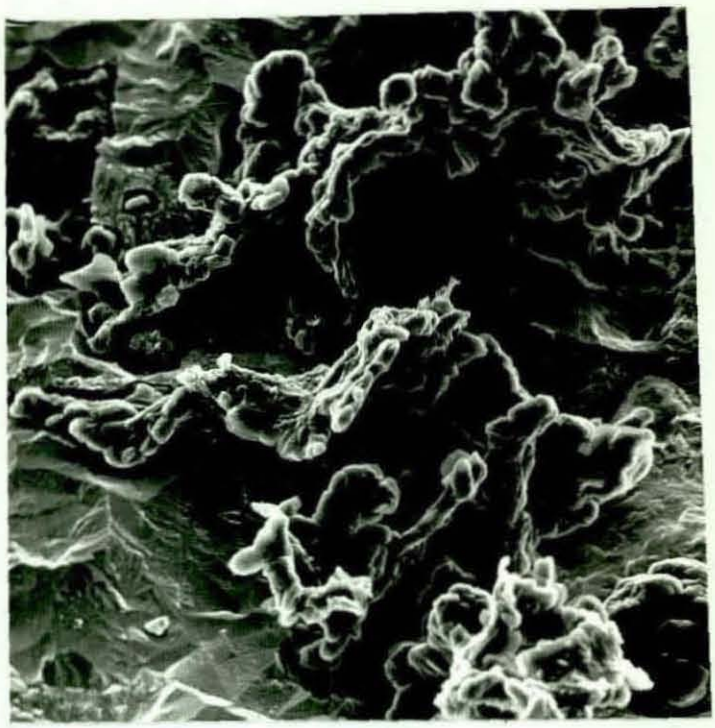

430X

Figure 38 Compacted Graphite, Deep Etched, Showing Interconnected Structure (Casting 1/2)

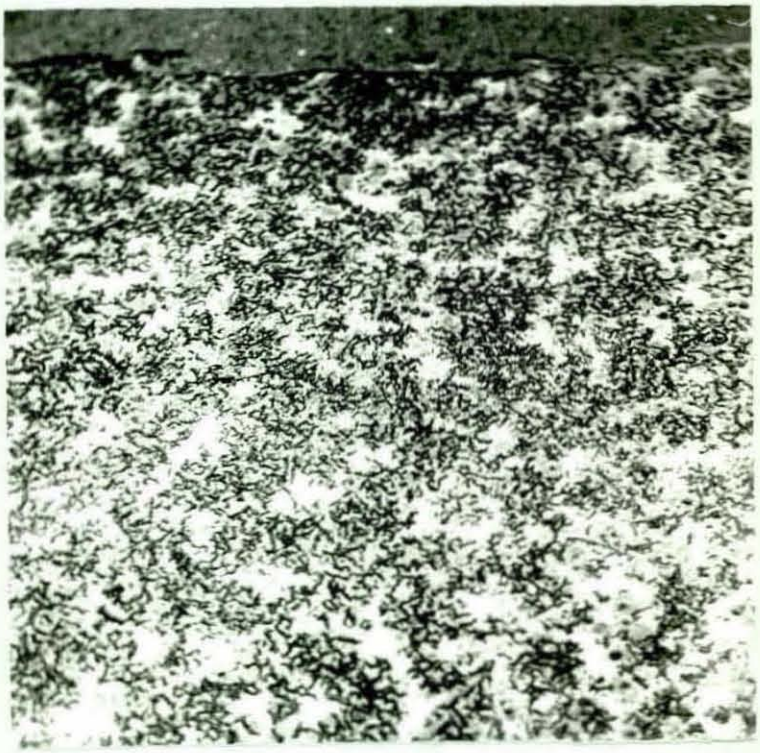

24X

Figure 39 Compacted Graphite, Deep Etched, Showing Eutectic Cell Structure (Casting 2/2)

860X

Figure 40 Nodular Graphite, Deep Etched (Casting 1/1)

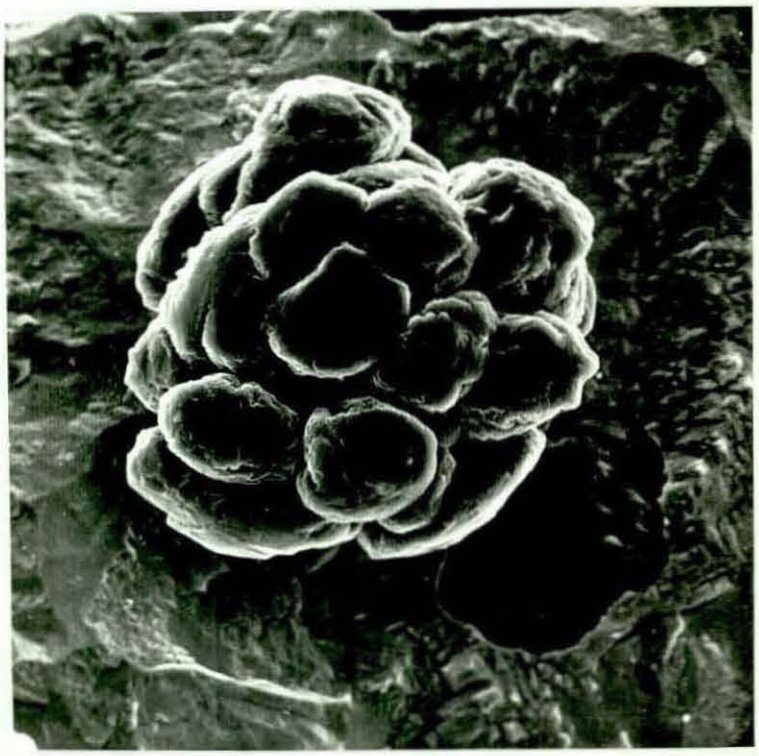

800X

Figure 41 Nodular Graphite, Deep Etched (Casting 2/3)

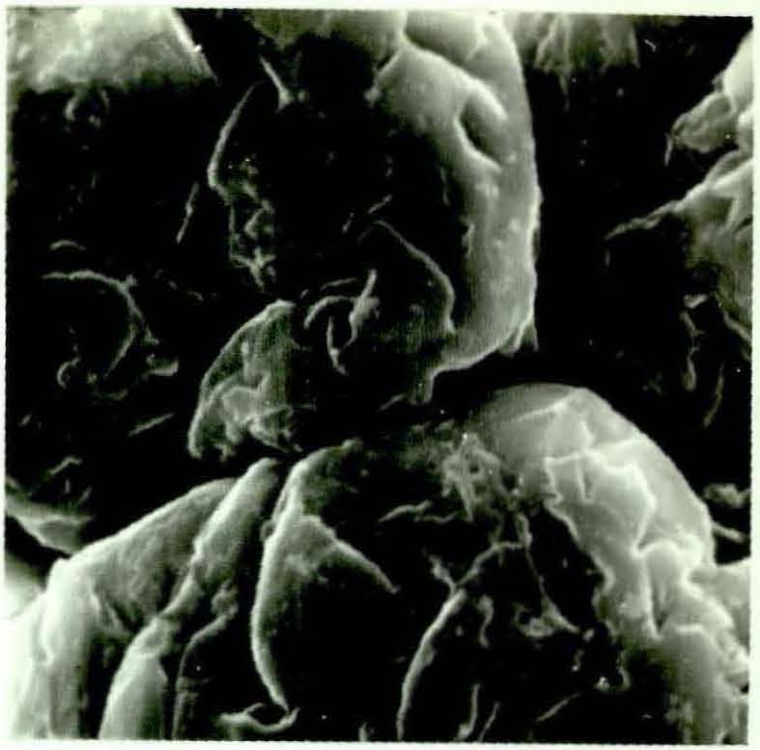

4300X

Figure 42 Nodular Graphite, Deep Etched (Casting 1/2)
Note laths of graphite visible on the surface

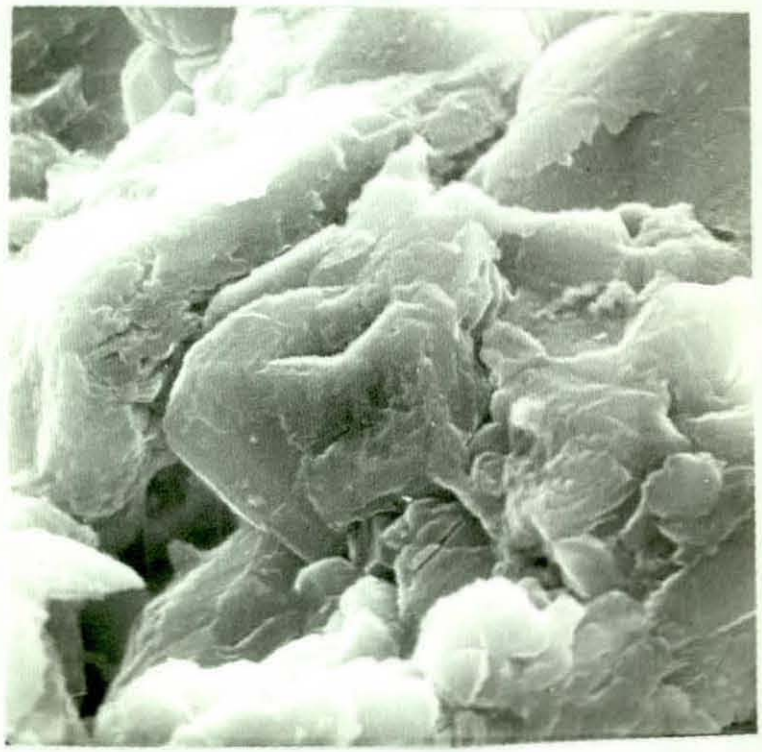

5000X

Figure 43 Compacted Graphite, Deep Etched (Casting 1/2)
Note laths of graphite visible on the surface

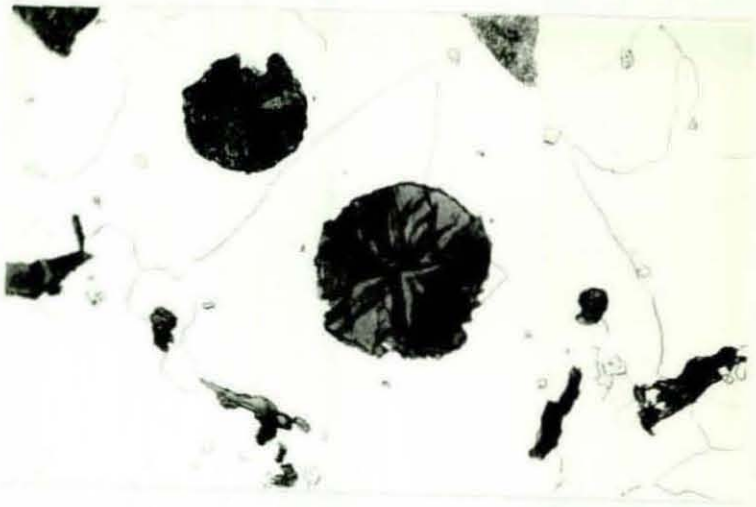

750X

Figure 44 Nodular Graphite: Birefringence Pattern (Polarised Light) (casting 2/13).

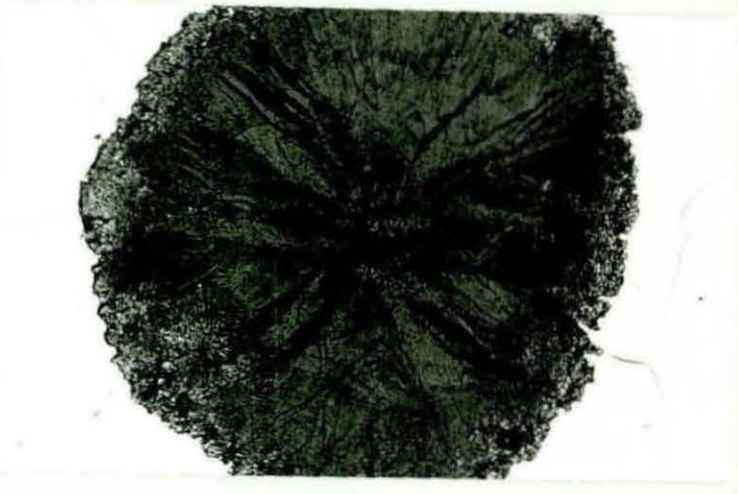

750X

Figure 45 Duplex Graphite Nodule (casting 1/27)

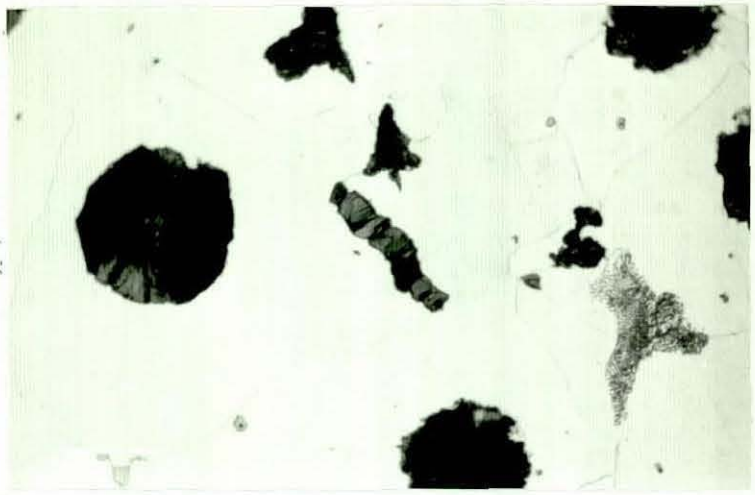

750X

Figure 46 Birefringence Pattern Revealed in Compacted Graphite (casting 1/23).

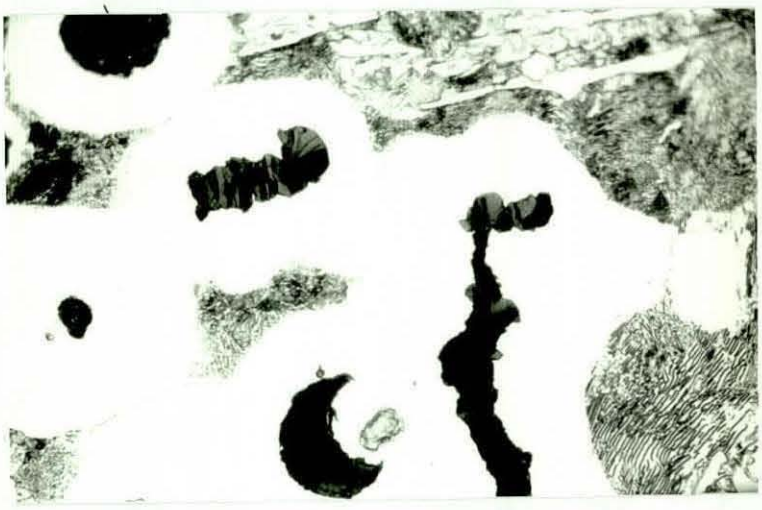

750X

Figure 47 Birefringence Patterns in Compacted Graphite (casting 2/10).

6.2.2.1 Optical Microscopy

Viewed using plane polarised light, birefringence patterns were observed in polished metallographic samples of nodular and compacted graphite. With the spheroidal form, the birefringence pattern had a preferred radial alignment and the individual crystallites revealed were frequently curved and often intersected with one another. These observations are illustrated in Figure 44. Many graphite spheroids also exhibited a duplex structure, consisting of an outer halo containing numerous inclusions and defects, and an inner core which was comparatively fault-free. This is illustrated in Figure 45 which additionally reveals that the radiating pattern is continuous through both parts of the duplex structure.

The birefringence pattern observed in compacted graphite was normally orientated perpendicular to the dominant growth direction as shown in Figure 46. At the ends of a few compacted graphite particles, the orientation of the birefringence changed to form a radiating pattern. This effect is illustrated in Figure 47.

6.2.2.2 Ion Etching

Ion etching provided further information about the internal structure of spheroidal and compacted graphite. Graphite nodules usually exhibited a pattern of concentric rings emanating from the nodule centre and two examples of this effect are shown in Figures 48 and 49. In a few nodules however, the etching traces formed chevron patterns which are best described by referring to the SEM micrographs shown in Figures 50, 51 and 52. Figures 52 and 53 additionally show that from the centre of the nodule to its periphery, there was a gradual change in the orientation of these etching traces so that the apex angle of the chevrons they produced increased and approached 180° at the edge of the spheroid.

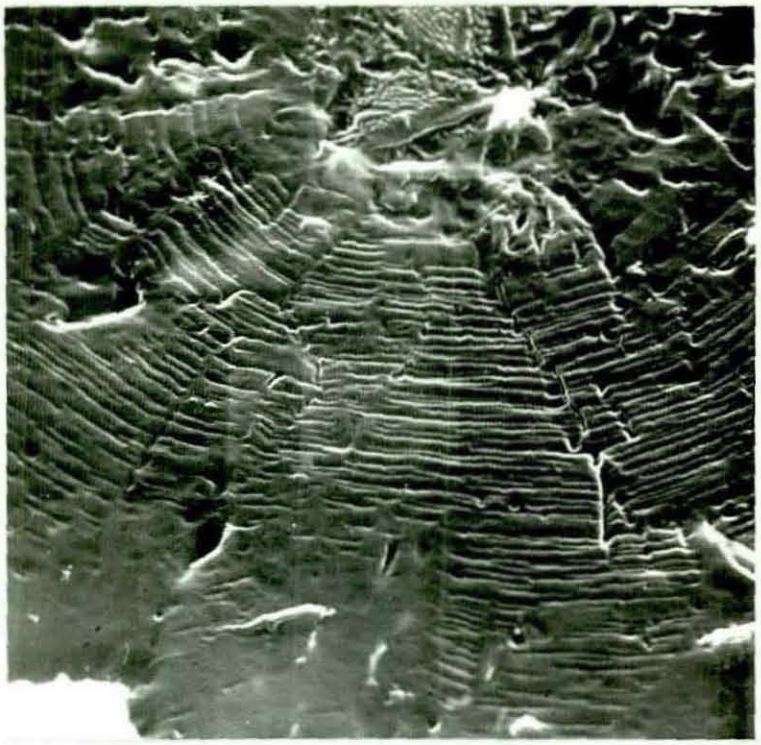

5000X

Figure 48 Nodular Graphite: Concentric Ring Pattern Produced by Ion Etching (SEM image) (casting 1/14).

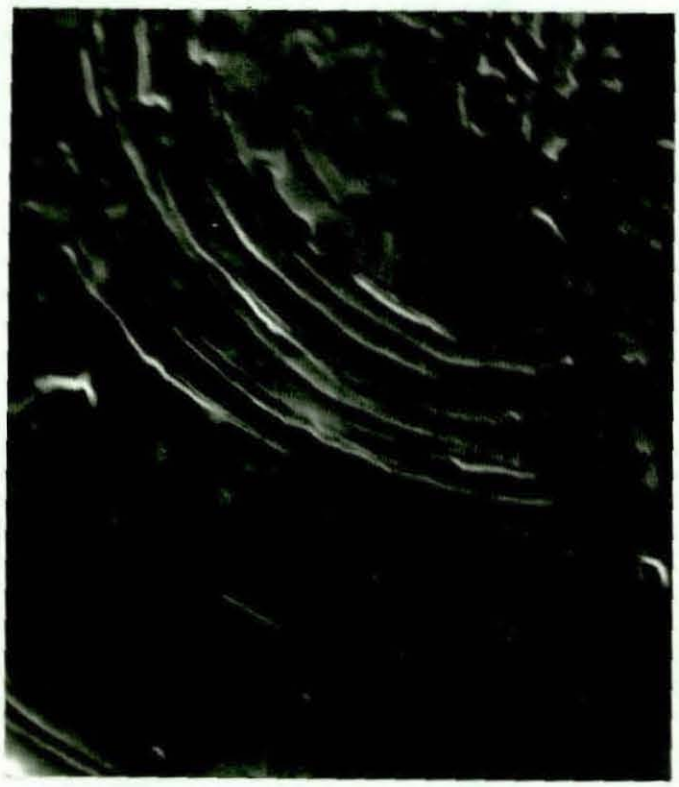

10,000X

Figure 49 Nodular Graphite: Concentric Ring Pattern Produced by Ion Etching (SEM image) (casting 1/14).

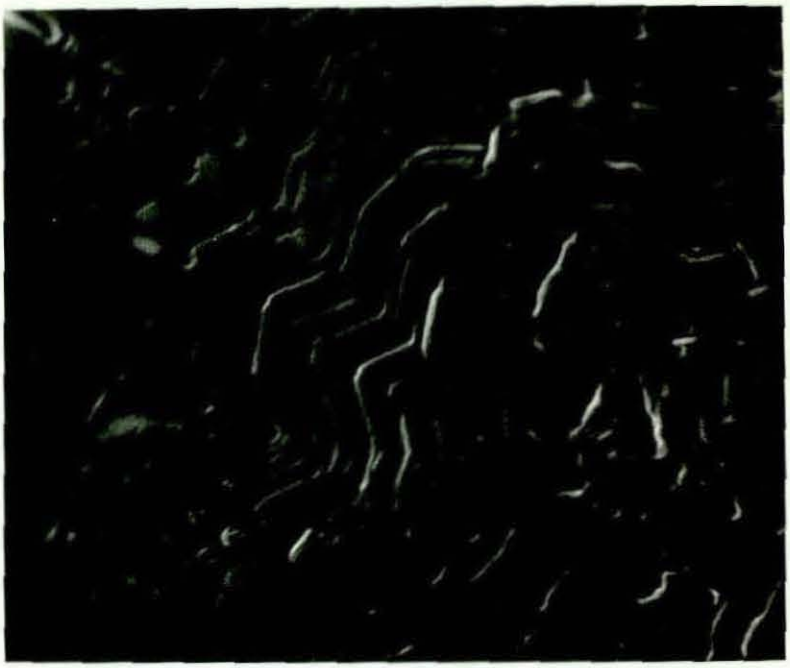

6000X

Figure 50 Nodular Graphite: Chevron Pattern Revealed by Ion Etching (SEM image) (casting 1/14)

6000X

Figure 51 Nodular Graphite: Chevron Pattern Revealed by Ion Etching (SEM image) (casting 1/14).

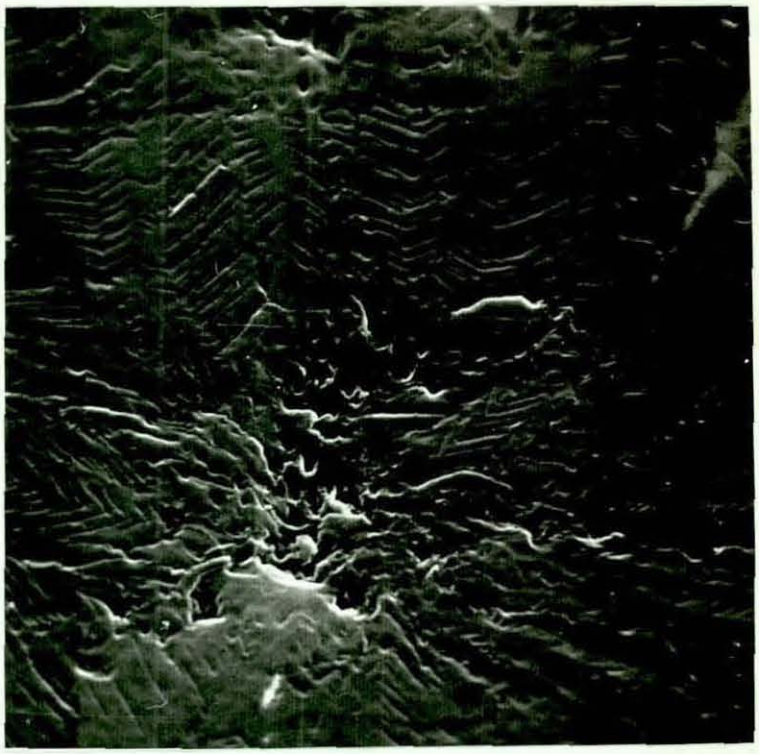

5000X

Figure 52 Nodular Graphite: Chevron Pattern Revealed by Ion Etching (SEM image) (casting 1/14)

8000X

Figure 53 Nodular Graphite: Change in the Orientation of the Chevron Pattern at the Nodule Periphery (casting 1/14).

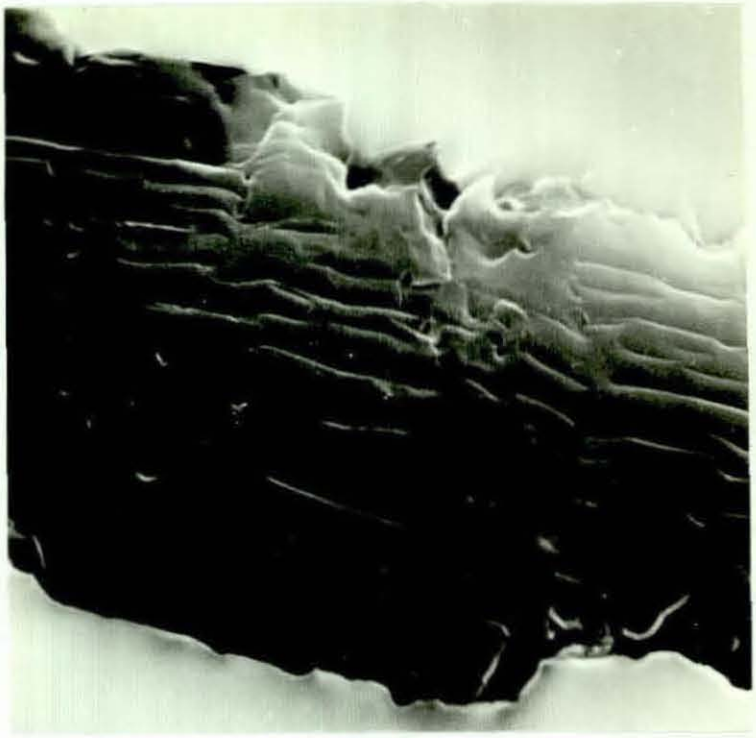

8000X

Figure 54 Compacted Graphite: Pattern Revealed by Ion Etching (SEM image) (casting 1/14).

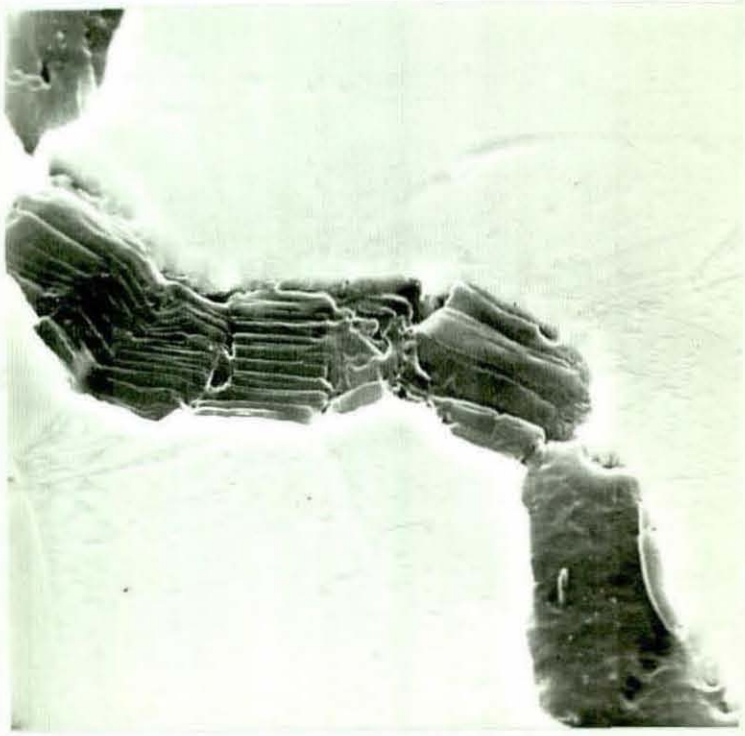

5000X

Figure 55 Ion Etched Compacted Graphite (SEM image) (casting 1/14).

5000X

Figure 56 Compacted Graphite: Change in Orientation of the Basal Plane Traces at the Growth End of Compacted Graphite (casting 1/14).

5000X

Figure 57 Compacted Graphite: Change in Orientation of the Basal Plane Traces at the Growth End of Compacted Graphite (casting 1/14).

750X

(a) Casting 1/10.

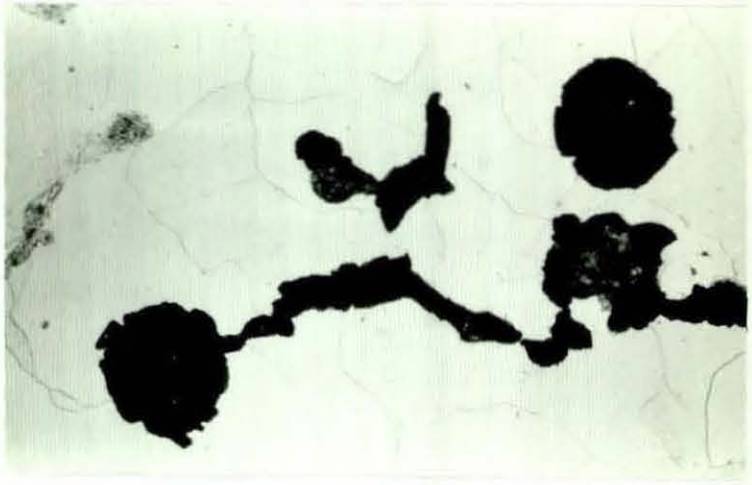

750X

(b) Casting 4/1.

Figure 58 Hybrid Nodular/Compacted Graphite Particles (Optical Micrographs)

800X

Figure 58(c) SEM Image of a Hybrid Nodular/Compacted Graphite Particle (casting 2/3).

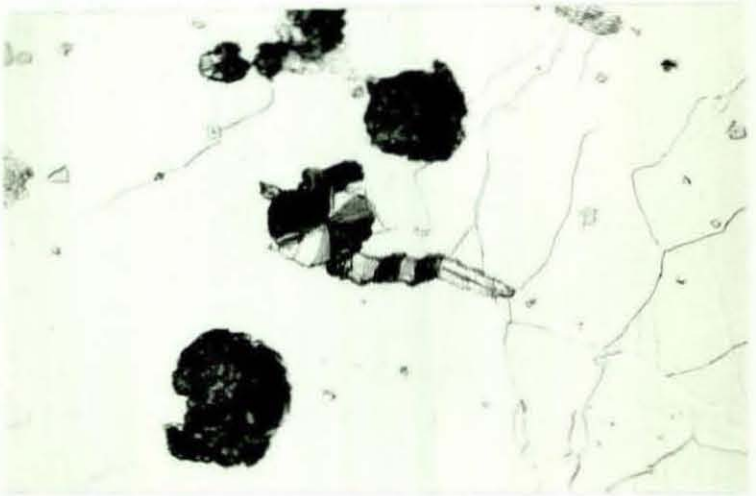

750X

Figure 58(d) Hybrid Nodular/Compacted Graphite Particle (Polarised Light) (casting 2/13).

The pattern revealed on etched compacted graphite surfaces normally consisted of traces running parallel to the dominant growth direction as illustrated in Figure 54. Major changes in the growth direction of the compacted graphite were accompanied by corresponding changes in the orientation of the traces, and this effect is demonstrated in Figure 55. At the apparent growth terminal of the compacted graphite, the orientation of the pattern changed so that the traces became perpendicular to the overall growth direction. Figures 56 and 57 show two examples of the latter phenomenon for different compacted graphite particles.

6.2.3 Hybrid Compacted/Spheroidal Graphite Particles

In addition to the compacted and nodular graphite morhpologies, compacted graphite cast irons also contained a few graphite particles that appeared to have both spheroidal and compacted characteristics. Two examples of the latter structure are shown in Figures 58a and 58b. Figure 58c additionally illustrates the appearance of a similar particle after deep etching its surrounding iron matrix.

Viewed under polarised light, the spheroidal and compacted sections of the hybrid structure exhibited respective birefringence patterns that were similar to the corresponding patterns noted previously with separate nodular and compacted graphite particles. This is illustrated in Figure 58d.

6.3 Elemental Distributions

Secondary ion mass spectrometry (SIMS) and X-ray microanalysis were employed to study the distributions of elements in the graphite, at the graphite/iron interface, and in the iron matrix of samples from a variety of different cast irons produced during the research

programme. The melt treatment additions used to produce each of these cast irons are given in Appendix IV together with the morphology of the graphite present in each sample.

6.3.1 Flake Graphite Cast Iron

A Cs^+ ion SIMS stepscan across several graphite flakes in iron A is shown in figure 59, which clearly shows enhanced oxygen and sulphur signals in the graphite phase. The additional sulphur peak appearing to the right of the figure corresponds to a manganese sulphide inclusion. A 2μm stepsize and a 150μm diameter image was used for this stepscan, giving a lateral resolution of approximately 10μm. Since the thickness of the graphite flakes was normally only 5-10μm, local variations in the signals for elements within the flakes are not well resolved, however, there is some evidence of more localised enrichments of sulphur and oxygen at the flake/iron interfaces.

In order to verify the previous observation, a further stepscan was carried out across a different graphite flake in the same sample. Using a 1μm stepsize and a 25μm diameter image, a lateral resolution of approximately 2μm was produced. These results are represented in Figure 60 and reveal significant oxygen and sulphur peaks in the interfacial region. Owing to the 2μm lateral resolution limit, the peaks in the sulphur and oxygen signals represent more localised enrichments of these elements at the graphite/iron interface than their appearance suggests. This stepscan also indicates that the oxygen signal remains relatively high throughout the graphite and does not decrease in the central portion to the same extent as sulphur. The enhanced oxygen level in the bulk of the flake graphite was later confirmed by carrying out a

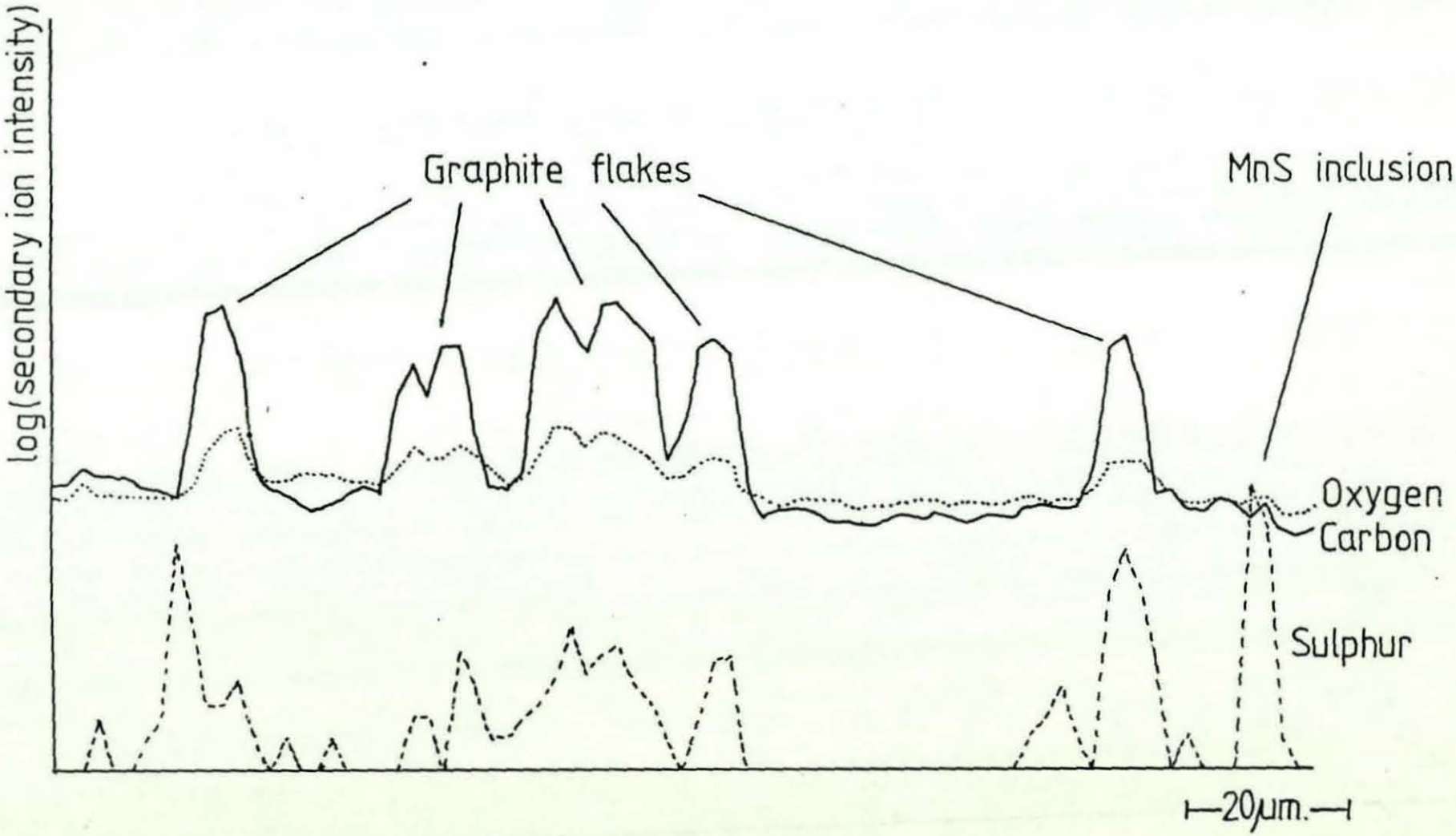

Figure 59 SIMS stepscan (Cs+ ions) across graphite flakes in iron A.

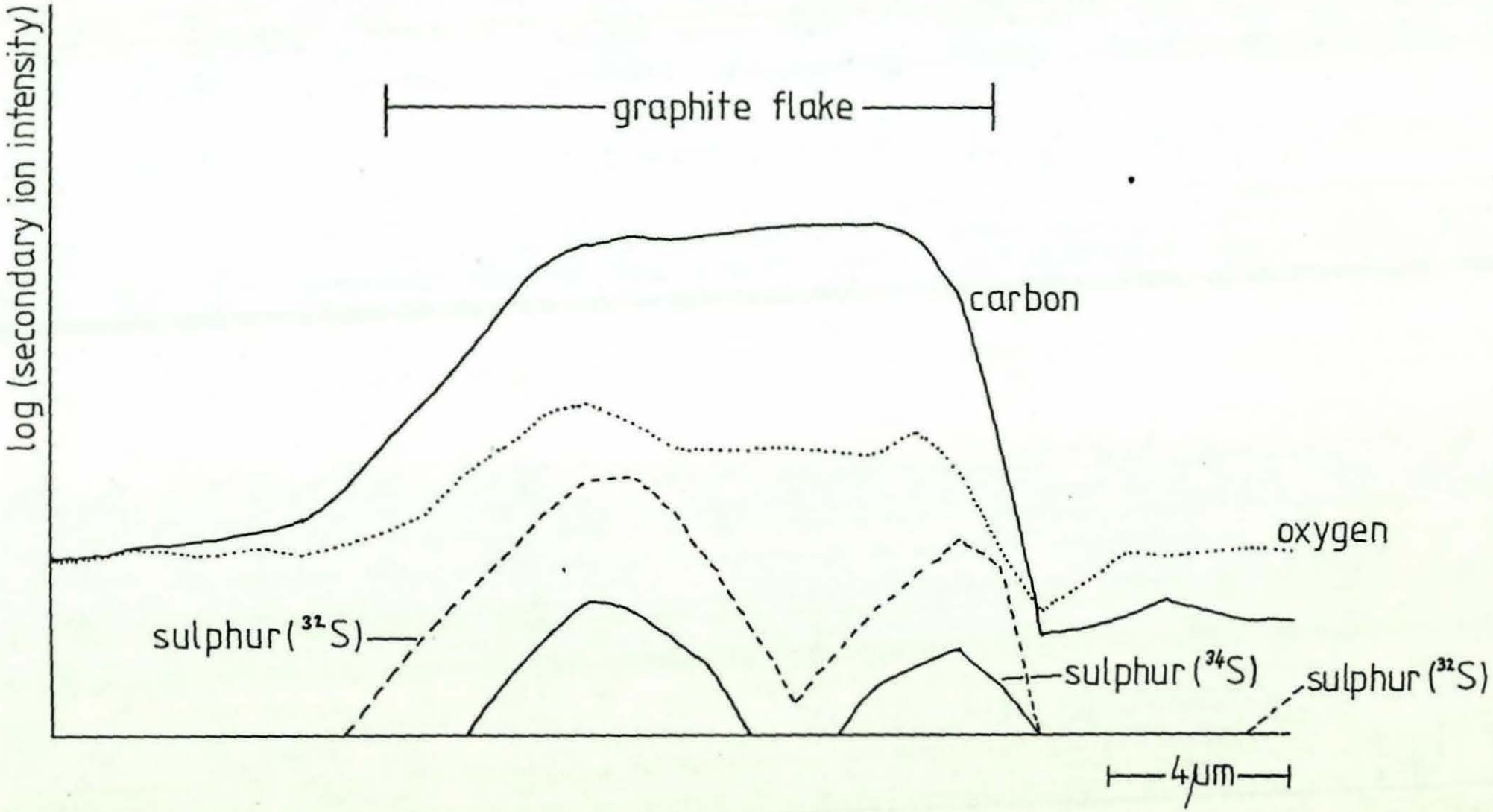

Figure 60. High-resolution SIMS stepscan (Cs+ ions) across a single graphite flake in iron A.

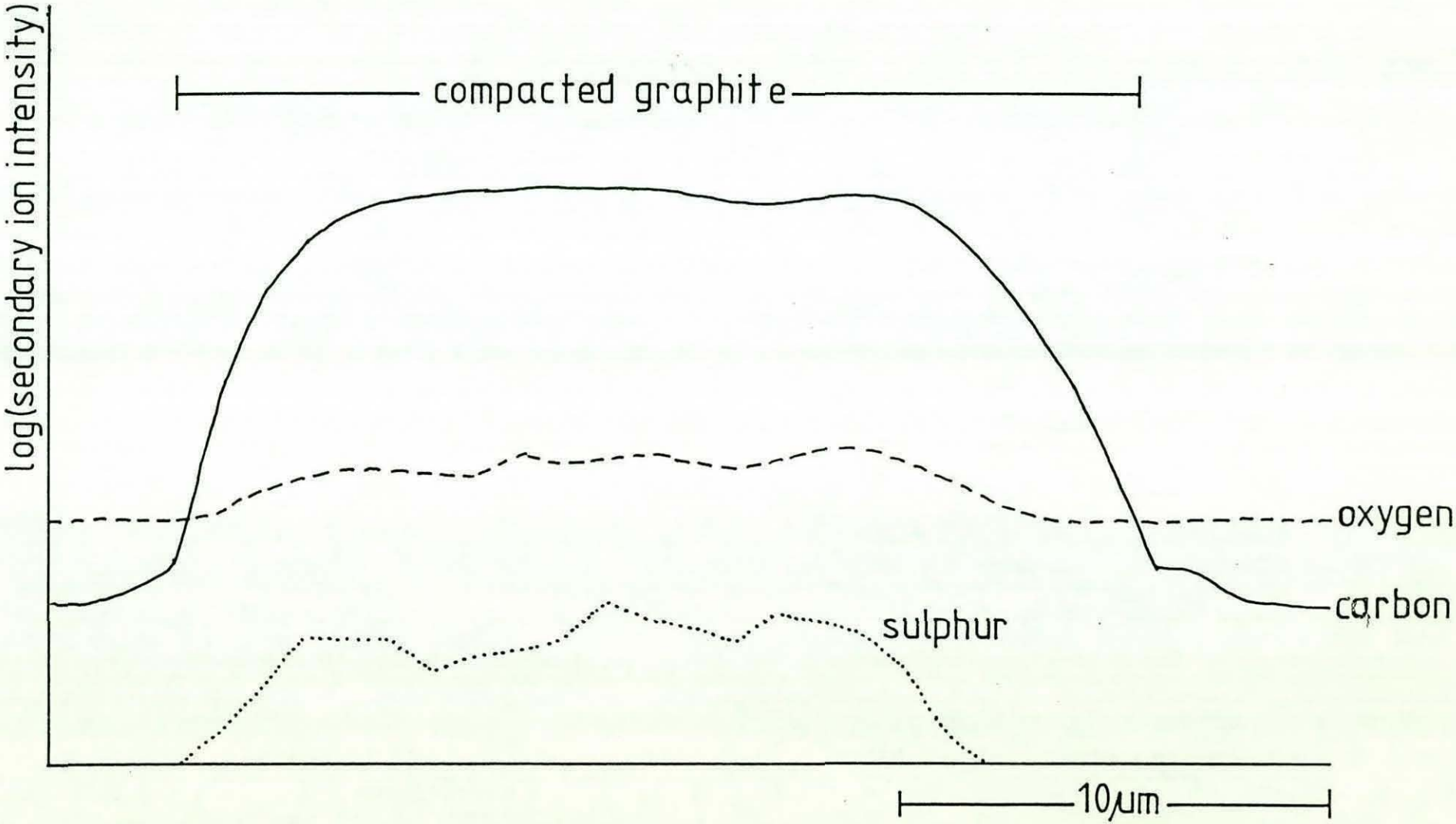

Figure 60a High resolution SIMS stepscan (Cs^+ ions) across compacted graphite in iron F.

stepscan across a compacted graphite particle (Figure 60a), taking care to maintain consistent experimental conditions in both of these analyses. Since the magnitude of the oxygen signal in the graphite phase in Figure 60a is significantly less than that in the central part of the graphite flake in Figure 60, this proves that the latter enhanced oxygen signal could not be due simply to an effect of the matrix on the secondary ion yield, but must indicate a real oxygen enrichment.

The oxygen signals in Figures 59 and 60 appear high in general due to the influence of a large background level from retained oxygen in the vacuum system. Since the latter is constant, it does not affect the variations in the oxygen signal seen between different parts of the specimen. It must also be noted that a small proportion of the observed sulphur signal may be due to the oxygen molecule O_2, which has the same molecular weight as atomic sulphur (ie 32). The sulphur distribution in Figure 60 was confirmed by recording the signal for the minor isotope ^{34}S, which, in spatial terms, coincided exactly with the mass = 32 scan. In addition, because an electronic filtering system was applied to all the recorded signals to discriminate against molecular secondary ions, it was expected that the oxygen molecule contribution would be extremely small. In view of this, the ^{32}S and ^{16}O signals were considered sufficiently accurate for all subsequent comparisons between oxygen and sulphur traces.

Figure 61 shows SIMS ion images for carbon, oxygen and sulphur in iron A and further illustrates the enrichments of oxygen and sulphur at the flake/iron interfaces. A number of discrete sulphur spots are also visible and these were shown to correspond to manganese sulphide inclusions. In order to ensure that the oxygen and sulphur

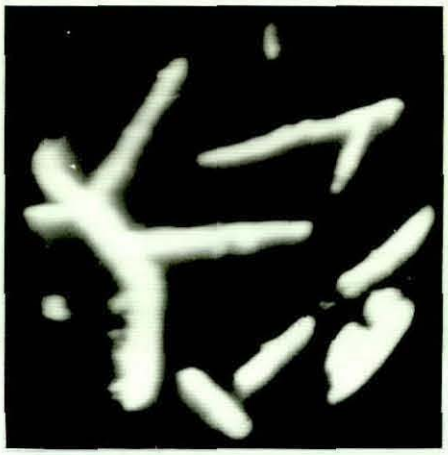

(a) Carbon Image

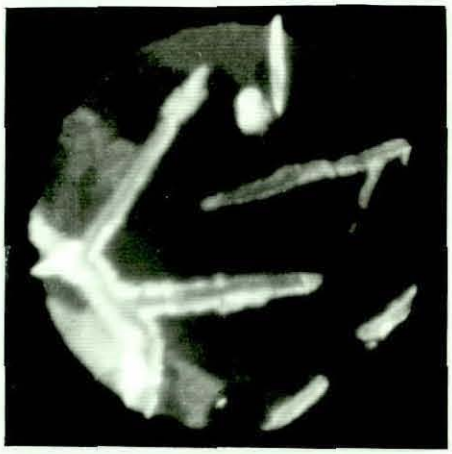

(b) Oxygen Image

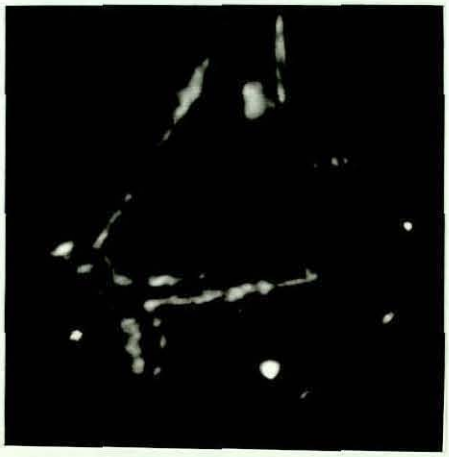

(c) Sulphur Image

Figure 61 SIMS Ion Images for Iron A

signals recorded were not caused by contamination during preparation of the specimen, the sample surface was etched in situ for several minutes using the ion beam. The continued removal of successive surface layers caused no detectable reduction in the intensities of the oxygen and sulphur signals.

To further study the distributions of oxygen and sulphur in flake graphite, a composition-depth profile was carried out on a flake that appeared optically to be positioned at right-angles to the primary ion beam. The carbon ion image for this flake is shown in Figure 62 and the results of the depth profile are represented in Figure 63. A periodicity in the sulphur level was recorded at intervals of approximately 2μm as the sputtered depth increased. No comparable variation in the oxygen signal was observed. At a depth of approximately 8.5μm, the depth profile displayed simultaneous peaks in the sulphur and oxygen signals, together with a rise in the iron level. It is likely that these features occurred at or close to the flake graphite/iron interface because measurements using optical microscopy showed that the average thickness of the graphite flakes in this specimen was approximately 10μm.

Figure 64 indicates that calcium is also present throughout the flake graphite although for the reasons explained earlier, the concentration of this element could not be determined. Some initial doubt was cast on this observation since the compound silicon carbide, analogous to the calcium atom, also has a mass number 40. However, examination of mass spectra, such as that shown in Figure 65 for a compacted graphite particle, eliminates this possibility since smaller peaks would be expected at mass numbers 41 and 42 due

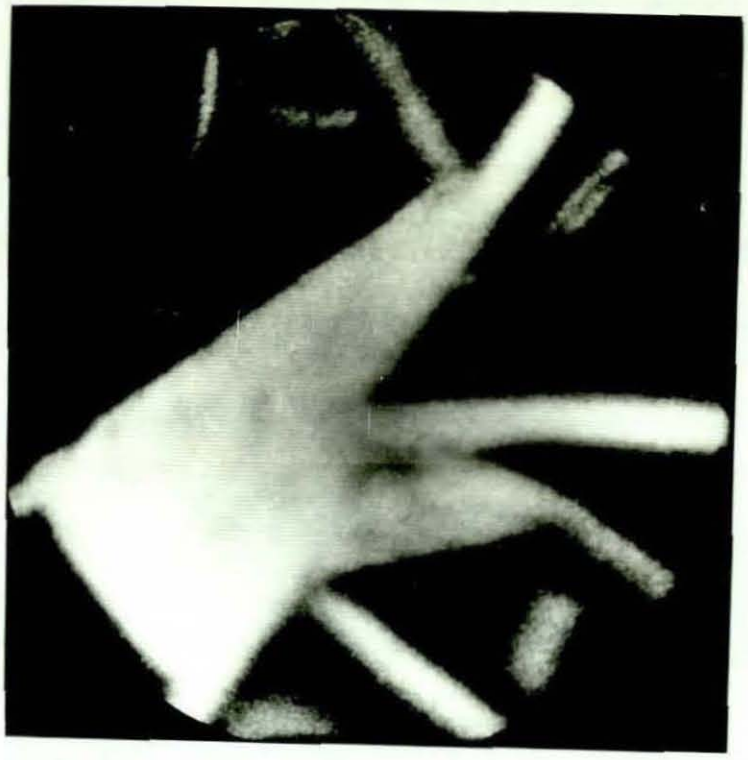

Figure 62 SIMS Carbon Image for a Graphite Flake in Iron A

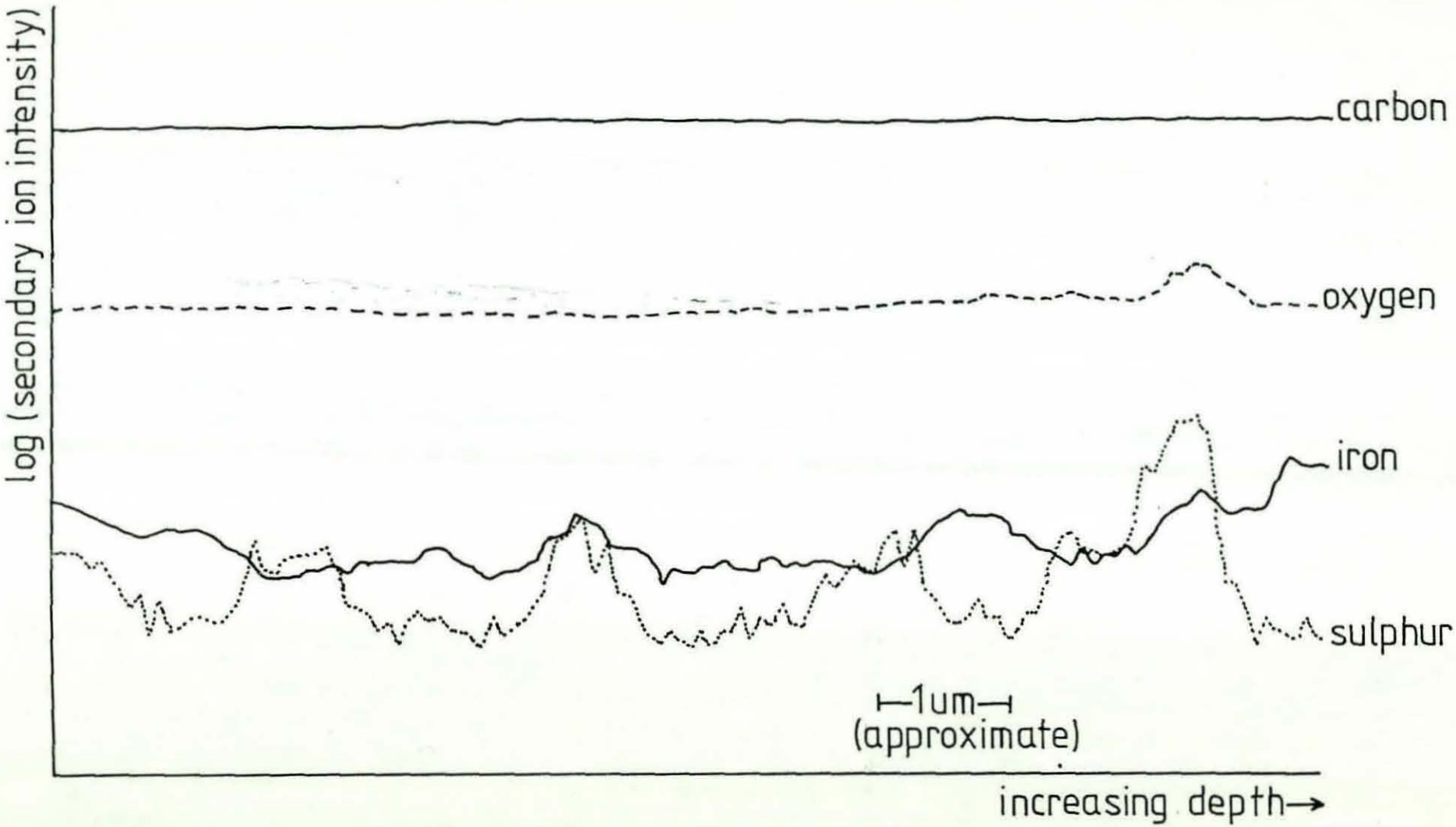

Figure 63. SIMS composition-depth profile (Cs^+ ions) into a graphite flake in iron A.

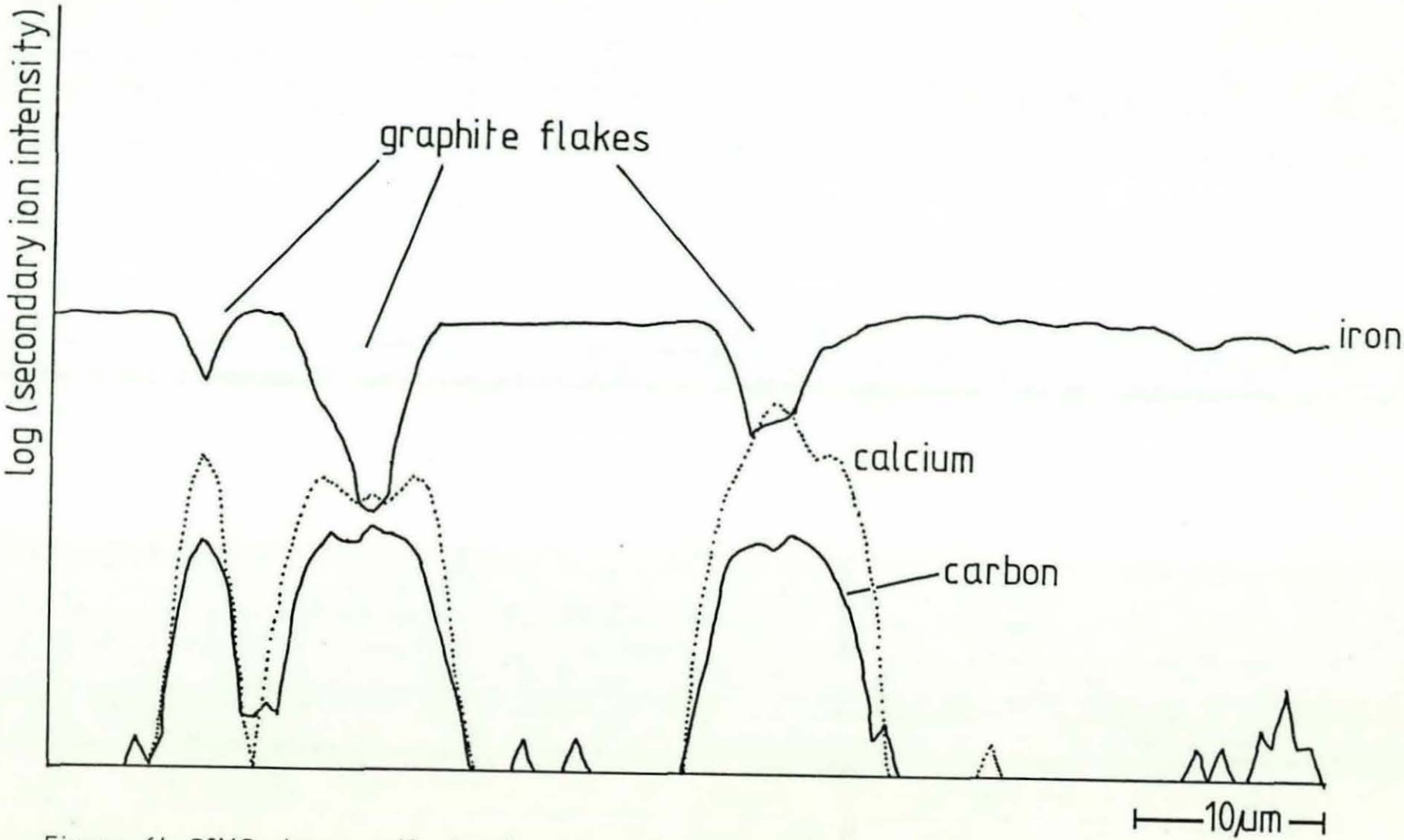

Figure 64. SIMS stepscan (O_2^+ ions) across graphite flakes in iron A.

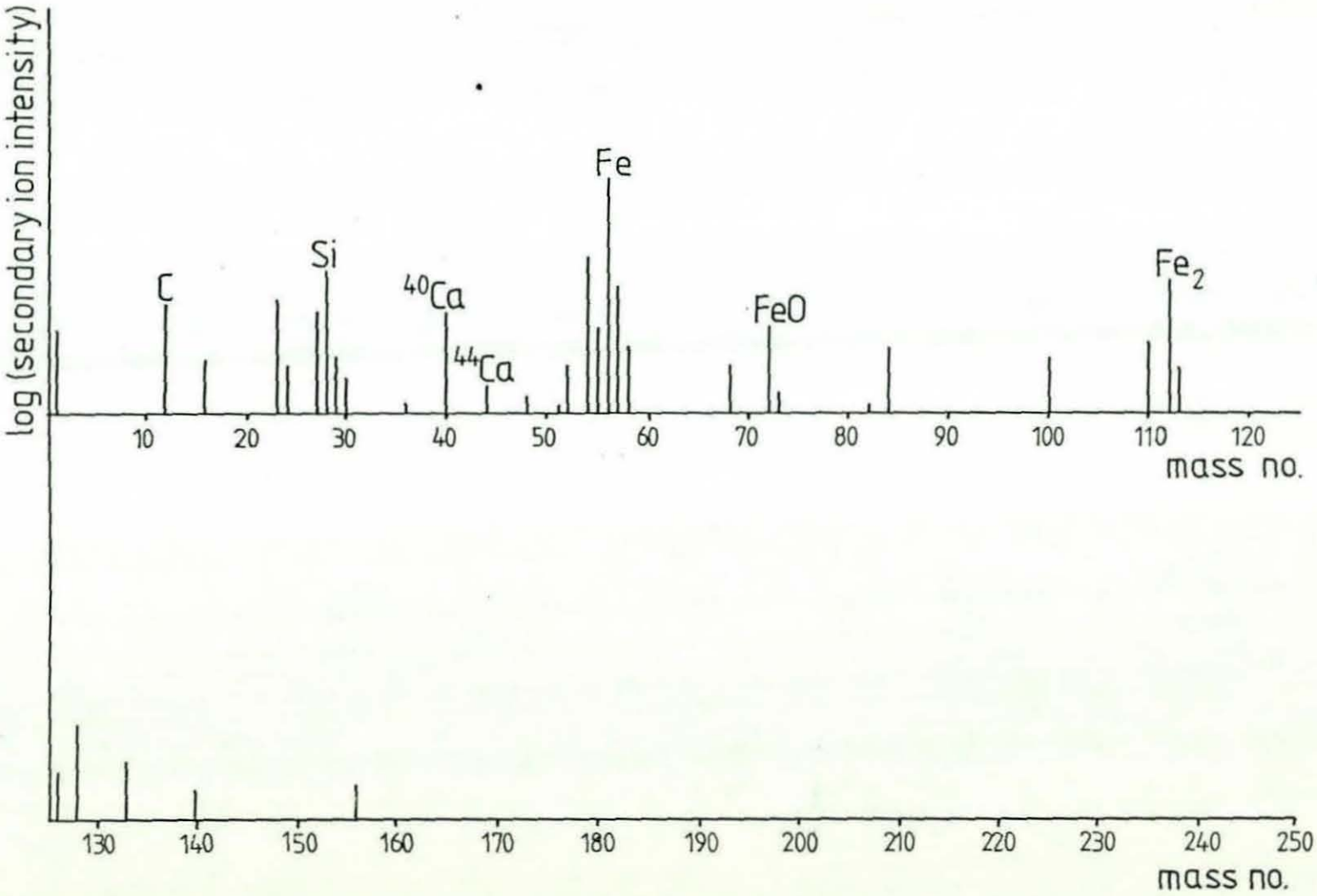

Figure 65. SIMS mass spectrum (25μm diam. area) from a C.G. particle in iron F.

to the other natural isotopes of silicon, ^{29}Si and ^{30}Si. The presence of calcium is confirmed by the smaller peak at mass number 44, corresponding to the naturally occurring isotope, ^{44}Ca.

It was also necessary to establish that the enhanced calcium signal recorded in the graphite relative to the iron matrix actually signified a calcium enrichment, and was not due to the difference in elemental sensitivity for calcium in the graphite and iron matrices. The latter judgement would be suspected if the calcium signal happened to be uniform throughout each graphite flake with no apparent difference between the levels recorded in different flakes. This was not in fact the case and the variations in the calcium signal shown in Figure 64 indicate that calcium enrichment had taken place in the graphite phase.

To further ensure that the calcium concentrated in the graphite was not due to surface contamination, the specimen surface was sputtered to a depth of 2μm. This caused no significant variation in the calcium levels recorded, confirming the calcium distribution within the graphite phase. Other elements, including cerium, were not detected in flake graphite.

6.3.2 Compacted/Spheroidal Graphite Cast Irons

6.3.2.1 Spheroidal Graphite

6.3.2.1.1 Rare Earth Elements

Figure 66 shows an O_2^+ ion SIMS stepscan across a duplex graphite nodule in iron B, which was produced using an addition of 0.1% cerium mischmetall. This indicates that the inner region of the nodule is enriched in cerium and lanthanum, with significantly lower

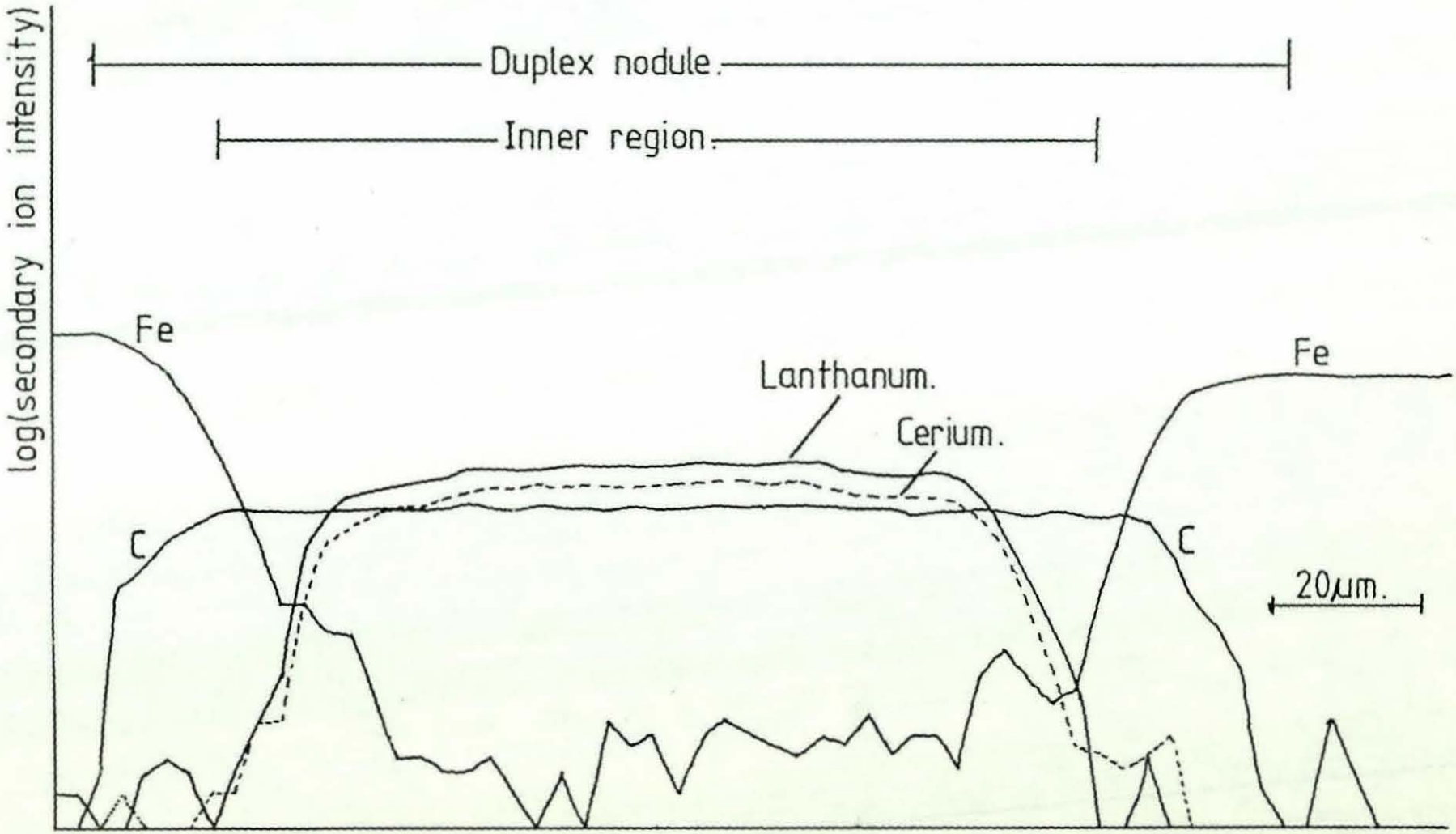

Figure 66. SIMS stepscan across a duplex-structured graphite nodule in iron B. (O_2^+ ions.)

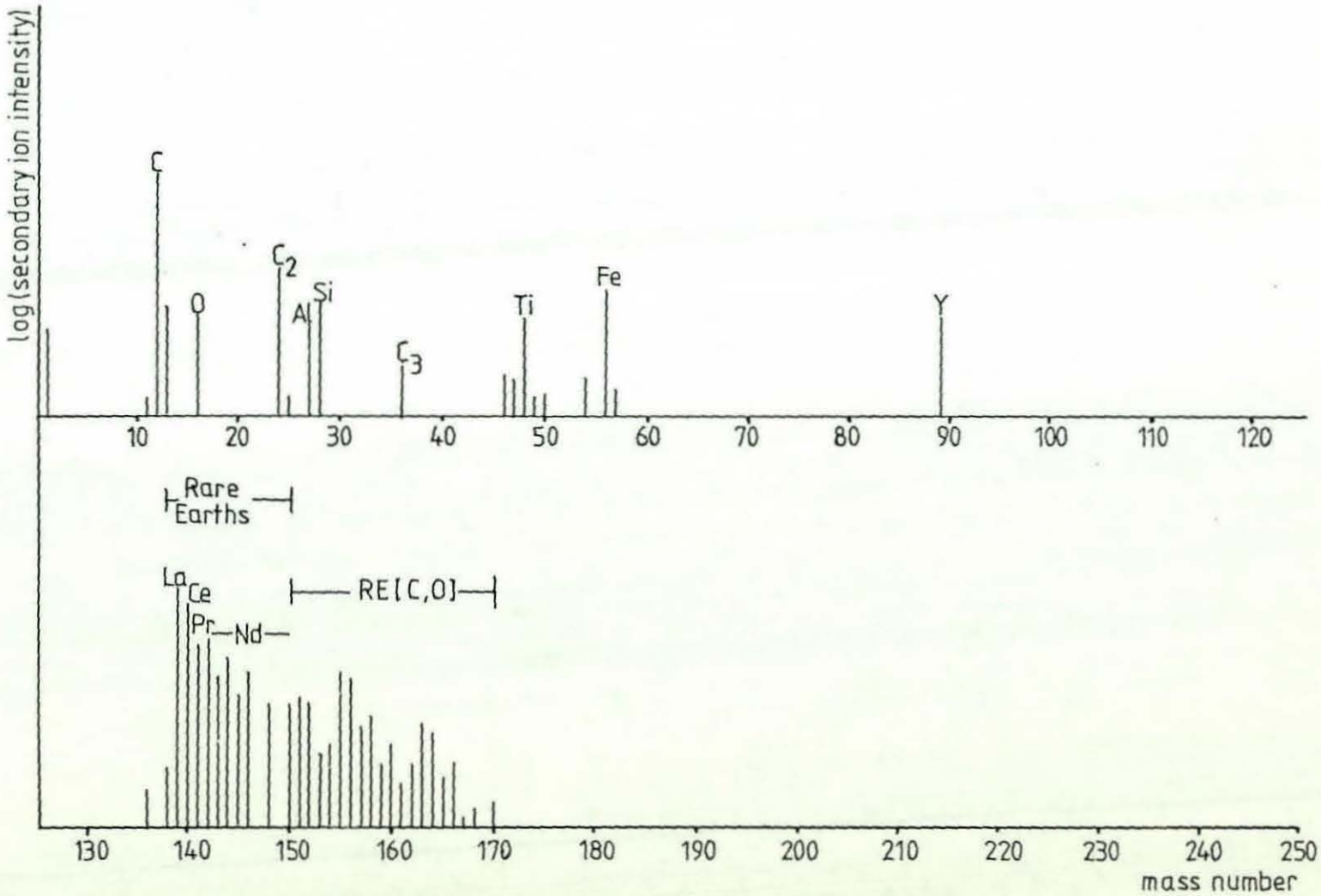

Figure 67. SIMS mass spectrum from the inner part of the duplex nodule represented in figure 66.

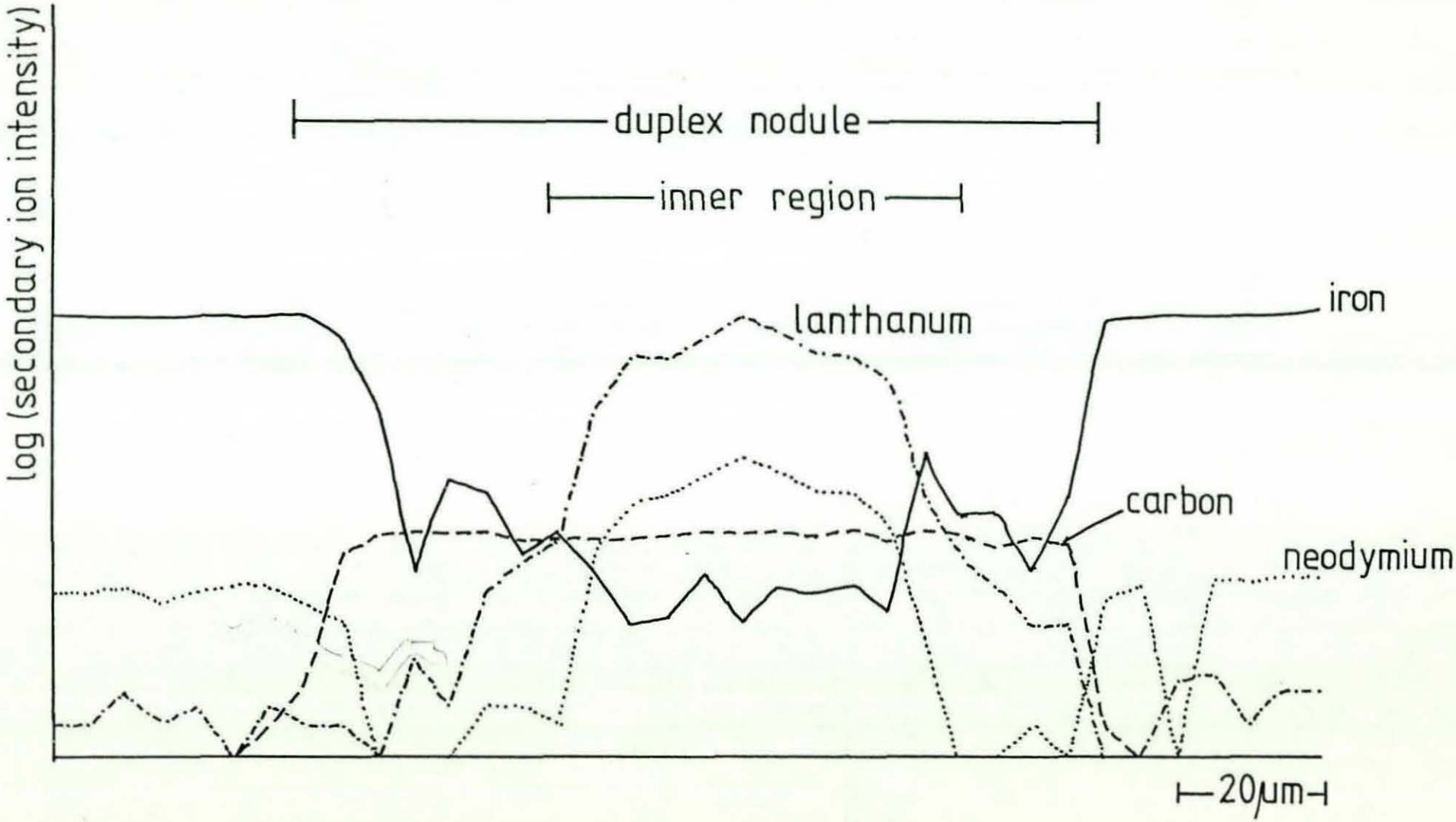

Figure 68. SIMS stepscan (O_2^+ ions) across a duplex graphite nodule in iron C.

concentrations of these elements in the surrounding halo. These results were confirmed by mass spectra. For example, Figure 67 indicates that in addition to yttrium, the rare earth elements cerium, lanthanum, praseodymium, and neodymium were all present in the central part of the graphite nodule structure. The latter mass spectrum is complicated by overlapping groups of peaks corresponding to elemental rare earths and associated rare earth compounds of the type (RE)C, (RE)O, and $(RE)C_2$. These results suggest that at least some of the rare earths in the inner nodule region were present in the form of carbides, but the oxide peaks may well have been caused by interaction between the elemental rare earths and the oxygen ions used for bombarding the specimen.

Similar results were obtained with duplex nodules in iron C, produced using a 0.16% lanthanum mischmetall treatment, and the SIMS stepscan shown in Figure 68 reveals lanthanum and neodymium enrichments in the inner region of the graphite nodule. Scanning electron microscopy examination of graphite nodules did not reveal the presence of any discrete inclusions that could have contributed to the strengths of these rare earth signals. In addition, Cs^+ ion SIMS stepscans carried out across graphite nodules in irons B and C revealed only very low sulphur and oxygen signals in the graphite phase, and these exhibited no detectable general correlation with the rare earth traces mentioned above. This is not an unexpected result in view of the very low bulk sulphur contents of these irons (iron B contained 0.006% sulphur and iron C contained 0.0019% sulphur). In one case, however, a 2 μm diameter particle was located in the centre of a graphite nodule in iron B using scanning electron microscopy (Figure 69). Energy-dispersive X-ray microanalysis carried out at this point revealed the presence of

1400X

Figure 69 Graphite Nodule in Iron B Showing Centrally Located Inclusion (SEM image)

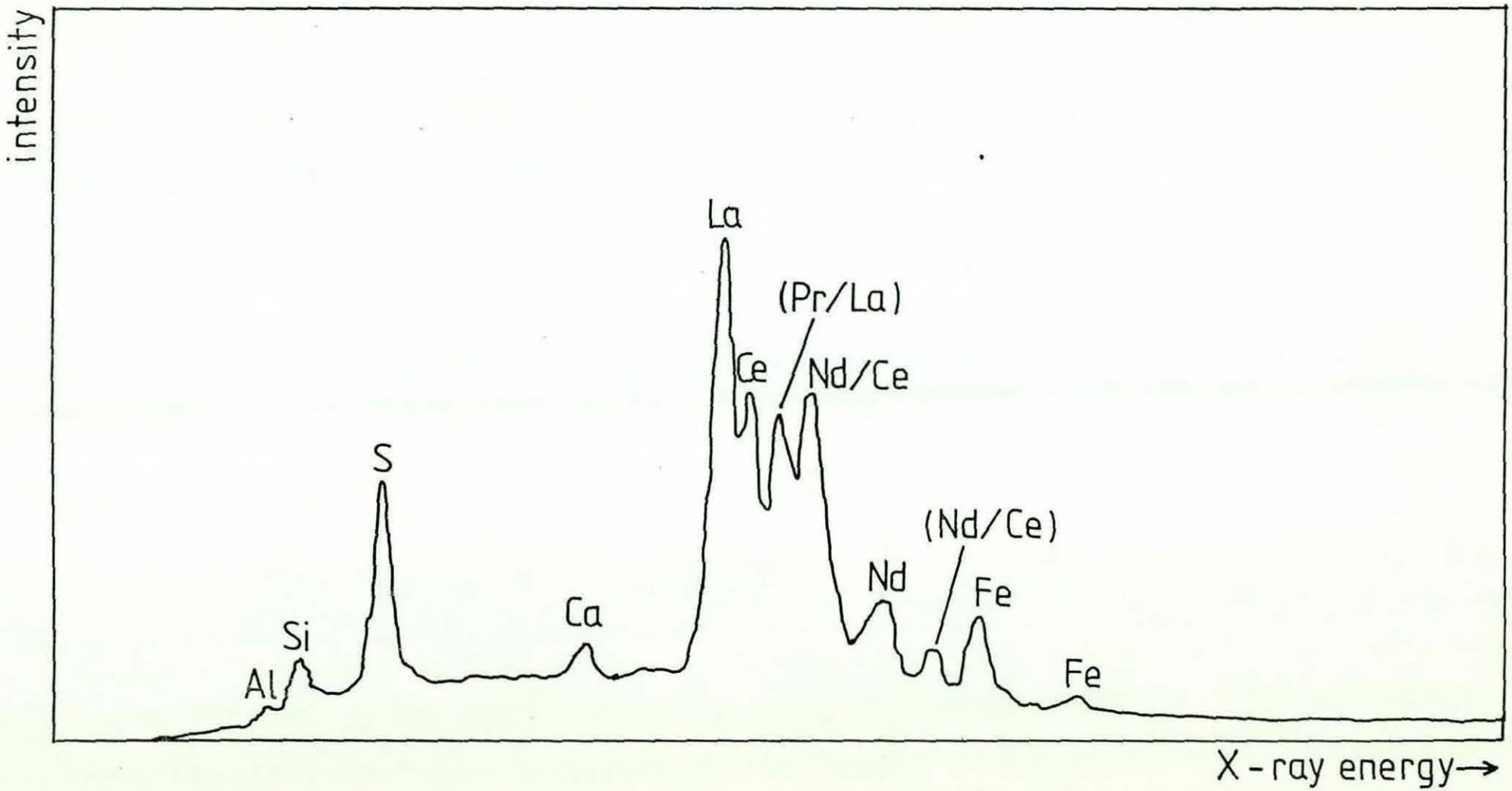

Figure 70. Energy-dispersive X-ray microanalysis of a particle located in the centre of a nodule in iron B.

lanthanum, cerium, praseodymium, neodymium, calcium, aluminium, silicon, iron and sulphur. The latter results are shown in Figure 70. The chemical nature of the particle is clearly very complex, and in view of its location in the nodule, it is likely that it represents the original nucleus of the graphite spheroid.

Significantly enhanced rare earth signals were not generally observed in the graphite phase in irons E and F. These irons were produced using a cerium mischmetall-calcium melt treatment process in which the mischmetall additions were much less than those used for the production of irons B and C. Where cerium was detected in duplex nodules in irons E and F, the signal for this element was usually lower in the outer region of the spheroid structure compared to the inner area (eg Figure 75). It is interesting to note that a similar effect was also observed with graphite nodules in iron D (Figures 78 and 79), which was treated with a magnesium ferro-silicon additive containing only 0.5% cerium. In only one case was the recorded cerium signal in a graphite spheroid in a cerium mischmetall-calcium treated iron found to be significantly greater than that in the surrounding iron matrix. This example is shown in Figure 71, which indicates that the increased cerium signal in the greater part of the nodule was accompanied by a higher iron signal and a lower calcium signal compared to the respective levels of these elements detected in similar examples. In contrast, another region of the nodule, which exhibited an enhanced calcium signal, was denuded in cerium, iron and silicon.

6.3.2.1.2 Calcium

SIMS analysis of irons E and F indicated that most of the nodular and compacted graphite in these samples were enriched in calcium

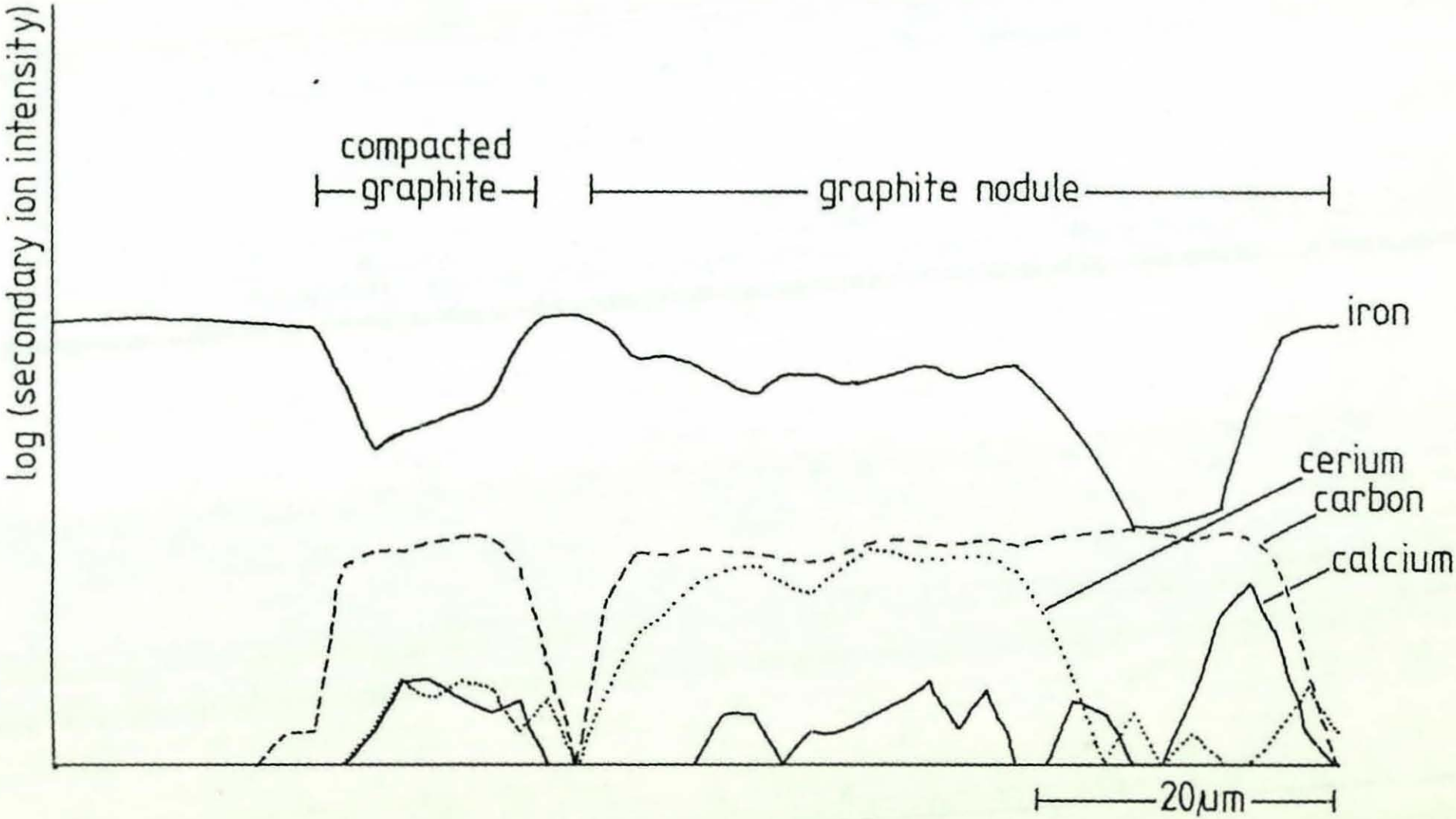

Figure 71. SIMS stepscan (O_2^+ ions) across nodular and compacted graphite in iron E.

(Figures 72 to 75). In addition, a comparison between Figures 72a and 72b reveals some correlation between the calcium, cerium, oxygen and sulphur signals recorded in the graphite. The latter observations suggest that at least some of the calcium and cerium present in the graphite phase in the cerium mischmetall-calcium treated irons may be in the form of compounds containing sulphur and oxygen. Figure 73a also reveals a joint cerium and calcium peak in the iron matrix adjacent to the graphite and a comparison with Figure 73b reveals that this area did not contain significant enrichments of sulphur and oxygen. Some evidence of an enhanced carbon signal was recorded in this region, indicating the presence of a carbide inclusion.

Calcium enrichment was also observed in graphite nodules in a spheroidal graphite cast iron produced using an addition of magnesium ferro-silicon (iron G). In this case, the calcium is likely to have originated as an impurity in the latter treatment alloy. The SIMS elemental maps shown in Figure 76 indicate the presence of calcium-rich areas in the graphite. A few calcium-containing particles were also found in the iron matrix surrounding the nodule, and a comparison of the ion images for different elements shown in Figure 76 indicates that these inclusions were also associated with magnesium, oxygen, sulphur and occasionally aluminium.

A composition -depth profile carried out in a duplex graphite nodule in iron F also indicated that the calcium distribution was confined to distinct areas approximately 0.5 μm in size. These results are illustrated in Figure 77, which shows two separate calcium peaks, one of which exhibits correlation with a cerium peak. It was not

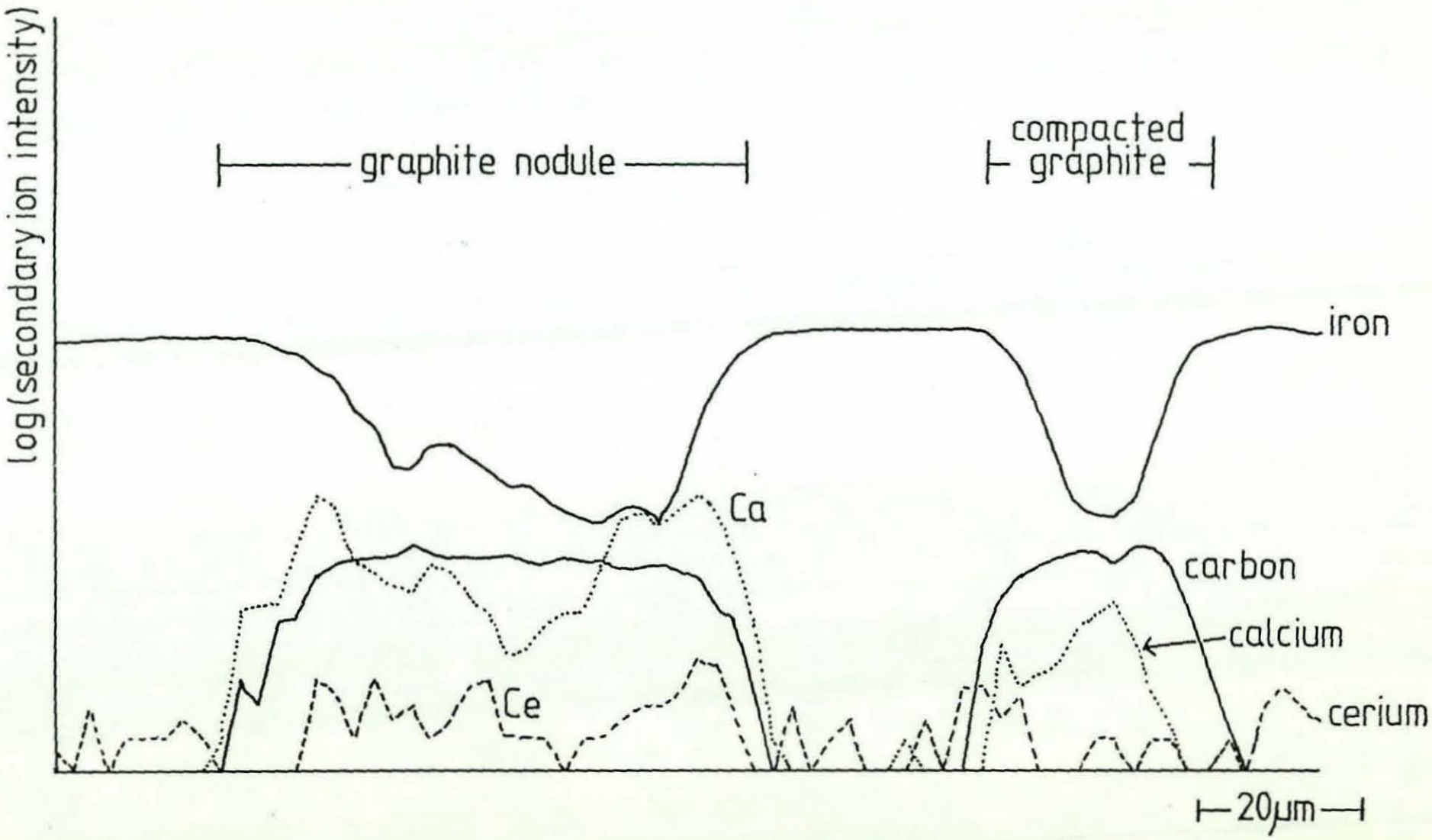

Figure 72. SIMS stepscans across nodular and compacted graphite in iron E.
72a. O_2^+ ions.

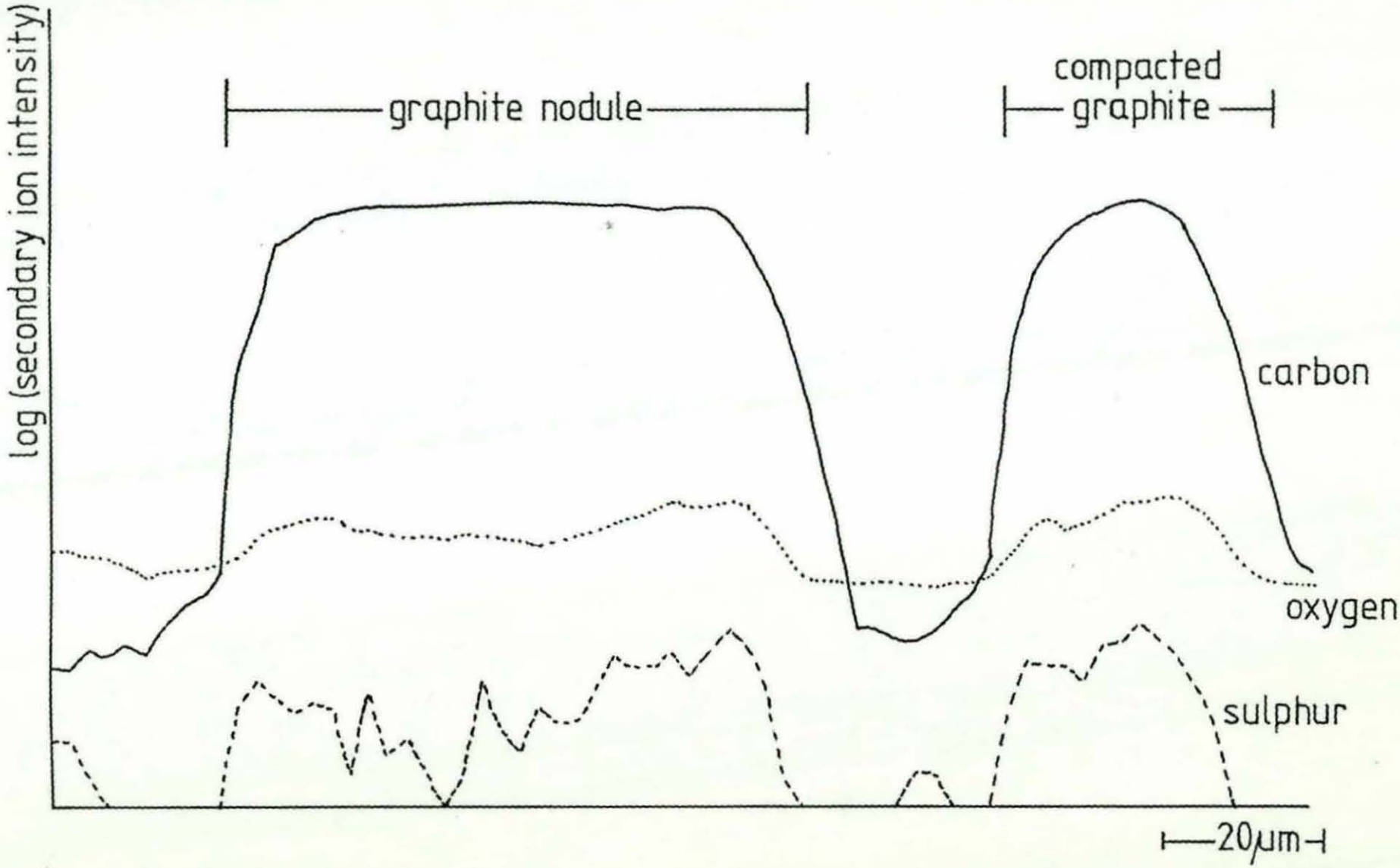

Figure 72 b. Cs+ ions. (same location as in figure 72a.)

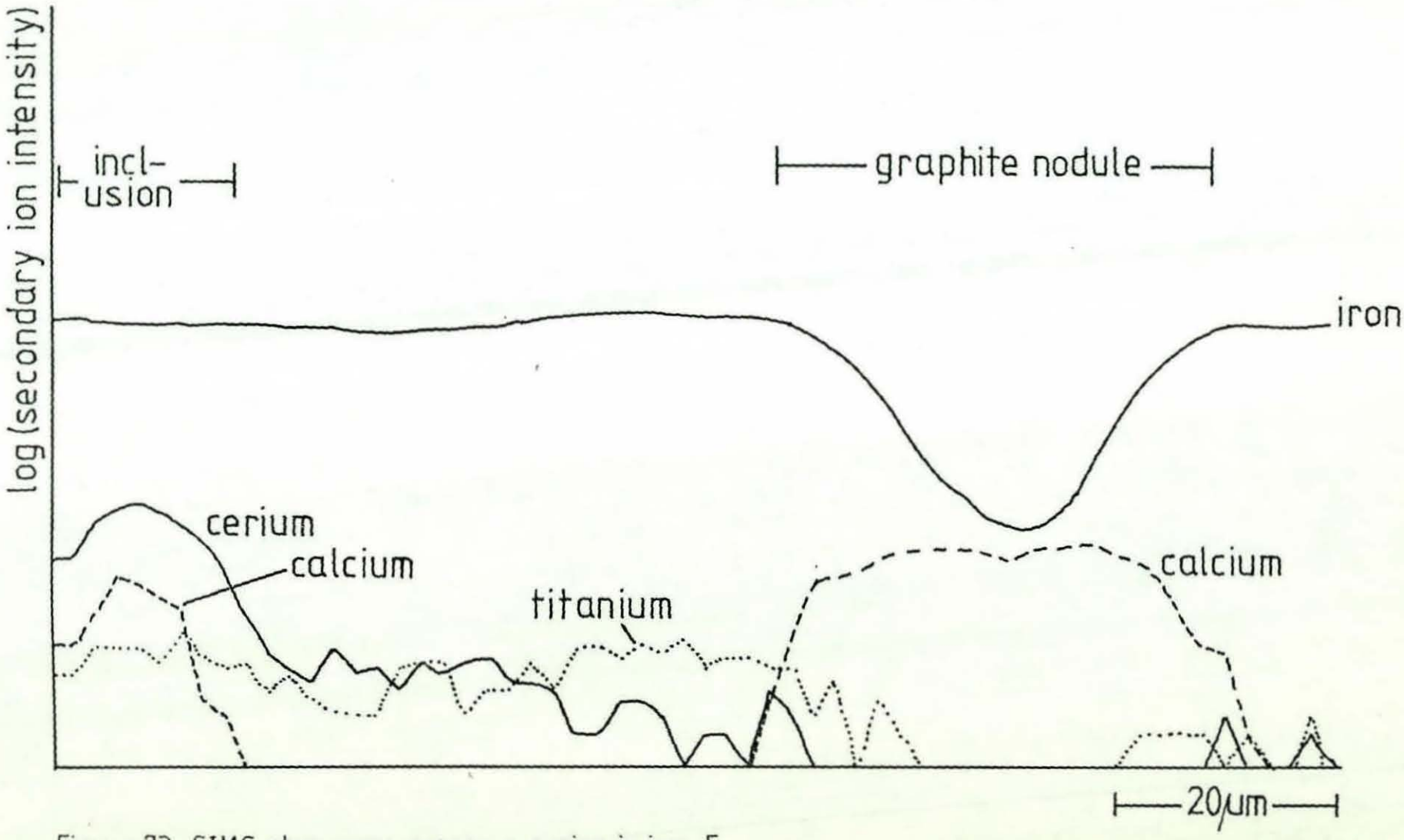

Figure 73. SIMS stepscans across a region in iron F.
73a. O_2^+ ions.

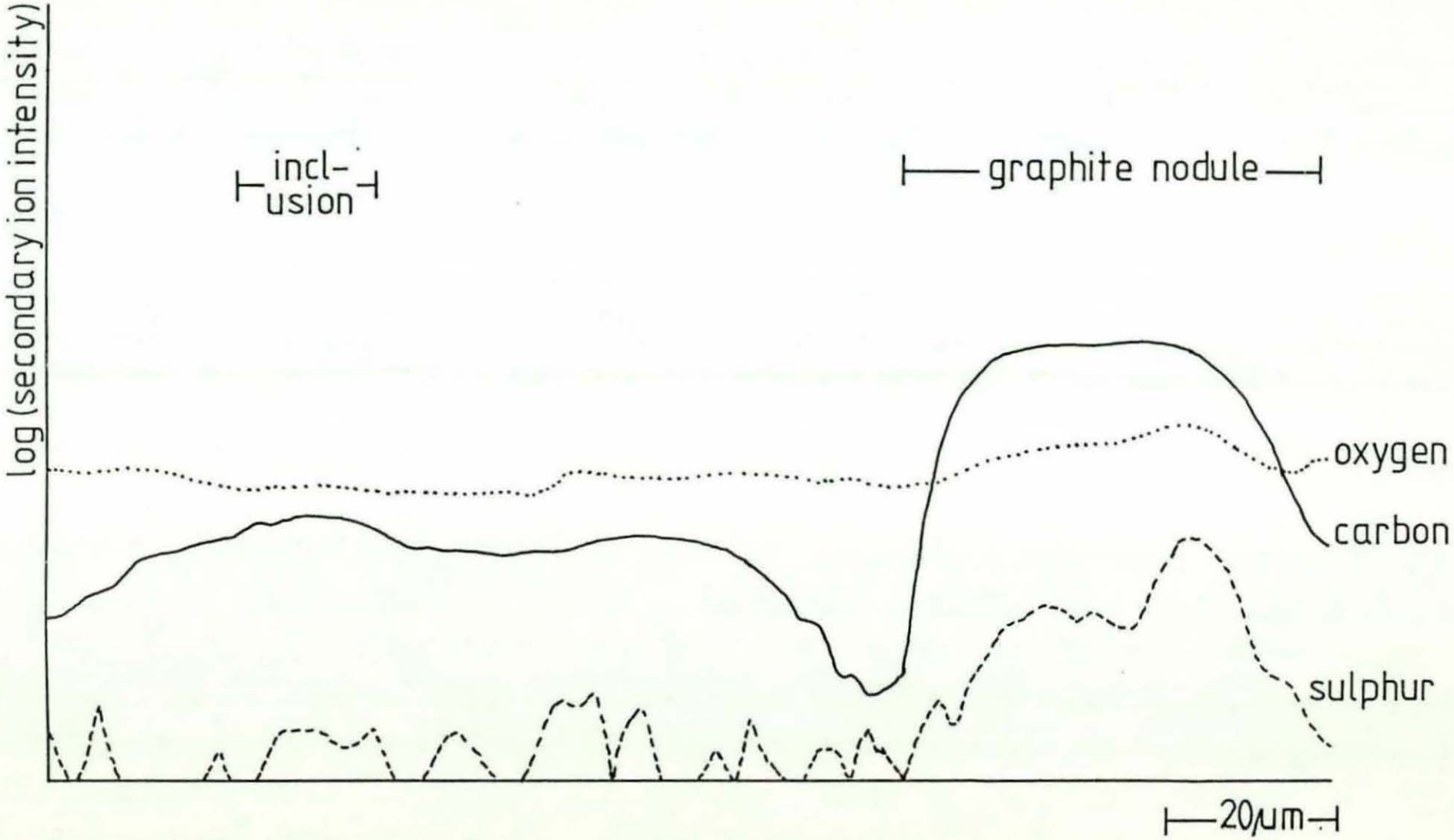

Figure 73b. Cs+ ions. (same location as in figure 73a.)

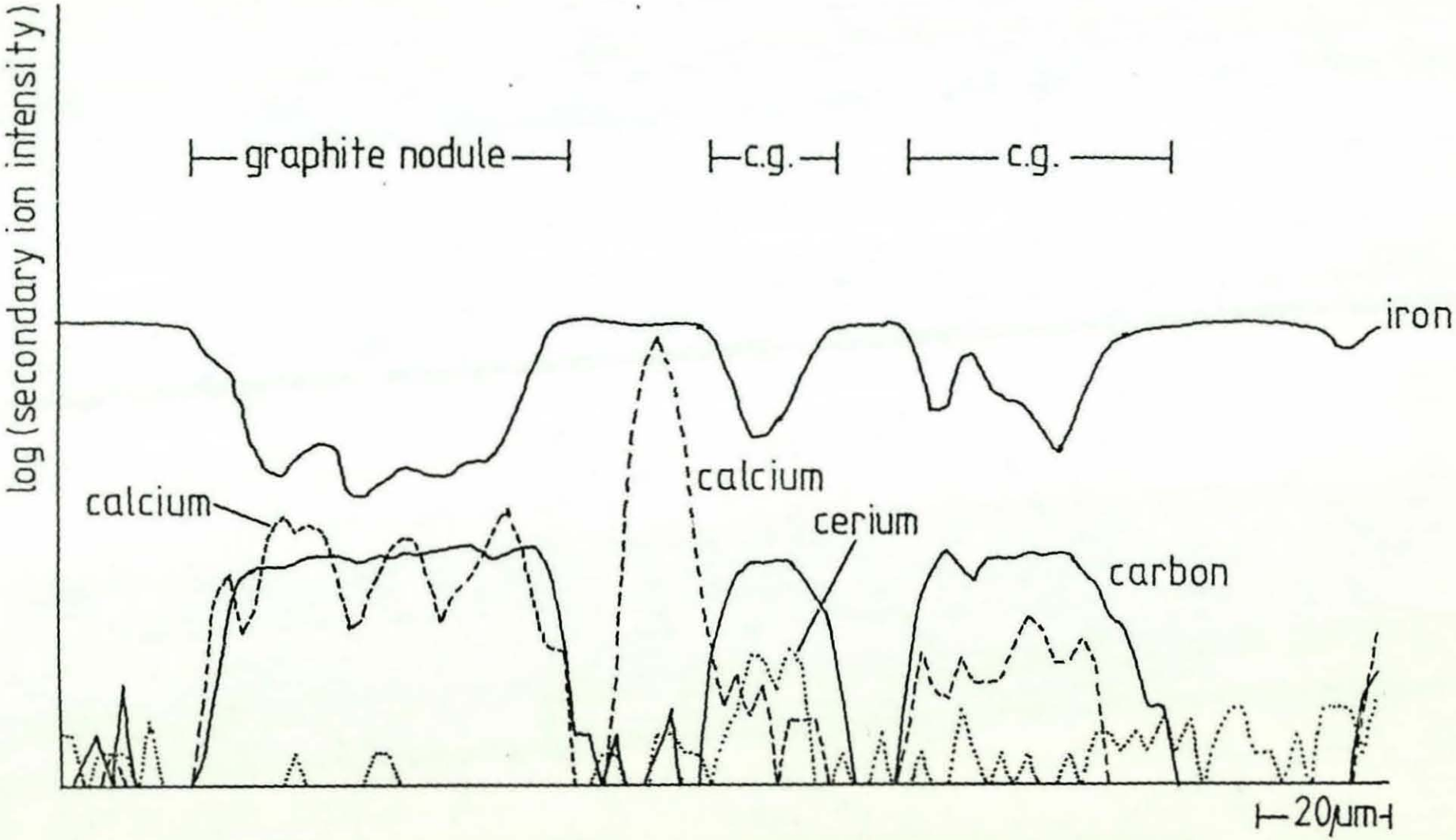

Figure 74. SIMS stepscan (O_2^+ ions) across nodular and compacted graphite in iron F.

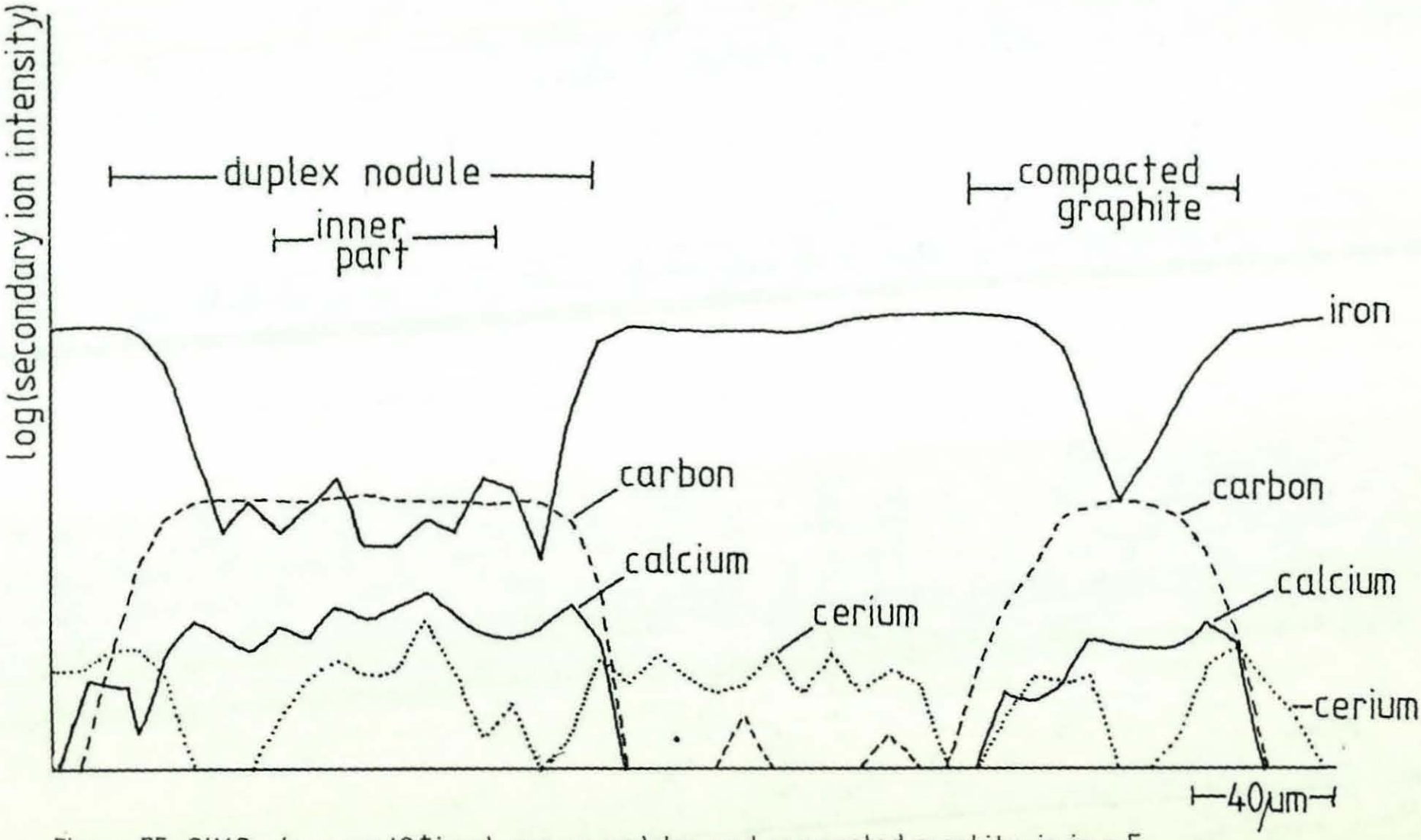

Figure 75. SIMS stepscan (O_2^+ ions) across nodular and compacted graphite in iron E.

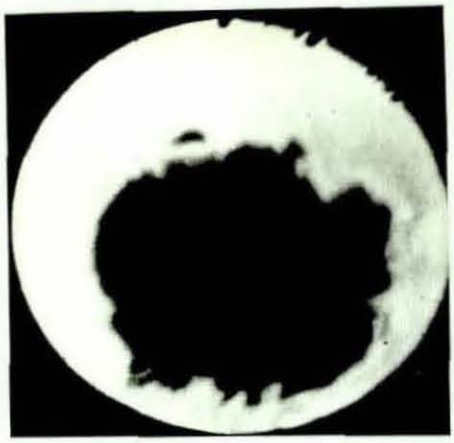

(a) Iron Image

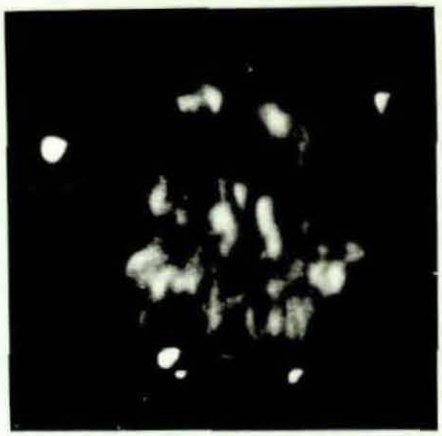

(b) Calcium Image

(c) Magnesium Image

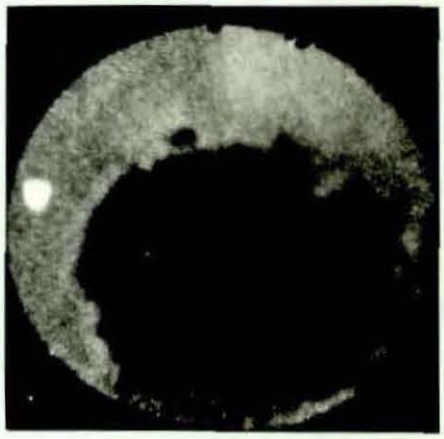

(d) Aluminium Image

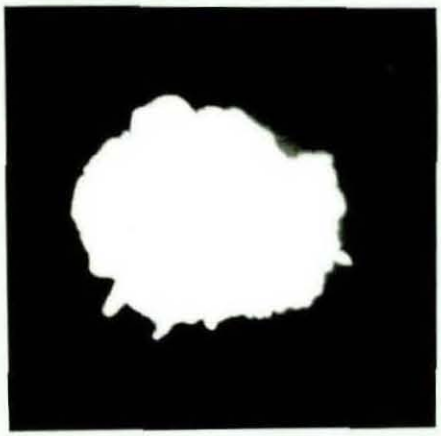

(e) Carbon Image

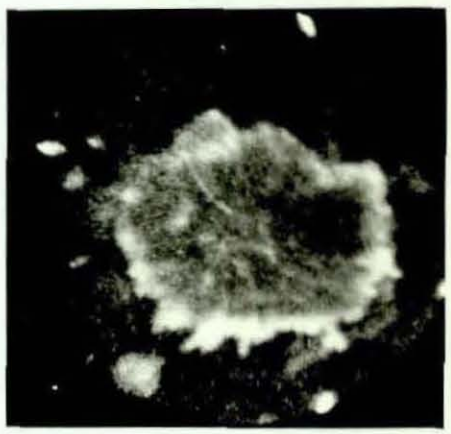

(f) Oxygen Image

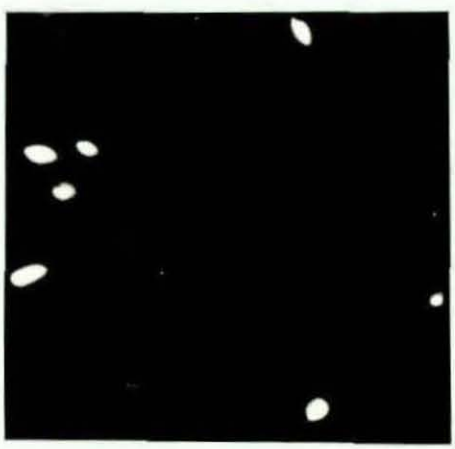

(g) Sulphur Image

Figure 76 SIMS Ion Images for Iron G

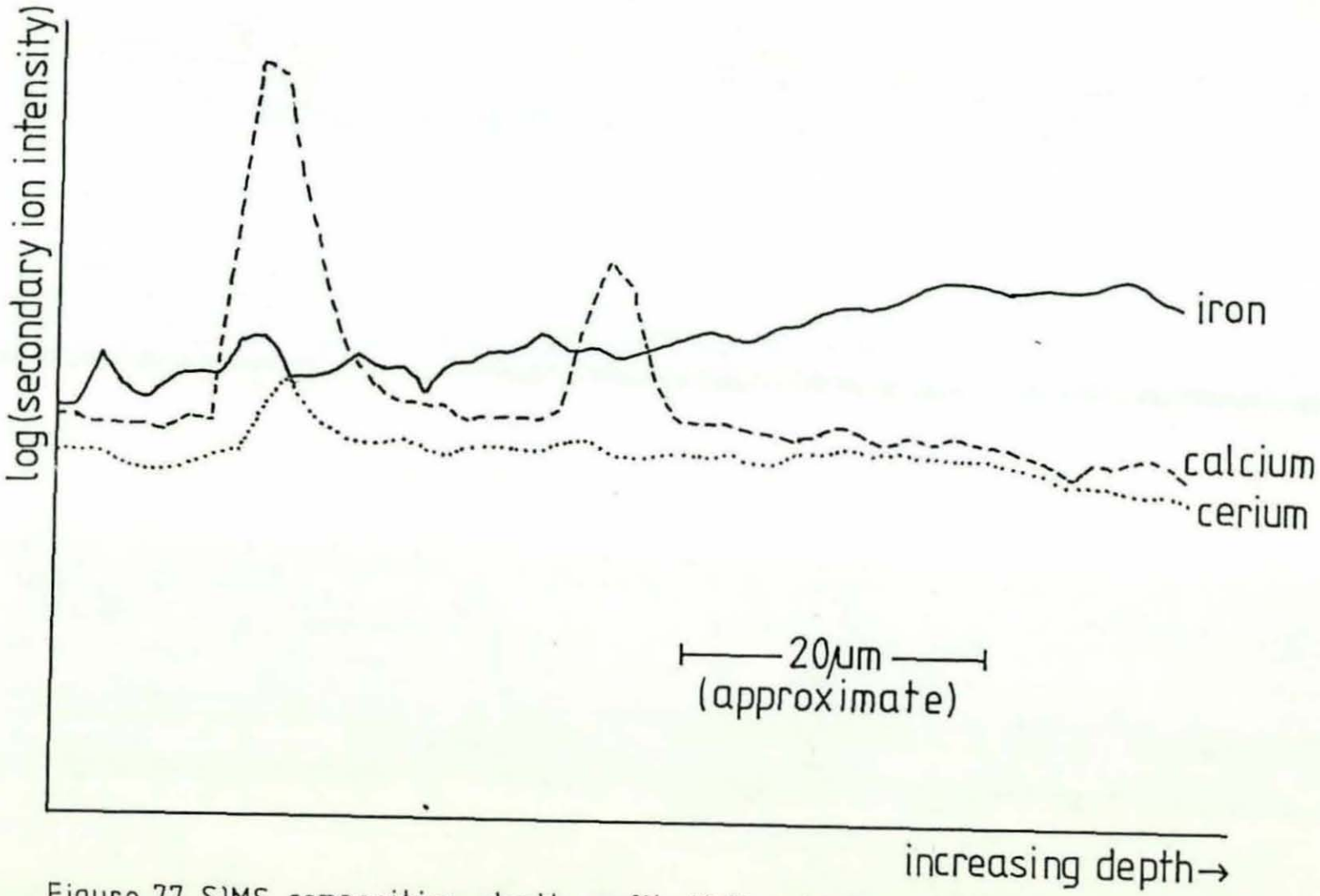

Figure 77. SIMS composition-depth profile (O_2^+ ions) into a duplex graphite nodule in iron F.

possible to record the variation in oxygen or sulphur during this depth profile since the latter elements may only be analysed with the required sensitivity when Cs^+ ions are used for bombarding the specimen.

Stepscans across duplex-structured graphite nodules in iron D (magnesium-titanium treatment) also revealed calcium enrichment. For example, in Figures 78 and 79, enhanced calcium signals were recorded in the spheroids and there was a tendency for the calcium level to be greater in the inner part of the duplex structure compared to the outer halo. These figures also show that the calcium signal peaked at the graphite/iron interfaces in these nodules. The latter effects were not observed with all the irons studied and it is interesting to note that the calcium distribution in a nodule in iron E (Figure 75) exhibited no significant variations that could be attributed to the duplex structure. Figures 78 and 79 additionally reveal that within the central part of the duplex nodule, the calcium and cerium traces have a high degree of correlation. As noted previously, this effect was also observed with a graphite spheroid in iron E (Figure 72). In contrast with the latter example, however, the sulphur signal shown in Figure 79b exhibits only a very small increase at the point where the calcium and cerium traces exhibit large peaks. This difference between the results for these irons may be attributed to the much lower bulk residual sulphur content of iron D (0.006% S) compared to iron E (0.013% S). This would tend to reduce the extent to which local variations in the sulphur level could be detected in the stepscan. The reduction in all the recorded signals that occurred at an early stage in the SIMS stepscan shown in Figure 79b was due to an electrostatic charging effect and is not important in the context of these experiments.

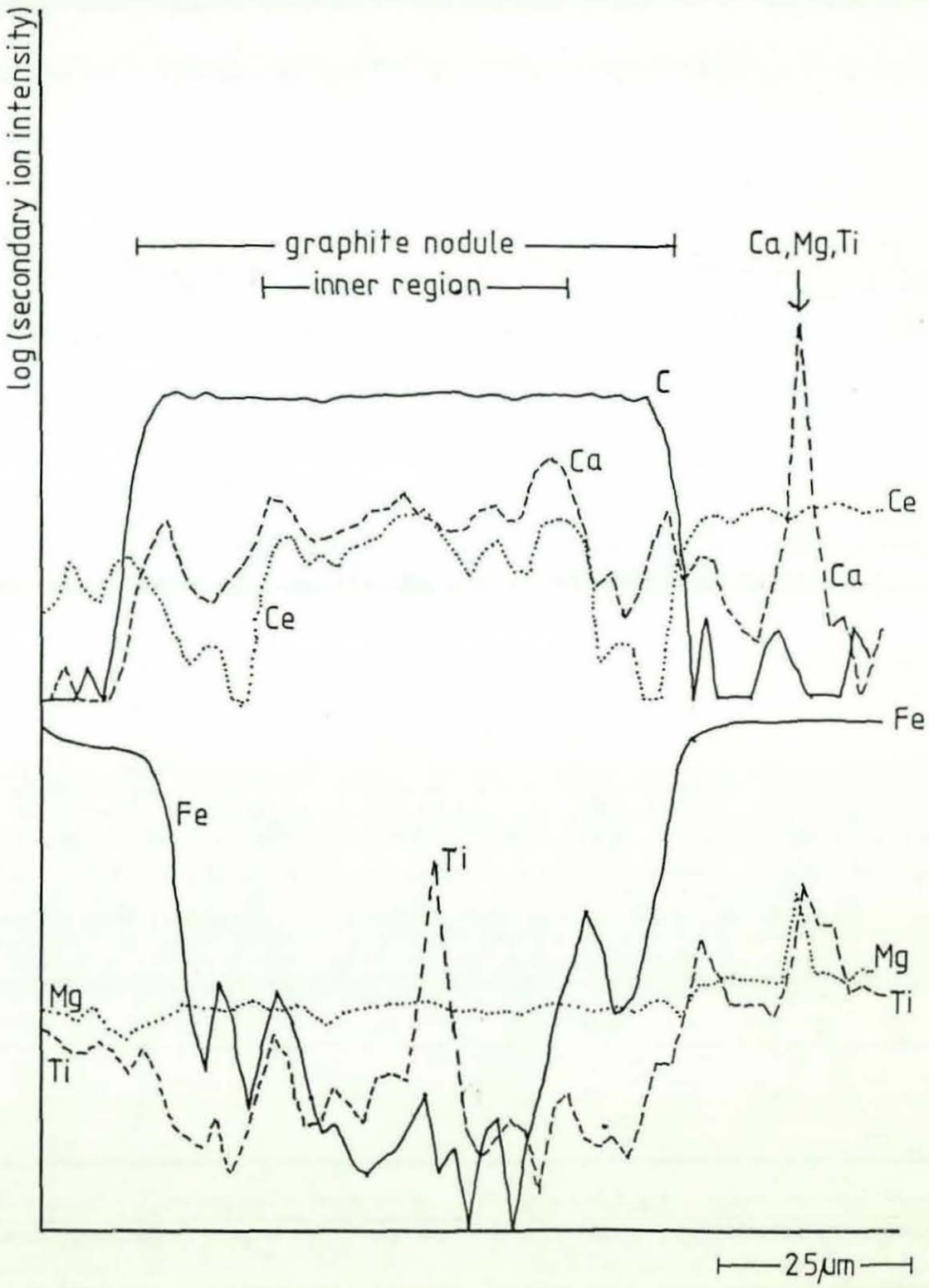

Figure 78. SIMS stepscan (O_2^+ ions) across a duplex graphite nodule in iron D.

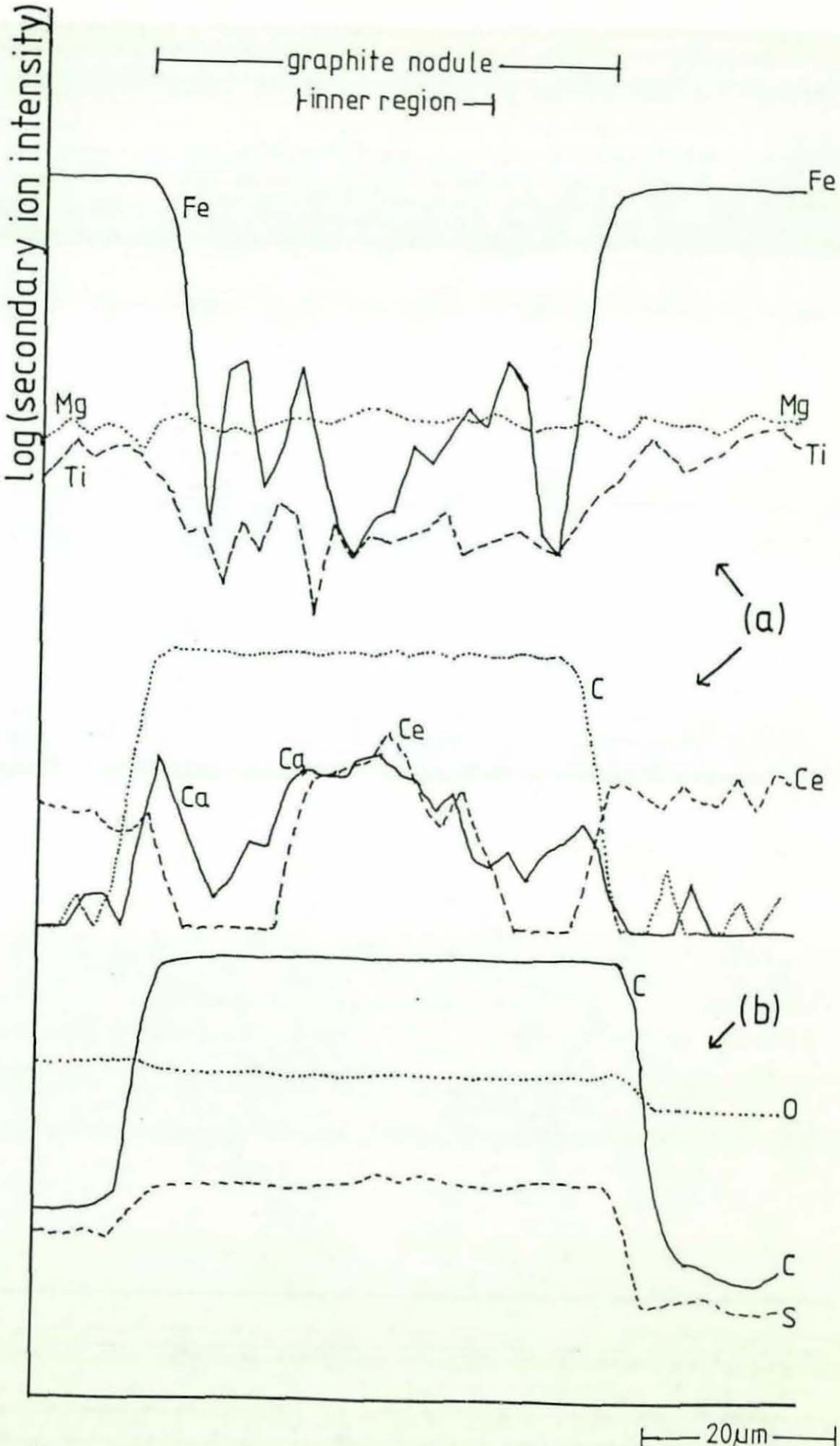

Figure 79. SIMS stepscans across a duplex graphite nodule in iron D : (a) O_2^+ ions ; (b) Cs^+ ions.

In contrast to the previous examples, duplex nodules in irons B and C, which exhibited the highest levels of rare earth enrichment, contained no detectable calcium concentrations.

6.3.2.1.3 Magnesium/Titanium

Figures 78 and 79 indicate that the graphite nodules in iron D produced with a magnesium-titanium melt treatment were not enriched in magnesium. In Figure 78, the magnesium peak shown in a position in the iron matrix adjacent to the nodule was found to coincide with increases in the calcium and titanium signals. A titanium peak was also observed at the centre of the graphite nodule represented in this stepscan and there is some evidence of joint titanium, iron, calcium and cerium peaks at the interfaces between the inner and outer parts of the duplex structure. Titanium peaks were not observed in stepscans across other nodules in the same iron.

6.3.2.1.4 Iron

Several stepscans across duplex graphite nodules in different irons showed that the iron level was higher in the outer region of the structure compared to the inner area. This effect is particularly evident in Figures 66, 68, 78 and 79 for irons B, C and D respectively. In addition, scanning electron microscopy and elemental mapping using energy-dispersive X-ray microanalysis clearly revealed a number of iron-rich inclusions which were situated only in the outer region. This is illustrated in Figures 80 and 81.

6.3.2.2 Compacted Graphite

In spite of careful specimen preparation, no duplex sructures could be detected in the rounded ends of compacted graphite particles.

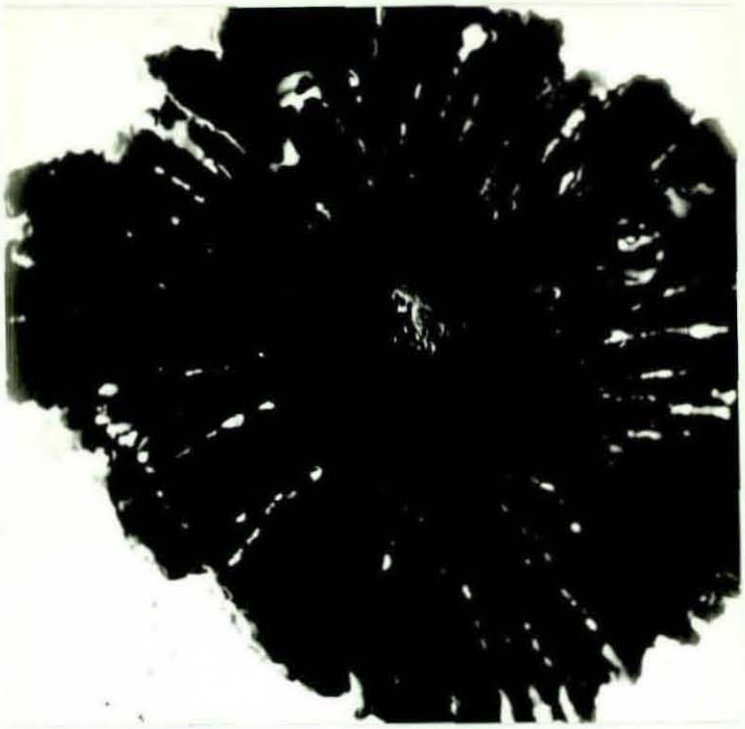

1250X

Figure 80 Inclusions Present in the Outer Region of a Duplex Graphite Nodule in Iron B

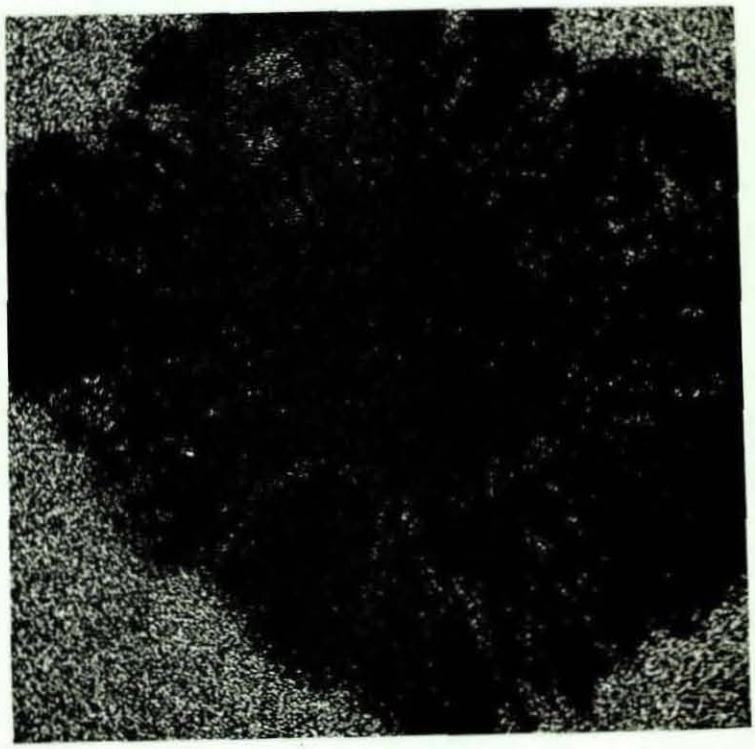

1250X

Figure 81 Elemental Map for Iron (Energy-Dispersive X-ray Microanalysis) - Corresponds to Nodule Shown in Figure 80

SIMS analyses of samples from iron B (eg Figure 82) indicated some cerium and lanthanum enrichment in compacted graphite, however, this appeared to a lesser extent than encountered in duplex nodules from the same sample (Figure 66). As illustrated in Figure 71, a similar effect was observed with adjacent compacted and nodular graphite particles in iron E. Figure 82 also reveals cerium, lanthanum and calcium peaks coinciding at two points in the iron matrix adjacent to the graphite. It was subsequently shown that these peaks originated from sulphide inclusions.

In most of the O_2^+ ion SIMS stepscans that were carried out across a graphite nodule and an adjacent piece of compacted graphite in irons E and F, the calcium signal was also slightly lower in the compacted graphite compared to the nodular graphite. This is illustrated in Figures 72a, 74 and 75.

With regard to the sulphur and oxygen distributions, Figure 72b indicates that the magnitudes of the signals for these elements in a compacted graphite particle were similar to those in an adjacent graphite nodule in the same sample. Compared to flake graphite, however, compacted graphite contained lower levels of sulphur and oxygen. This is illustrated by comparing Figure 83, for compacted graphite (iron F) with Figure 60, for flake graphite (iron A). These two stepscans can be directly compared because care was taken to maintain a constant set of examination conditions for both samples.

SIMS analysis of irons I and J, produced by magnesium-aluminium and calcium-zirconium additions respectively, revealed no detectable enrichment of aluminium or zirconium in the graphite phase.

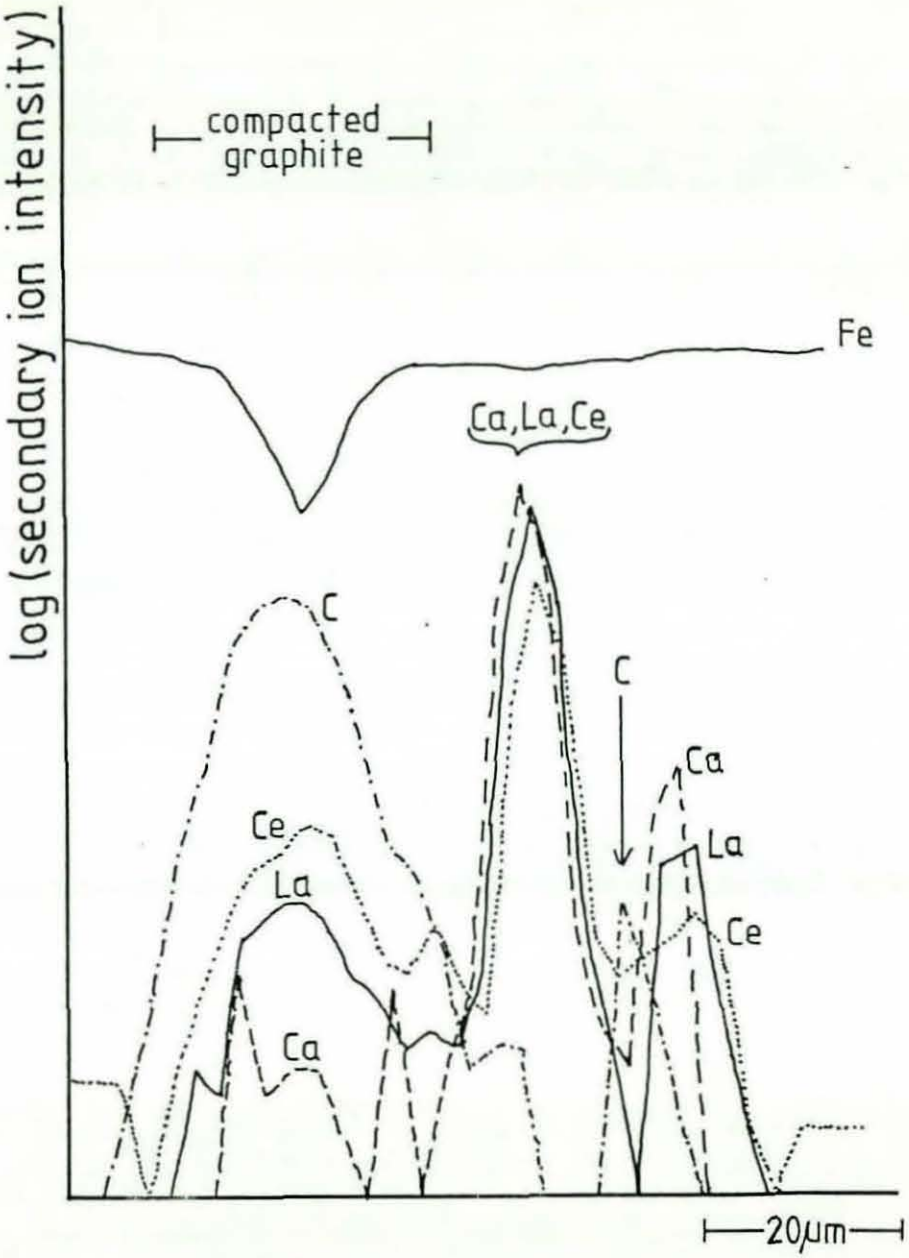

Figure 82. SIMS stepscan (O_2^+ ions) across compacted graphite in iron B.

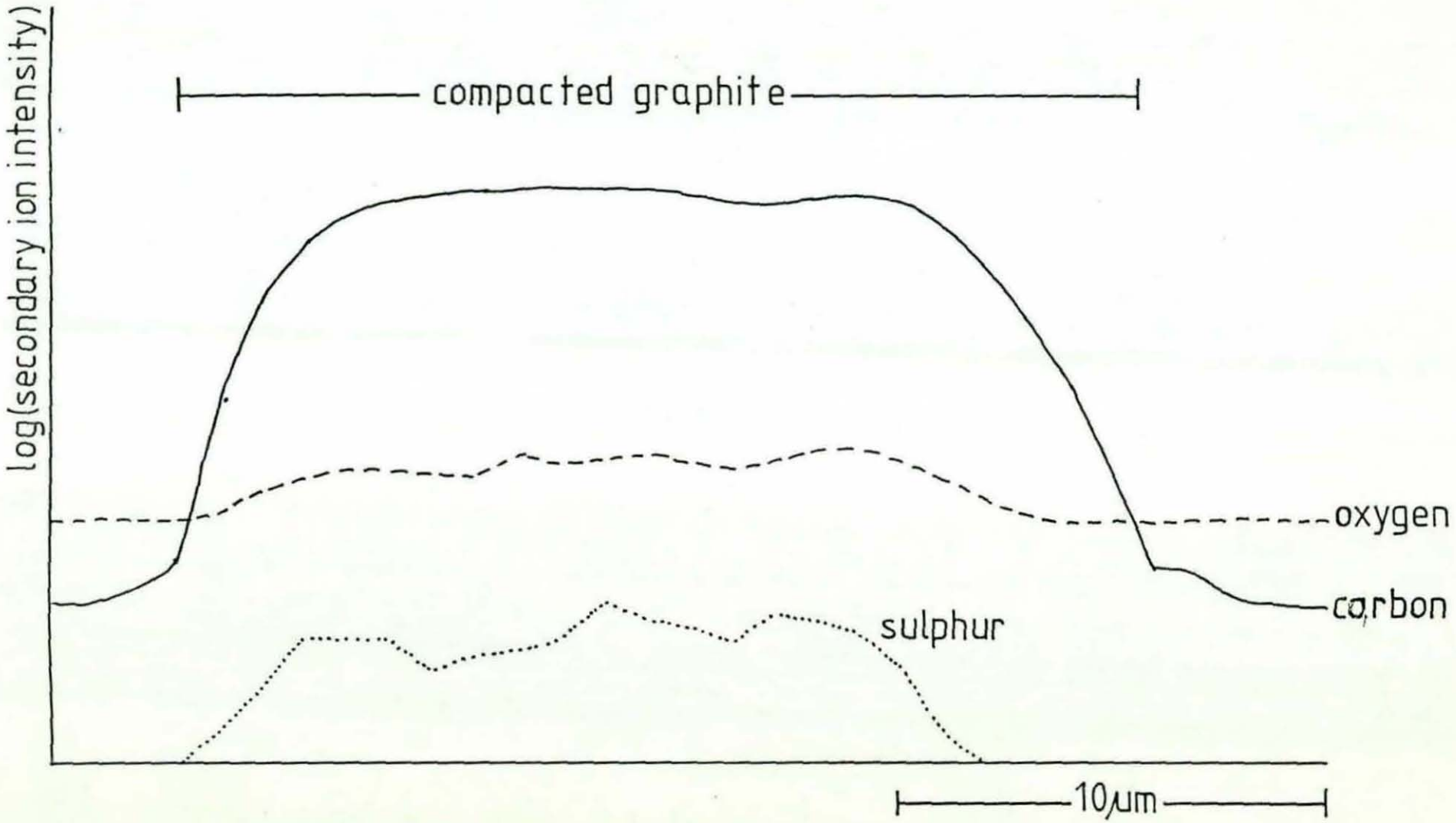

Figure 83. High resolution SIMS stepscan (Cs^+ ions) across compacted graphite in iron F.

6.3.2.3 Iron Matrix

6.3.2.3.1 Rare Earth Elements

In addition to the rare earth enrichments found in the graphite phase, cerium and lanthanum also occurred in irons B, C, D, E, F and G in discrete particles which were distributed in a grouped fashion in the iron matrix. Optically these particles appeared to occur most commonly in irons B and C, which also contained the highest bulk residual levels of rare earth elements (see Appendix I). The groups of cerium-bearing inclusions were normally located in or adjacent to pearlite areas, and elemental mapping using SIMS confirmed that the latter regions were also depleted in iron, silicon, and aluminium. In irons B and C, which were treated only with rare earth elements, the particles were usually additionally associated with oxygen, sulphur, phosphorous and the carbo-nitride molecule. A few of the inclusions also contained calcium and/or titanium, vanadium and chromium. The above observations are illustrated in Figure 84 which shows SIMS ion images for an area containing a group of cerium-rich particles in iron B, together with an optical micrograph of the same region, photographed prior to the SIMS analysis. It is also interesting to note that with this sample, different rare earth elements do not appear to be uniformly distributed in all the rare-earth bearing inclusions. This is further illustrated by the results shown in Figure 85, of energy-dispersive X-ray microanalysis carried out with a different particle in iron B. This figure reveals the presence of cerium, neodymium and phosphorous but not lanthanum. Since the volume of material analysed using this technique was 1-2μm in diameter, and because the inclusion in question had similar lateral dimensions, some

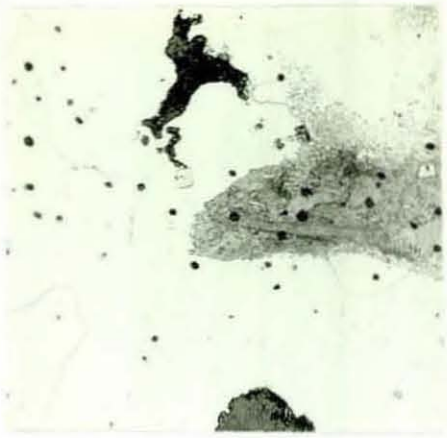

(a) Optical Micrograph

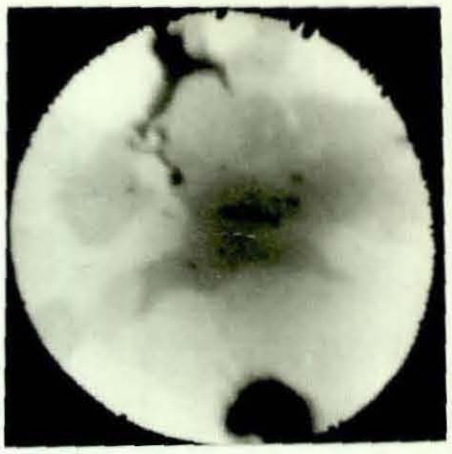

(b) Iron Image

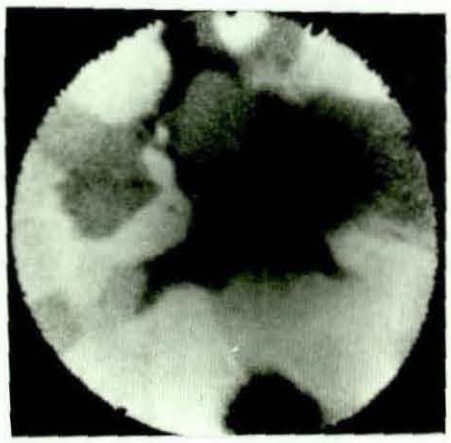

(c) Silicon Image

(d) Cerium Image

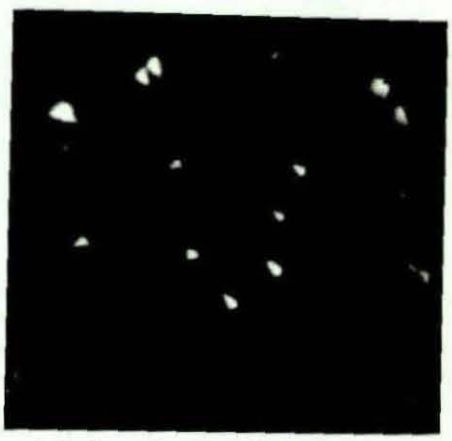

(e) Lanthanum Image

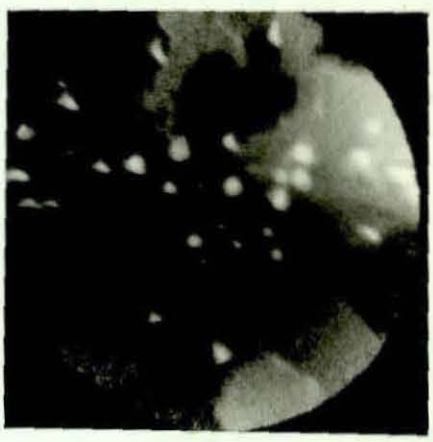

(f) Oxygen Image

(g) Sulphur Image

(h) Phosphorus Image

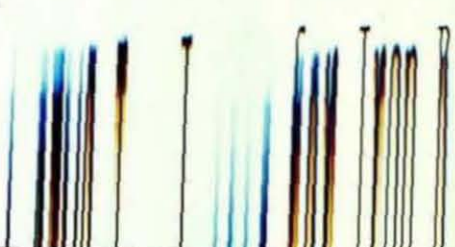

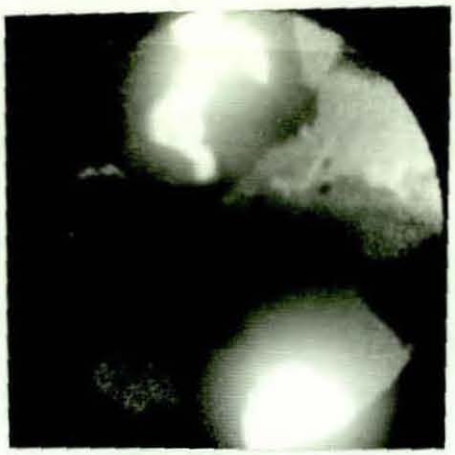

(i) Carbon Image

(j) Carbo-nitride (CN) Image

(k) Calcium Image

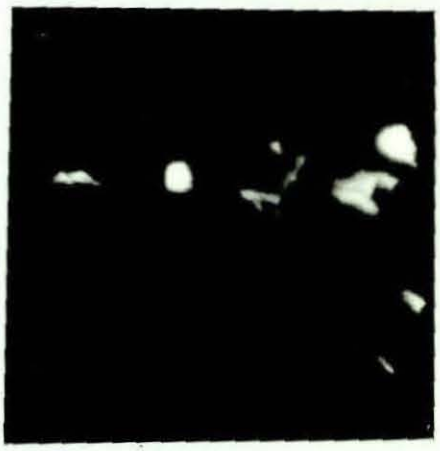

(l) Titanium Image

(m) Vanadium Image

(n) Chromium Image

Figure 84 Continued

6250X

Figure 85(a) Rare-earths Bearing Particle in Iron B, Analysed Using Energy Dispersive X-ray Microanalysis (See Figure 85(b)) SEM Image

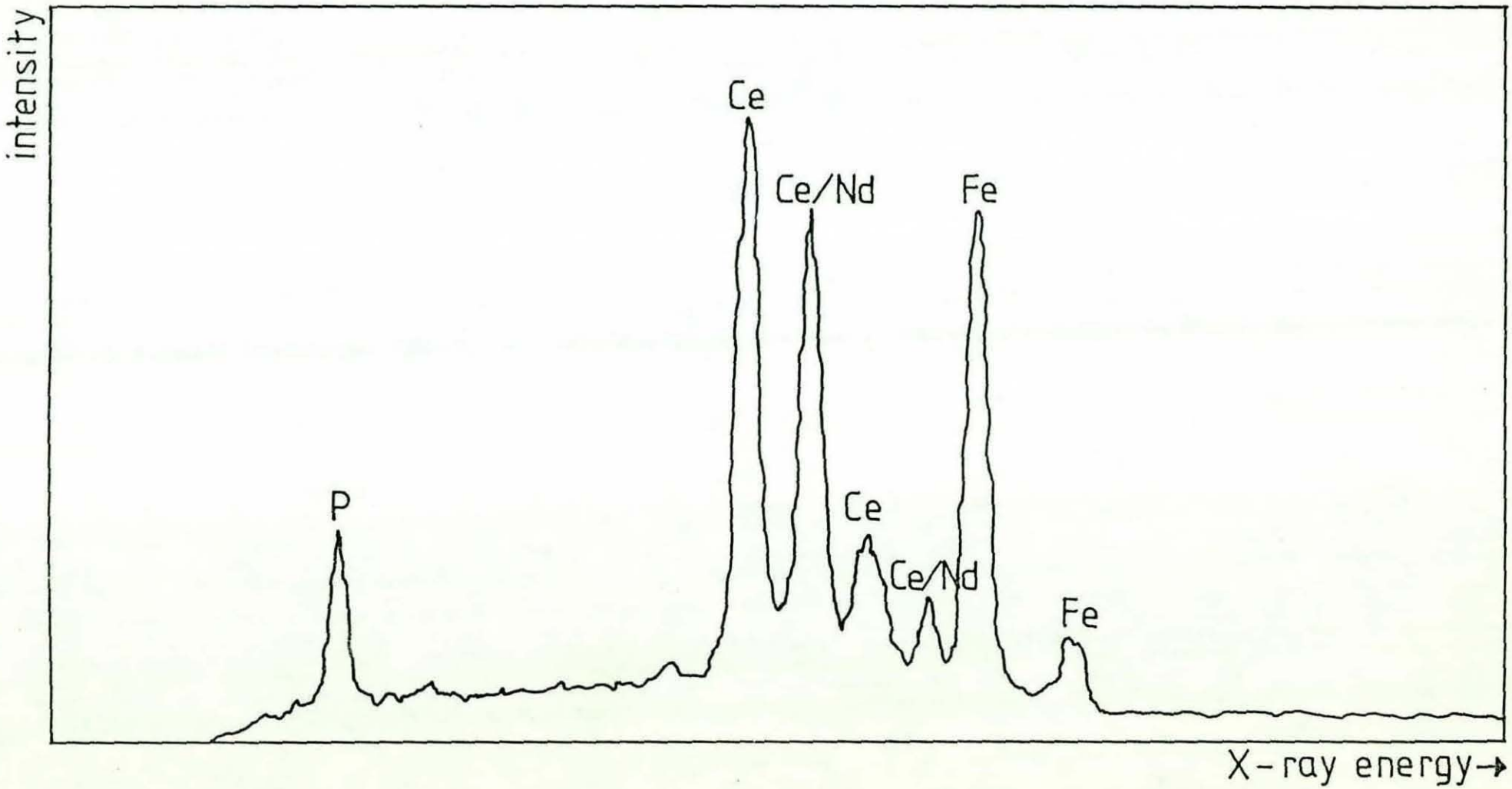

Figure 85 b. Energy-dispersive X-ray microanalysis of a particle in the iron matrix of iron B.

overlap may have occurred with the adjacent pearlite. On this basis, it is possible that the iron signal recorded in the analysis was due predominantly to the contribution from the region surrounding the particle.

In contrast to the results of SIMS analyses carried out with irons B and C, the cerium-rich inclusions identified in irons E and F (produced using combined calcium-rare earth additions) did not show a high degree of correlation with the sulphur and oxygen signals, which were mainly associated with calcium. This is illustrated by a comparison of the ion images shown in Figure 86 for an area in iron F. Figure 87 additionally indicates that the cerium distribution in this iron has a greater correlation with the titanium, vanadium and chromium ion images compared to the irons treated only with rare earth elements.

SIMS spot analyses were also carried out on areas of special interest in the vicinity of a group of cerium-bearing particles in iron F. These results are shown in figure 88 and exhibit certain characteristic features which indicate the way in which cerium is distributed in the iron matrix and how it interacts with other solutes. The cerium-bearing inclusion, for example, is shown to be enriched in rare earth metals, vanadium, chromium, titanium, calcium and magnesium. The enhanced peak occurring at mass number 166 additionally indicates the presence of cerium carbo-nitride. The peaks occurring around mass number 156 correspond to CeO and other rare earth compounds of this type. These oxides were formed spontaneously as a result of interaction between elemental rare earths and the oxygen ions used for bombarding the specimen. They could not have been originally present in the sample, since cerium

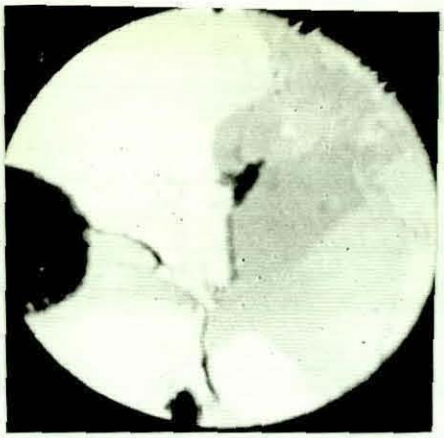

(a) Iron Image

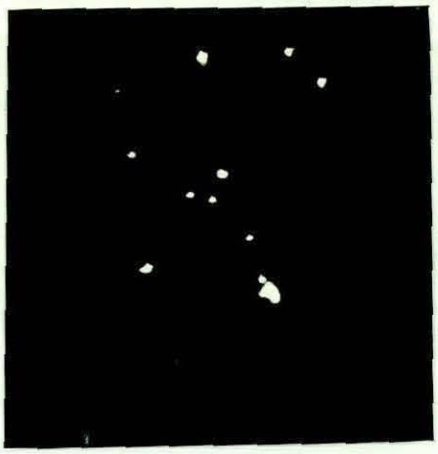

(b) Calcium Image

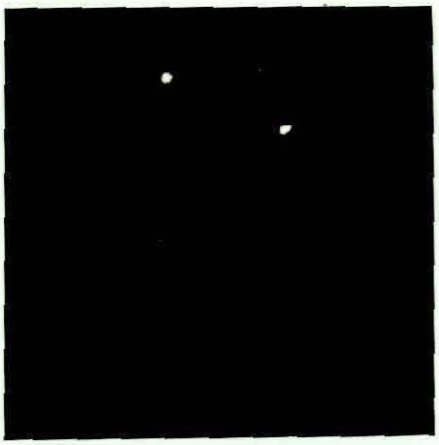

(c) Cerium Image

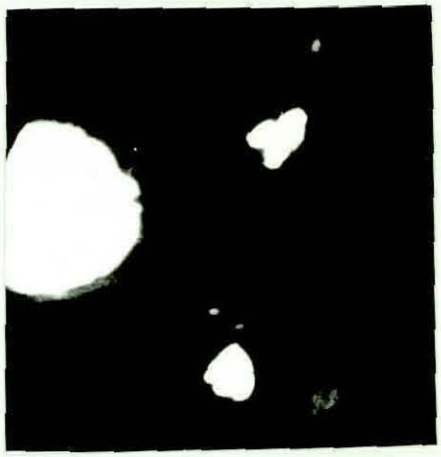

(d) Carbon Image

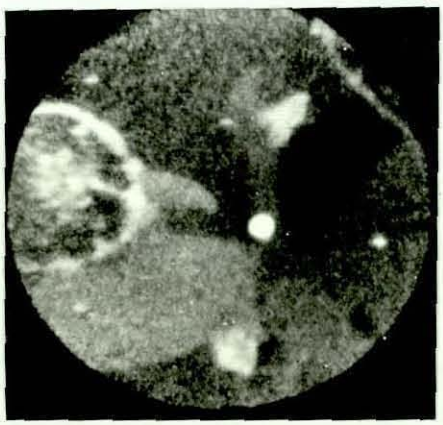

(e) Oxygen Image

(f) Sulphur Image

Figure 86 SIMS Ion Images for Iron F

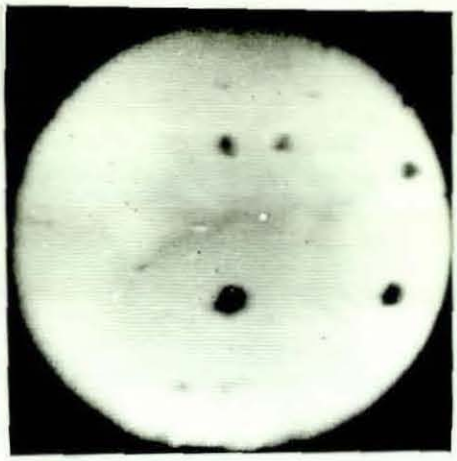

(a) Iron Image

(b) Cerium Image

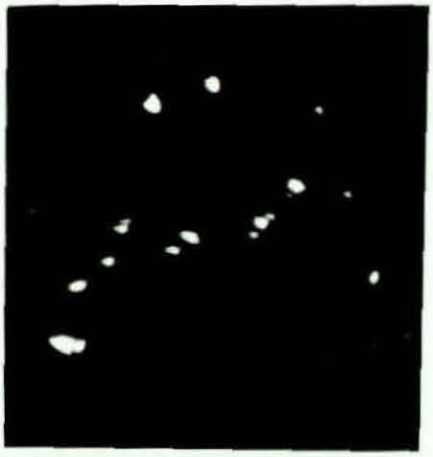

(c) Titanium Image

(d) Vanadium Image

(e) Chromium Image

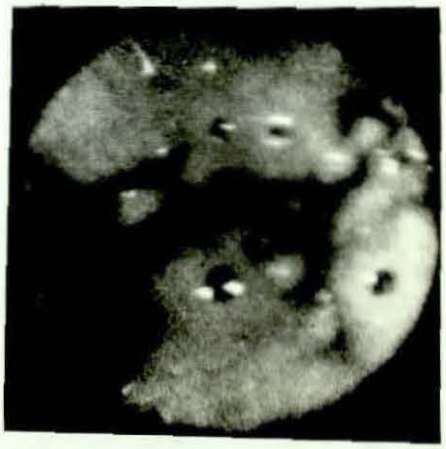

(f) Aluminium Image

Figure 87 SIMS Ion Images for Iron F

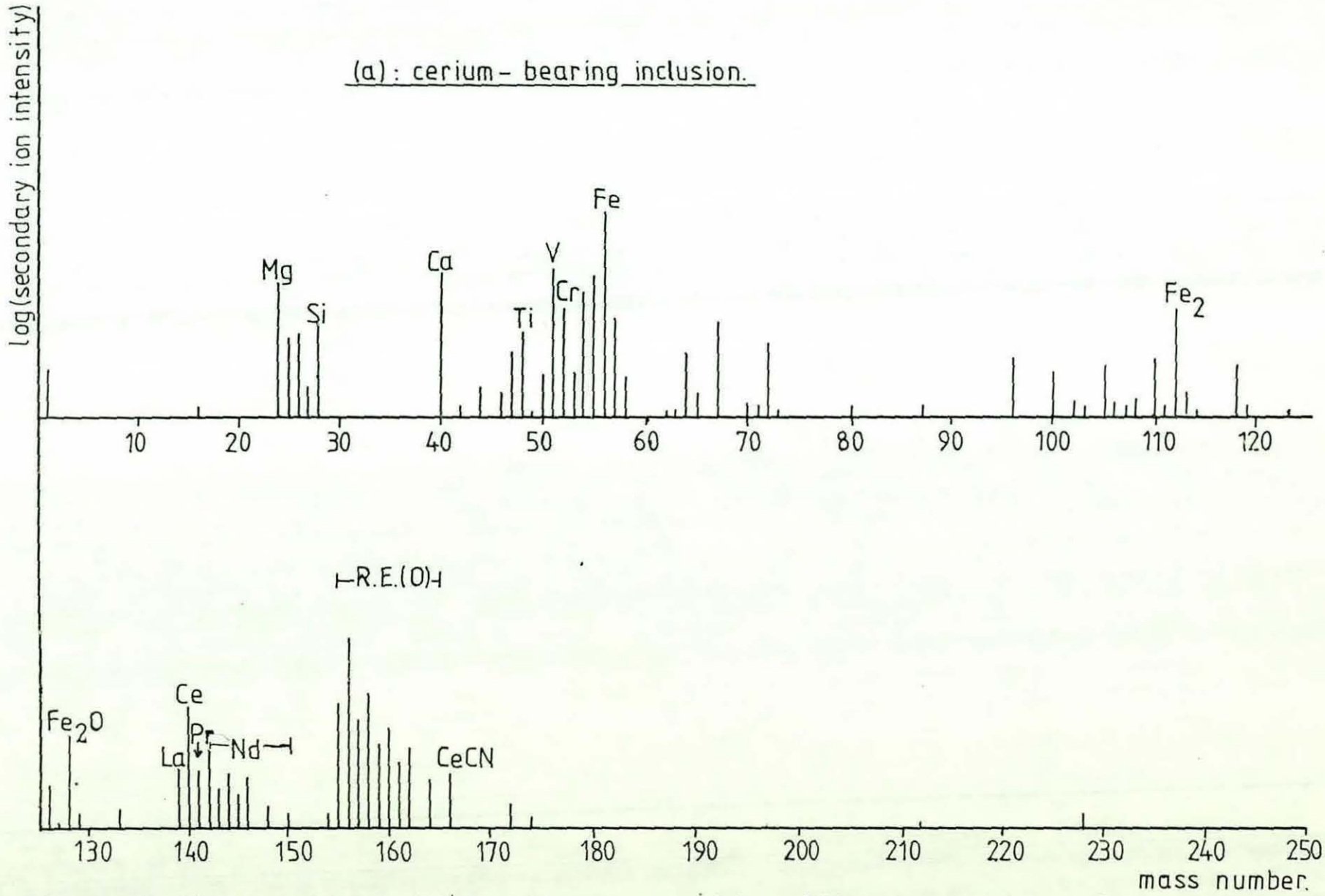

Figure 88. SIMS mass spectra (O_2^+ ions, 25μm diam. area) from different regions in iron F.

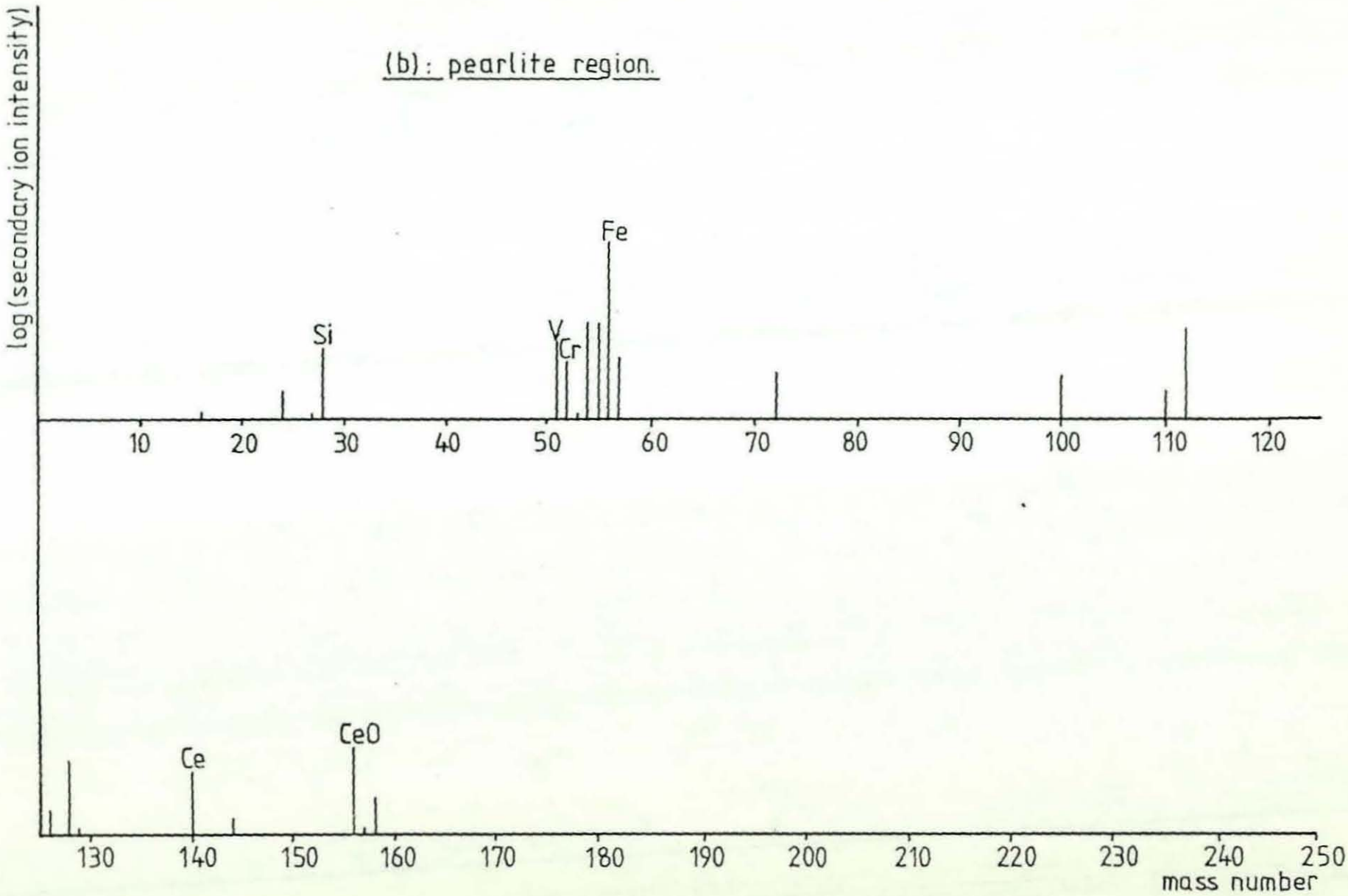
(b): pearlite region.
log (secondary ion intensity)
Si
V
Cr
Fe
Ce
CeO
10
20
30
40
50
60
70
80
90
100
110
120
130
140
150
160
170
180
190
200
210
220
230
240
250
mass number

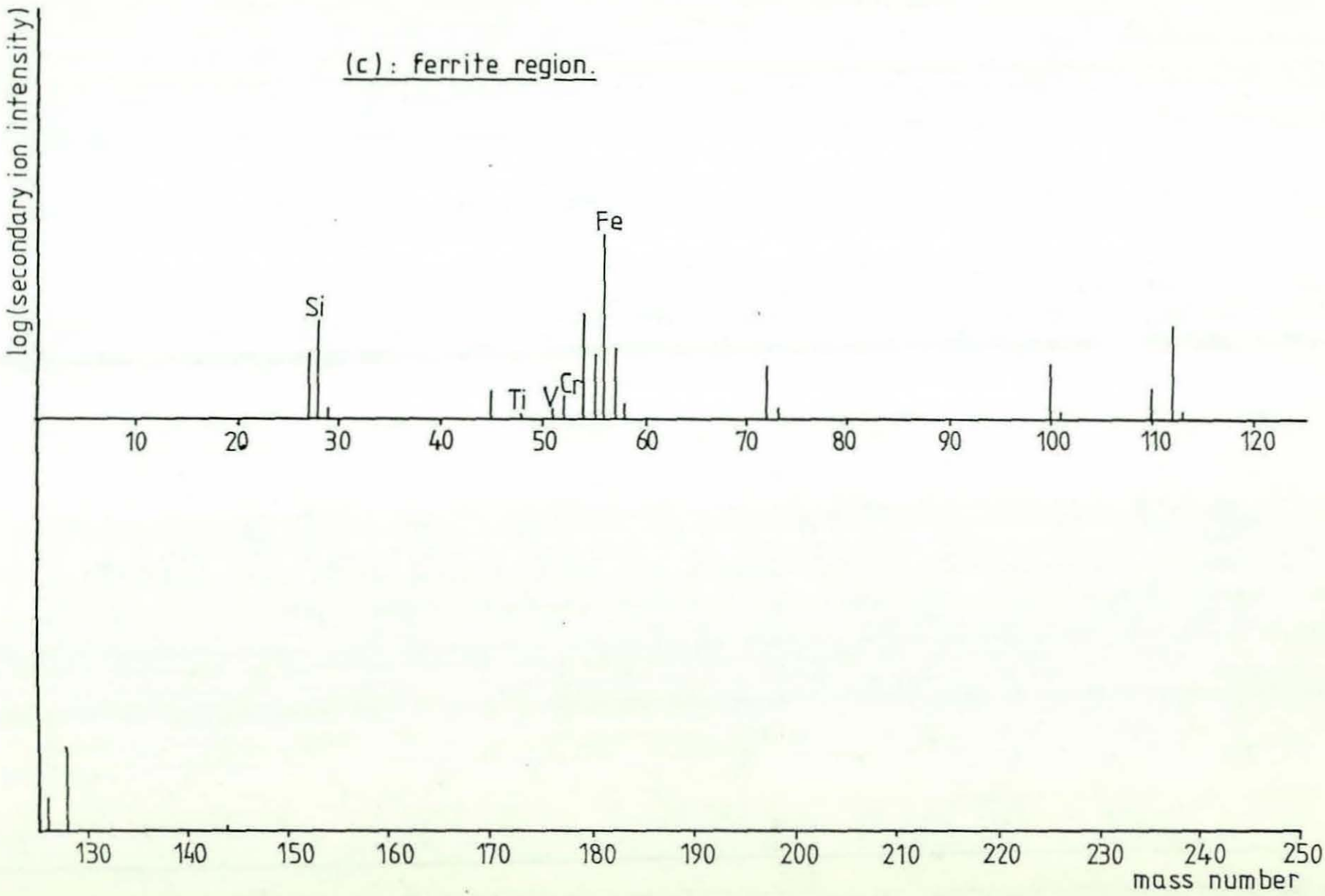
(c): ferrite region.
log(secondary ion intensity)
Si
Ti
V
Cr
Fe
10
20
30
40
50
60
70
80
90
100
110
120
130
140
150
160
170
180
190
200
210
220
230
240
250
mass number

and oxygen would have shown much greater correlation in the ion images. The pearlite area surrounding the particle also contained cerium (although more uniformly distributed), vanadium, and chromium. No cerium was detected in the ferritic region, which exhibited very low titanium, vanadium, chromium, and aluminium signals.

6.3.2.3.2 Calcium

Calcium-rich particles were distributed randomly in the iron matrices of most the irons studied. In irons E and F (cerium mischmetall-calcium silicide melt treatment), these inclusions were commonly associated with sulphur and sometimes oxygen or cerium. A few of the calcium-bearing particles also contained titanium. These observations are illustrated in Figures 89 and 86.

6.3.2.3.3 Magnesium-Titanium and Magnesium-Aluminium

SIMS ion images showing the distributions of different elements in iron H (produced using magnesium and titanium additions) are shown in Figure 90. Most of the magnesium-bearing particles revealed in this figure also contain titanium and calcium, and one additional coincidence with cerium can also be distinguished. As noted previously, a joint magnesium-calcium-titanium inclusion was also revealed in the iron matrix during a stepscan across a graphite nodule in iron D. Figure 90 additionally indicates that some of these particles also contain one or more of the following: oxygen, sulphur, carbo-nitride. A comparison between all of the ion images shown in this figure is made difficult by the fact that the area pf the sample in which the electronegative species (carbon, carbo-nitride, sulphur, oxygen) are imaged is slightly different to that used for the other elements shown. The association between

(a) Iron Image

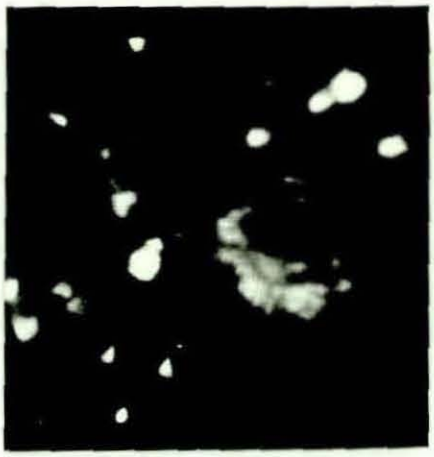

(b) Calcium Image

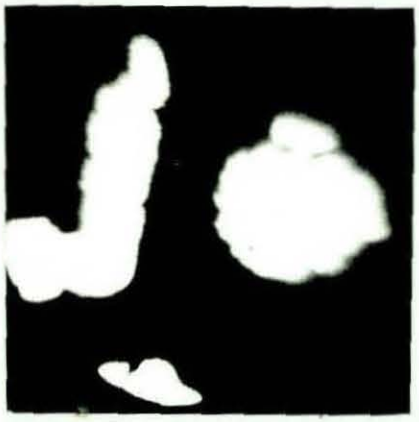

(c) Carbon Image

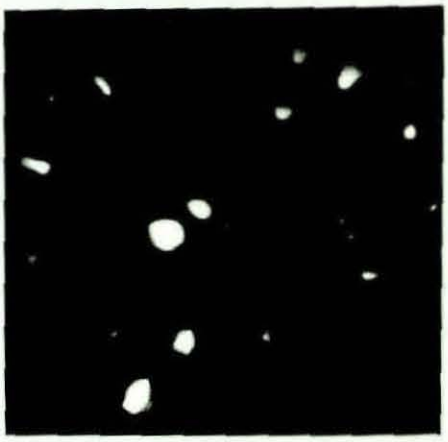

(d) Sulphur Image

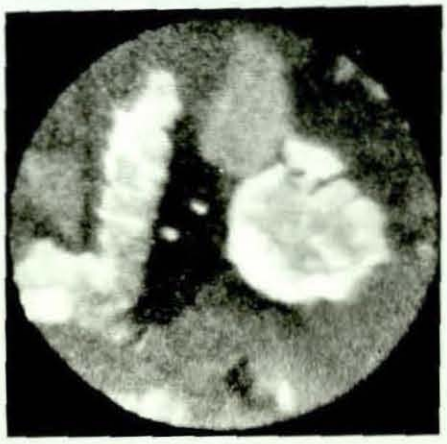

(e) Oxygen Image

Figure 89 SIMS Ion Images for Iron E

(a) Iron Image

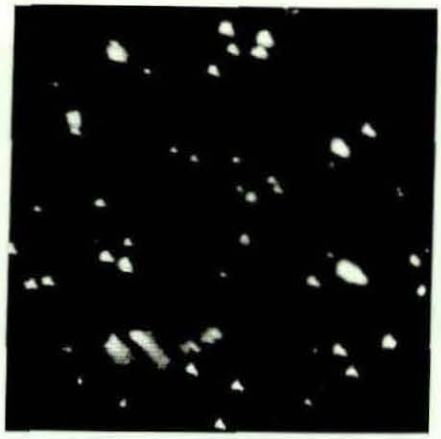

(b) Titanium Image

(c) Calcium Image

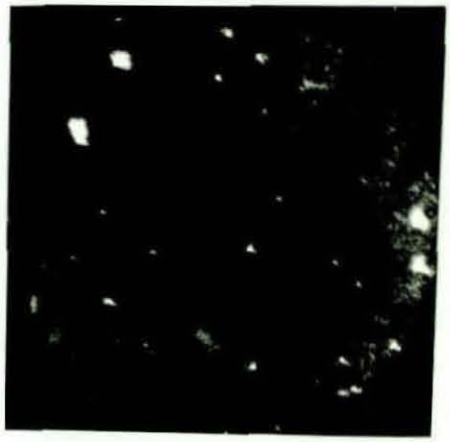

(d) Magnesium Image

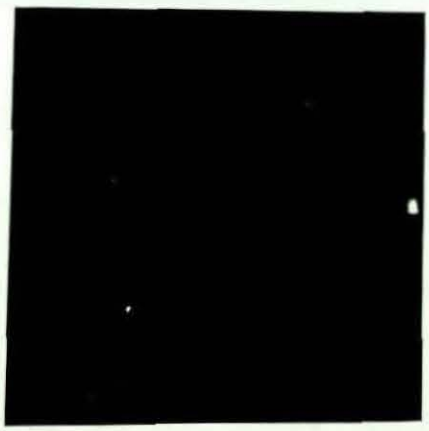

(e) Cerium Image

Figure 90 SIMS Ion Images for Iron H

(Figure continues over page)

(f) Carbon Image

(g) Carbo-nitride (CN) Image

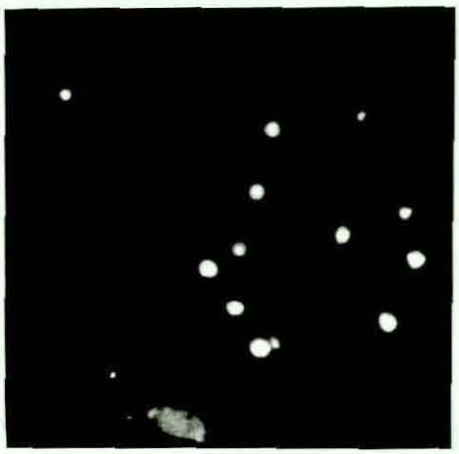

(h) Sulphur Image

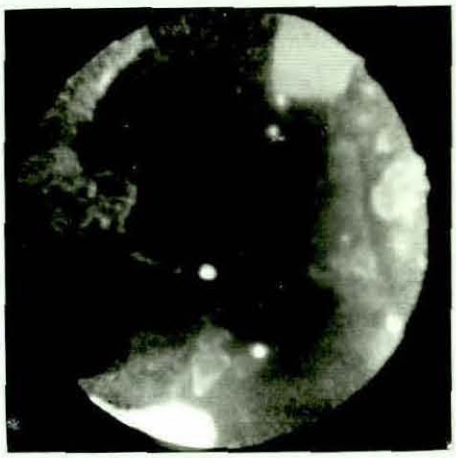

(i) Oxygen Image

Figure 90 Continued

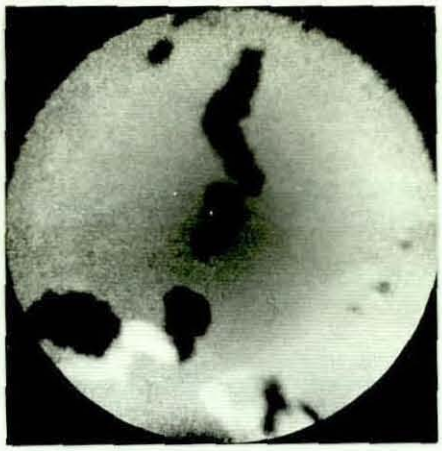

(a) Iron Image

(b) Titanium Image

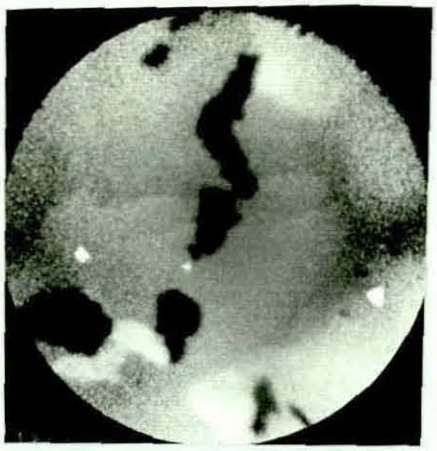

(c) Aluminium Image

(d) Magnesium Image

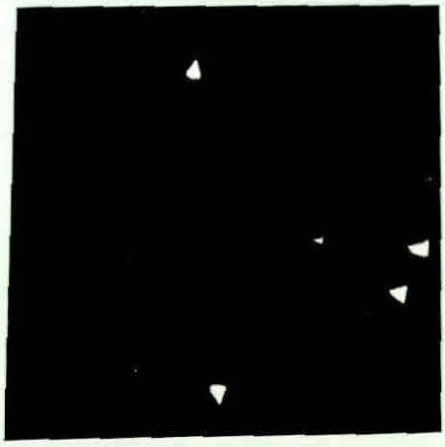

(e) Calcium Image

Figure 91 SIMS Ion Images for Iron I

(Figure continues over page)

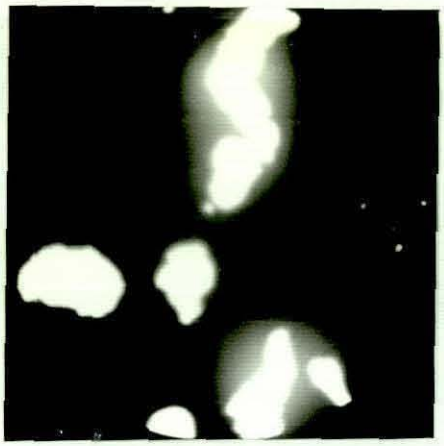

(f) Carbon Image

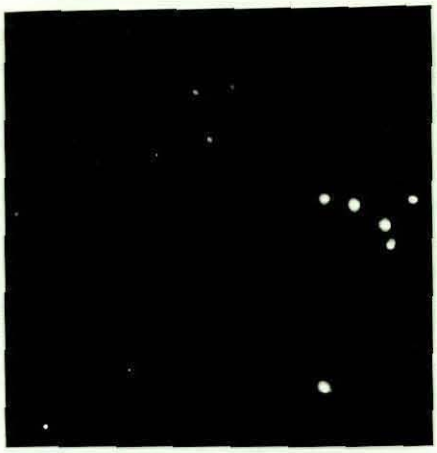

(g) Carbo-nitride (CN) Image

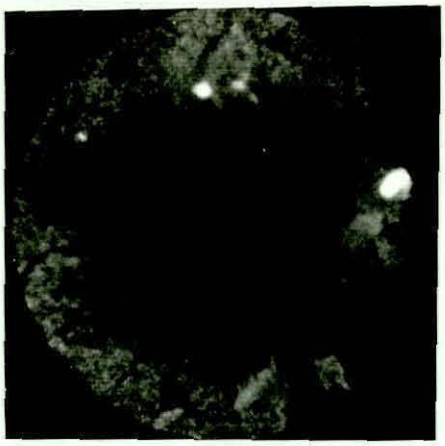

(h) Oxygen Image

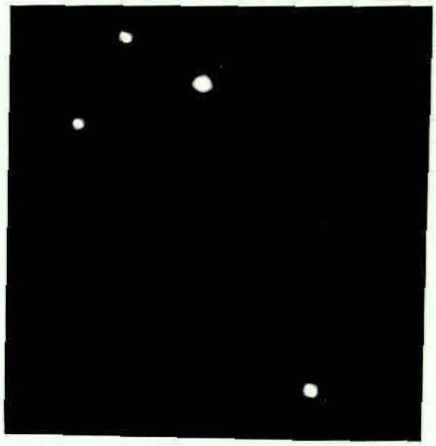

(i) Sulphur Image

Figure 91 Continued

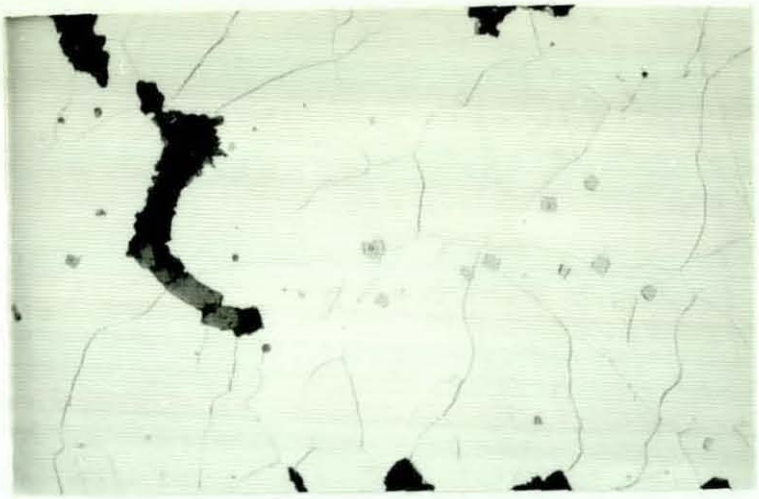

750X

Figure 92 Optical Micrograph Showing Titanium-rich Inclusions in Iron H

10,000X

Figure 93 Titanium-rich Inclusion in Iron F (SEM Image)

magnesium, calcium, oxygen and sulphur is further illustrated in Figure 16 for iron G (magnesium melt treatment).

Figure 91 shows a similar set of SIMS ion images for an area of iron I, which was produced using a magnesium-aluminium melt treatment. In this figure, magnesium again shows some association with one or more of the following: calcium, aluminium, titanium, oxygen, sulphur, and the carbo-nitride molecule.

Many of the titanium-bearing particles represented in Figures 90 and 91 were plainly visible using an optical microscope. For example, Figure 92 shows a distribution of titanium-rich inclusions in iron H, and similar particles with an average diameter of 5μm were observed in all the irons studied. The appearance of one such inclusion in iron F is also shown in Figure 93. The angular morphology suggests that these inclusions are based on titanium carbide or carbo-nitride.

6.3.2.3.4 Calcium-Zirconium

SIMS analysis of iron J, which was produced using a calcium-zirconium melt treatment, revealed that the zirconium distribution showed a high degree of correlation with the titanium, vanadium and calcium distributions in the iron matrix. This is illustrated by a comparison of the ion images for different elements shown in Figure 94. The optical micrograph shown in Figure 95 reveals that the zirconium-rich inclusions had a similar appearance to the titanium-bearing particles observed in the other cast irons (Figure 92), with the exception that many of them contained a darker inner core. Some inclusions in iron J were associated with degenerate forms of graphite, and this is illustrated in Figure 96.

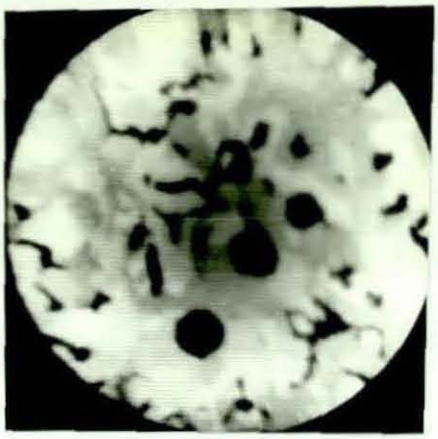

(a) Iron Image

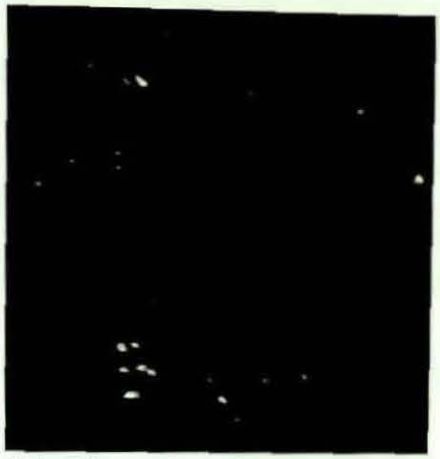

(b) Zirconium Image

(c) Titanium Image

(d) Vananium Image

(e) Calcium Image

Figure 94 SIMS Ion Images for Iron J

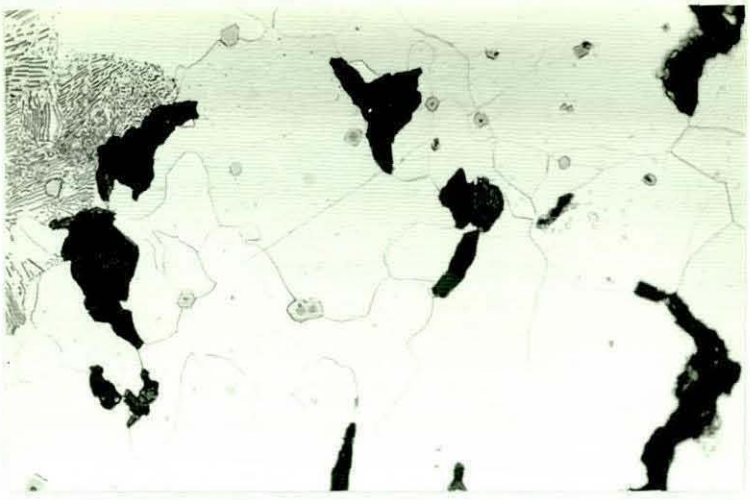

750X

Figure 95 Optical Micrograph of Iron J, Showing Duplex Zirconium-Titanium Inclusions

750X

Figure 96 Association Between Zr-Ti Inclusions and Degenerate Forms of Graphite in Iron J

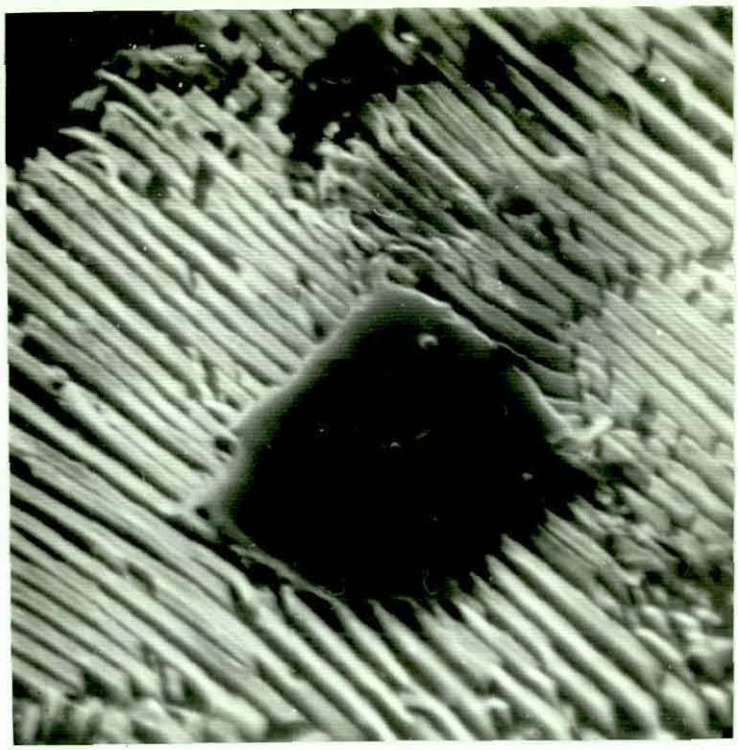

7000X

Figure 97 Duplex Zirconium-Titanium Inclusion in Iron J, Analysed Using Energy-Dispersive X-ray Microanalysis (See Figures 98(a) and 98(b)) (SEM Image)

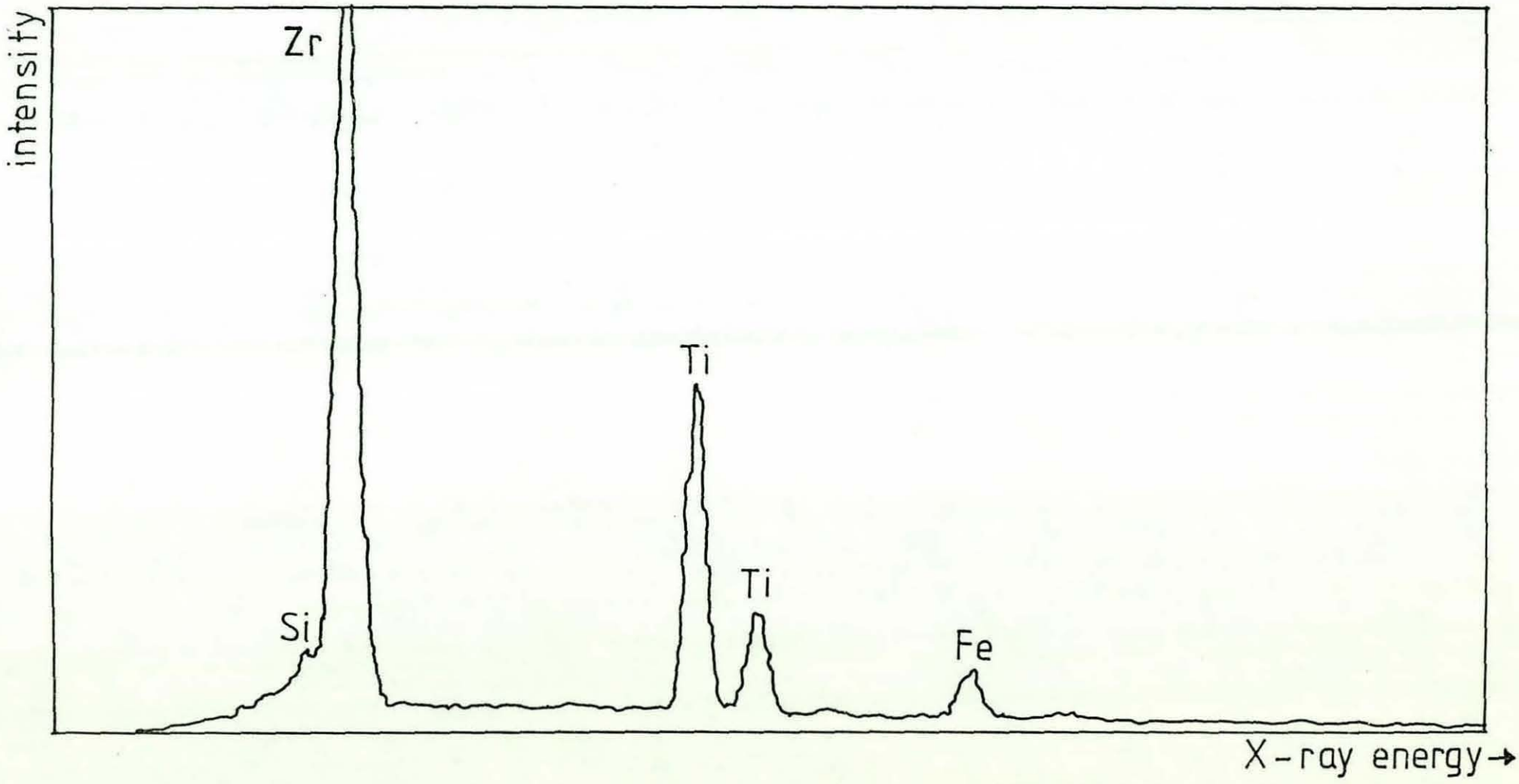

Figure 98. Energy-dispersive X-ray microanalysis of a zirconium-bearing particle in iron J.
98a.: inner region.

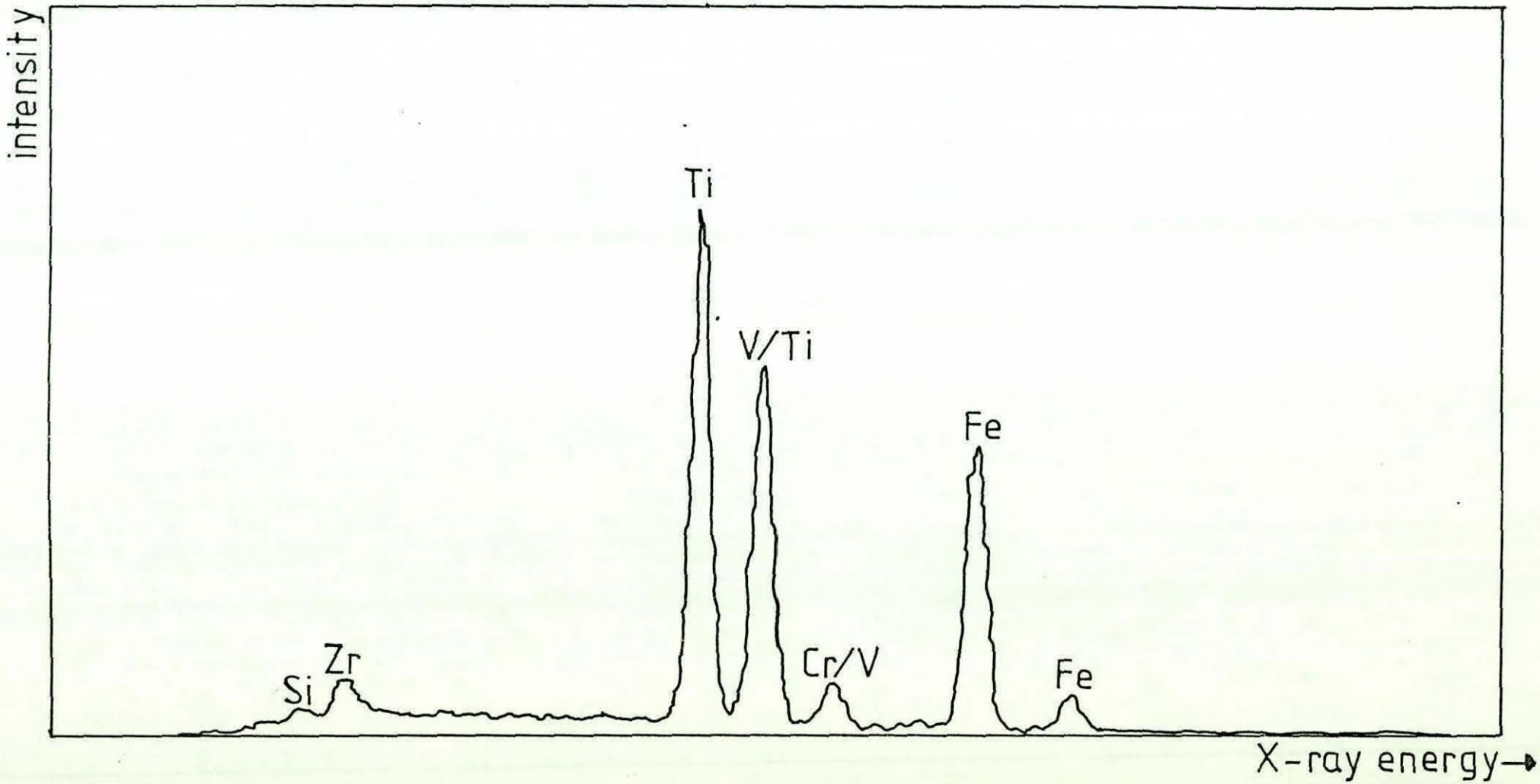

Figure 98 b. : outer region.

In the scanning electron microscope image shown in Figure 97, the inner core of the particle appears lighter owing to a difference between the secondary electron current produced by the inner and outer regions. Energy-dispersive X-ray microanalysis was subsequently carried out in different areas of this particle and the results are shown in Figures 98a and b. The energy spectrum for the inner region exhibits a large zirconium peak and a smaller titanium peak. In comparison to this, the outer area exhibits larger titanium, vanadium, chromium and iron peaks, and a smaller zirconium peak. As explained previously, the volume of material analysed using the X-ray microanalysis technique is approximately 2μm in diameter, and some of the smaller peaks shown in Figures 98a and 98b could be due to a small overlap between the area of interest and the adjacent region. It can be concluded, however, that the inner area of the inclusion contained a large percentage of zirconium, whereas the outer region contained comparatively greater percentages of titanium, vanadium and chromium.

6.4 Summary of Elemental Distributions Results

6.4.1 Graphite Phase

6.4.1.1 Flake Graphite (Iron A)

Oxygen and sulphur were concentrated at the flake graphite/iron interface. Oxygen enrichment (at a lower level than at the interface) was also detected throughout the interior of the graphite flake.

In a composition-depth profile through a graphite flake positioned with the 'c' axis approximately parallel to the impinging ion beam, the sulphur signal exhibited periodic behaviour.

The flake graphite also contained calcium and the results indicate that the level of this element in the graphite phase was greater than that in the surrounding iron matrix.

6.4.1.2 Nodular and Compacted Graphite

The levels of sulphur and oxygen present in the graphite phase were lowest for the spheroidal and compacted forms and highest for the flake form.

In some irons, rare earth elements were concentrated in the central part of graphite nodules exhibiting the duplex structure. At least some of these elements appear to have occurred in the form of carbides. Compacted graphite present in the same specimens contained lower rare earth concentrations.

The calcium enrichment observed within graphite spheroids was non-uniform. In some nodules, the calcium was associated with sulphur and oxygen. Compacted graphite exhibited a slightly lower calcium signal than adjacent nodules in the same sample.

Nodular and compacted graphite were not found to contain general enrichments of magnesium, titanium, aluminium or zirconium.

The outer regions of duplex nodules contained iron-rich inclusions.

A particle believed to represent the nucleus of a graphite nodule contained lanthanum, cerium, praseodynium, neodymium, calcium, aluminium, silicon, iron and sulphur.

6.4.2 Iron Matrix

Manganese sulphide inclusions were present in the iron matrix of iron A (untreated base iron).

Rare earth elements occurred in discrete particles situated predominantly in pearlitic areas of the iron matrix. In irons B and C, these inclusions additionally contained one or more of the following: oxygen, sulphur, phosphorus, carbo-nitride (CN), calcium, titanium, vanadium, chromium. In irons E and F, the inclusions showed less association with sulphur and oxygen, but usually contained titanium, vanadium and chromium. There was also some evidence that the latter particles were carbo-nitride compounds.

Calcium-rich particles were commonly associated with sulphur, and sometimes one or more of the following elements: oxygen, cerium, titanium.

Magnesium-rich particles occurring in irons D, G and I contained one or more of the following additional elements and molecules: titanium, calcium, cerium, aluminium, oxygen, sulphur, carbo-nitride (CN).

Titanium-rich inclusions had the characteristic morphology of titanium carbide/carbo-nitride compounds.

In duplex-structured particles occurring in iron J, the inner region was comparatively rich in zirconium whereas the outer part contained a greater proportion of titanium, vanadium and chromium.

CHAPTER 7

DISCUSSION

7. DISCUSSION

7.1 The Structure of Graphite

7.7.1 Spheroidal Graphite

Certain of the results obtained using polarised light microscopy indicate that the nodular graphite form is composed of a number of individual crystallites radiating from a common area in the centre of the spheroid. These crystallites were often curved and frequently intersected with each other (Figures 44 and 45), supporting Morrogh's (26) proposal that the crystallites become curved and twisted during growth.

The protuberances visible on the imperfect nodule shown in Figure 41 may represent the ends of these crystallites. However, this effect was only rarely observed and the graphite normally exhibited a more spherical appearance giving little indication of the internal structure (eg Figure 40).

Figures 40, 41 and 42 also suggest the presence of a layered arrangement of graphite laths at the spheroid surface. Since it is well established (15, 16, 17, 55) that at the nodule periphery the basal planes are oriented predominantly at right angles to the spheroid radii, these graphite laths must have grown mainly in the 'a' axis direction and are essentially basal plane laminae. The possibility of an 'a' axis growth mechanism occurring in spheroidal graphite is further supported by recent work carried out by Purdy and Audier (17). The latter research involved high resolution lattice imaging of graphite using transmission electron microscopy and indicated the presence of an amorphous carbon phase in the neighbourhood of growth steps on the surface of graphite spheroids. Assuming this was not an effect caused during specimen preparation,

a possible interpretation of this observation is that a lateral growth process in the 'a' axis direction occurs through the deposition and subsequent crystallisation of the amorphous carbon.

Further information on the internal structure of spheroidal graphite was provided by ion-etching the sectioned surface of graphite nodules in situ in plane polished samples of cast iron. On the basis of the previously discussed observations of graphite laths on the spheroid surface, it is likely that the patterns revealed by the ion etching indicate the boundaries between individual graphite layers or laths within the crystallites. In one nodule, (Figure 48), which was more heavily etched than similar examples, it appears that a number of the inter-crystallite boundaries have also been revealed.

The surface relief patterns produced by the ion bombardment (Figures 48 to 53) confirm certain of the observations reported by Hunter and Chadwick (1) and others (2, 4, 31, 32, 54). In particular, the experiments showed that suitably-etched graphite nodules exhibit a pattern of either concentric rings (Figures 48 and 49) or chevrons (Figures 50, 51 and 52), and that with the latter effect, the chevron angle is greater at the periphery of the nodule than towards the centre. It has been shown by Hunter and Chadwick (1) that the concentric ring and chevron patterns are representative of non-diametral, and diametral or near-diametral spheroid sections respectively.

As explained previously, the revised version of Morrogh's model for nodular graphite growth suggested by Double and Hellawell (3, 34) is clearly able to predict the above phenomena, and the inherent chevron present in the proposed cone-helix crystallite (Figures 6

and 7) gives obvious correlation with the chevron pattern observed experimentally.

It is also interesting to note that with increasing additions of nodularising elements to an initially untreated base iron (Figures 15a and 33), the flake graphite present in the microstructure initially becomes finer and more curved (Figures 15b and 36). This implies that the progressive removal and/or prevention of sulphur and oxygen adsorption on the graphite initially leads to an increase in the ability of the graphite flakes to bend and curve while still growing locally in the 'a' axis direction. This phenomenon has also been noted by Sadocha and Gruzleski (62). Since the further addition of nodularising elements eventually results in compacted and spheroidal graphite formation (Figures 15c, d and e and Figures 38 and 40), this supports the possibility of a highly curved 'a' axis growth mechanism (such as that proposed by Double and Hellawell) occurring in spheroidal graphite.

On the above basis, Double and Hellawell's proposed refinement of Morrogh's model for spheroidal graphite growth is clearly favoured over the original model suggested by Morrogh (Figure 3 (26)). As explained previously, the latter model cannot adequately account for all of the phenomena observed experimentally in etched graphite nodules.

The duplex structure which was observed in graphite nodules (Figure 45) has been attributed to a two-stage growth process that occurs when the local melt composition in the region of the growing spheroid is hypereutectic. In this mechanism, the initial growth of the nodule takes place in contact with the melt and the second stage

(which produces the outer halo) occurs by the solid state diffusion of carbon after the nodule is surrounded by austenite (18, 36, 37, 69). This suggestion is supported by the observation of iron-rich inclusions in the outer region (Figures 80 and 81), which have been predicted by Oldfield et al (27). It has also been shown that the thickness of the outer shell is comparable with that which would be expected on the basis of carbon diffusion from the surrounding austenite (36, 37).

7.1.2 Compacted Graphite

Figures 54 and 55 indicate that the basal planes in compacted graphite are predominantly aligned parallel to the major growth direction, as with the flake graphite morphology. In contrast, the results of ion etching experiments carried out by Liu et al (51) and Pan et al (43) appear to suggest that compacted graphite grows predominantly along the 'c' axis. This proposal is doubted because in the present research as well as in several other publications (2, 4, 11, 30, 31), the traces revealed by the ion etching had a shallower and less rugged appearance compared to those shown by Liu et al and Pan et al. The features which were assumed by these investigators to indicate the basal plane structure are in fact similar to artefacts observed in the present research and attributed to surface cracks formed on the graphite during the polishing of the specimens. Several of these artefacts are visible in Figures 55, 56 and 57. This suggests that the results of the present experiments indicate the true basal plane orientation in compacted graphite.

Electron diffraction studies carried out by Itofuji et al (55) have confirmed that most of the surface of a compacted graphite particle is composed of basal planes. In addition, it has been shown in the

present research and in other works (15, 16, 17, 55) that in the peripheral regions of graphite nodules, the basal planes are similarly aligned parallel to the graphite surface. This clearly also applies to flake graphite with its well-established 'a'-axis growth habit, and can be attributed to the anisotropy of the graphite crystal structure: the average bond strength between the carbon atoms in the (0001) basal plane is in the regions of 420-500 kJ mol^{-1} (5), whereas these planes are relatively weakly inter-bonded by Van der Waal's forces of only 4-8 kJ mol^{-1} (5). This indicates that it would be energetically more favourable for the basal planes to form the surfaces of graphite structures.

Figures 56 and 57 additionally suggest that the basal planes remain oriented parallel to the graphite surface even at the end of the compacted graphite. Again, these results are confirmed by the electron diffraction studies reported by Itofuji et al (55), and this phenomenon has also been predicted by a number of other researchers (45, 56, 57). For the reasons discussed above, this behaviour would be expected since it would allow a minimum graphite-iron interfacial energy to be attained on termination of the compacted graphite growth period.

7.1.3 Hybrid Compacted/Nodular Graphite Particles

The occurrence of graphite structures exhibiting both compacted and nodular graphite characteristics (Figures 58a, b, c and d) is consistent with suggestions that the compacted graphite structure develops following the degeneration of spheroidal graphite particles (43, 46). However, these results initially appear to weaken the argument for a growth direction which is predominantly along the 'a' axis in compacted graphite. This is because the formation of the

hybrid structure would, on the above basis, imply that a sharp change in the crystallographic growth habit must occur at some stage in the growth process. However, certain other experimental observations indicate that the latter phenomenon is not uncommon in compacted graphite growth. For example, Figure 55 demonstrates that the basal plane orientation can change readily to accommodate variations in the growth direction of a distorted compacted graphite particle. In addition, Figure 57 shows that a branch in the compacted graphite structure is accompanied by a corresponding shift in the alignment of the basal planes. These observations suggest that similar changes in the basal plane orientation are possible during the formation of hybrid compacted/spheroidal graphite structures.

7.2 The Influence of Solute Elements

7.2.1 Sulphur and Oxygen

Sulphur and oxygen are the most important elements in graphite morphology control, and although they are often assumed to behave in a similar manner, there is some evidence to suggest that this may not in fact be the case (5, 6, 8, 58). In the present experiments, both elements were shown to concentrate at the flake graphite/iron interface in agreement with the results of Johnson and Smartt (58, 59). However, Figure 60 indicates that a uniform oxygen level is also maintained throughout the graphite phase. This suggests that it is oxygen rather than sulphur which is most likely to adsorb on the prism plane of the graphite, thus promoting the flake graphite morphology by producing a non-faceted interface with a high growth velocity. This is also supported by a comparison of the carbon-oxygen and carbon-sulphur bond energies (1077 $kJmol^{-1}$ and 699 $kJmol^{-1}$ respectively (63)) which suggests that oxygen would

adhere more strongly than sulphur to the prism plane. Although further research would clearly be required to verify this hypothesis, it does offer a possible explanation for the higher oxygen signal from the central part of the flake graphite. A similar mechanism would be expected to operate in compacted graphite, which was shown to grow predominantly along the 'a' axis of the graphite crystal lattice as with the flake form. The oxygen and sulphur levels in compacted graphite were found to be significantly less than in the flake morphology owing to the lower activities of these elements in the metal resulting from the melt treatment processes. It is interesting to note that sulphur and oxygen were also detected in spheroidal graphite. Initially, this appears to contradict the view that neutralisation of the influence of oxygen and sulphur is a prerequisite for the production of nodular graphite iron. However, even assuming that equilibrium was established in the various reactions considered important in graphite morphology control, the melt will still contain oxygen and sulphur in solution at concentrations which may well be within the detection limits of SIMS. Thus it appears to be a feature of this highly sensitive technique that the relatively lower sulphur and oxygen levels in spheroidal graphite could be observed.

The periodicity of the sulphur signal revealed by depth profiling is a particularly interesting feature of the graphite flakes. This can be interpreted on the basis of the substructure within the graphite phase where each flake is built up of a number of laminae each having a thickness of a few microns. As discussed previously, analogous substructures were observed in compacted and nodular graphite particles after ion bombardment of the graphite surface, and Hunter and Chadwick (1) revealed the substructure in flake

graphite by means of a thermal etching technique. The results of experiments carried out by Purdy and Audier (17) using high resolution transmission electron microscopy additionally indicate that graphite flakes contain regions of imperfect crystallinity alternating with volumes of amorphous carbon. It was suggested that the stability of the latter was due to the segregation of impurity elements such as oxygen and sulphur. The periodic sulphur signal can therefore be tentatively attributed to the concentration of this element at the interfaces between the individual graphite layers. The segregation of sulphur to these areas would be expected on the basis of the well established surface activity of this element, and it is suggested that although some sulphur may adsorb on the graphite in a similar fashion to oxygen, the primary influence of sulphur occurs in the interfacial regions.

7.2.2 Rare Earth Elements

The occurrence of numerous rare earth sulphide/oxide/phosphide particles in the iron matrix of the compacted and nodular graphite irons produced using mischmetall treatment is consistent with the highly negative free energies of formation for these compounds. Taking into account the free energies of solution of the individual components in iron, the values for the reactions between cerium and sulphur and cerium and oxygen in liquid iron at a temperature of 1600°C are given below:

$$(\%Ce) + (\%S) = CeS(s) \quad ,\Delta G = -564.8 \text{ kJmol}^{-1} \quad (126, 148, 149)$$

$$(\%Ce) + 2(\%O) = CeO_2(s) \quad ,\Delta G = -1017.0 \text{ kJmol}^{-1} \quad (126, 149, 150)$$

These results suggest that in the absence of other nodularising elements such as calcium and magnesium, a major function of the rare earths in cast iron is to desulphurise and deoxidise the melt so

that less free sulphur and oxygen are available to promote flake graphite growth.

One inclusion which contained a number of rare earth elements in addition to calcium, aluminium, silicon, iron, and sulphur, was also found in the centre of a graphite nodule in iron B (Figures 69 and 70). Similar observations have been reported in a number of publications (8, 33, 49, 64-67), in which it was suggested that the inclusions act as heterogeneous substrates for graphite nucleation. For the reasons explained previously, it is unlikely that the nature of the nucleus can exert a lasting influence on the graphite morphology, although the number of nuclei present in the melt is clearly important.

The concentration of rare earth elements in the inner part of the duplex nodule structure (eg Figures 66, 67 and 68) has also been detected by Taran et al (68) using electron probe microanalysis. It is also interesting to note that in spite of the spatial resolution problems associated with the autoradiography technique (75), Lyubchenko et al (32) produced a similar result using this method. Taran et al were unable to detect cerium enrichment in the compacted graphite, and again, it is a feature of the high sensitivity of SIMS that the comparatively lower levels of this element in the compacted form were observed in the present research. As the enhanced rare earth signals are restricted to the inner nodule region, this local concentration of rare earth elements must occur during the period of time when the graphite is surrounded by liquid iron. It is also apparent from the appropriate binary phase diagrams (95), that the liquid iron becomes enriched in rare earth elements as solidification progresses, and that similar behaviour would be expected of sulphur and oxygen. It may therefore be concluded that

as the activities of the rare earths in the liquid increase, the thermodynamics of reactions involving the precipitation of rare earth compounds on the graphite substrate become more favourable. On this basis, it seems probable that at least some of the rare earth concentration in the inner region of the graphite can be attributed to the above effect.

Of the possible compounds involved, the rare earths oxides and sulphides have highly negative free energies of formation and are therefore very stable. The values for the appropriate reactions between cerium, sulphur and oxygen in solution in iron have been given previously. With regard to the rare earth carbides, a comparison of the above data with that for the formation of cerium dicarbide (which is the most stable of the cerium-carbon compounds (125)), indicates that the latter is comparatively less stable at temperatures at and below those used for the melt treatment processes in these experiments. For example, at 1600°C:

$(\%Ce) + 2(\%C) = CeC_2(s)$, $\Delta G = -321.3$ kJmol^{-1} (125, 126, 127)

(c.f. -564.8 kJmol^{-1} for CeS, and -1017.0 kJmol^{-1} for CeO_2)

In comparing the thermodynamics of these reactions, it is important to note that the free energy changes relate to equilibrium conditions which do not necessarily exist in a cast iron melt. On this basis, the occurrence of rare earth carbide compounds may be feasible in regions where the carbon activity approaches unity. The observation of peaks at masses corresponding to rare earth carbides (eg LaC, mass 151; CeC, mass 152) and dicarbides (eg LaC_2, mass 163; CeC_2, mass 164) in Figure 67 (centre of a duplex graphite nodule) appears to support the latter proposal. As explained previously, the rare earth oxides (eg CeO, mass 156) which are also

indicated in this figure, probably formed spontaneously as a result of interactions between elemental rare earths and the O_2^+ primary ion beam.

The result that the enhanced cerium signal occurred to a lesser extent in compacted graphite than in adjacent duplex nodules may be attributed to the different solidification characteristics of compacted and spheroidal graphite. In the growth of the inner part of a duplex nodule, the graphite is completely surrounded by liquid, whereas with the compacted form, only a relatively small proportion of the graphite is in contact with the melt (ie the growing tip). This may cause a significant difference in the level of rare earth compound adsorption occurring on the graphite.

It has been suggested in a number of publications that nodularising elements, including cerium, have a direct influence on the graphite growth process (12, 13, 14, 68). For example, Hillert and Lindblom (12) and Taran et al (68) suggest that nodulariser atoms adsorb on the graphite crystal and, by aiding the development of crystal defects, promote the defect-assisted growth mechanism of spheroidal graphite. However, no direct evidence to support this proposal has been reported and, as explained above, the enrichment of rare earth elements in the graphite phase may be attributed to the precipitation of compounds on the graphite, which acts as a heterogeneous nucleation site. The observations of rare earth sulphide and oxide particles in the iron matrix of cast irons indicate that the primary role of the rare earths in the graphite growth process is to control the dissolved sulphur and oxygen contents of the melt.

The high chilling tendency noted with irons produced using cerium mischmetall additions greater than 0.12-0.13% can be attributed to high residual levels of the individual rare earth elements in solution in the iron. As noted in chapter 4, the Henrian interaction parameters of the major constituents of mischmetall on carbon in liquid iron have been reported to be negative (eg at 1600°C, $e_C^{Ce} = -0.10$; $e_C^{La} = -0.10$ (121)). The presence of the rare earths in solution in the iron therefore increases the amount of carbon that can remain dissolved in the iron for a given carbon activity and reduces the quantity of this element which precipitates out as graphite. This leads to the eventual predominance of the iron-cementite reaction over the iron-graphite reaction. With lower mischmetall treatment levels, less of the rare earths addition is held in solution because of the preferential formation of compounds with solutes such as sulphur and oxygen. This accounts for the observation that cerium mischmetall treatment levels less than around 0.12% had little effect on the chilling tendency.

With regard to the mischmetall-calcium treated irons, the observed lack of rare earth sulphide and oxide particles in these samples is difficult to explain on the basis of equilibrium thermodynamics unless the reaction kinetics are also taken into account. For example, at a temperature of 1600°C, the free energies of formation for cerium and calcium sulphides are given by:

$$(\%Ce) + (\%S) = CeS(s) \quad ,\Delta G = -564.8 \text{ kJmol}^{-1} \qquad (126, 148, 149)$$

$$(\%Ca) + (\%S) = CaS(s) \quad ,\Delta G = -378.7 \text{ kJmol}^{-1} \qquad (127, 148, 149)$$

Consideration of this data alone implies that the formation of cerium sulphide is thermodynamically the most favourable of the above compounds. However, other information must also be taken into

account when comparing these values. For example, cerium and iron are completely soluble in each other in the liquid state (149), whereas the solubility of calcium in liquid iron is extremely low ($< 10^{-4}$ wt % at 1600°C (95)). Because of the latter, the activity of the calcium in solution would be high, and this factor would favour the calcium-sulphur and calcium-oxygen reactions in liquid iron. In addition, calcium has a vapourising point of 1487°C and will therefore be in a gaseous state at 1550°C, whereas cerium, with a vapourising point of 3467°C, will be a liquid at this treatment temperature. The kinetics of the calcium-sulphur reaction will therefore be appreciably more favourable than the cerium-sulphur reaction, and this also applies to the corresponding oxide formation reactions. These factors account for the greater number of calcium sulphide and oxide precipitates compared to the number of cerium compounds of the same type detected in cerium mischmetall-calcium treated irons.

Under the above conditions, one function of the rare earths in graphite morphology control appears to be due to their effect on elements such as titanium. In nodular iron production using magnesium additons, a small amount of cerium is often incorporated into the treatment alloy for its ability to neutralise the deleterious influence of elements including titanium, which could otherwise cause degeneration of the spheroidal graphite shape. In this respect, the SIMS analysis showed that in the mischmetall-calcium treated irons, cerium shows a large degree of association with titanium, and may therefore be expected to reduce the influence of the latter element on the graphite growth process. The mass spectrum shown in Figure 88a indicates that the inclusions formed may contain carbo-nitride compounds.

7.2.3 Calcium and Magnesium

The general enrichment of calcium which is often observed in the graphite phase irrespective of the graphite morphology suggests that this element does not have a direct role in graphite shape control. In addition, the correlation between the calcium, oxygen and sulphur traces recorded in one spheroid (Figure 72) indicates that discrete sulphide/oxide precipitates may be responsible for at least some of these calcium enrichments. This is supported by the results shown in Figures 76 and 77, which show that the calcium distribution is not uniform throughout the graphite phase. Numerous calcium sulphide and oxide inclusions also occurred in the iron matrix of most of the irons studied. On the basis of these results, the major role of calcium in the nodularisation process appears to be through desulphurisation and deoxidation of the melt.

Similarly, the association of magnesium with sulphide and oxide particles indicates that under the experimental conditions used, magnesium also functions primarily by the above mechanism. In contrast to the present research, the results of Fidos (70) indicate a slightly increased magnesium signal in graphite spheroids from a cast iron treated with nickel-magnesium and boron. Because of the similarity between the analysis method used by Fidos and the SIMS technique employed in the present research, Fidos' results cannot be attributed to an effect of the matrix on the secondary ion yield for magnesium. Consequently, it appears that this element can be enriched in graphite nodules under certain conditions. Further research is clearly required to study this effect and its influence, if any, on the graphite growth process.

7.2.4 Titanium, Aluminium and Zirconium

The SIMS analysis of iron H, which was produced using a magnesium-titanium melt treatment, showed that several inclusions occurring in the iron matrix contained titanium in addition to magnesium and calcium. Similar coincidences were revealed between the elements magnesium, calcium, aluminium and titanium in iron I (magnesium-aluminium treatment), and calcium, zirconium, titanium and vanadium in iron J (calcium-zirconium treatment). In addition to these elements, some particles contained sulphur, oxygen and/or molecular carbo-nitride. These results suggest that the abilities of titanium, aluminium and zirconium to reduce the nodularising effects of magnesium and calcium additions may be partly attributed to chemical combinations between these elements, involving the formation of carbide and carbo-nitride compounds. Because of the wide range of elements identified in the particles, it is likely that some inclusions contained a variety of compounds which formed on the same substrate. Further work would be required to determine the exact chemical nature of the compounds involved.

In contrast to the results reported by Hrusovsky (57) and Su et al (45), aluminium was not found to occur in the graphite phase under the present experimental conditions. This indicates that this element does not have a direct influence on the graphite growth process. Titanium and zirconium were also not normally associated with the graphite, although in thin casting sections, zirconium carbo-nitride particles were occasionally situated in areas of the microstructure which contained degenerate spheroidal and compacted graphite. A similar observation involving titanium carbide inclusions has been reported by Sawyer and Wallace (100). It is likely that these particles are segregated at the solidification

front of the growing austenite rather than being evidence of a direct effect of titanium and zirconium in graphite morphology control.

In grey irons, titanium, aluminium and zirconium promote the formation of pro-eutectic austenite dendrites and refine the dendrite structure (23, 91, 92, 93). The reasons for these effects are not well established although it has been suggested that the carbides, nitrides and carbo-nitrides of these elements provide suitable substrates for the nucleation of austenite dendrites prior to the solidification of the austenite-graphite eutectic. This behaviour would appear likely on the basis that the titanium carbo-nitride particles form in the melt prior to solidification of the bulk of the cast iron (94). Furthermore, the formation of these inclusions would lower the local carbon content of the melt, enabling austenite dendrite nucleation to occur at a higher temperature than would normally be possible.

Although the promotion of austenite dendrite formation would be expected to reduce the undercooling because of the latent heat released by austenite growth, titanium, aluminium and zirconium actually increase the undercooling in grey cast irons (23, 91, 92, 93). One reason for this, at least in the case of titanium (92), is that this element has a detrimental effect on the graphite nucleating conditions in a grey iron melt. It has been suggested (92, 151) that this is due to the formation of titanium sulphide inclusions which, unlike manganese sulphide, are not effective substrates for the nucleation of graphite. Since a value for $e_C^{Ti} = -0.16$ has been reported (121), the undercooling must also be increased due to the influence of titanium on the amount of carbon

that is retained in solution in the iron. It has further been suggested by Minkoff (152) that the segregation of titanium at the solidification front of the growing austenite would also cause constitutional undercooling at this interface.

In the present study, the addition of titanium and zirconium to the base iron melt led to the formation of ASTM type D flake graphite instead of the larger and less branched type A form (Figures 22 and 27). This behaviour has also been reported in several publications including those of Ruff and Wallace (23, 92). The ASTM type D flake structure is typical of undercooled grey irons and can also be produced by a high cooling rate (Figure 17), which also leads to an increase in the degree of undercooling (20). The graphite which is eventually nucleated in the interdendritic liquid regions is fine and highly branched as a result of the higher driving force for growth and the decrease in the time available for carbon diffusion. The influence of a high cooling rate in addition to titanium or zirconium melt treatment was found to have a cumulative effect on the flake graphite morphology, producing even finer type D graphite than either of these individual factors (Figure 24).

In the commercial production of nodular and compacted graphite cast irons, the occurrence of titanium sulphide is highly unlikely because the free energies of formation for magnesium, cerium and calcium sulphides are comparatively much more negative (153). Since the latter compounds are known to be effective substrates for graphite nucleation, titanium would not be expected to cause a large reduction in the nucleation state of these irons. Thus, the effect of this element on the promotion of undercooling is also lower. Clearly, this would not affect the influences of titanium due to

segregation at the austenite/liquid interfaces and the interaction effect on the carbon in solution. However, it is possible that in nodular and compacted graphite irons, the net influence of this element may be to oppose undercooling by promoting austenite formation and the release of latent heat.

It is well established that in compacted graphite microstructures, a large degree of undercooling caused by a high cooling rate promotes an increase in the nodularity. This is because large driving forces favour the defect-assisted growth mechanism of spheroidal graphite (5). On the basis of the above discussion, it is possible that titanium and zirconium reduce the undercooling in thin sections of compacted graphite castings through their effect on austenite dendrite formation. Although further research would be required to verify this hypothesis, it does offer an explanation for the smaller overall section sensitivity of the magnesium-titanium, calcium-zirconium and magnesium-zirconium treated compacted graphite castings in comparison to those produced using cerium mischmetall-calcium additions. This is also supported by the observation of an interdendritic pattern in the compacted graphite present in thin sections of the calcium-zirconium treated iron (Figures 28b and c), indicating that a large amount of pro-eutectic austenite was present. The high zirconium content employed in the latter treatment (0.3% Zr) compared to the titanium levels used for the magnesium-titanium method (maximum 0.17% Ti) would, on the above basis, account for the difference between the section sensitivities of the CG irons produced by these methods.

The similarity between the behaviour of titanium and zirconium in cast irons is also demonstrated by the occurrence of joint titanium

and zirconium-bearing inclusions in cast irons treated with ZrFeSi. Because the general appearance of these particles was very similar to the titanium carbo-nitride inclusions observed in other irons (Figures 92 and 95), it is probable that they are also carbo-nitride compounds of a more complex nature. The apparent compatability between the zirconium-rich and the titanium-rich regions of the duplex particles would be expected on the basis that these elements have the same crystal structure, similar lattice parameters and are completely miscible in all phases (154). These characteristics also apply to the respective carbides and nitrides of these elements (155, 156). The observation that the inner phase of the duplex inclusion contained a higher concentration of zirconium may be attributed to the higher melting point of this metal compared to titanium, causing the zirconium-rich phase to be precipitated first. Although the binary nitride systems (ZrN-TiN) and carbide systems (ZrC-TiC) form a continuous series of solid solutions, the binary systems involving vanadium and zirconium (ie ZrN-VN and ZrC-VC) have only limited mutual solid solubility (155, 156). Since vanadium was also shown to be present in the titanium-rich outer region of the inclusion, this would account for the formation of two distinct phases in the particles rather than a single phase containing all the elements detected.

7.3 Melt Treatment Processes for the Production of Compacted Graphite Cast Iron

Microstructural examination of the castings produced using various types of melt treatment showed that a compacted graphite structure containing less than 20% of the nodular graphite form is produced over a range of different melt treatment compositions.

7.3.1 Cerium Mischmetall

The most suitable cerium mischmetall addition level for CG iron production was found to be around 0.065% for the experimental conditions used. This contrasts significantly with the addition level of 0.09-0.10% cerium mischmetall used industrially in one foundry (118). This can be attributed to different process conditions. For example, the melt sulphur levels used in the foundry cited above are normally within the range 0.01-0.015%, whereas the average sulphur content of the melts treated only with cerium mischmetall in this study was 0.008%. Consequently, a lower mischmetall addition level was required under the latter condition to desulphurise the melt to a sufficient degree for compacted graphite formation. Other variations in the base melt composition, in addition to factors such as the melt volume, the holding time between treatment and casting, and the various temperatures involved in the production procedures, would also be expected to have some influence on the addition levels required.

7.3.2 Cerium Mischmetall-Calcium

Simmons and Briggs (114) have listed minimum additions of 0.016% cerium and 0.24% calcium for CG iron production using a 0.01% sulphur base iron. These levels are within the respective addition ranges for these components determined in the present research, where the average base melt sulphur content for the compacted graphite castings identified in Figure 13a was also 0.01%. The results of this study also indicate that the treatment composition range for CG iron production using cerium mischmetall and calcium is wider than that suggested in the report by Simmons and Briggs (114). Furthermore, it has also been demonstrated that the compacted graphite structure can be produced by melt treatment with a combination of calcium silicide and calcium fluoride alone.

The observation that the hardness of the 4 mm section of irons treated with calcium was, on average, greater than with castings produced using joint mischmetall-calcium additions, suggests that the latter type of treatment is comparatively more efficient at producing suitable graphite nucleation sites. A low inoculation efficiency for calcium is also indicated by the result that for the same zirconium addition level, a casting produced by calcium-zirconium treatment showed greater chilling in the 4 mm section compared to one produced using magnesium and zirconium additions. A large number of graphite nucleation sites also promotes a high level of nodularity in the final microstructure (43, 128, 131, 132). This would explain why a high percentage of calcium in the joint mischmetall-calcium treatment was found to result in a comparatively low level of nodular graphite in thin sections of compacted graphite castings.

7.3.3 Magnesium

As predicted in several publications (82, 83, 84), the production of CG iron using magnesium additions proved to be difficult owing to the very close control required with the process conditions and the residual magnesium content of the treated iron. The difference between under- and over-treatment was found to be less than 0.01% residual magnesium, and Evans and Dawson (82) have suggested that this range may in fact be as small as 0.005%. The production difficulties occur as a result of the low boiling point of magnesium (1107°C), which causes this element to be in a vaporous state at the treatment temperature. This leads to a swift and violent reaction in the ladle, rapid fading, and a heightened sensitivity to variations in the process conditions. These problems can be managed by using the Inmold treatment process (108-111), although an

investigation of this method was outside the scope of the present research programme.

7.3.4 Magnesium-Titanium

The use of titanium in conjunction with magnesium resulted in a considerable increase in the range of magnesium addition levels for which the compacted graphite morphology was produced. This is in agreement with the results published in a number of reports (eg 82, 138). This effect of titanium may be explained by assuming that the formation of the titanium carbo nitride compounds containing magnesium becomes progressively more likely as the magnesium content increases. Although thermodynamic data on the formation of these compounds are not available, it is not likely that their free energies of formation are more negative than for magnesium sulphide or magnesium oxide. Thus with small magnesium and titanium additions (where the magnesium level is not sufficient to desulphurise and deoxidise the melt to the degree required for complete nodularisation of the graphite phase), the magnesium reacts preferentially with sulphur and oxygen, producing compacted graphite cast iron. At higher magnesium addition levels, the formation of magnesium-titanium compounds may become feasible, which would be expected to reduce the nodularising effect of the magnesium.

On this basis, the deleterious influence of titanium on the magnesium nodularisation process would only become significant when both the magnesium and the titanium levels are above certain values. The latter would depend on the quantities of dissolved sulphur and oxygen in the melt and the relative thermodynamic stabilities of the oxides, sulphides, and magnesium-titanium compounds. This proposal

is supported by the observation that magnesium additions of around 0.045% produced compacted graphite irrespective of the presence of up to 0.18% titanium in the melt. Furthermore, Lux (22) reports that for nodular iron production using pure magnesium, the titanium content of the melt can be as high as 0.04-0.08% before the effect of the titanium becomes important. This is in broad agreement with the results of this study, which indicated that only residual titanium contents above 0.05-0.06% had a significant despheroidising influence in the compacted graphite irons treated with more than 0.07% magnesium.

Evans and Dawson (82) report that for a base iron containing less than 0.02% sulphur, suitable residual magnesium and titanium contents for CG iron production are 0.015-0.035% and 0.06-0.13% respectively. In the present study, the limiting residual magnesium levels for compacted graphite iron production in the 25 mm section of the casting were found to be 0.007% minimum and 0.028% maximum for a titanium level greater than 0.06%. Again, the difference bewteen these results and the corresponding values reported by Evans and Dawson, may be attributed to the low average base melt sulphur content of 0.006% in the magnesium-titanium treated castings produced in the present work. The results also showed that under the experimental conditions used, titanium levels at least as great as 0.18% could be tolerated with a minimum residual magnesium level of 0.007%.

7.3.5 The Development of Melt Treatment Processes

Information on the role of solute elements in the graphite growth process is valuable in the development of new melt treatment practices. The present research has identified the distributions of several

elements which are important in this respect, and it is clear from the results that the control of sulphur and oxygen must be the primary consideration when deciding which additives to use in the production of different graphite morphologies.

With regard to compacted graphite iron production, the nodularising elements commonly employed include magnesium, calcium, and cerium. The latter is usually added together with other rare earth metals in the form of mischmetall.

Of the above additives, magnesium has a comparatively low vaporisation temperature and is highly reactive at the melt treatment temperature. This causes problems in the control of this element within the residual levels required for satisfactory compacted graphite microstructures. The use of titanium in conjunction with magnesium results in a large increase in the range of magnesium additions over which the desired structure is produced, and also has a beneficial influence on the section sensitivity of the compacted graphite morphology. However, titanium is an undesirable impurity in nodular iron production, and for this reason, scrap from processes which utilise this element as a major component of the treatment alloy must often be isolated, resulting in an increase in the net production cost.

With regard to cerium, the relatively high expense of this element is an immediate disadvantage. Furthermore, the addition levels required for CG iron production using rare earth metals alone can result in excessive carbide formation particularly in thin sections. This means that heat treatment is often a necessary stage in the manufacture of castings, and this also raises the overall production costs in the foundry.

With melt treatment alloys containing calcium as a main constituent, there is a problem that the high addition levels of this element which may be required to produce a significant effect on the graphite morphology may also lead to excessive dross formation. The latter must be avoided if high quality is to be maintained in castings production. The results of the present work also suggest that in comparison with cerium mischmetall and magnesium ferro-silicon, calcium silicide is a less effective inoculating agent. The use of this additive as the sole nodularising component of the treatment alloy may therefore result in poor nucleation conditions unless alternative steps are taken to improve these.

Other problems involved in CG iron manufacture are related to the difficulties of producing the required microstructure in thin sections. The present research has clearly shown that there is scope for experimentation with other additive compositions, and those containing zirconium appear particularly promising. The results indicate that the latter could ease the difficulties associated with compacted graphite formation in thin sections. However, there is a need for further research to be carried out to fully assess the addition levels required for CG iron production, investigate the chilling properties of the irons produced, and determine the harmfulness of residual zirconium in recycled scrap. One immediate disadvantage of zirconium is its high cost, which would limit the use of this element in industrial melt treatment practice.

CHAPTER 8

CONCLUSIONS AND SUGGESTIONS FOR FURTHER WORK

8. CONCLUSIONS AND SUGGESTIONS FOR FURTHER WORK

8.1. Conclusions

8.1.1 Growth and Structure of Graphite

The following conclusions are made on the basis of the optical and scanning electron microscopy results.

(a) In a cast iron microstructure, graphite spheroids are isolated from each other, whereas compacted graphite is interconnected within eutectic cells. The latter effect occurs to a lesser extent than with the flake form.

(b) The growth of spheroidal graphite can be best explained in terms of a mechanism involving local growth predominantly along the 'a' axis of the graphite crystal structure. The cone-helix crystallite model suggested by Double and Hellawell (3, 34) is a refinement of Morrogh's original model for spheroidal graphite growth (26), and appears to offer the best interpretation of the phenomena observed by ion-etching the graphite phase.

(c) In compacted graphite, the predominant overall growth direction is along the 'a' axis of the graphite crystal lattice as with the flake form.

(d) With a compacted graphite casting, a reduction in the section thickness results in an increase in the percentage of perfect and degenerate nodular graphite occurring in the microstructure, and a decrease in the average size of individual graphite particles. With ASTM type A flake graphite microstructures, decreasing the section thickness promotes the formation of ASTM type D flake graphite.

8.1.2 Elemental Distributions and the effect of treatment elements on the graphite morphology

(a) Spheroidal and compacted graphite contain lower levels of sulphur and oxygen than the flake form. In the latter type of graphite, these elements occur predominantly at the graphite-iron interface. Oxygen is also distributed uniformly at a lower level within flake graphite and is considered to adsorb on the prism plane promoting a high interface mobility. In addition, localised sulphur concentrations occur at periodic intervals through the graphite flake and this may be explained in terms of the segregation of sulphur to the interfaces between the individual graphite laminae. This effect is considered to reduce the interfacial energy and encourage the extended interface characteristic of flake graphite iron.

(b) Compacted graphite microstructures can be produced using the following individual and combined melt treatments: magnesium ferro-silicon (5.5% Mg); cerium mischmetall (50% Ce, bal other rare earths); lanthanum mischmetall (65% La, bal other rare earths); calcium silicide (33% Ca); CaSi + cerium mischmetall; MgFeSi + ferro-titanium; MgFeSi + ferro-aluminium (50% Al); MgFeSi + zirconium ferro-silicon (38.2% Zr); CaSi + ZrFeSi. The percentages of these additives required for compacted graphite formation under the conditions used in these experiments are given in Chapter 6. For the same base melt composition and section thickness, the percentage nodularity of the microstructure increases with increasing addition level of the nodularising components.

(c) With a combined cerium mischmetall-calcium silicide melt treatment, the individual effects of these nodularising components on the graphite morphology are cumulative. Increasing the percentage of calcium relative to that of mischmetall in the joint addition is beneficial for reducing the section sensitivity of the compacted graphite produced. The latter may be related to a comparatively lower ability for calcium to promote suitable sites for graphite nucleation.

(d) The use of titanium in conjunction with magnesium melt treatment increases the range of magnesium addition levels for which the compacted graphite morphology is produced. With the base melt composition and process conditions described in Chapter 5, this effect is particularly noticeable with larger casting section thicknesses and with melt titanium contents in excess of 0.06%. Compared to cerium mischmetall-calcium melt treatment, compacted graphite microstructures produced using the magnesium-titanium method are less section-sensitive.

(e) Preliminary experiments have indicated that the section sensitivities of compacted graphite cast irons produced using magnesium-zirconium and calcium-zirconium treatments are less than that for a magnesium-titanium treated casting.

(f) In compacted/spheroidal graphite cast irons produced using rare earth additions alone, the rare earth elements are enriched in the inner regions of graphite nodules exhibiting a duplex structure, and to a lesser extent in compacted graphite. At least some of this enrichment may be attributed to the formation of rare earth carbides. Cerium and lanthanum also

occur in particles associated with one or more of the following: oxygen, sulphur, phosphorous, carbo-nitride, calcium, titanium, vanadium, chromium. These particles are normally situated in or adjacent to pearlitic areas of the iron matrix.

(g) Calcium is distributed throughout the graphite phase in discrete areas where it may occur predominantly in the form of sulphide and oxide inclusions. This phenomenon is not considered to have a direct effect on the graphite growth process.

(h) In compacted/spheroidal graphite cast irons produced using joint cerium mischmetall-calcium melt treatments, the rare earths occur primarily in particles which also contain titanium, vanadium and chromium, but which are not generally associated with sulphur and oxygen. The particles are normally located in or adjacent to pearlitic areas of the iron matrix and are probably carbo-nitride compounds.

(i) Calcium also occurs in discrete particles frequently associated with sulphur and oxygen, and distributed randomly throughout the iron matrix.

(j) In the irons studied in this research, magnesium was not enriched in the graphite phase but occurred in particles associated with one or more of the following: sulphur, oxygen, carbo-nitride, calcium, titanium, cerium, aluminium.

(k) Aluminium, titanium and zirconium are not enriched in the graphite phase.

(l) In compacted/spheroidal graphite irons produced by calcium-zirconium treatment, zirconium occurs in particles which are also associated with calcium, titanium, vanadium and chromium. These particles have a duplex structure, the inner part of which contains most of the zirconium and the outer part, most of the titanium, vanadium and chromium.

(m) From the SIMS and X-ray microanalysis results, a number of suggestions have been made regarding the functions of different elements in the graphite growth process. These are discussed in the preceeding chapter.

8.2 Suggestions for Further Work

8.2.1 The Role of Solute Elements in Graphite Morphology Control

Sulphur and Oxygen

Certain of the results obtained in this research programme indicate that sulphur and oxygen behave differently in cast iron, and it was also suggested that oxygen may be more important than sulphur in graphite morphology control. Further work is clearly required to verify this, and to clarify the individual roles of these elements in the graphite growth process. This is difficult to achieve through the study of commercial cast irons, in which both sulphur and oxygen are normally present.

A possible approach to this problem would be to use pure Fe-C-Si alloys into which controlled amounts of either sulphur or oxygen are introduced. To further improve the purity of the materials, and to avoid contamination of the melt from the atmosphere, the casting process could be carried out in a vacuum or in a neutral gas atmosphere such as helium or argon. The Department's vacuum casting equipment or vacuum tube-furnace would be suitable for this purpose.

Sulphur could be added by mixing iron sulphide with a low oxygen content into the charge material before melting. Oxygen could be introduced by using pure iron oxide and melting and casting in a carbon monoxide atmosphere as described by Kevarian and Taylor (6). The amount of oxygen remaining in the melt at equilibrium would depend upon the partial pressure of the carbon monoxide gas.

By studying separate sulphur and oxygen treated cast irons using optical and scanning electron microscopy in addition to secondary ion mass spectrometry, further information would be provided on the individual roles and influences of these elements in the graphite growth process. To further improve the accuracy of these analyses, the possibility of contamination of the specimen surface prior to SIMS analysis could be reduced by fracturing the cast samples in situ in the vacuum chamber of the instrument. This would require slight modification to the University's existing SIMS facility.

Nodularising Elements

This research has also indicated that the major function of the common nodularising elements is to form compounds with sulphur and oxygen, reducing the effects of these solutes on the graphite morphology. The rare earth elements were also shown to concentrate in certain parts of the graphite phase in nodular and compacted graphite irons. However, it was suggested that this phenomenon has no direct influence on the graphite growth process. Again, experiments using very pure Fe-C-Si alloys may provide further evidence to support the above proposal. It is well established (58, 62, 79, 80, 81) that the nodular graphite morphology can be produced in cast iron if the starting materials are sufficiently pure. The

controlled addition of spectrographically pure cerium to this type of melt should enable any direct effects of this additive on the graphite growth process (for example, improvements in the spheroidal shape) to be studied in greater detail. Microstructural examinations of the cast irons before and after cerium treatment could be correlated with the results of elemental distribution analysis using secondary ion mass spectrometry. The latter technique would also be useful in confirming the absence or presence of sulphide and/or oxide precipitates due to the very low (but perhaps significant) levels of sulphur and oxygen which will still be present in the melt following purification.

Denodularising Elements

A closer study of the way in which titanium, aluminium and zirconium cause degeneration of the nodular graphite shape and promote the formation of compacted graphite would also be aided by using pure starting materials and the vacuum casting method. By producing a spheroidal graphite cast iron melt without the use of nodularising agents, any interaction between these elements and the titanium, aluminium and zirconium added to the melt would be eliminated. In this way, the direct influences (if any) of the denodularisers on the graphite morphology could be investigated.

It would also be beneficial to study how titanium and zirconium affect the section sensitivity of compacted graphite cast irons. Differential thermal analysis could be used to gauge the precise effect of these elements on the cooling curve produced for a range of different cooling rates. The results could subsequently be correlated with the microstructures produced, and examination of specimens rapidly quenched from different stages in the

solidification process would provide information on the effect of titanium and zirconium on austenite dendrite formation.

8.2.2 Investigation of the Production of Compacted Graphite Cast Iron using Calcium-Zirconium and Magnesium-Zirconium Additions

As part of this research programme, a small series of experiments were carried out to investigate the production of CG iron by treatment of a zirconium-bearing melt with calcium and magnesium. Although only a limited number of results were obtained, they indicated that Ca-Zr and Mg-Zr treatment can lead to compacted graphite microstructures which have a low section sensitivity. The latter property is industrially very desirable, but in order to confirm this characteristic and to determine the optimum process conditions it would be necessary to conduct extensive series of melts on the scale of those which were carried out with cerium mischmetall-calcium and magnesium-titanium additions. These experiments could be further improved by relating the nodularity of the graphite structure to the cooling rate of the appropriate section thickness. The latter could be estimated mathematically using finite elements, and measured directly with the aid of thermocouples. It would also be beneficial to investigate the harmfulness of remelting zirconium bearing scrap for the production of nodular and compacted graphite iron, and to compare the mechanical and thermal properties of the zirconium treated CG irons with those for similar materials produced using more conventional methods (eg Mg-Ti treatment).

Should these experiments favour the zirconium-bearing material, they should be followed by trials carried out in a commercial foundry.

REFERENCE LIST

1. Hunter, M J, Chadwick G A. Journal of the Iron and Steel Institute, 1972, **210**, 117-123.

2. Hamasumi, M. AFS Cast Metals Research Journal, 1965, **1**, 9-23.

3. Double, D D, Hellawell, A. In: Proceedings of 2nd Symposium on Metallurgy of Cast Iron, Geneva, Switzerland, May 29-31, 1974.

4. Tsuchikura, H, Kusakawa, T, Okumoto, T. In: Proceedings of 3rd Int Conf on Electron Microscopy, London, 1954, 368-373.

5. Subramanian, S V, Kay D A R, Purdy, G R. Transactions of the American Foundrymen's Society. 1982, **90**, 589-603.

6. Kevarian, J, Taylor, H F. Transactions of the American Foundrymen's Society, 1957, **65**, 212-221.

7. M^{c}Swain, R H, Bates, C E, Scott, W D. AFS Cast Metals Research Journal, 1974, **10**, 181-189.

8. Francis, B. Metallurgical Transactions, 1979, **10A**, 21-30.

9. Fredriksson, H, Wetterfall, S E. In: Proceedings of 2nd Symposium on Metallurgy of Cast Iron, Geneva, Switzerland, May 29-31, 1974.

10. Nieswaag, H, Zuithoff, A J. In: Proceedings of 2nd Symposium on Metallurgy of Cast Iron, Geneva, Switzerland, May 29-31, 1974.

11. Aleksandrov, N N, Milman, B S, Osada, N G, Ilicheva, L V, Andreev, V V. Russian Castings Production, September 1975, 365-366.

12. Hillert, M, Lindblom, Y. Journal of the Iron and Steel Institute, 1954, **176**, 388-390.

13. Basdogan, M F, Kondic, V, Bennett, G H J. Transactions of the Amercian Foundrymen's Society, 1982, **90**, 263-273.

14. Minkoff, I, Nixon, W C. Journal of Applied Physics, 1966, **37**, 13, 4848-4855.

15. Stauss, H E, Von Batchelder, F W, Salkovitz, E I. Journal of Metals, March 1951, 249.

16. Yamamoto, S, Kawano, Y, Murakami, Y, Chang, B, Ozaki, R. Transactions of the American Foundrymen's Society, 1975, **83**, 217-226.

17. Purdy, G R, Audier, M. In: Proceedings of 3rd Int Symposium on Physical Metallurgy of Cast Iron, Stockholm, Sweden, August 29-31, 1984.

18. Morrogh, H, Williams, W J. Journal of the Iron and Steel Institute, 1948, **158**, 1, 306-322.

19. Strizik, P, Jeglitsch, F. AFS Int Cast Metals Journal, 1976, **1**, 23-30.

20. Lui, P C, Loper, C R, Kimura, T, Park, H K. Transactions of the American Foundrymen's Society, 1980, **88**, 97-118.

21. Loper, C R, Voigt, R C, Yang, J R, Sun G X. Transactions of the American Foundrymen's Society, 1981, **89**, 529-542.

22. Lux, B. Giessereiforschung in English, 1970, **22**, No 2 (65-81) and No 4 (158-176).

23. Wallace, J F. Transactions of the American Foundrymen's Society, 1975, 83, 363-378.

24. Johnson, W C, Kovacs, B V, Clum, J A. Scripta Metallurgica, 1974, 8, 1309-1315.

25. Minkoff, I. In: The Preparation and Properties of Solid State Materials, Vol 4, Chapter 1. Ed: W R Wilcox. Marcel Dekker Inc, 1979.

26. Morrogh, H. BCIRA Journal of Research and Development, 1955, 5, 12, 655-673.

27. Oldfield, W, Geering. G T, Tiller, W A. In: Proceedings of Conference on the Solidification of Metals, Brighton, December 4-7, 1967. Iron and Steel Institute Publication No 110.

28. Subramanian, S V, Ghosh, D, Kay, D A R. Iron and Steel Making, March 1980, 18-25.

29. Lux, B, Minkoff, I, Mollard, F, Thury, E. In: Proceedings of 2nd Symposium on Metallurgy of Cast Iron, Geneva, Switzerland, May 29-31, 1974.

30. Mitsche, R, Modl-Onitsch, E M, Dichtl, H J, Muller, E K. Giessereiforschung in English, 1969, 21, 2, 76-84.

31. Zatulovskii, S S, Khusnutdinov, G D, Khorukhin, V Ya, Chermouol, A V. Russian Castings Production, 1968, 9, 406-408.

32. Lyubchenko, A P, Uritskiy, Yu S, Varganov, V V. Russian Metallurgy, 1981, 5, 78-82.

33. Lalich, M J, Hitchings, J R. Transactions of the American Foundrymen's Society, 1974, 84, 653-664.

34. Double, D D, Hellawell, A. Acta Metallurgica, 1974, 22, 481-487.

35. Janowak, J F, Gundlach, R B, Eldis, G T, Rohrig, K. AFS Int Cast Metals Journal, December 1981, 28-42.

36. Lux, B, Mollard, F, Minkoff, I. In: Proceedings of 2nd Symposium on Metallurgy of Cast Irons, Geneva, Switzerland, May 29-31, 1974.

37. Hunter, M J, Chadwick, G A. Journal of the Iron and Steel Institute, 1972, 210, 9, 707-717.

38. Hecht, M, Margarie, J C. AFS Cast Metals Research Journal, 1973, 9, 35-37.

39. Khan, M H. In: Proceedings of 46th International Foundry Congress, Madrid, 1979.

40. Riding, A, Gruzleski, J E. AFS Cast Metals Research Journal, 1971, 7, 162-164.

41. Su, K C, Ohnaka, I, Yamauchi, I, Fukusako, T. In: Proceedings of 3rd International Symposium on Physical Metallurgy of Cast Iron, Stockholm, Sweden, August 29-31, 1984.

42. Gan, Y, Loper, C R. Transactions of the American Foundrymen's Society, 1983, 91, 781-788.

43. Pan, E N, Ogi, K, Loper, C R. Transactions of the American Foundrymen's Society, 1982, 90, 509-527.

44. Htun, K M. AFS Cast Metals Research Journal, 1970, 6, 2, 49-57.

45. Su, J Y, Chow, C T, Wallace, J F. In: Proceedings of 49th International Foundry Congress, Chicago, April 14-17, 1982.

46. Itofuji, H, Kawano, Y, Inoyama, N, Yamamoto, S, Chang, B, Nishi, T. Transactions of the American Foundrymen's Society, 1983, **91**, 831-840.

47. Dinescu, L, Cracium, S, Popescu, M, Haltrich, K, Tarasescu, M. In: Proceedings of 49th International Foundry Congress, Chicago, April 14-17, 1982.

48. Chakrabarti, A K, Banerjee, P. In: Proceedings of Conference on Solidification Technology in the Foundry and Cast House, University of Warwick, Coventry, September 15-17, 1980. Metals Society.

49. Warrick, R J. AFS Cast Metals Research Journal, 1966, **2**, 3, 97-108.

50. Guoging, X, Zongsen, Y, Mobley, C E. Transactions of the American Foundrymen's Society, 1982, **90**, 943-958.

51. Liu, P C, Loper, C R, Kimura, T, Pan E N. Transactions of the American Foundrymen's Society, 1981, **89**, 65-78.

52. Liu, P C, Loper, C R. Scanning Electron Microscopy, 1980, 407-418.

53. Li, C, Wu, D, Ho, Z, Hu, W. Chinese Journal of Mechanical Engineering, 1982, **18**, 2, 58-65.

54. Nechtelberger, E, Lux, B. Giesserei - Praxis, 1984, 11, 177-187.

55. Itofuji, H, Kawano, Y, Yamamoto, S, Inoyama, N, Yoshida, H, Chang, B. Transactions of the American Foundrymen's Society, 1983, **91**, 313-324.

56. Xijun, D, Peiyue, Z, Qifu, L. In: Proceedings of 3rd International Symposium on Physical Metallurgy of Cast Iron, Stockholm, Sweden, August 29-31, 1984.

57. Hrusovsky, J P. Formation, Production and Properties of Compacted Graphite Iron. PhD Thesis, Case Western Reserve University, USA, May 1982.

58. Johnson, W C, Smartt, H B. Metallurgical Transactions, 1977, **8A**, 553-565.

59. Johnson, W C, Smartt, H B. Scripta Metallurgica, 1975, **9**, 1205-1210.

60. M^{c}Swain, R H, Bates, C E. In: Proceedings of 2nd Symposium on Metallurgy of Cast Iron, Geneva, Switzerland, May 29-31, 1974.

61. Jackson, K A. In: Progress in Solid State Chemistry, Vol 4, Chap 2. Ed: H Reiss. Pergamon Press, 1967.

62. Sadocha, J P, Gruzleski, J E. In: Proceedings of 2nd Symposium on Metallurgy of Cast Iron, Geneva, Switzerland, May 29-31 , 1974.

63. Handbook of Chemistry and Physics, 65th Edition, 1984. Ed: R C Weast. CRC Press.

64. Lalich, M J. In: Proceedings of 2nd Symposium on Metallurgy of Cast Iron, Geneva, Switzerland, May 29-31, 1974.

65. Muzumdar, K M, Wallace, J F. Transactions of the American Foundrymen's Society, 1973, 81, 412-423.

66. Olette, M, Kohn, A, Kozakevitch, P. Fonderie, 1965, 229, 87-99.

67. Kusakawa, T. In: Proceedings of 3rd International Symposium on Physical Metallurgy of Cast Iron, Stockholm, Sweden, August 29-31, 1984.

68. Taran, Yu N, Lev, I E, Belai, G E, Yatsenko, A I. Russian Castings Production, 1965, 8, 358-360.

69. Lyubchenko, A P, Mozharov, M V, Bobro, Y G. Physics of Metals and Metallography, 1961, 12, 2, 63-68.

70. Fidos, H. AFS International Cast Metals Research Journal, 1980, 5, 23-29.

71. Fidos, H. In: Proceedings of 49th International Foundry Congress, Chicago, April 14-17, 1982.

72. Lyubchenko, A P, Mozharov, M V. Russian Castings Production, 1965, 159-164.

73. Bolotov, I E, Syreishchikova, V I, Guterman, S G. Physics of Metals and Metallography, 1957, 4, 144-146.

74. Lyubchenko, A P, Sherman, D G, Mozharov, M V. Russian Castings Production, 1963, 280-282.

75. Skrebtsov, A M. Metalloved. Term. Okrab. Met., 1982, 9, 47-49.

76. Hughes, I C H. Journal of the Australian Institute of Metals, 1965, 10, 1, 4-16.

77. Van Rooyen, G T, Paul, G. Metal Science, 1974, 8, 370-382.

78. Pohl, D, Roos, E, Scheil, E. Giesserei Technisch Wissenschaftliche Beihefte, 1960, 27, 1513-1521.

79. Parthasarathi, M N. Journal of the Indian Institute of Metals, 1951, 5, 227.

80. Morrogh, H, Williams, W J. Journal of the Iron and Steel Institute, 1947, 155, 321-371.

81. Kevarian, J, Taylor, H F, Wulff, J. American Foundryman, 1953, 23, 85-91.

82. Evans, E R, Dawson, J V, Lalich, M J. AFS International Cast Metals Journal, June 1976, 13-18.

83. Scheinert, H, Liesenberg, O. Giessereitechnik, 1978, 24, 4, 108-112.

84. Nechtelberger, E, Puhr, H, von Nesselrode, J B, Nakayasu, A. In: Proceedings of 49th International Foundry Congress, Chicago, April 14-17, 1982.

85. Young, S. In: Proceedings of 46th International Foundry Congress, Madrid, 1979.

86. Mountford, F A. British Foundryman, 1966, 59, 4, 141-151.

87. Powell, J. British Foundryman, 1984, 77, 11, 472-483.

88. In: Typical Microstructures of Cast Meals, 3rd Edition. Eds: Boultbee, E F, Schofield, G A. Institute of British Foundrymen, 1981.

89. Naro, R L, Wallace, J F. AFS Cast Metals Research Journal, 1970, 16, 131-134.

90. Elliott, J F, Gleiser, M, Ramakrishna, V. Thermochemistry for Steelmaking Vol 2. Addison-Wesley, 1963.

91. Tartera, J. AFS International Cast Metals Journal, 1980, 5, 4, 7-14.

92. Ruff, G F, Wallace, J F. Transactions of the American Foundrymen's Society, 1976, 84, 705-728.

93. Basutkar, P K, Yew, S A, Loper, C R. Transactions of the American Foundrymen's Society, 1969, 77, 321-328.

94. Gomstock, G. Titanium in Iron and Steel. John Wiley, 1955.

95. Kubaschewski, O. Iron-Binary Phase Diagrams. Springer-Verlag, 1982.

96. Kagawa, A, Okamoto, T. In: Proceedings of 3rd International Symposium on Physical Metallurgy of Cast Iron, Stockholm, Sweden, August 29-31, 1984.

97. Oldfield, W. Transactions of the American Foundrymen's Society, 1971, 79, 455-458.

98. Lyubchenko, A P. Russian Castings Production, 1972, 9, 375-376.

99. Sofroni, L, Riposan, I, Chira, I. In: Proceedings of 2nd Symposium on Metallurgy of Cast Iron, Geneva, Switzerland, May 29-31, 1974.

100. Sawyer, J C, Wallace, J F. Transactions of the American Foundrymen's Society, 1968, 76, 386-404.

101. Horie, H. Journal of the Japanese Foundrymen's Society, 1982, 54, 5, 295-300.

102. Linebarger, H F, M^{c}Cluhan, T K. In: Proceedings of Symposium on Industrial Applications of Rare Earth Elements, Las Vegas, USA, August 25-26, 1980, American Chemical Society.

103. Morrogh, H. Transactions of the American Foundrymen's Society, 1952, 60, 439.

104. Gschneidner, K A. Rare Earth Alloys. Van Nostrand, 1961.

105. Cooper, K P, Loper, C R. Transactions of the American Foundrymen's Society, 1978, 86, 267-272.

106. Sekimoto, Y, Igarashi, Y, Kojo, K. In: Proceedings of 3rd International Symposium on Physical Metallurgy of Cast Iron, Stockholm, Sweden, August 29-31, 1984.

107. Tsutsumi, N, Imamura, M, Hashida, Y, Hori, S. Report of the Castings Research Laboratory, Waseda University. Report No 32, November 1981, 33-41.

108. Dunks, C M. Foundry Trade Journal, 1981, 151, 3217, 108 and 110.

109. Moor, D W, Hearnshaw, B M. Foundry Trade Journal, 1981, 151, 3217, 90-107.

110. Michie, D. Transactions of the American Foundrymen's Society, 1983, 91, 855-866.

111. Fowler, J, Stefanescu, D M, Prucha, T. Transactions of the American Foundrymen's Society, 1983, 91, 361-372.

112. Private communication with Dhr van der Randen, De Globe Foundries, Tegelen-Belfeld, the Netherlands, May 1983.

113. Best, K J, Gumbinger, D, Hillner, G F. Foundry M & T, 1982, 11, 72 and 75.

114. Simmons, W, Briggs, J. In: Proceedings of 49th International Foundry Congress, Chicago, April 14-17, 1982.

115. Rice, M A, Malizio, A B, Brooks, H F. Transactions of the American Foundrymen's Society, 1974, 82, 15-26.

116. Stefanescu, D M, Loper, C R. Giesserei-Praxis, 1981, 5, 73-96.

117. Sissener, J, Smelteverk, B. AFS Cast Metals Research Journal, 1972, 8, 178-181.

118. Private communication with Hr J von Nesselrode, Krupp Mak Maschinenbau GmbH, Kiel, West Germany, May 1983.

119. Krivosheev, A E, Belai, G E, Rudnitskii, L S, Bokov, L F. Russian Castings Production, 1967, 3, 116-119.

120. Stefanescu, D M, Loper, C R. Transactions of the American Foundrymen's Society, 1981, 89, 425-436.

121. Ansara I. Thermochemical Data for the Steel Industry Vol 2. Commission des Communautes Europeennes Recherche CECA No 7210-CA/3/303. November 1981.

122. Evans, W J, Carter, S F, Wallace, J F. Transactions of the American Foundrymen's Society, 1981, 89, 293-322.

123. M^{c}Cluhan, T K. Transactions of the American Foundrymen's Society, 1967, 75, 372-375.

124. Stefanescu, D M, Voigt, R C, Loper, C R. Transactions of the American Foundrymen's Society, 1981, **89**, 119-130.

125. Gschneidner, K A, Kippenhan, N. Rare Earth Information Centre, Report No IS-RIC-5. Rare Earth Information Centre, Ames, Iowa 50010, USA.

126. Vahed, A, Kay, D A R. Metallurgical Transactions, 1975, **6B**, 285-287.

127. Sigworth, G K, Elliott, J F. Metal Science, 1974, **8**, 298-310.

128. Stefanescu, D M, Martinez, F. Transactions of the American Foundrymen's Society, 1982, **90**, 39-46.

129. Martinez, F, Stefanescu, D M. Transactions of the American Foundrymen's Society, 1983, **91**, 593-606.

130. Stefanescu, D M, Martinez, F, Chen, I G. Transactions of the American Foundrymen's Society, 1983, **91**, 205-216.

131. Loper, C R, Lalich, M J, Park, H J, Gyarmaty, A M. In: Proceedings of 46th International Foundry Congress, Madrid, 1979.

132. Kimura, T, Loper, C R, Cornell, H H. Transactions of the American Foundrymen's Society, 1980, **88**, 443-450.

133. Cornell, H H, Loper, C R, Pan, E N, Ogi, K. Transactions of the American Foundrymen's Society, 1984, **92**, 401-408.

134. Gan, Y, Loper, C R. Transactions of the American Foundrymen's Society, 1983, **91**, 807-814.

135. Pan, E N, Ogi, K, Cornell, H H, Loper, C R. Transactions of the American Foundrymen's Society, 1982, **90**, 82-121.

136. Riposan, I, Sofroni, L. AFS International Cast Metals Journal, 1978, **3**, 23-28.

137. Roach, R. FWP Journal, 1979, **19**, 12, 7-20.

138. Sergeant, G F, Evans, E R. British Foundryman, May 1978, 115-124.

139. Schellong, R D. AFS Cast Metals Research Journal, 1967, **3**, 1, 30-38.

140. Foundry Practice No 200 (December 1979). Foseco International Ltd.

141. Foote Mineral Company, Ferroalloy Division. Technical Data Bulletin No 243-A.

142. Foseco International Ltd UK Patent No 2066297. Foundry Trade Journal, January 1983, 107.

143. Ruff, G F, Vert, T C. Transactions of the American Foundrymen's Society, 1979, **87**, 459-464.

144. Altstetter, J D, Nowicki, R M. Transactions of the American Foundrymen's Society, 1982, **90**, 959-970.

145. Donaldson, E G. Casting Engineering and Foundry World, 1982, Fall, 23-32.

146. Ahmed, W U, Gawlick, L J. Modern Casting, 1983, **73**, 1, 20-21.

147. Private communication with Hr K Wackermann, Production Manager, August Kupper Foundry, Heiligenhaus, West Germany, May 1983.

148. Elliott, J F, Gleiser, M. Thermochemistry for Steelmaking Vol 1. Addision-Wesley, 1960.

149. Gatellier, C. Thermochemical Data for the Steel Industry Vol 2. Communautes Europeennes Recherche CECA No 7210-CA/3/303. November 1981.

150. Vahed, A, Kay D A R. Metallurgical Transactions, 1976, **7B**, 375-383.

151. Oldfield, W. British Cast Iron Research Association Journal, 1960, **8**, 177-192.

152. I Minkoff. The Physical Metallurgy of Cast Iron. John Wiley and Sons, 1983.

153. Wilson, W G, Kay, D A R, Vahed, A. Journal of Metals, 1974, **26**, 14-23.

154. Murray, J L. Bulletin of Alloy Phase Diagrams, 1981, **2**, 2, 197-201.

155. Miller, G L. Zirconium. Book 2 in series on the Metallurgy of the Rarer Metals. Butterworths Scientific Publications, 1957.

156. Norton, J T, Mowry A L. Metals Transactions, 1949, **1**, 1, 133-136.

157. Underwood, E E, Berry J T. Transactions of the American Foundrymen's Society, 1981, **89**, 755-766.

158. Underwood, E E. Acta Stereol, 1982, 103-121.

159. Tsutsumi, N, Imamura, M. Report of the Casting Research Laboratory, Waseda University, Japan, Report No 33, 1982, 25-31.

160. White, C V, Flinn, R A, Trojan, P K. Transactions of the American Foundrymen's Society, 1981, **89**, 639-644.

161. American Society for the Testing of Metals. Special Technical Publication No A247-67 (reapproved 1972).

APPENDIX I

Melt Treatment Additions and X-ray Fluorescence Analyses

Melt Treatments and X-Ray Fluorescence Analyses

(a) Mischmetall-Calcium Treatments

CASTING REFERENCE	% ADDITION		XRF ANALYSIS (wt %): Before (A) and After (B) treatment									
	Ca	MM		C	Si	Mn	S	P	Ce	Ca	La	Ti
1/1	0.48	0.06	A	3.76	1.86	0.15	0.013	0.017	<0.001	0.0006	N/A	0.021
			B	3.79	3.02	0.16	0.013	0.017	0.020	0.0044	N/A	0.025
1/2	0.26	0.03	A	3.91	1.90	0.54	0.013	0.019	<0.001	0.0013	N/A	0.026
			B	3.53	2.78	0.60	0.013	0.021	0.004	0.0020	N/A	0.030
1/3	0.38	0.045	A	3.70	1.87	0.22	0.013	0.017	<0.001	0.0009	N/A	0.034
			B	3.57	2.86	0.24	0.012	0.017	0.007	0.0029	N/A	0.038
1/4	0.59	0.03	A	3.76	1.62	0.21	0.011	0.027	<0.001	0.0007	N/A	N/A
			B	3.56	2.96	0.24	0.010	0.023	0.011	0.0087	N/A	N/A
1/5	0.20	0.021	A	3.90	2.24	0.25	0.014	0.026	<0.001	<0.0010	N/A	N/A
			B	3.75	2.95	0.26	0.011	0.027	0.005	<0.0020	N/A	N/A
1/6	0.16	0.016	A	3.82	1.86	0.21	0.012	0.023	<0.001	0.0010	N/A	N/A
			B	3.70	2.46	0.21	0.011	0.023	0.004	0.0020	N/A	N/A
1/7	0.16	0.052	A	3.73	1.93	0.23	0.012	0.023	<0.001	<0.0010	N/A	N/A
			B	3.76	2.64	0.23	0.014	0.025	0.007	0.0010	N/A	N/A
1/8	0.14	0.04	A	3.92	2.01	0.22	0.011	0.023	<0.001	0.0002	N/A	0.030
			B	3.83	2.69	0.22	0.011	0.023	0.006	0.0013	N/A	0.032
1/9	0.11	0.03	A	3.96	2.19	0.21	0.012	0.025	<0.001	0.0010	N/A	N/A
			B	3.88	2.58	0.22	0.011	0.019	0.010	0.0012	N/A	N/A
1/10	0.42	0.01	A	3.90	1.80	0.23	0.015	0.022	<0.001	<0.0010	N/A	0.027
			B	3.74	2.84	0.23	0.014	0.022	0.003	0.0040	N/A	0.031
1/11	0.25	0.005	A	3.86	1.70	0.24	0.013	0.019	<0.001	<0.0010	N/A	0.029
			B	3.78	2.54	0.23	0.011	0.019	<0.001	0.0020	N/A	0.032
1/12	0.00	0.021	A	4.00	2.24	0.20	0.017	0.022	<0.001	0.0016	N/A	0.028
			B	3.99	2.23	0.20	0.018	0.022	0.002	0.0008	N/A	0.030

CASTING REFERENCE	% ADDITION		XRF ANALYSIS (wt %): Before (A) and After (B) treatment									
	Ca	MM		C	Si	Mn	S	P	Ce	Ca	La	Ti
1/13	0.17	0.00	A	4.04	1.03	0.24	0.010	0.021	<0.001	0.0006	N/A	0.024
			B	4.06	5.10	0.21	0.0097	0.031	<0.001	0.0027	N/A	0.039
1/14	0.00	0.075	A	3.78	2.61	0.21	0.0059	0.028	<0.001	0.0008	N/A	0.029
			B	3.68	3.11	0.22	0.0072	0.026	0.026	0.0007	N/A	0.030
1/15	0.00	0.14	A	3.78	2.61	0.21	0.0059	0.028	<0.001	0.0008	N/A	0.029
			B	3.68	2.97	0.23	0.0082	0.025	0.060	0.0006	N/A	0.030
1/16	0.00	0.05	A	3.81	2.56	0.24	0.0084	0.023	<0.001	0.0006	N/A	0.026
			B	3.65	3.18	0.23	0.0073	0.024	0.008	0.0005	N/A	0.029
1/17	0.00	0.125	A	3.81	2.56	0.24	0.0084	0.023	<0.001	0.0006	N/A	0.026
			B	3.66	3.08	0.24	0.0085	0.022	0.029	0.0005	N/A	0.029
1/18	0.00	0.048	A	4.01	2.32	0.21	0.0070	0.032	0.0028	0.0007	N/A	0.029
			B	3.92	2.90	0.21	0.0074	0.033	0.016	0.0007	N/A	0.034
1/19	0.00	0.092	A	4.01	2.32	0.21	0.0070	0.032	0.0028	0.0007	N/A	0.029
			B	3.90	2.90	0.21	0.0088	0.027	0.030	0.0006	N/A	0.031
1/20	0.36	0.016	A	3.91	1.62	0.20	0.006	0.031	0.0028	0.0006	N/A	0.050
			B	3.78	2.62	0.19	0.0048	0.032	0.0062	0.0029	N/A	0.055
1/21	0.22	0.076	A	3.91	1.62	0.20	0.006	0.031	0.0028	0.0006	N/A	0.050
			B	3.82	2.67	0.19	0.0044	0.032	0.026	0.0019	N/A	0.055
1/22	0.48	0.00	A	3.90	1.07	0.25	0.0025	0.028	0.0037	0.0011	N/A	0.053
			B	3.70	2.17	0.21	0.0009	0.030	0.0007	0.0036	N/A	0.052
1/23	0.79	0.00	A	3.90	1.07	0.25	0.0025	0.028	0.0037	0.0011	N/A	0.053
			B	3.70	2.39	0.21	0.0005	0.034	0.0042	0.0043	N/A	0.053
1/24	0.36	0.00	A	3.72	1.73	0.22	0.005	0.028	0.0022	0.0009	N/A	0.049
			B	3.65	2.82	0.21	0.004	0.030	0.0005	0.0028	N/A	0.051
1/25	0.00	0.20	A	3.60	2.57	0.25	0.005	0.029	0.007	N/A	N/A	0.057
			B	3.55	3.15	0.25	0.006	0.026	0.081	N/A	N/A	0.058

CASTING REFERENCE	% ADDITION		XRF ANALYSIS (wt %): Before (A) and After (B) treatment									
	Ca	MM		C	Si	Mn	S	P	Ce	Ca	La	Ti
1/26	0.00	0.06 (Lanthanum -MM)	A	3.85	2.32	0.23	0.0019	0.020	<0.001	N/A	0.007	0.053
			B	3.79	2.95	0.23	0.0019	0.019	<0.001	N/A	0.041	0.056
1/27	0.00	0.16 (Lanthanum -MM)	A	3.85	2.32	0.23	0.0019	0.020	<0.001	N/A	0.007	0.053
			B	3.79	2.64	0.24	0.0019	0.020	<0.001	N/A	0.125	0.054

Notes

MM = Cerium mischmetall unless otherwise stated
N/A = Not analysed

SIMS Analysis Samples

B - 1/25
C - 1/27
E - 1/1
F - 1/3

(b) Magnesium-Titanium Treatments

CASTING REFERENCE	% ADDITION		XRF ANALYSIS (wt %): Before (A) and After (B) treatment							
	Mg	Ti		C	Si	Mn	P	S	Mg	Ti
2/1	0.08	0.10	A	3.93	1.77	0.22	0.024	0.010	0.003	0.11
			B	3.79	2.91	0.22	0.024	0.013	0.012	0.12
2/2	0.045	0.04	A	3.77	1.60	0.23	0.024	0.005	0.004	0.06
			B	3.71	2.71	0.24	0.022	0.006	0.014	0.068
2/3	0.082	0.04	A	3.77	1.60	0.23	0.024	0.005	0.004	0.06
			B	3.68	2.59	0.24	0.025	0.006	0.018	0.069
2/4	0.025	0.07	A	3.98	1.57	0.23	0.021	0.0043	0.001	0.090
			B	3.83	2.57	0.22	0.022	0.0052	0.005	0.095
2/5	0.00	0.00	A	3.82	2.11	0.22	0.022	0.0050	<0.001	0.033
			B	3.70	2.72	0.21	0.021	0.0065	<0.001	0.037
2/6	0.00	0.17	A	3.82	2.11	0.22	0.022	0.0050	<0.001	0.033
			B	3.67	2.66	0.21	0.022	0.0058	<0.001	0.10
2/7	0.05	0.10	A	4.04	1.22	0.22	0.023	0.0067	<0.001	0.10
			B	3.85	2.69	0.22	0.027	0.0060	0.028	0.10
2/8	0.13	0.10	A	4.04	1.22	0.22	0.023	0.0067	<0.001	0.10
			B	3.92	2.31	0.22	0.026	0.0060	0.021	0.11
2/9	0.046	0.00	A	3.81	1.83	0.22	0.024	0.0053	<0.001	0.024
			B	3.70	2.84	0.22	0.024	0.0052	0.010	0.032
2/10	0.069	0.00	A	3.81	1.83	0.22	0.024	0.0053	<0.001	0.024
			B	3.67	2.70	0.22	0.027	0.0051	0.013	0.031
2/11	0.042	0.07	A	3.87	1.50	0.22	0.027	0.006	0.008	0.079
			B	3.74	2.64	0.22	0.025	0.006	0.007	0.081
2/12	0.103	0.07	A	3.87	1.50	0.22	0.027	0.006	0.008	0.079
			B	3.66	2.86	0.22	0.028	0.005	0.026	0.081

CASTING REFERENCE	% ADDITION		XRF ANALYSIS (wt %): Before (A) and After (B) treatment							
	Mg	Ti		C	Si	Mn	P	S	Mg	Ti
2/13	0.044	0.17	A	4.02	1.67	0.16	0.026	0.004	0.003	0.14
			B	3.80	3.23	0.18	0.028	0.004	0.017	0.182
2/14	0.110	0.17	A	4.02	1.67	0.16	0.026	0.004	0.003	0.14
			B	3.84	2.91	0.18	0.026	0.004	0.033	0.174
2/15	0.018	0.00	A	4.01	1.63	0.22	0.027	0.005	<0.001	0.023
			B	3.84	2.87	0.22	0.026	0.005	0.005	0.031
2/16	0.091	0.17	A	3.94	1.51	0.21	0.026	0.007	0.008	0.17
			B	3.74	2.74	0.22	0.026	0.007	0.022	0.18
2/17	0.042	0.14	A	3.87	1.56	0.19	0.025	0.004	<0.001	0.11
			B	3.71	2.84	0.20	0.026	0.004	0.008	0.13
2/18	0.104	0.04	A	3.92	1.61	0.18	0.027	0.0065	<0.001	0.05
			B	3.76	3.01	0.19	0.028	0.0064	0.027	0.055

SIMS Analysis Samples

A - 2/5
D - 2/8
H - 2/14

(c) Magnesium-Aluminium, Calcium-Zirconium, and Magnesium-Zirconium Treatments

CASTING REFERENCE	ADDITIONS		XRF ANALYSIS (wt %): Before (A) and After (B) treatment									
			C	Si	Mn	S	P	Ti	Ca	Mg	Zr	Al
3/1	0.08% Mg, 0.41% Al	A	3.95	1.95	0.005	0.0034	0.027	0.033	N/A	0.014	N/A	0.04
		B	3.77	2.81	0.017	0.0032	0.025	0.038	N/A	0.032	N/A	0.25
4/1	0.60% Ca, 0.5% Zr	A	3.95	0.78	0.24	0.0058	0.026	0.054	0.001	0.005	0.007	N/A
		B	3.59	2.75	0.23	0.0042	0.027	0.057	0.005	0.003	0.20	N/A
4/2	0.055% Mg, 0.5% Zr	A	3.95	0.78	0.24	0.0058	0.026	0.054	0.001	0.005	0.007	N/A
		B	3.71	2.82	0.23	0.0046	0.029	0.056	0.002	0.005	0.18	N/A

Note

N/A = Not Analysed

SIMS Analysis Samples

I - 3/1
J - 4/1

APPENDIX II

Nodularity Assessment Methods

Nodularity Assessment Methods

Several techniques to assess the percentage nodularity of the microstructures were considered before adopting the procedure described in Section 5.2.2.

The simple estimation method involves comparing the microstructure of the sample in question with memorised or actual photographic or schematic standards, and is commonly used in the industry to give a rapid assessment of treated metal prior to casting. However, the results depend greatly on the discretion of the assessor, and this is clearly illustrated in Table 3 which reveals significant differences in the nodularities assigned to seven samples by two different estimators who were experienced in using the technique.

Image analysis has been reported in a number of publications (157-160) as a technique for evaluating the nodularity of microstructures. This method employs a computer to distinguish between different graphite forms and, according to White et al (160), it produces less biased and more reproducible results than manual estimation techniques. Unfortunately, the required computer software was not available for the image analysis facilities at the University, and it was considered that the time needed to develop the appropriate programme was much greater than the time saved by not using a reliable manual estimation method.

A standard line counting procedure which involved placing a grid over an image of the specimen on a closed-circuit television screen and comparing the number of intersections with nodular and compacted graphite particles, resulted in errors due to the difference in shape between these two graphite forms. For example, consider two pieces of graphite of similar area on the screen, one compacted and

one nodular. The compacted graphite particle would on average intersect with a greater number of lines than the nodule owing to the shape difference. This has the overall effect of increasing the recorded percentage of compacted graphite relative to that of the spheroidal form.

The latter problem is avoided when using the point counting method. This involved placing a grid of equally-spaced points over the television screen and comparing the number occuring within nodules with the number occuring within compacted graphite particles. To produce an accurate measurement of the nodularity however, either the spacing between the grid points must be small, or the magnification on the television screen must be high so that a significant number of points occur in all graphite particles. To produce an average nodularity value for the whole specimen, the technique is very tiring and time-consuming.

A technique involving physically counting the number of nodular and compacted graphite particles in several areas of the specimen was eventually adopted on the grounds that it gives reasonably accurate and reproducible results (160), and that it is the method recommended by the American Society for Testing and Materials (161).

Sample	First Assessor % Nodularity	Second Assessor % Nodularity	Difference
1	10	10	0
2	20	20	0
3	25	20	5
4	30	50	20
5	50	40	10
6	50	60	10
7	60	40	20

Table 3 Difference in Results Obtained by Two Different Assessors Using the Simple Estimation Method

APPENDIX III

Percentage Nodularity and 4 mm Section Hardness Values

(a) Mischmetall-Calcium Treated Irons

CASTING REFERENCE	Average Nodularity Measured in Sections (% Nodules)							Average Hardness of 4 mm Section(Hv)
	4 mm	7 mm	10 mm	14 mm	18 mm	20 mm	25 mm	
1/1	82	65	62	66	59	43	63	166
1/2	68	35	19	6	2	5	4	194
1/3	63	67	44	43	42	50	43	362
1/4	90	61	53	61	72	65	75	320
1/5	85	45	32	13	12	12	19	176
1/6	FLAKE	FLAKE	FLAKE	FLAKE	FLAKE	FLAKE	FLAKE	149
1/7	65	30	19	7	4	4	3	261
1/8	78	34	34	8	8	8	9	274
1/9	67	26	10	-	-	-	7	184
1/10	57	35	-	-	-	-	48	167
1/11	43	20	18	15	17	15	18	196
1/12	FLAKE	FLAKE	FLAKE	FLAKE	FLAKE	FLAKE	FLAKE	155
1/13	FLAKE	FLAKE	FLAKE	FLAKE	FLAKE	FLAKE	FLAKE	168
1/14	93	25	-	-	-	-	8	204
1/15	81	79	-	-	-	-	68	607
1/16	61	42	-	-	-	-	9	205
1/17	80	82	-	-	-	-	73	232
1/18	FLAKE	FLAKE	FLAKE	FLAKE	FLAKE	FLAKE	FLAKE	130
1/19	59	25	-	-	-	-	36	208
1/20	55	18	-	-	-	-	25	233
1/21	78	60	-	-	-	-	25	217
1/22	75	22	-	-	-	-	25	358
1/23	61	35	-	-	-	-	41	270
1/24	61	17	-	-	-	-	3	326
1/25	92	-	-	-	-	-	50	560
1/26	90	-	-	-	-	-	4	612
1/27	90	-	-	-	-	-	15	595

Notes

Castings 1/26 and 1/27 were treated with Lanthanum mischmetall

Average value of the 4 mm section hardness for non-flake graphite castings treated with a combined cerium mischmetall-calcium addition = Hv 229

(b) Magnesium-Titanium Treated Irons

CASTING REFERENCE	Average Nodularity Measured in Sections (% Nodules)							Average Hardness of 4 mm Section (Hv)
	4 mm	7 mm	10 mm	14 mm	18 mm	20 mm	25 mm	
2/1	75	21	-	-	-	-	6	235
2/2	70	19	11	5	4	6	4	246
2/3	53	32	-	-	-	-	13	208
2/4	FLAKE	FLAKE	FLAKE	FLAKE	FLAKE	FLAKE	FLAKE	223
2/5	FLAKE	FLAKE	FLAKE	FLAKE	FLAKE	FLAKE	FLAKE	119
2/6	FLAKE	FLAKE	FLAKE	FLAKE	FLAKE	FLAKE	FLAKE	161
2/7	51	17	-	-	-	-	10	212
2/8	95	91	-	-	-	-	70	222
2/9	64	15	-	-	-	-	8	184
2/10	63	31	-	-	-	-	23	215
2/11	61	12	-	-	-	-	2	215
2/12	59	56	-	-	-	-	16	214
2/13	26	18	-	-	-	-	17	197
2/14	61	30	-	-	-	-	25	202
2/15	FLAKE	FLAKE	FLAKE	FLAKE	FLAKE	FLAKE	FLAKE	113
2/16	55	26	-	-	-	-	18	222
2/17	35	20	-	-	-	-	12	208
2/18	62	43	-	-	-	-	32	214

(c) Magnesium-Aluminium, Calcium-Zirconium, and Magnesium-Zirconium Treated Irons

CASTING REFERENCE	Average Nodularity Measured in Sections (% Nodules)							Average Hardness of 4 mm Section (Hv)
	4 mm	7 mm	10 mm	14 mm	18 mm	20 mm	25 mm	
3/1	58	16	-	-	-	-	17	231
4/1	14	2	3	2	2	2	1	551
4/2	40	15	13	10	9	8	8	188

Note

Average value of the 4 mm section hardness for non-flake graphite castings produced using a combined magnesium-titanium treatment = Hv 216

APPENDIX IV

Origins and Microstructures of Samples Analysed Using SIMS

Sample Code	Casting Reference	Melt Treatment	Graphite Structure
A	2/5	None	ASTM Type A flake
B	1/25	0.20% Cerium Mischmetall	52% nodules, 48% CG
C	1/27	0.16% Cerium-free MM	15% nodules, 85% CG
D	2/8	0.13% Mg; 0.10% Ti	70% nodules, 30% CG
E	1/1	0.48% Ca; 0.06% Ce-MM	63% nodules, 37% CG
F	1/3	0.38% Ca; 0.045% Ce-MM	43% nodules, 57% CG
G	-	*	100% nodules
H	2/14	0.110% Mg; 0.17% Ti	25% nodules, 75% CG
I	3/1	0.08% Mg; 0.41% Al	17% nodules, 83% CG
J	4/1	0.60% Ca; 0.5% Zr	1% nodules, 99% CG

* Sample G composition: C 3.60%, Si 2.51%, Mn 0.30%, S 0.021%, P 0.024%, Mg 0.051%, Ce 0.003%

ACKNOWLEDGEMENTS

I would like to express my appreciation to the Science and Engineering Research Council for supporting the investigation, and to Professor R J Sury for the provision of laboratory facilities.

Grateful thanks are also due to:

Bill Simmons, David Pattle and Foseco International Ltd for the provision of X-ray fluorescence analyses, certain materials, and for several useful discussions.

Leopold Lazurus Ltd for the provision of pig iron.

Dr David Sykes of Loughborough Consultants Ltd for the use of the SIMS facility.

Bert Goodman and Alf Haigh for helping in many practical aspects of the research programme.

Finally, I am deeply indebted to Dr R A Stark for his supervision of the research project.